A Full Hydro- and Morphodynamic Description of Breaker Bar Development

Jacobsen, Niels Gjøl

Publication date:
2011

Document Version
Publisher's PDF, also known as Version of record

A Full Hydro- and Morphodynamic Description of Breaker Bar Development

PhD Thesis

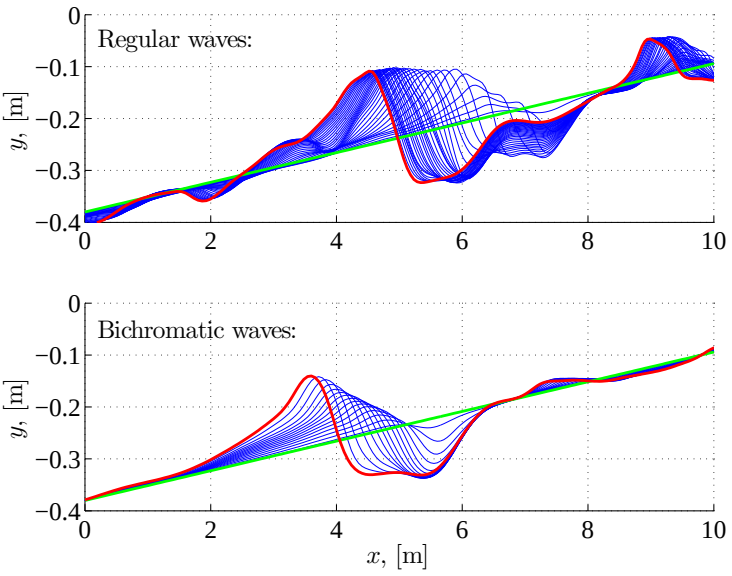

Niels Gjøl Jacobsen
DCAMM Special Report No. S136
April 2011

DTU Mechanical Engineering
Department of Mechanical Engineering

A Full Hydro- and Morphodynamic Description of Breaker Bar Development

Niels Gjøl Jacobsen

April 2011

Department of Mechanical Engineering
Section of Coastal, Maritime and Structural Engineering
Technical University of Denmark

Published in Denmark by
Technical University of Denmark

Section of Coastal, Maritime and Structural Engineering
Department of Mechanical Engineering
Technical University of Denmark
Nils Koppels Alle, Building 403, DK–2800 Kgs. Lyngby, Denmark
Phone +45 4525 1360, Telefax +45 4588 4325
E-mail: info.skk@mek.dtu.dk
WWW: http://www.mek.dtu.dk/

Publication Reference Data

Jacobsen, N. G.
A Full Hydro- and Morphodynamic Description of Breaker Bar Development
PhD Thesis
Technical University of Denmark, Department of Mechanical Engineering
DCAMM Special Report, no. S136
April, 2011
ISBN: 978-87-90416-64-5
Keywords: Cross shore sediment transport, morphological development, breaker bars, free surface modelling, VOF method, wave breaking, RANS equations

Contents

Nomenclature

Conventions, Operators and Indices

Conventions

a/A	Scalar
$\mathbf{a}$	Vector / Tensor of rank 1
$\mathbf{A}$	Tensor of rank 2

Subscript

$\square_0$	(i) Deep water properties (ii) Property for $\gamma = 0$
$\square_1$	Property for $\gamma = 1$
$\square_b$	Related to bed load
$\square_B$	Break point parameters
$\square_c$	Value at the crest of the breaker bar
$\square_e$	Edge interpolated value on finite area mesh
$\square_{eq}$	Equilibrium property
$\square_f$	Quantity taken on cell face
$\square_{model}$	Model solution in relaxation zone
$\square_{nw}$	Component of field in computational cell next to a wall
$\square_p$	Potential theory
$\square_{\text{rms}}$	Root mean square of a given quantity
$\square_s$	Related to suspended sediment transport
$\square_{target}$	Target solution in relaxation zone

$\Box_\tau$ Tangential component of a vector at the wall

$\Box_w$ Quantity taken on wet part of face / cell

Superscript

$\Box^+$ Component given in terms of wall coordinates, $\Box^+ = \Box u_f/\nu$

$\Box^*$ Predicted value in the bed level filtering routine

$\Box^{**}$ Corrected value in the bed level filtering routine

$\Box^I$ Incident harmonic wave amplitude

$\Box^R$ Reflected harmonic wave amplitude

Operators

δ Numerical differentiation

$\cdot$ Inner product

$:$ Double inner product

$\times$ Cross product

∇ Gradient operator, $(\partial/\partial x, \partial/\partial y, \partial/\partial z)^T$

∇_h Two-dimensional, horizontal gradient operator, $(\partial/\partial x, \partial/\partial y$ (z is assumed vertical)

$\hat{\Box}$ 90° counter clockwise rotation of 2D vector

$\Box^T$ Transpose of a tensor of either rank 1 or 2

$\tilde{\Box}$ Ensemble averaging

$\bar{\Box}$ Averaging

Greek Characters

α (i) Wave propagation direction relative to global coordinate system (ii) Turbulence closure coefficient (iii) Motion of bed load relative to the direction of the bed shear stress

α_1 Number of grain diameter from bed, where velocity gradient is evaluated

α_c Response function in behavioural modelling

α_R Relaxation zone weight

β	(i) Slope of the bed (ii) Turbulence closure coefficient
β_0	Turbulence closure coefficient
β^*	Turbulence closure coefficient
χ_ω	Turbulence closure coefficient
χ_R	Relaxation zone coordinate
δ_b	Distance from the bed, where the reference concentration is defined
ϵ	Turbulent dissipation rate
ϵ_C	Error due to the curvature of the FAM mesh
η	Surface elevation
η_p^*	Approximate surface elevation over single computational element
γ	VOF-ratio function
γ_m	Diffusion parameter on the mesh motion
κ	von Karman's constant
κ_γ	Curvature of the free surface
λ	Width of the relaxation zone
λ_b	Linear concentration
λ_{Bs}	Spatial lag between point of breaking and maximum sediment flux
μ	Dynamic molecular viscosity
μ_d	Dynamic friction coefficient
μ_s	Static friction coefficient
ν	Kinematic molecular viscosity
ν_t	Kinematic eddy viscosity
$\tilde{\nu}_t$	Kinematic eddy viscosity in suspended sediment conservation equation
ω	Characteristic frequency of turbulence, $k-\omega$-model
Ω	Dean's parameter

Ω_{HK} A parameter used for classification of the cross shore sediment flux

$\mathbf{\Omega}$ Rotation tensor, $1/2(\nabla\mathbf{u} - (\nabla\mathbf{u})^T)$

ϕ (i) Velocity potential (ii) Some arbitrary scalar quantity

ϕ_r Angle of repose

ϕ_{crest} Phase lead of the friction velocity over the wave crest

ϕ_{trough} Phase lead of the friction velocity over the wave trough

Φ Some quantity in γ-weighting

$\boldsymbol{\phi}$ Some arbitrary vector

ϖ Weight on bed level change in mesh motion

ρ Density

σ Cyclic wave frequency

σ^* Turbulence closure coefficient

σ_c Schmidt number

σ_d Turbulence closure coefficient

σ_{do} Turbulence closure coefficient

σ_g Geometric standard deviation on sediment grain distribution

σ_ω Turbulence closure coefficient

σ_T Surface tension coefficient

$\theta^\pm$ Argument to each wave harmonic $(\sigma t \pm kx)$

θ' Shields parameter due to shear stress

θ'_c Critical Shields parameter due to shear stress on arbitrary bed slope

θ'_{c0} Critical Shields parameter due to shear stress on horizontal bed

τ_b Magnitude of the bed shear stress

$\boldsymbol{\tau}$ Reynolds stress tensor

ξ_s Distance from the shore to the location, where the cross shore profile becomes horizontal

ζ_0 The Irribaren number

Roman Characters

a (i) Orbital amplitude of the near bed wave motion (ii) Amplitude of wave harmonic (cos-term) (iii) Constant in bed load transport formulation

A Constant in Dean's profile

A_f Face area

AR Cell aspect ratio

b Amplitude of wave harmonic (sin-term)

B^* Bar parameter used for the number of cross shore bars

c Volumetric concentration of suspended sediment

c_0 The maximum possible volumetric concentration

c_b Bed reference concentration

c_s Coefficient including drag and lift on sediment grain

C (i) Wave celerity (ii) Quantifying the direction of cross shore sediment flux in relation to Ω_{HK}

C_{lim} Turbulence closure coefficient

$\mathbf{c}_f$ Face centre

$\mathbf{c}_V$ Volume centre

d Median grain diameter

D (i) Deposition due to suspended sediment transport (m/s) (ii) Water depth in pure current

D_v Deposition due to suspended sediment transport (m^3/s)

e_d Sediment porosity

E (i) Wave energy (ii) Erosion due to suspended sediment transport (m/s)

E_v Erosion due to suspended sediment transport (m^3/s)

$\mathbf{e}_g$	Unit vector parallel to $\mathbf{g}$. Direction follows the positive orientation of the coordinate system.
$\mathbf{e}_n$	Unit vector, $n = x, y, z$
f	Wave frequency
f_β	Turbulence closure function
f_m	Morphological acceleration factor
F	Flux contribution in the Exner equation
$\mathbf{f}_D$	Drag force on sand grain
$\mathbf{f}_f$	Friction force on sand grain
g	Magnitude of the gravity vector, $\mathbf{g}$
G	(i) Constant in the expression for $\mathbf{S}_R$ (ii) Growth factor in the mesh stretching
$\mathbf{g}$	Acceleration vector due to gravity
h	Bed level elevation / water depth
h'	Cut-off in the swash zone
h_b	Bed level in relation to bed load
h_s	Bed level in relation to suspended sediment transport
H	Wave height
H_s	Significant wave height
Δh_u	The vertical extend of the undertow profile
$\mathbf{I}$	Identity matrix
k	(i) Turbulent kinetic energy (ii) Magnitude of the wave number vector
k_N	Nikuradse' roughness height
$\bar{k}_k$	Period averaged turbulence directly from the RANS model
$\bar{k}_\mathbf{u}$	Contribution to the period averaged turbulence due to stochastic motion
K_*	Coefficients used for classification of beach states

K_R	Coefficients for computing S_R
K_S	Coefficients for computing S_R
L	The wave length
M	Miche's parameter
n	Coordinate normal to a cell face
$\mathbf{n}$	General unit normal vector
$\mathbf{n}_s$	Gradient normal to a fluid interface / boundary
$\mathbf{N}$	Normal vector of arbitrary length
p	Total pressure
p^*	Excess pressure
p_{EF}	Propability of sediment grain mobility
$\mathcal{P}_k$	Production of k
$\mathcal{P}_\omega$	Production of ω
q_b	Magnitude of the bed load transport along $\mathbf{e}_x$
q_s	Magnitude of the suspended sediment transport along $\mathbf{e}_x$
q_t	Magnitude of the total sediment transport along $\mathbf{e}_x$
$\bar{Q}_s$	Integrated cross shore suspended sediment flux
$\mathbf{q}_b$	Bed load transport vector
$\mathbf{q}_s$	Suspended sediment transport vector
R	Reflection coefficient
R_N	Reflection coefficient from a natural beach
RTR	Relative tidal range
s	Density of sediment relative to surrounding fluid
S	Beach state
S_R	Roughness function
$\mathbf{S}$	Strain tensor, $1/2(\nabla\mathbf{u} + (\nabla\mathbf{u})^T)$

$\mathbf{S}_R$	Radiation stress tensor
t	Time
t_m	Morphological time
T	Wave period
T_m	The averaging period for the morphological modelling
T_p	Peak wave period
TR	Tidal range
u	Velocity component in Cartesian coordinates
$u_{c,h}$	Net shoreward current specified at the inlet
u_f	Magnitude of the friction velocity vector
u_m	Maximum in the near bed orbital velocity
$\bar{u}_r$	Average velocity of the undertow profile
$\mathbf{u}$	Velocity field, $\mathbf{u} = (u,\ v,\ w)$
$\mathbf{u}'$	Fluctuating velocity field, $\mathbf{u}' = (u',\ v',\ w')$
$\mathbf{u}_b$	Bed load transport velocity
$\mathbf{u}_f$	Friction velocity vector
$\mathbf{u}_m$	Velocity of the vertices in the computational mesh
$\mathbf{u}_r$	Relative velocity in bed load formulation
$\mathbf{u}_{r,V}$	Relative velocity in VOF formulation
v	Velocity component in Cartesian coordinates
V	Cell volume
V_γ	Volume of water in the computational domain
w	Velocity component in Cartesian coordinates
w_s	Magnitude of the fall velocity
$\mathbf{w}$	Submerged weight of sediment grain
$\mathbf{w}_s$	Fall velocity vector

x	Spatial coordinate
$\mathbf{x}$	Coordinate vector, $\mathbf{x} = (x,\ y,\ z)$
y	Spatial coordinate
y_u	Centroid of the undertow profile
z	Spatial coordinate
z_0	Roughness height
Z	The Rouse parameter

Preface

The present Ph.D. thesis is submitted as part of the requirement for obtaining a Ph.D. degree from the Technical University of Denmark. The Ph.D. has been conducted at the Department of Mechanical Engineering under the main supervision of Dr. Techn. Jørgen Fredsøe.

I am grateful for the guidance and supervision from Jørgen Fredsøe, who has excelled in giving a clear goal for the Ph.D. study in its entity, however, still within wide boundaries.

I would also like to thank all other staff in the section of Coastal, Maritime and Structural Engineering for help and interesting discussions throughout the project. Among these special thanks should be given to associate professors Jacob H. Jensen and David R. Fuhrman and Ph.D. students Kasper H. Kærgaard and Ole Lindberg.

April 24$^{\text{th}}$ 2011, Kgs. Lyngby

Niels Gjøl Jacobsen

The present version is the revised Ph.D. thesis, where the comments from the external examiners have been incorporated. The external examiners were associate professor Diane Foster (Uni. of New Hampshire), professor Dano Roelvink (UNESCO–IHE) and professor Erik Damgaard Christensen (Tech. Uni. of Denmark), and their comments are greatly appreciated.

December 3$^{\text{rd}}$ 2011, Kgs. Lyngby

Abstract

The present thesis considers a coupled modelling approach for hydro- and morphodynamics in the surf zone, which is based on a solution to the Reynolds Averaged Navier-Stokes (RANS) equations with a Volume of Fluid (VOF) closure for the surface tracking.

The basis for the numerical approach is the surface tracking method in the open-source CFD toolbox OpenFoam®, which is released by OpenCFD®. This basic version has been extended with the ability for modelling surface water waves and sediment transport in the surf zone. The validation of these functionalities are described as part of the project. The inequilibrium in the sediment transport field leads to a morphological change in the bed level, which is incorporated through a movement of the computational mesh. This allows for an integrated coupling with the hydrodynamics. The morphological module is also developed as part of this work.

The numerical model is applied onto several physical settings. Firstly, the morphological response is turned off, and the hydrodynamics and the sediment transport patterns in the surf zone are described. The description considers these processes as a function of several non-dimensional variables, namely the surf similarity parameter, ζ_0, and Dean's parameter in various forms, Ω and Ω_{HK}. This investigation has an emphasis on (i) the spatial and temporal lag-effects in the hydrodynamics, and between the hydrodynamics and the sediment transport and (ii) the integrated net cross shore suspended sediment transport flux as a function of either of the variables ζ_0, Ω, or Ω_{HK}.

Secondly, the bed is allowed to evolve under the influence of the sediment transport processes. The development of breaker bars in both laboratory scale settings and prototype scale settings is considered. The temporal development of the cross shore profile is simulated for several combinations of wave forcing and sediment grain diameters. The variation is described with emphasis on the development of the crest level of the breaker bar, the variation in the bed shear stress on the crest of the breaker bar, and its migration speed.

Additionally, a net onshore current over a breaker bar is considered, where this current mimics the presence of a horizontal circulation cell. The

development of the breaker bar is described for different values of the net onshore current speed. This description is undertaken with and without a coupling to the morphology.

Abstract in Danish

Denne afhandling betragter en integreret løsningsmetode til hydro- og morfodynamikken i brydningszonene. Metoden er baseret på en løsning af de Reynoldsmidlede Navier-Stokes ligninger, som er koblet med en numerisk metode til bestemmelse af overfladens placering (Volume of Fluid).

Udgangspunktet for denne model er den implementerede metode til bestemmelse af overfladens placering, som er tilgængelig i den frie CFD (Computational Fluid Mechanics) pakke kaldet OpenFoam®, der er frigivet af OpenCFD®. Denne grundlæggende version er blevet udvidet med muligheden for at modellere overfladebølger samt sediment transport i brydningszonen. Valideringen af disse komponenter er beskrevet i afhandlingen. Uligevægten i sedimenttransportfeltet resulterer i en morfologisk ændring af bunden, hvilket er medtaget ved at flytte beregningsnettet. Beregningsmodulet, som håndterer disse flytning, er ligeledes en del af nærværende arbejde.

Beregningsmodellen er benyttet på en række fysiske problemstillinger. Som udgangspunkt er koblingen til det morfologiske respons slået fra, og hydrodynamikken, samt den af hydrodynamikken inducerede sedimenttransporten i brydningszonen, er beskrevet. Disse mekanismer er søgt beskrevet som en funktion er forskellige dimensionsløse parametre, nemlig ζ_0 (kaldet "surf similarity parameter") og to udgaver af Deans parameter, Ω og Ω_{HK}. Beskrivelsen har hovedfokus på (i) rumlige og tidslige forskydninger imellem processer internt i hydrodynamikken og imellem hydrodynamikken og sedimenttransporten samt (ii) den integrerede tværtransport hidrørende fra den suspenderede sedimentransport. Denne er betragtet som en funktion af ζ_0, Ω og Ω_{HK}.

Bunden tillades herefter at udvikle sig under indflydelse af gradienter i sedimenttransporten. Udviklingen af revler i både laboratorie- og prototypeskala er undersøgt. Den tidslige udvikling af revlen er simuleret for flere kombinationer af bølgeparametre og korndiametre. Fokus er på udviklingen af revlens toppunkt, den tidslige variation af bundforskydsningsspændingen over revlens toppunkt, samt vandringshastigheden af dette.

Derudover er en indadrettet strøm påtrykt hen over en revle, hvilket efterligner tilstedeværelsen af en horisontal recirculation. Udviklingen af

revlen er beskrevet som en funktion af styrken af denne strøm. Beskrivelsen er givet både med og uden en kobling til det morfologiske modul.

Chapter 1

Introduction

In recent years, coastal threats due to global warming, the resulting acceleration of sea level rise, and changes in storm and precipitation patterns have gained a lot of focus. One of the questions arising from such an accelerated change is, whether or not shorelines can keep pace with the increase in sea level rise. Is the Bruun rule (Bruun, 1962) applicable or not for this problem, or will the cross shore sediment delivery be too small, resulting in net eroding shores?

The increasing presence of humans in nearshore areas means that the fate of the shoreline cannot be ignored, and measures need to be taken to protect our shorelines. Such measures could be a combination of hard solutions such as groynes, breakwaters (surface piercing or submerged), revetments, seawalls and soft solutions such as sand nourishment in the dune system, on the shore or offshore on the breaker bars (Komar, 1998).

Any of these solutions or the omission of any action needs evaluation. This requires an accurate longterm modelling framework for the shoreline evolution. Irrespective of the type of prediction framework, it is important to decide on the relevant spatial and temporal scales. Three relevant scales for the cross shore profile are depicted in figure 1.1. When considering e.g. the modelling of decadal behaviour level I and perhaps level II need direct modelling, whereas it is not possible to directly include the effect of wave orbital ripples on level III. The residual effects of the ripples on the sediment transport hence needs to be parameterised in a proper way. The way to include this parameterisation is still unknown.

Examples of decadal models are those of Plant *et al.* (1999, 2001), which are based on a behavioural pattern with a coupling between the breaker bar position and the instantaneous environmental forcing; these models are discussed in §2.5.1. The breaker bar migrates towards an equilibrium, which is described based on the instantaneous wave height. The models rely on emperical formulations of the breaker bar position. As these formulations are

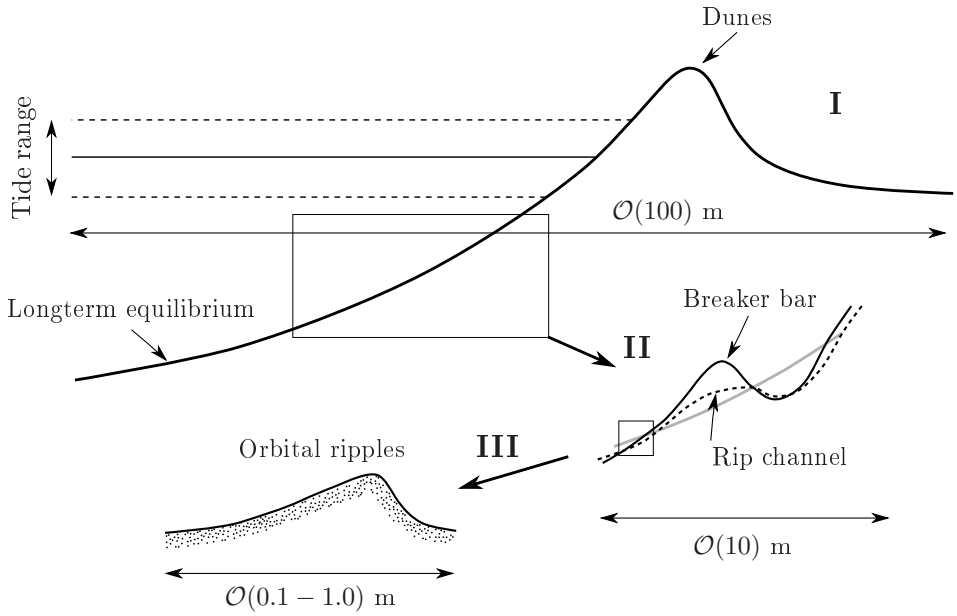

Figure 1.1: *A conceptual sketch of the scales in the cross shore profile. I: Longterm equilibrium profile, which is perturbed with a more dynamic breaker bar/rip channel system (II). The less exposed parts of the bed are covered with orbital ripples (III).*

exclusively based on measurements from FRF, Duck, North Carolina, U.S.A., it has not been tested, whether or not the fitted parameters are "universal" or depend on e.g. sediment grain distribution or the prevailing environmental forcing at that specific location. This makes the models difficult to use as an engineering tool, because decadal measuring campaigns are rare and thus a validation of the model at any location through a hindcasting will prove impossible. Therefore, more knowledge of the actual physical processes taking place in the coastal zone should be built into such behavioural models to increase the engineering applicability. Such physical processes could be all residual effects from non-resolved features. Such an increased incorporation of knowledge of the processes into the behavioural models is also one of the main conclusions in the review by de Vriend *et al.* (1993).

Process oriented morphodynamic models include profile models being 1DH (H: horizontal) depth integrated cross shore models, which assume longshore uniformity, and area models, which are either 2DH depth integrated models or 3D with a hydrostatic assumption. These latter models relax the requirement for longshore uniformity. The range of modelling approaches are described in §§2.5.2–2.5.3.

The vertical variation of the velocity field in the surf zone cannot be

modelled using depth integrated models, as the velocity field has on- and offshore contributions over the vertical. The offshore directed part of the velocity profile is termed the undertow. To remedy this lack in modelling ability, a quasi three dimensional modelling is included, where the undertow is computed in a parametric fashion (e.g. Deigaard *et al.*, 1991b; Drønen and Deigaard, 2007). The computation of the undertow relies on a local fulfilment of the vertical force balance. This results in a sharp transition in the sediment transport patterns at the breakpoint (see Drønen and Deigaard, 2007, figure 9). This sharp transition calls for the inclusion of smoothing and/or lag-effects in the transition between the part of the coastal zone dominated by shoaling waves and that dominated by wave breaking. These lag effects have been incorporated in many fashions in previous models, and the formulations depend on the modelling approach for waves, current, and sediment transport, see e.g. §2.5.2. The variation of these lag-processes is typically an unknown function of the environmental forcing and sediment properties.

To circumvent the empirical modelling of these spatial and temporal lags, the present thesis will consider the modelling of sediment transport under breaking waves with a 2DV (V: vertical) model, which in an explicit manner handles the free surface elevation using a Volume of Fluid (VOF) method for surface tracking. The modelling of sediment transport under breaking waves in 2DV models has to the author's knowledge only been considered by Christensen *et al.* (2000); Ontowirjo and Mano (2008, 2009). Ontowirjo and Mano (2009) is also the only work, where the sediment transport modelled using a Reynolds averaged Navier-Stokes model with a VOF closure has been used as input to a morphological module. The details in Ontowirjo and Mano (2009), however, are limited, and the methodology in coupling the hydro- and morphodynamics is not presented.

The scope of the present thesis is to consider the combined hydro- and morphodynamic processes over the cross profile with an emphasis on the processes close to the breakpoint. This near field description of the breaking and the resulting mobilisation of the sediment cannot be achieved in the other modelling frameworks mentioned above. The model will be used firstly on a constant sloping bed, and the processes as a function of the surf similarity parameter (§2.3.2) or variants of Dean's parameter (§2.2) are considered. The modelling framework is also applied on a description of the morphological development, where the bed level changes in a tight coupling with the instantaneous flow field and sediment transport processes.

The goal is to obtain a better understanding of the sediment transport processes in the surf zone and their intricate coupling with the hydro- and morphodynamic feedback mechanisms. This type of model allows for a de-

tailed description of all processes and can therefore be used to map the parameters governing the phase-lags in the surf zone. This can eventually lead to an improvement of the less sophisticated process and behaviour oriented tools, which are applicable for engineering purposes.

1.1 Outline of the Thesis

The outline of the present thesis is as follows.

A background overview of the hydrodynamic and sediment processes in the nearshore area is described in §2. This description covers the hydrodynamics of breaking and non-breaking waves and the corresponding induced currents in both the long- and cross shore directions. Furthermore, the enforced sediment transport and resulting morphological response is discussed.

A detailed description of the adopted numerical model is given in §3, where each of the individual modules are considered. The Navier-Stokes equation, turbulence closure and VOF-handling is briefly presented, whereas the methods for wave generation/absorption, sediment transport and morphological coupling are considered in detail, since they have been implemented as part of this work.

The validation of the individual pieces of the proposed model is considered in §4. This validation covers turbulence modelling, wave modelling with both breaking and non-breaking benchmark test cases, and the modelling of sediment transport in closed channels and below breaking waves.

In §5 the hydrodynamics and sediment transport over a bed of constant slope are considered over a range of surf similarity parameters. A discussion of the interplay between hydrodynamic and sediment transport is given and phase-lags are described. Furthermore, estimates of erosional and accretional beach types are given.

The full coupling between the hydro- and morphodynamic modules is considered in §6. A set of yearly average and storm conditions is investigated for two grain diameters. The morphological response for only bed load and both bed and suspended load is considered under regular wave forcing. Furtheremore, the effect of a net current over a barred cross shore profile is considered.

The thesis is terminated with a discussion (§7) and a conclusion (§8).

Chapter 2

Background

2.1 Terminology

The nearshore area characterises the boundary between land and sea, and it is a place where considerable sediment transport processes take place. When looking at the nearshore area it is common to consider, what happens in two main directions, namely the cross shore and longshore directions.

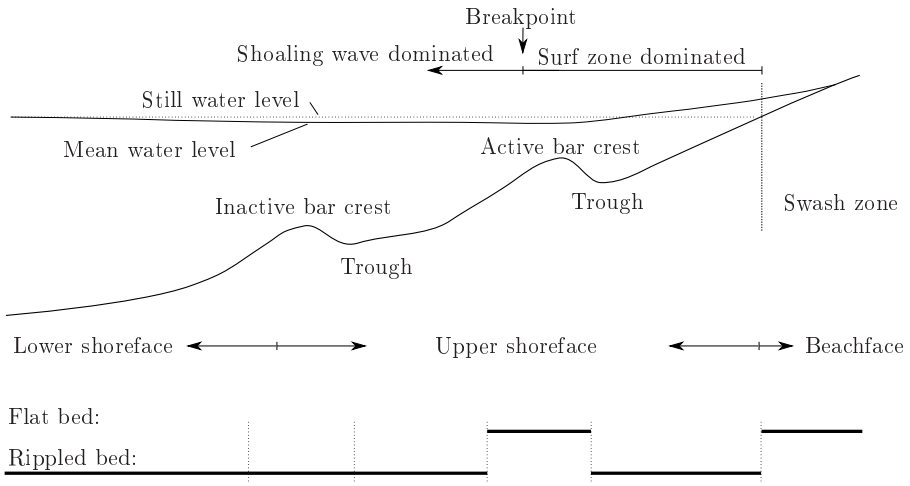

Figure 2.1: *The terminology used for the main features in the nearshore zone in a cross shore vertical plane. Note that the bed is termed rippled over the outer bar, as it is instantaneously inactive, i.e. outside the surf zone.*

A sketch of a cross shore profile is shown in figure 2.1. When considering the nearshore area, there is a terminology for the instantaneous picture and another terminology for the longer term. Over the short term, the cross shore is divided into a region, where waves are breaking, called the surf zone, which

is shoreward of the breakpoint, see figure 2.1. The waves are shoaling seaward of the breakpoint. Shoaling is the conservative process of a change in wave height due to a change in the water depth. Over the long term perspective, the near shore area is divided into the upper and lower shorefaces, where the upper shoreface is predominantly affected by the surf zone processes, and therefore it contains all of the breaker bars. The lower shoreface is mainly dominated by hydrodynamic and sediment transport processes related to shoaling waves.

The breaker bars can be longshore uniform or rhythmic features, see §2.2 and figure 2.2. The longshore features can be intersected by deeper parts, which are called rip channels. Rhythmic features are also called crescentic bars, and they are depicted in figure 2.2b,c. As can be seen from this figure, they interact and can connect with the shoreline. The different topological layouts of the breaker bars have been classified into several beach states, which will be discussed in §2.2.

Near the shoreline the broken waves run up on the shore and form the swash zone, which, contrary to the progressive short waves in the surf zone, has the characteristics of a (partly) standing wave (see Hughes and Turner, 1999, figure 5.6). A thin sheet of water runs up the beach in this zone and, depending on the state of saturation of the beach, a fraction of the water is infiltrated into the beach. This water is then exfiltrated as the swash lens retreats.

In figure 2.1, the two bars are given different attributes, namely active and inactive respectively, which describe their instantaneous morphological state. When waves are breaking seaward of the bar, wave induced turbulence and wave induced currents will result in large sediment transport rates, which modify the shape of the breaker bar. The opposite holds for the inactive bar, as the sediment transport rates are orders of magnitude smaller for shoaling waves, why the morphological response is equally weak. The inactive bar will become active as soon as it is subject to surf zone dominated processes, i.e. the occurrence of a storm with larger waves or a lowering of the mean water level due to tidal motion. The number of cross shore bars will be discussed in §2.2.2. The number of bars ranges from none to as many as five.

The hydrodynamic conditions are sufficiently calm for the generation of wave orbital ripples under shoaling waves and in the bar troughs, see sketch in figure 1.1. These are extremely important features, when considering the residual effects of the sediment transport in the near shore area and especially important for the longterm cross shore sediment delivery. This is the case because the instantaneous magnitude and direction of sediment transport is considerably influenced by the presence of ripples relative to the flat bed conditions.

In the longshore direction the bars are seldomly straight but are intersected by deeper parts called rip channels. These can be found between otherwise straight bars, crescentic bars, or transverse bars, e.g. see figure 2.2 and Dalrymple *et al.* (2011). This results in a longshore variation in the width of the surf zone, as waves break farther onshore in the rip channels compared to the position of the breaker bars. The rip channels mentioned above are characterised by a strong seaward current, which is sustained by a shoreward current over the bars. The strength of the current in the rip channel oscillates at frequencies smaller than that of the incident waves. Field experiments by MacMahan *et al.* (2004) showed the oscillations to be coupled to long periodic motion in the surf zone. This long periodic motion is termed infragravity waves, and they will be described further in §2.3.3.

2.2 Beach Classification

In the present section an introduction to beach classification will be given under the assumption that the beach in question is neither affected by man-made structures nor forms a closed system due to the presence of naturally occurring head-lands or similar hard features (see Short and Masselink, 1999). In addition to this, it will be assumed that the beach is not tidally dominated; a brief account of tidal effects on the shoreface morphology is given in §2.2.3.

2.2.1 Single-Bar Configurations

Wright and Short (1984) have classified beach topology based on field studies of Australian beaches. Generally this classification has been supported with additional observations from Japan (Sunamura and Irie, 1988) and daily observations using photographic equipment over a period of two years at the FRF laboratory in Duck, North Carolina (Lippmann and Holman, 1990). The classification scheme differs slightly between the different authors. The one outlined by Wright and Short (1984) (see figure 2.2) is followed here.

Both Wright and Short (1984) and Lippmann and Holman (1990) use the parameter

$$\Omega = \frac{H_B}{w_s T} \tag{2.1}$$

to classify the beach states. This parameter is called Dean's parameter following Dean (1973)*. H_B is the breaking height, w_s is the sediment fall

*This parameterisation is according to Short (1999) first suggested by Gourlay (1968).

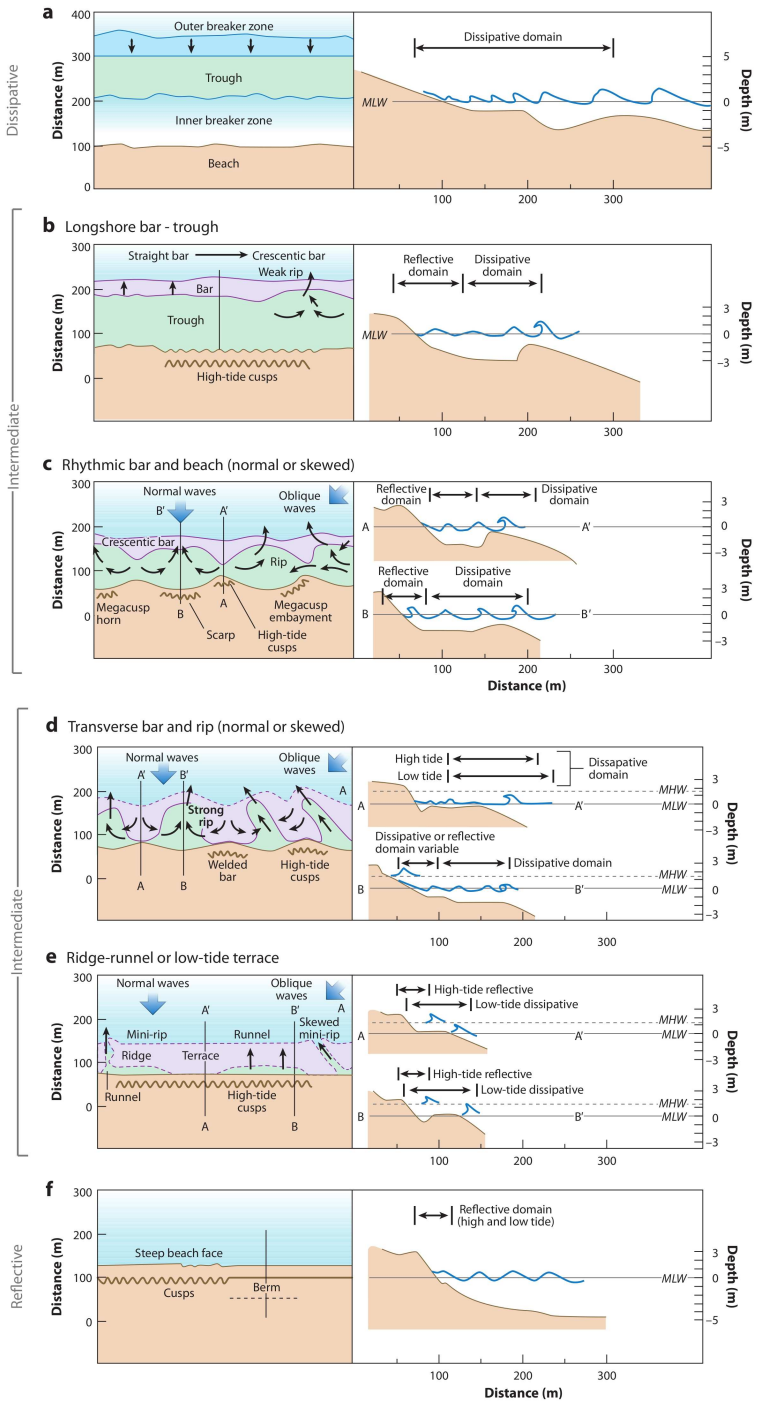

Figure 2.2: *The layout of the beach states for a single bar configuration. From Dalrymple* et al. *(2011)*

velocity, and T is the wave period. Sunamura and Irie (1988) use

$$K_* = \frac{\bar{H}_B^2}{g\bar{T}^2 d} \tag{2.2}$$

where over-bar means daily averages, g is the modulus of the gravitational vector, $\mathbf{g}$, and d is the median grain diameter. Both of these parameters express a relation between the incident waves and the sediment properties.

The classification scheme as suggested by Wright and Short (1984) consists of 6 beach states, see figure 2.2. Lippmann and Holman (1990) suggest 8 beach states, which is merely a subdivision of the two states "Longshore Bar-Trough" (LBT) and "Transverse Bar and Rip" (TBR). The two additional states originate from a process based consideration, where those in Wright and Short (1984) are based on field observations.

The sequence of states is shown in in figure 2.2, where the two extremes are the reflective beach state ($\Omega < 1$) and the dissipative beach state ($\Omega > 6$). These are longshore uniform, and they are seen on swell and storm dominated coasts respectively. On the dissipative beach state, the sediment is typically finer than that on the reflective beaches. In the fully reflective beach state, there are no breaker bar present. Instead the beach profile has a sudden depth increase called a step (figure 2.2f). The dissipative state is erosive and the reflective beach state is accretive.

The classification works with a set of accretional and erosional sequences, where the beach state is accretional as long as Ω (K_*) is decreasing and erosional for increasing Ω (K_*). Here the terms accretional and erosional states reflect the overall cross shore sediment transport direction, i.e. on- and offshore respectively.

Is the Process Reversible?

The sequence from fully dissipative to reflective beach state goes through four intermediate states, where the bar progressively moves onshore (Ω decreases, hence accretion) and the bar is eventually connected to the beach face. According to Wright and Short (1984) this process is reversible, whereas Lippmann and Holman (1990) do not address this, because the erosional sequence is on a too short time scale relative to their measuring technique. Sunamura and Irie (1988) find that the crescentic beach state only develops under decreasing Ω (K_*), and their erosion/accretion process is cyclic with 3 intermediate accretional states and 3 intermediate erosional states. This difference might arise from the time scales, where the accretional sequence (fair weather) has time scales that are typically of the order weeks and month, whereas the erosional sequence (storm) occur over hours and days. An example of the latter is given in Holman *et al.* (2006), where the storm event

is described as "system resets", where all rhythmic behaviour is erased and replaced by longshore straight bars. This can occur within the scale of hours.

Lippmann and Holman (1990) find that the fully dissipative state is generally unstable, where rip channels are immediately formed with a lowering in storm intensity (lowering Ω). The instability of such straight bars has been addressed using linear stability analysis, e.g. Deigaard *et al.* (1999a).

Rate of Change

The rate of change of the beach state was addressed by Wright and Short (1984), and their hypothesis was compiled into figure 2.3. Following intuition it is seen that the rate of change is small for a low energy event and large for a high energy events, which is intuitively correct. Furthermore, they propose that the rate of change also goes asymptotically toward an equilibrium state. This hypothesis explains, why the beach seems to jump several states during storm events after long periods of calm weather as the initial profile is far from the dissipative one. The hypothesis can only be used qualitatively, whereas quantitative modelling using the beach states and their modulation toward an equilibrium seem out of reach. An example where such a model would break down can be discussed based on the field observations by Holman *et al.* (2006). Here a large scale crescentic feature ($\mathcal{O}(1)$ km) is untouched by a considerable storm, and only the smaller crescentic features, superimposed along the larger one, are straightend. These smaller crescentic features reappear following the storm event. Here the same type of beach state is superimposed on each other with different length scales, however, only the smaller scales are subject to significant morphological change during the storm event.

2.2.2 Effect of Multiple Bars

Multiple cross shore bars are found on many beaches around the world. The classification of these is addressed by Short and Aagaard (1993) in a compilation of their own work combined with a review of previous works. Additional complexity is introduced, since the inner bar(s) can be active in a given instance, in which the outer bar(s) can remain inactive and only subject to shoaling waves. The outer bar(s) can then become active under more severe hydrodynamic forcing. This means that the inner bar(s) can for instance go through an accretional sequence, whereas the outer bar(s) remain fixed. Hence, a classification using Ω or K_* loses its meaning for all of the bars simultaneously. The shape of the individual bars, however, still reflects those in the classification scheme for single bars as given by Wright and Short (1984) (see figure 2.2). Greenwood and Davidson-Arnott

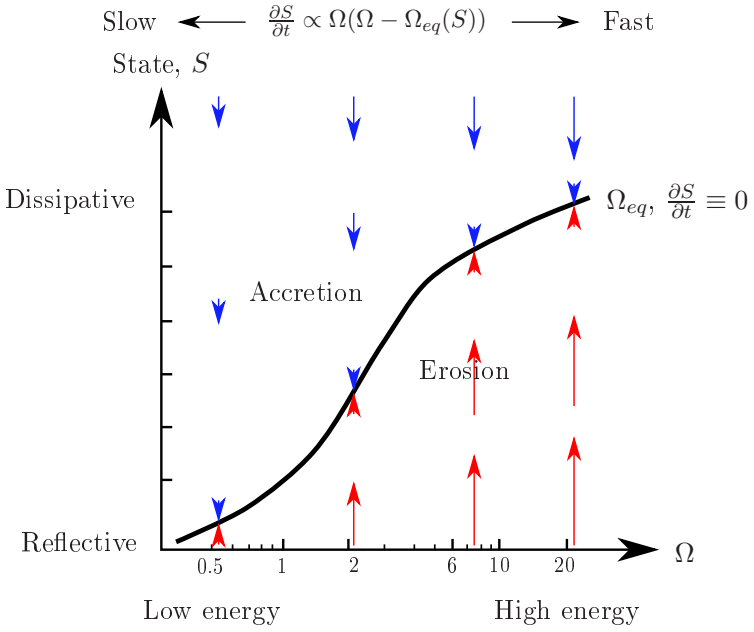

Figure 2.3: *The rate of change of a beach state relative to an initial state, wave forcing and equilibrium state, Ω_{eq}. The length of the arrow represents a relative rate of change. After Wright and Short (1984), fig. 12.*

(1975) similarly report that the outer bar system at Kouchibouguac Bay, New Brunswick, Canada, change over considerably larger time scales than the inner bar system. The inner bar system can consist of as much as 3 cross shore bars over a wide range of beach states.

The cross shore bar spacing is addressed by Short and Aagaard (1993) based on theoretical considerations of standing edge or leaky waves (see §2.3.3) during storm events. Based on these considerations, a bar parameter

$$B^* = \frac{\xi_s}{g\beta T_p^2} \tag{2.3}$$

is introduced. Here ξ_s is the distance from the shoreline to where the slope of the profile tends to zero (see also figure 2.6), β is the gradient of a linear approximation to the nearshore profile, and T_p a representative wave period during storm events. Based on this, no bars are found for $B^* < 20$, one bar for $B^* \simeq 20 - 50$, two bars for $B^* \simeq 50 - 100$, three bars for $B^* \simeq 100 - 400$ and four bars for $B^* > 400$. E.g. steep and swell dominated coasts have no bars, and gently sloping and storm dominated coasts will exhibit multiple longshore bars.

Since Short and Aagaard (1993) use the incident wave period in eq. (2.3), it can be questioned whether this expression reflects an infragravity perspec-

tive on the nearshore bar formation process. The form of eq. (2.3) originates from the solution of edge waves (see §2.3.3), which are strongly reasonant in the cross shore direction, hence the use of T_p instead of a representative wave period for the edge waves is merely a scaling consideration.

Besides the fact that a formation process governed by infragravity type waves is questionable, see discussion in §2.4.2, the proposed expression does fit the observed number of bars remarkably well.

2.2.3 Effect of Tides

The effect of tides on the development of the nearshore beach morphology introduces two additional mechanisms. The first is the translation of the instantaneous shoreline across the beach profile due to the tidal motion, which introduces a cross shore variation in the location of surf and swash zone sediment transport processes. Thus part of a profile can be subject to these two types of transport mechanisms in addition to shoaling waves and aeolian sediment transport over a single tidal cycle, see Masselink and Turner (1999).

Additionally, the tidal motion results in an oscillating water level inside the beach. The swash zone then acts on both saturated and unsaturated beds, which favours off- and onshore sediment transport, respectively.

In addition to Ω, another dimensionless parameter is introduced. Namely the relative tide range

$$RTR = \frac{TR}{H_B} \quad , \tag{2.4}$$

where TR is the tidal range. For $RTR > 15$, the beach is classified as a tidal flat irrespectively of the magnitude of Ω. RTR is more meaningfull than the classification scheme using an absolute tidal range, such as micro, meso and macro tidal-ranges.

2.3 Nearshore Hydrodynamics

This section considers the range of nearshore hydrodynamic phenomena from the intra-wave orbital motion through wave breaking, induced mean surface elevations to the resulting wave induced currents. A description of the production of turbulence and its advection and diffusion is given. Measurements of bed shear stresses below breaking waves in the surf zone are presented.

2.3.1 Intra-Wave Hydrodynamics

The basic water particle motion below non-breaking waves is elliptical, where the ellipses become circular in deep water and straight lines in shallow wa-

ter, see figure 2.4A-C. Including higher order effects into this description, the elliptical motion is distorted and there is a slight forward drift in the movement, which is called the Stokes drift (Mei, 1999). This drift is of second order in wave height, and its vertical distribution depends on whether it is evaluated using an Eulerian or a Lagrangian approach, see 2.4D. In the former case, it is located between the trough and crest, and it is located between the bottom and the mean water level in the latter case. The forward drift is compensated by a return current for closed systems such as wave flumes and the cross shore profile; for example see Sumer and Fredsøe (2001) for an experimental evidence. In addition to the elongation of the orbital trajectories, the surface elevation become less and less sinusoidal with decreasing water depth. This is seen as increasingly shorter and steeper crests and wider troughs, see figure 2.4A-C. In shallow water the Stokes perturbation theory breaks down, see e.g. Fenton (1990) figure 2.

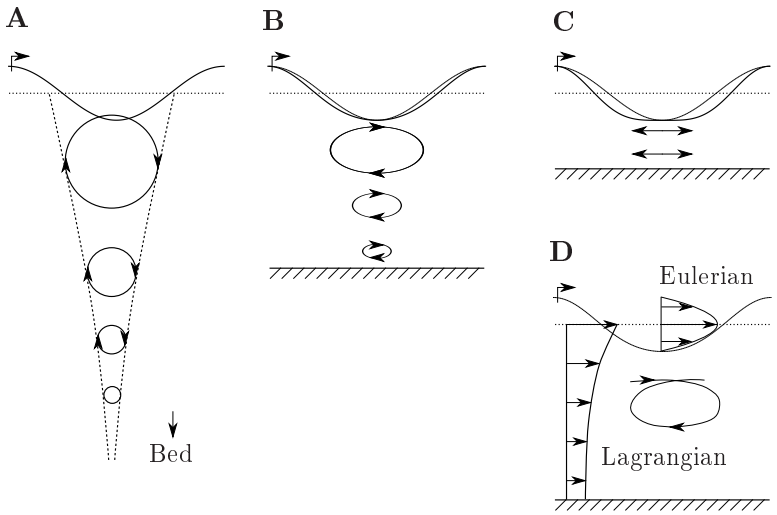

Figure 2.4: *Sketch of the orbital velocities in deep water (A), over intermediate water depths (B), and in shallow water (C). The thin line shows the corresponding Airy wave. D: Sketch of the effect of open orbital trajectories and the resulting drift from both Eulerian and Lagrangian perspectives.*

Near Bottom Flow

The potential theory breaks down at the bottom boundary, because it allows for a finite slip velocity. However, viscous forces are to obtain a zero velocity at the boundary.

Transition from laminar to turbulent wave boundary layers occurs at $Re_w = u_m a/\nu \simeq 10^5$, where u_m is the maximum orbital velocity, a is the

orbital amplitude, and ν the molecular viscosity. For Reynolds numbers slightly larger than the critical, turbulence only covers a small fraction of the wave period, a fraction which increases with increasing Reynolds number (Jensen *et al.*, 1989).

The oscillating pressure gradient in the boundary layer is out of phase with the free stream velocity, explaining why the velocity within the boundary reverses prior to the free stream velocity. This can be measured as a phase-lag between the freestream velocity and the bed shear stress. This phase-lag is 45° for laminar boundary layers, whereas it decreases to $\mathcal{O}(10°)$ in turbulent wave boundary layers due to the increased momentum exchange over the vertical (e.g. Jensen *et al.*, 1989, figure 11). Excess turbulence can result in an even smaller phase-lag (Fredsøe *et al.*, 2003), who found values as small as 5°.

Current and Waves

The superposition of waves and current has a significant effect on the magnitude and the vertical distribution of the current, as the eddy viscosity in the turbulent wave boundary layer is larger than the corresponding for pure current. This results in a smaller velocity gradient and hence a smaller depth integrated flux over the water depth due to the current. This current is important for the net sediment flux, as the period averaged sediment flux is zero under pure sinusoidal motion. As discussed in Fuhrman *et al.* (2009), a net sediment transport can be found by adding either a current or second order terms to the free stream velocity. The numerical simulations by de Vriend *et al.* (1993) showed that the combination of wave and currents relative to pure tidal induced current results in an increase in the sediment transport rates by an order of magnitude.

2.3.2 Wave Propagation and Breaking

Waves propagating from deep to shallow water in the nearshore area are subject to shoaling, refraction, and wave breaking. These processes are (i) change in wave height due to a change in water depth and/or the presence of a current, (ii) curving of wave fronts due to oblique wave incidence relative to bottom contours and or the presence of a current, and (iii) dissipation of organised wave energy into turbulence and heat.

The presence of surface water waves give rise to an excess momentum flux, which can be expressed in terms of the radiation stress tensor (Longuet-

Higgins and Stewart, 1964)

$$\begin{aligned}\mathbf{S}_R &= \begin{bmatrix} S_{xx} & S_{xy} \\ S_{yx} & S_{yy} \end{bmatrix} \\ &= \frac{1}{2}E \begin{bmatrix} (1+G)\cos^2\alpha + G & (1+G)\sin\alpha\cos\alpha \\ (1+G)\sin\alpha\cos\alpha & (1+G)\sin^2\alpha + G \end{bmatrix}\end{aligned} \tag{2.5}$$

where the last equality is evaluated using linear wave theory (Longuet-Higgins, 1970a). Here E is the wave energy

$$E = \frac{1}{8}\rho g H^2 \tag{2.6}$$

and α is the propagation direction relative to a global $x-y$ coordinate system. $G = 2kh/\sinh 2kh$, where k is the modulus of the wave number vector and h is the local water depth.

The two first processes (i) and (ii) are energy flux conserving, whereas the wave breaking, (iii), is strongly dissipative. The preservation or lack of energy flux conservation has an important effect on nearshore current patterns, see §2.3.4.

The wave front increases in steepness up to the point of breaking, because the wave crest travels faster than the wave trough (see Lamb, 1945, §187). This steepening is accompanied by an increase of wave energy on the higher bound harmonics leading to a gradual decrease in the accuracy of the Stokes perburbation theory. This is considered in more detail in §4.1.6.

Wave Breaking

Wave breaking has been classified in 3 types of breaking being (i) spilling, (ii) plunging, and (iii) surging breakers. These breaker types follow each other for increasing steepness of the beach profile under fixed wave forcing. This has been classified using the surf similarity parameter defined as

$$\zeta_0 = \frac{\tan\beta}{\sqrt{H_0/L_0}} \quad , \tag{2.7}$$

where $\tan\beta$ is the beach slope and the index 0 stand for deep water properties. The breaker type as a function of the surf similarity parameter is given in table 2.1.

Spilling breakers occur as the wave crest becomes unstable, and a zone in front of the wave crest is generated, which is characterised by large rotation and production of turbulence. This volume of water is termed the surface roller, and it is passively advected as the wave propagates. Turbulence is spread from this region downward (Nadaoka *et al.*, 1989). The plunging breaking occurs as an overturning of the wave crest, when its speed exceeds

Table 2.1: *Breaker type as a function of the surf similarity parameter, ζ_0 (Fredsøe and Deigaard, 1992).*

Type:	**Range:**
Spilling breakers	$\zeta_0 < 0.5$
Plunging breakers	$0.5 < \zeta_0 < 3.3$
Surging breakers	$3.3 < \zeta_0$

the propagation speed of the wave (Peregrine, 1983). When the forward projected water hits the water surface in front of the wave crest, it can either reflect on the surface, continue through the water surface, or a combination hereof. The second option combined with intense vortical motion is hypothesised to cause the formation of a breaker bar, see §2.4.2. The different possibilities are sketched in figure 2.5. The violent impact causes the generation of vortices in the water column. Pedersen *et al.* (1995) considered theoretically the generation of these and their subsequent interaction with the bed. They found that they can induce large bed shear stresses. After the initial breaking both of these breaking types propagate toward the shoreline as broken waves, which are characterised by a surface roller and continuous dissipation of wave energy. The surging breaking type is an instability at the toe of the steep wave front.

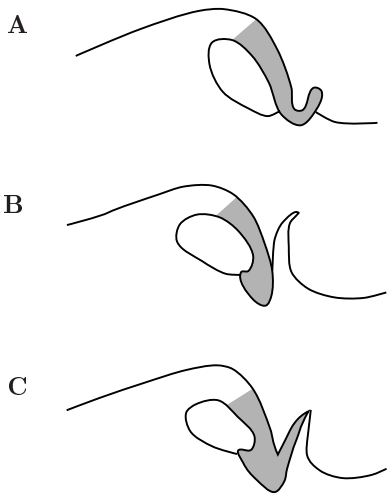

Figure 2.5: *The different possible types of motion of the water during impact of the water jet in a plunging breaker. After Peregrine (1983)*

Reflection from the Shoreline

The reflection of wave energy, R_N^2, from a beach increases with increasing surf similarity parameter. Elgar *et al.* (1994) experimentally verified that the Miche parameter

$$M = \frac{16g^2}{(2\pi)^2} \frac{\tan^5 \beta}{H_0^2 f^4} \tag{2.8}$$

describes the amount of reflection reasonably well. They verified that $R_N^2 = M$ for $M < 1.0$ and otherwise $R_N^2 = 1.0$. Here f is the wave frequency. Elgar *et al.* (1994) found for large offshore wave energy that $R_N^2 < 0.03$, which is the detectable limit, i.e. reflection is negligible for small surf similarity parameters.

Oblique Descending Eddies

In the breaking process, what is termed oblique descending eddies are generated. These are found to have a considerable effect on sediment suspension in a laboratory experiments by Nadaoka *et al.* (1988b), and they are indirectly identified in the field by Nadaoka *et al.* (1988a)[†]. The obliquely descending eddies are inherently 3-dimensional vortical structures, which rotate around an axis from the water surface directed seaward and downward. The numerical modelling of these has been undertaken by Christensen and Deigaard (2001).

2.3.3 Infragravity Motion

Long periodic motion in the near shore area is termed infragravity motion. This motion is typically defined as having a period in excess of 20 s (Aagaard and Masselink, 1999). Its presence has been suggested as the cause for the generation, location and shape of morphological features in the nearshore zone, see §§2.2.2 and 2.4.2. Such infragravity motion is caused by several mechanisms. One of these are the release of bound long waves in wave trains due to breaking. The bound long waves are described by Longuet-Higgins and Stewart (1964) in terms of variations in the radiation stress tensor over a group length. Another forcing mechanism is related to the cross shore variation in the breakpoint (Symonds *et al.*, 1982).

The long waves reflect on the shore and return seaward for normal wave incidence. A superposition of the incoming and reflected long waves creates a standing wave pattern with no longshore variation. These waves are called

[†]They are also easily identified in BBC (2009) from 03:11 to 04:00, where they have been recorded in the field using high speed cameras.

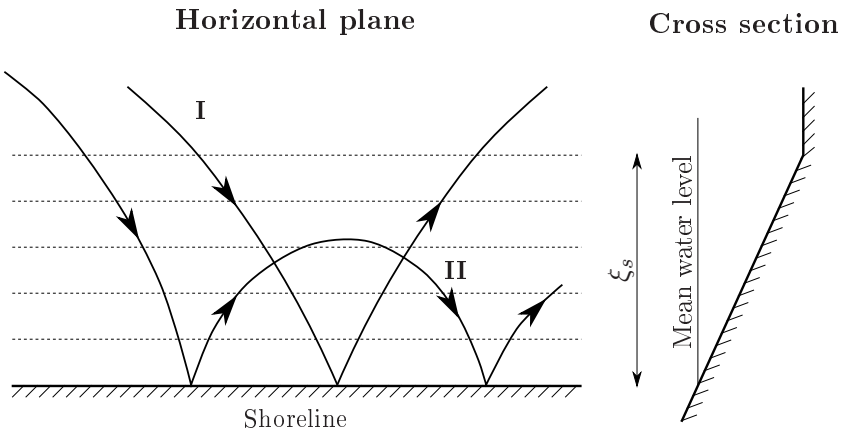

Figure 2.6: *Sketch of the concept of infragravity wave becoming trapped in the nearshore region due to refraction. I: Infragravity wave, which does not become trapped. II: Infragravity wave, which does become trapped (edge wave).*

leaky waves. For obliquely incident wave trains, the long waves can become trapped on the sloping part of the profile, because the waves refract 180°, see figure 2.6. This type is called edge waves, and they can be either propagating or standing in the longshore direction. In the latter case, the standing pattern is induced by limitations in the extend of the beach by e.g. head lands or theoretically by the incidence of two identical wave trains from opposite directions. The shape of these standing wave patterns depends strongly on the beach profile (Dally, 1987; Reniers *et al.*, 2004), thus the pattern will vary over long time scales, e.g. the morphological time scales of bathymetrical variations.

The two mechanisms described above are directly related to the wave breaking and the irregularity of the wave field. An instability mechanism in the longshore current forms a long period oscillation with even lower frequency ($\mathcal{O}(1-10)$ min). This instability is called shear waves (see Aagaard and Masselink, 1999, p. 86).

2.3.4 Mean Quantities

When considering the radiation stress tensor, $\mathbf{S}_R$, from eq. (2.5) under either shoaling, refraction or wave breaking, it is seen that

$$\nabla_h \cdot \mathbf{S}_R \neq \mathbf{0} \quad , \tag{2.9}$$

where ∇_h is the gradient operator in the horizontal plane. The expression deviates from $\mathbf{0}$, because the wave height changes under any of those processes.

This means that the gradient in the momentum flux must be balanced by a pressure gradient, and it leads to the concept of set-down of the mean water level outside the surf zone and a set-up of the mean water level inside the surf zone, see figure 2.1 and e.g. Svendsen (2006). Note that there exist a spatial phase-lag between the point of breaking and the location of the beginning of the setup for plunging breaker, as the organised motion of the wave is firstly transformed into an organised vortical structure that has a non-zero contribution to the momentum flux (Battjes, 1988). It is similarly discussed in Roelvink and Stive (1989), who state that energy decay models used to model the surface elevation "*may be a good predictor of the wave height decay as observed from the wave surface variance (a manifestation of primarily the potential energy), but this is not necessarily so for the total energy.*" Roelvink and Stive (1989) introduced a spatial lag between the production and dissipation of turbulent kinetic energy and found improvements on undertow estimates.

Vertical Shear Stress Distribution

Outside the surf zone Deigaard and Fredsøe (1989) showed in 2 dimensions there is a zero shear stress distribution over the vertical outside the boundary layer. This can intuitively be extended to both shoaling and refraction in 3 dimensions following their conservative nature. Since no energy dissipation takes place outside the boundary layer, no rotation can be introduced in the water column, thus wave generated currents cannot be forced. This has also been proved by Dingemans *et al.* (1987) for arbitrary bathymetrical layouts. Furthermore, they found that the driving force can be described by wave energy dissipation, which is termed the rotational part of $\mathbf{S}_R$.

When including wave breaking this radically changes. Dyhr-Nielsen and Sørensen (1970) qualitatively discuss the distribution of radiation stresses over the vertical in the surf zone, and they compared it to the distribution of the pressure gradient from the wave set-up. This requires a non-zero bed shear stress in the cross shore direction to yield equilibrium in the moment.

The shear stress distribution over the vertical in the cross shore direction has been considered by Dally and Dean (1984); Svendsen (1984); Deigaard and Fredsøe (1989). Deigaard and Fredsøe (1989) included a horizontal stress term at the bottom of a control volume extending from above the surface to some arbitrary level. This stress term, which is due to organised wave motion, is non-zero due to wave energy dissipation in the direction of propagation. This term is important for the vertical shear stress distribution.

Cross Shore Current

A circulation current is present in the surf zone, and the seaward directed current near the bed is called the undertow. It balances a shoreward volume flux around the mean water level with contributions from the Stokes drift, the flux due to the advection of the surface roller, and the shear driven flow originating from the shear under the surface roller. Outside the surf zone the only shoreward mass flux is due to the Stokes drift, hence to distinguish between the two zones, the balancing of the Stokes drift is in the following termed the return flow. This produces a mean flow field as the one measured experimentally by Nadaoka and Kondoh (1982), see figure 2.7. The depicted flow field reveals that the undertow is confined to near the bed, whereas the return flow is largest near trough level. This has important consequences for the sediment transport rate. Furthermore, note that due to continuity conservation, there is a vertical flux over water immediately shoreward of the breakpoint.

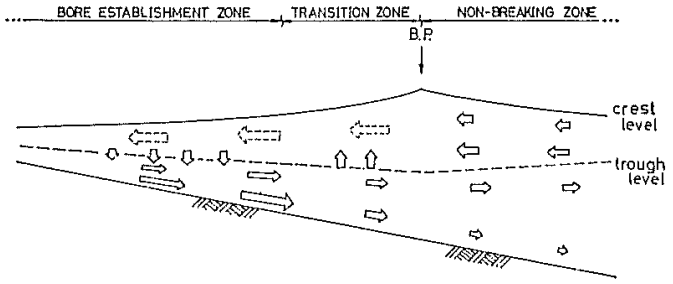

Figure 2.7: *The mean recirculation in the cross shore direction measured in a laboratory flume (Nadaoka and Kondoh, 1982, their figure 16). The arrows inside the surf zone are dashed as no measurements could be performed in the aerated region.*

Deigaard *et al.* (1991b) use the shear stress distribution to model the undertow profile under spilling wave breaking in a localised manner. This means that there is a local fulfilment of force equilibrium, where the effect of cross shore acceleration of the undertow is not included. Compared to experimental results they obtain good results.

Streaming

Longuet-Higgins (1953) considered the boundary layers below linear water waves and found that a net current in the propagation direction is generated due to the spatial non-uniformity in the wave boundary layer. This mech-

anism is called streaming, and it has been verified experimentally outside the surf zone. The process related to streaming is also present in the surf zone, however, it is of secondary importance in terms of the amount of extracted energy. This also means that the shoreward steady streaming near the bed is overtaken by the undertow, and the streaming fingerprint cannot be recognised in period averaged velocity profiles, see e.g. Huang *et al.* (2010) figure 8. Several authors have performed velocity measurements inside the surf zone (Nadaoka and Kondoh, 1982; Ting and Kirby, 1994; Cox, 1995), however it is not clear from their measurements, whether the lack of the streaming fingerprint is due to a too coarse vertical resolution near the bed or the fact that the streaming component is not present at all.

Longshore Current

Only the cross shore current has been considered until now. In the longshore direction, the gradient in the shear component of $\mathbf{S}_R$ can only be balanced by a bed shear stress in the longshore direction, hence carrying evidence of a longshore current. This was addressed theoretically by Bowen (1969); Longuet-Higgins (1970a,b); Thornton (1970). Their work mainly differs in the definition of the bed shear stress, with either linear or quadratic dependency on the velocity and constant or spatially varying friction factor. A numerical solution is required in the case of a spatially varying friction factor. Furthermore, Thornton (1970) models the focusing of the longshore current on breaker bars.

It was previously mentioned that no wave induced current is present outside the surf zone due to the conservative nature of the wave processes occurring here. This is not entirely correct as a current is induced by the longshore current due to momentum exchange in the cross direction and thus beyond the breakpoint (Longuet-Higgins, 1970b), see figure 2.8.

The Combined Picture

The combination of the cross shore circulation and longshore current gives rise to a corkscrew motion as identified from the shear stress distribution in 3-dimensions derived by Deigaard (1993) for breaking waves over a horizontal bed. This motion is also discussed qualitatively by Longuet-Higgins (1970a), and it is depicted in figure 2.8.

The hydrodynamic description changes, if rip channels are included, because the undertow is weakened and the shoreward flux of water over the bar returns seaward through the rip channels. This further changes the characteristics of the longshore current, which attains a meandering form due to the periodic strong seaward currents. The seaward flux through the rip channels

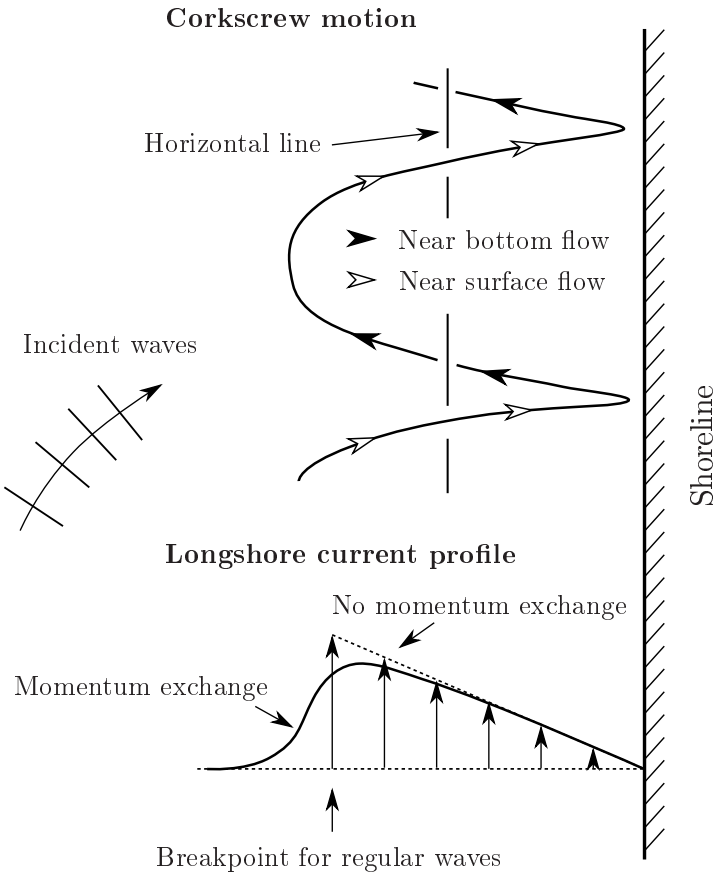

Figure 2.8: *A sketch of the longshore current profile on a cross shore profile of constant slope depicted with and without cross shore momentum exchange. The corkscrew motion in the surf zone is also depicted.*

is also present for normal incident waves and no longshore current component. The current pattern then forms circulation cells in the horizontal plane (see e.g. figure 2.2 or Wright and Short, 1984, figure 5).

A discussion of the inclusion of irregular and directional spread waves into the modelling of the longshore current can be found in Fredsøe and Deigaard (1992) pp. 137–142.

2.3.5 Turbulence Characteristics and Bed Shear Stresses

The turbulence in the surf zone is mainly generated in the surface region as clearly seen from particle image velocimetry (PIV) measurements by Kimmoun and Branger (2007). They also conclude that the proper way of making the turbulent kinetic energy non-dimensional is by using gh, which is based

on an intercomparison with their own results and previous measurements of the turbulent kinetic energy under breaking waves. While Kimmoun and Branger (2007) consider a combined spilling-plunging sequence, Ting and Kirby (1994) consider the cases of either spilling or plunging breakers and their measurements are in line with the more recent results.

The two experiments discussed above are conducted on a constant sloping bed. Scott *et al.* (2005) conducted measurements of the turbulent quantities over a frozen barred profile in a large scale wave flume. Both regular and irregular waves were tested. The waves broke seaward of the bar crest, which is also seen in experiments with loose sediment beds. This resulted in the largest value for the turbulent kinetic energy at the crest of the breaker bar, whereas the turbulence was generally lower in the bar trough. Over the breaker bar the turbulence level is high over the entire water column, whereas there is a non-uniform distribution in the trough with the largest values near the water surface. Furthermore, Scott *et al.* (2005) found that the turbulent kinetic energy was generally smaller in the case of irregular waves.

The turbulence properties under breaking waves have been measured extensively in both laboratory and field settings, whereas the measurements of bed shear stresses are less frequently considered. Measurement of bed shear stresses on smooth beds can be obtained using hot films such as has been done in Deigaard *et al.* (1991a), using laser measurements over rough boundaries Cox (1995); Cox *et al.* (1996), or using PIV (Kimmoun and Branger, 2007). Except in the work by Kimmoun and Branger (2007), all measured the bed shear stresses are under spilling breakers, and they find that the bed shear stress is largest around the breakpoint, and it decreases shoreward. Shoreward of the breakpoint the amount of turbulence is considerably larger than offshore, which will affect the sediment transport processes. The large amount of turbulence is due to turbulent kinetic energy from the breaking process, which extends the entire water column. Both experiments find that the periodicity of the waves is reflected in the bed shear stress shoreward of the breakpoint.

Kimmoun and Branger (2007) measured the bed shear stress under a combined spilling-plunging event, and they found a correlation between a surface piercing vortical structure and a considerable offshore directed bed shear stress. There is a large gradient in the bed shear stress just seaward of the breakpoint, which suggest a convergence point for sediment transport. This is a potential breaker bar forming mechanism, which will be discussed in §2.4.2.

2.3.6 Other Hydrodynamic Features

Other hydrodynamic features having an impact on sediment transport patterns, which will not be considered in detail, are that of wind generated currents, storm surges, and the presence of shelf currents. Furthermore, the detailed effect of air-water mixture on both turbulence dissipation due to bubble deformation by turbulent stresses, and the effect of bubbles on suspended sediment transport is omitted. The two latter processes are hypothesised to have opposite effects. Increased turbulent dissipation lowers the eddy viscosity, and hence the ability of sustaining sediment grains at a given level is weakened, whereas the rising of bubbles can carry sediment grains to higher levels in the water column. Neither of these processes are included in the present thesis.

2.4 Sediment Transport and Resulting Morphology

2.4.1 Sediment Transport in the Nearshore Area

Under purely sinusoidal movement the net sediment transport is vanishing, however, there is an intricate interaction between wave and current, the presence of wave non-linearity, and wave irregularity. Outside the surf zone the presence of bound waves in wave groups are found to limit the suspended sediment flux in the propagation direction, as the velocity field from the long bound wave is against the propagation direction under the larger of the waves in the wave group (Deigaard *et al.*, 1999b). They also note that higher harmonics are not treated in their model, and these could potentially counteract the effect of bound long waves, as they result in an increased net forward sediment flux, which has been addressed by e.g. Fuhrman *et al.* (2009).

The effect of turbulence from breaking waves inside the surf zone is important for sustaining sediment in suspension as seen in e.g. Deigaard *et al.* (1986). Furthermore, the combination of wave breaking and the presence of a current in the surf zone increases the transport capacity considerably. The effect of undertow in terms of breaker bar formation is discussed in §2.4.2.

Effect of Wave Irregularity on the Sediment Transport

The complex sediment transport patterns under non-regular waves were considered by Dally (1987) with an emphasis on the morphological response (see §2.4.2). The integrated cross shore flux was the focus in the experiments by Baldock *et al.* (2010, 2011), where the former is carried out in small scale and the latter in large scale laboratory wave flumes. It should be mentioned that they focus on wave conditions, which are in the reflective and intermediate

range with respect to the beach state, i.e. $\Omega \simeq 1.0 - 6.0$. They find that the superposition of long free waves onto a short wave favours shoreward sediment transport, whereas an irregularity in the wave field introduced through either bichromatic or irregular wave fields favours offshore transport. When the corresponding regular wave is net erosive, the irregularity results in an increased offshore directed sediment transport. They conclude that the introduction of wave irregularity is the same as an increase in Ω.

This conclusion might, however, be related to the fact that Ω is in the intermediate range, in which the change from shoreward to seaward sediment transport fluxes must take place. At least the numerical simulations by Rakha *et al.* (1997) suggest that their numerical model to a reasonable degree can predict the sediment fluxes under irregular waves, when compared to measurements ($\Omega \simeq 14$). When replacing the irregular waves with a representative regular waves, Rakha *et al.* (1997) found a large increase in the sediment transport fluxes and a considerable increase in the gradient of the transport field. The author does not know of experiments, which can reveal the effect of irregular waves versus regular waves for clearly dissipative beach states, i.e $\Omega \simeq 10 - 20$.

2.4.2 Hypotheses for Formation of Breaker Bars

In the context of classification, as described in §2.2, the formation hypothesis is typically based on the infragravity wave theory. Here, the cross shore location of the bars is related to the nodes/antinodes of the standing wave depending of whether bed load or suspended sediment transport is dominant. This is hypothesised to be due to the two period averaged circulation cells, which are found on top of each other, see figure 2.9A. These circulation cells are induced by a weak variation in the mean water level. This mean variation is similar to that of standing waves on a horizontal bed, see e.g. Gislason *et al.* (2009). The difference between horizontal and sloping beds is that, while the wave length and the height of the standing wave are constant in space for horizontal beds, the wave height increases and the wave length decreases with decreasing water depth over sloping beds.

The rhythmicity of crescentic bars is similarly related to the longshore wave length of standing edge waves. The formation process is thus entirely described by an infragravity forcing without any feedback as shown in figure 2.10(a).

The simplicity of this formation process is striking, and its popularity is summarised nicely as: *"The notion of a forcing template is attractive because the characteristics of the morphological pattern, in particular the spatial scales, can be predicted deterministically based solely on properties of the template"* (Coco and Murray, 2007, p. 272).

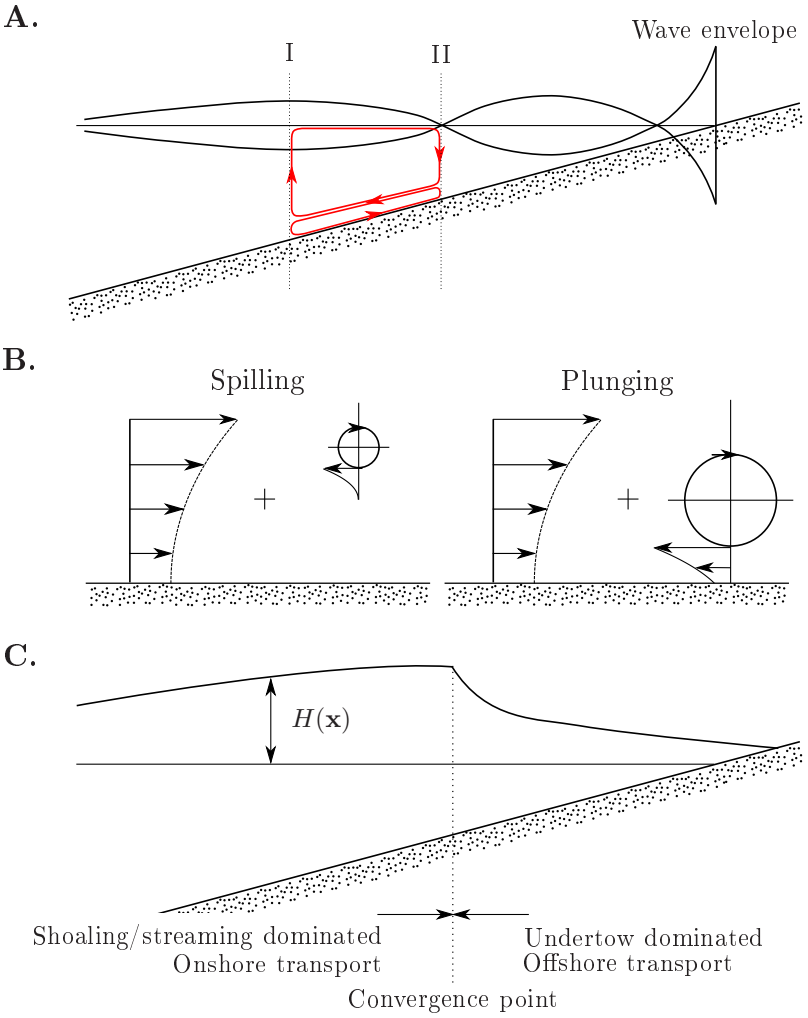

Figure 2.9: *Formation hypotheses. A: Convergence of sediment transport under standing infragravity waves. B: The plunging breaker hypothesis following Miller (1976). C: Onshore transport due to streaming and shoaling outside the surf zone and offshore transport due to undertow in the surf zone (Modified after Fredsøe and Deigaard, 1992, figure 11.2).*

Questioning the Infragravity Formation Hypothesis

As attractive as it might be, the infragravity hypothesis has been contradicted by a combination of theoretical, experimental and numerical work. These works instead support the much more complex feedback driven hypothesis (see figure 2.10(b)). As pointed out by Dally (1987) the shape of the beach profile significantly influences the analytical solution of the location of the nodal points for the cross shore standing infragravity wave,

however this modification of the forcing template to changes in beach profile is not considered in the formation hypothesis, i.e. no feedback mechanism.

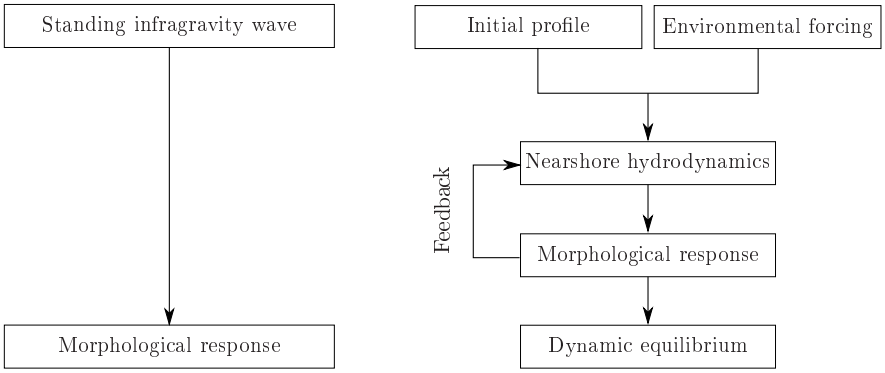

(a) Infragravity forcing without feedback

(b) Feedback driven morphological development

Figure 2.10: *Conceptual presentation of formation hypotheses with and without feedback mechanisms.*

Dally (1987) conducted laboratory experiments of bar formation under bichromatic wave forcing, which favours strong infragravity wave forcing. Nevertheless, his results clearly favoured the undertow as the dominant process for breaker bar development. Furthermore, field experiments regarding the spacing and dynamics of crescentic bars (van Enckevort *et al.*, 2004; Holman *et al.*, 2006) concludes that the irregularity and the non-linear processes such as merging and splitting of crescentic bars can hardly be explained by the presence of standing edge waves nor linear stability theory for that matter, because both of these theories would have resulted in much more regular spacings. Similarly for beach cusps, Masselink *et al.* (2004) found no experimental evidence of a forcing template in their field study.

Linear stability theories, as the name suggests, cannot describe non-linear phenomena such as merging and splitting. These processes require e.g. a complex depth integrated area model as the one by by Reniers *et al.* (2004). They used it to describe the development of the beach profile under irregular directional spread wave fields. They found that infragravity motion is linked to the longshore spacing between the irregularly placed rip channels. By removing the influence of infragravity motion on the sediment transport in an otherwise identical simulation, Reniers *et al.* (2004) showed that the resulting morphology was qualitatively unchanged. The only considerable difference being a less smooth bathymetry in the case of no infragravity

component in the sediment transport. This supports that coupling between morphological features and infragravity waves, which has been measured in the field, is the effect rather than the cause. This coupling is discussed by Masselink *et al.* (2004) in the case of beach cusps, where triad interaction[‡] between the incoming waves and the stationary beach cusp can cause a growth in edge wave energy; this was also pointed out by Bowen (1997). In the latter, however, it is discussed in the context of the possibility of infragravity waves generating bedforms, i.e. incident waves together with edge waves were hypothesised to cause the emergence of beach cusps.

The presence of infragravity waves is seen to merely distribute sediment more smoothly and might be responsible for the initial perturbations needed by instability theories "*(...) but such an assumption would significantly reduce the role of edge waves to just one of the many possible sources of morphodynamic instability*" (van Enckevort *et al.*, 2004).

Feedback Driven Hypothesis

As mentioned above, the experiments by Dally (1987) favoured the undertow for the development of breaker bars. It was discussed in §2.3.4 that the undertow is strongest near the bottom, whereas the return flow is strongest farther away from the bed. As suspended sediment is mainly confined to the lower part of the water column, the offshore transport mechanism disappears as the undertow separates from the bed and becomes the return flow. Together with an onshore sediment transport due to streaming effects and non-linear waves offshore the breakpoint (e.g. Fuhrman *et al.*, 2009), sediment converges and a breaker bar develops (see figure 2.9C).

This process describes a different kind of forcing template hypothesis, which is quite opposite that of the infragravity hypothesis. The hypothesis is summarised in figure 2.10(b). It consists of a set of environmental forcings such as wind, waves and currents and an initial beach profile. The induced hydrodynamic and sediment transport patterns affect the morphology, which in its turn change the transport patterns. This feedback process continues until an equilibrium is achieved or the environmental forcing changes. Experimental evidence on the dependence of the initial profile can be found by comparing tests 2 and 3 in Eagleson *et al.* (1963). Here the equilibrium profiles are compared under the same forcing but for 2 different initial profiles (different plane slope), and they are seen to differ. The feedback process is well described by Greenwood and Davidson-Arnott (1975) pp. 143–146 (without using the term), where a complex plan view with inner and outer

[‡]Triad interaction is the exchange of energy between three waves with frequencies fulfilling special requirements. One of these frequencies can be 0, e.g. a fixed bed feature such as beach cusps.

crescentic bars is described. Greenwood and Davidson-Arnott (1975) suggest that the formation of bars is an accumulative process rather than a scoured one, where shoreward sediment transport capacities are subject to a rapid decrease due to breaking. They do not address the existence of the undertow and assume that the total shoreward flux of water to exit through rip channels.

Plunging Breaker Hypothesis

Miller (1976) suggested based on laboratory experiments that the vortices generated by plunging breakers is the key mechanism for creating the bar-trough feature, see figure 2.9B. This suggestion is based on two test cases with plunging and spilling breakers, and he noted that the spilling breakers transported sediment shoreward without creating any prominent features (except wave orbital ripples). The plunging breakers on the other hand led to a bar-trough morphology. The large scale vortices are undoubtedly relevant in the case of plunging breakers, where they penetrate to the bottom. However, the conclusion that spilling breakers cannot create bar-trough morphology is incorrect as seen in e.g. the laboratory experiments by Baldock *et al.* (2010). An explanation on his results can be found by estimating $\Omega \simeq 1.5$, which based on the classification described in §2.2 is an accretive beach state and almost fully reflective. This means that no morphological features are supposed to appear and the sediment transport should be directed shoreward.

2.4.3 On- or Offshore Bar Migration

Is Cross-Shore Migration a Cross-Shore Effect?

Typically, waves have an oblique angle of incidence relative to the shoreline. As discussed in §2.3.4 this results in a longshore current. Additionally, the morphological feature prior to a storm is likely to be in one of the intermediate beach states with longshore rhythmic morphological features. Such a rhythmic feature has been reported to be migrating in the longshore direction with a rate of 20 m/day and 150 m/day respectively (Mason *et al.*, 1984; Ruessink *et al.*, 2000).

The cross shore migration pattern has been extensively studied in the field over a single cross shore survey line. In interpreting the results a longshore uniformity is implicitly or explicitly assumed, which yields values for the cross shore migration rates of the breaker bar. However, Ruessink *et al.* (2000) applied the ARGUS-technique and identified the position of the breaker bars indirectly. Based on these results a 2D horizontal picture of the breaker bar locations were obtained. The analysis showed that on a short

time scale, 85% of the cross shore migration of the breaker bar during that particular experiment was caused by the longshore migration of a longshore rhythmic feature. In the study by Mason *et al.* (1984) 15 cross shore lines were surveyed. Due to a longshore migration of a crescentic bar of 20 m/-day, there was an apparent onshore migration of 18 m/day along one profile line and an apparent offshore migration of 9 m/day along another line. This means that an Eulerian perspective on beach morphology can result in wrong conclusions as conceptually sketched in figure 2.11.

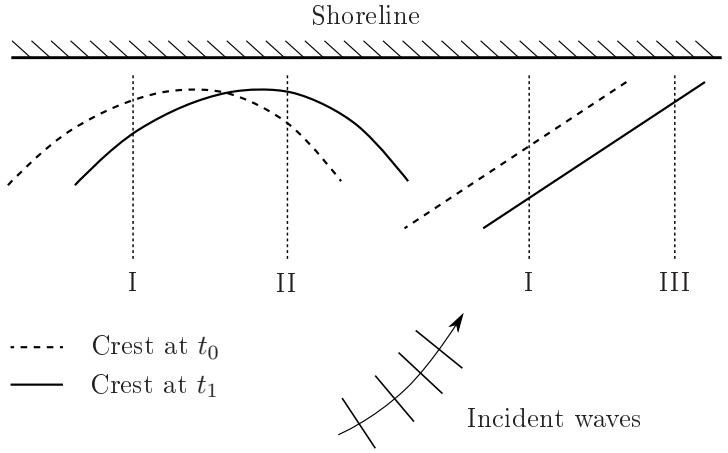

Figure 2.11: *Conceptual sketch of the conclusions drawn in an Eulerian perspective, when the bars are migrating with constant form, while not being longshore uniform and parallel. I: Offshore migration. II: Onshore migration. III: New bar appear.*

On longer time scales, it is shown from similar experiments at FRF, Duck (Lippmann and Holman, 1990) that the cross shore exchange of sediment is governed by cross shore sediment transport, since 74% of the cross shore movement of the breaker bar occurred as an offshore migration of a longshore uniform feature. Lippmann and Holman (1990) showed that there is a significant correlation between incident wave height and cross shore migration of the breaker bar. An increase in wave height preceded an offshore migration and a decrease in wave height favoured onshore migration.

A similar long term analysis is presented by Clarke and Eliot (1988), who found that over a 10 year period the two most important eigenfunctions from an EOF analysis (empirical orthogonal function) explain 70–80% and 5–14% of the variability respectively. The two modes are cross shore transport and horizontal circulation modes, respectively. It is not surprising that the cross shore transport is so important, since the beach is enclosed, however, the

importance of the second eigenmode reveals the 3-dimensionality of the bar migration pattern.

This means that on shorter time scales an Eulerian observation of a cross shore beach profile change could be due to a longshore migration of an otherwise unchanged rhythmic feature. On the longer time scale, however, where the accumulated effect of multiple wave lengths and/or variations in the longshore current direction reveals itself as an actual cross shore exchange of sediment.

It should be pointed out that the cross shore migration of straight longshore bars is also experienced in nature, where cross shore migration of the breaker bar reflects an actual migration, see e.g. Birkemeier (1984); Aagaard *et al.* (2004). In these two field surveys the trend is offshore and onshore bar migration respectively. In the field study by Aagaard *et al.* (2004) the breaker bar weld onto the beachface and supply sediment to the beach on an otherwise eroding shoreline.

Direction and Rate of Migration

Birkemeier (1984) (his figure 8) considers the offshore migration of longshore uniform features at FRF, Duck during large storms. Here offshore migration rates of up to 30 m/day is found. This storm induced offshore migration cannot have any longshore non-uniformity, as the wave forcing by far exceed the one necessary to obtain straight 2D breaker bars (see classification system by Lippmann and Holman, 1990). The offshore migration rate contrasts the slow onshore migration during fair weather conditions. During a six month period of calm weather the outer bar at FRF, Duck, merely migrated 85 m onshore (0.5 m/day).

Birkemeier (1984) used empirical orthogonal function (EOF) on an interannual data set, where the EOF is a decomposition method into unknown basis functions, which are a part of the solution to an eigenvalue problem. Birkemeier (1984) shows that at FRF, the most prominent variability in the beach profile is controlled by large storms, whereas the effect of seasonal variations are of relative minor importance in reshaping the beach profile.

The onshore migration occurs when the waves are breaking shoreward of the bar under consideration. Oppositely, offshore bar migration occur when the surf zone extend farther shoreward than the breaker bar position.

Onshore migration rates are tabulated by Sunamura and Irie (1988) to $\mathcal{O}(1-5)$ m/day and single migration rates as large as 30 m/day. One of these is reported by Sallenger *et al.* (1985) and is the onshore migration of parts of a crescentic bar.

The conceptual model by Plant *et al.* (2001) reveals that the onshore migration of breaker bars subject to small waves can result in an accelerated

decay in breaker bar height. This happens, because the parameter H/h_c, where h_c is the water depth over the bar crest, decreases resulting in further decay in breaker bar height.

Does an Equilibrium Bar Position Exist?

The dynamic equilibrium was investigated by Eagleson *et al.* (1963), who found that under some conditions, the beach profile reached an equilibrium position, and in other experiments the beach profile reached a quasi-steady state equilibrium. The quasi-steady state exhibits a slow variation due to be interaction between hydro- and morphodynamics. The process is as follows: Spilling breakers causes slight changes to a quasi-steady bathymetry, hence inducing a change from spilling to plunging breakers. The plunging breakers subsequently reverse the changes to the bathymetry and the wave breaking changes to spilling breakers. The bathymetry in the deeper parts of the flume is invariant to these subtle changes near the breakpoint.

The experiments by Eagleson *et al.* (1963) were all for Ω between 1.0 and 2.0, and the experiments all lasted more than 100 hours using laboratory waves. This suggests that it might be possible to achieve a dynamic equilibrium under fair weather conditions, however, the experiments does not answer the question with respect to storm conditions, i.e. $\Omega \geq 6.0$.

2.5 Modelling of the Complete System

2.5.1 Equilibrium / Behavioural Modelling

The hypothesis on beach stage changes by Wright and Short (1984) (see §2.2) is adopted by Plant *et al.* (1999) in a model, which adjusts the position of the bar crest based on the environmental forcing. The rate of change in the bar crest position is modelled to behave in an exponential manner with respect to the equilibrium position. The equilibrium position is based on the current hydrodynamic forcing. The model takes the form

$$\frac{\mathrm{d}x_c}{\mathrm{d}t} = -\alpha_c(t)\left[x_c(H(t),t) - x_{c,\mathrm{eq}}(H(t),t)\right] \tag{2.10}$$

where x_c is the bar crest position and $x_{c,\mathrm{eq}}$ is the corresponding (time dependent) equilibrium bar crest position. α_c is a time dependent response coefficient, which is assumed to depend on the sediment transport rate, hence $\alpha_c(t) \propto H(t)^j$, where $j \simeq 3$. Furthermore, they model $x_{c,\mathrm{eq}}$ as proportional to H. This simple model (when fitted) compares well with field measurements of bar crest position over a decade.

The adoption of an equilibrium modelling approach is also suggested by Hansen *et al.* (2004). Hansen *et al.* (2004) use an area modelling concept

based on the MIKE21 framework (see §2.5.3) to compute the wave field, the depth averaged hydrodynamics and the resulting sediment transport. An equilibrium profile is parameterised and its shape parameters are fitted every morphological time step obeying the following constraints: (i) the volumetric change of a cross shore profile fits that of the gradients in the longshore sediment transport and (ii) the bar crest moves toward an equilibrium position in an exponential manner, i.e. offshore movement if the waves break offshore of the bar crest and onshore if the waves pass the bar crest without breaking. They simulate the rip spacing under constant hydrodynamic forcing and achieve realistic rip spacings, which are in the order of 5–10 times the width of the surf zone.

2.5.2 Profile Modelling

Many different approaches have been taken over the last 3 decades attempting to model the evolution of a breaker bar profile in the vertical plane. One of the first, if not the first, to include the effect of undertow in the beach profile development is the work by Dally and Dean (1984). They use an analytical expression for the undertow profile and combine it with an exponential decay for the distribution of the sediment concentration. Their model does qualitatively predict both accretive and erosional profiles, however, their predictions compare poorly with laboratory measurements.

Roelvink and Stive (1989) model the wave height distribution using an energy decay model, and the sediment transport is modelled using the energetic formulation by Bailard (1981) extended to include the effect of turbulent stirring. Roelvink and Stive (1989) compare the results with measurement and find that the lag between production and dissipation of turbulent kinetic energy has a considerable effect on the undertow and the resulting morphological response. They also find that removing wave asymmetry in the sediment transport formulation results in a more seaward located bar crest and the exclusion of long waves yields a less smooth cross shore profile with hardly any change in the location of the crest of the breaker bar. The former results from a decreased shoreward sediment transport in shoaling waves with the removal of wave asymmetry (e.g. Fuhrman *et al.*, 2009)

In Roelvink and Brøker (1993), 5 different profile models for nearshore hydro- and morphodynamics are compared. All the models except one rely on energy considerations in modelling the wave height distribution in the surf zone. The exception solves the mild-slope equations. None of the models are capable of predicting the wave height variation due to plunging breakers, thus the models can only be expected to be used under erosive conditions. Qualitatively, the models perform reasonably well, however, it is apparent from the results for especially regular waves that the transition from shoaling

to breaking waves is found as a near discontinuity in the cross shore sediment transport distribution. This near-discontinuity has been addressed by several authors, and has been handled in different way.

Handling the Near-Discontinuity in Sediment Flux

In the formulation by Dally and Dean (1984) the undertow is determined uniquely by the wave breaking, thus the undertow "dissolves" immediately at the breakpoint. This results in an abrupt change in the transport capacities. To remedy this, the computed transport distribution is multiplied by a redistribution function, which is termed *transport spreading*. Similarly, in Drønen and Deigaard (2007), the sediment fluxes are smoothed using a diffusion term, which are included to represent that such "*effects can be due to the gradual development in the breaking process, hysteresis in the conditions for the onset and cessation of wave breaking, the gradual adaptation of the undertow to shear stress from surface rollers, the inertia in the undertow and lag effects in the development of suspended sediment concentration profiles.*" They find (with their choice of coefficients) that this smoothing by far is more important in modelling a bar shaped feature relative to the inclusion of a lag effect in the development of the surface roller cross sectional area.

Profile Modelling using Boussinesq Waves

Another approximation to the intra-wave description is obtained using the Boussinesq approximation for the modelling of the waves (e.g. Madsen and Schäffer, 1998, for a review). The Boussinesq approximation is based on potential theory, hence the dissipation of wave energy is commonly described by including an additional term in the momentum equation (Deigaard, 1989; Schäffer *et al.*, 1993). The latter closure is applied in a range of models e.g. Rakha *et al.* (1997); Karambas and Koutitas (2002); Wenneker *et al.* (2011). They are all similar in terms of the wave modelling, however, the determination of the bed shear stress and the modelling of the sediment transport reveal a wide range of approaches. In Rakha *et al.* (1997) the intra-wave determination of the bed shear stress is based on Fredsøe (1984), from which the suspended sediment profile is determined deterministically having assumed an eddy viscosity distribution. The opposite model approach is that of Karambas and Koutitas (2002), where the bed shear stress and sediment transport formulations are based on complex empirical formulations, which are developed to encompass a wide range of wave-current cases.

An improvement on this method is found in Wenneker *et al.* (2011), where the excess momentum flux due to waves is computed using a Boussinesq approximation and transferred to a 3D hydrostatic model (Delft3D), which is

used to compute the hydrodynamics. This model has been validated against prototype laboratory experiments and field measurements. Generally, reasonable results are found.

Regularisation of the Irregular Forcing

An important result from Rakha *et al.* (1997) is that while the cross shore variation in wave height is well captured using a regular wave as a representative for irregular wave forcing, the sediment transport, and hence the resulting morphology, is poorly modelled using such an regularisation. This is simply a consequence of having wave breaking to occur at the same location. The regularisation results in a considerable increase in sediment transport rates (see Rakha *et al.*, 1997, their figure 15). On the other hand, the details in how the irregular waves are generated, e.g. using JONSWAP or Pierson-Moskiwitz spectra, is less important.

Profile Modelling using Solution to Navier-Stokes Equations

The modelling of the wave propagation and breaking in the surf zone was compared with field experiments by Torres-Freyermuth *et al.* (2007). They used a VOF method for tracking the free surface elevation with a solution to the Reynolds Averaged Navier-Stokes equations for the hydrodynamics, and a $k - \epsilon$ turbulence model (see e.g. §3.1.1) for representing the turbulence production and dissipation. They found that it is possible to predict the wave spectrum across the surf zone accurately. The field site is subject to near-normal incident waves, hence the assumption of two-dimensionality is reasonable.

Recently, Ontowirjo and Mano (2009) published results, where a full solution to the Navier-Stokes equations with surface tracking and sediment transport modelling was used to simulate the development of a breaker bar. The information on the methodology is scarce and the conclusions are not supported by the reported results, however, one figure showing a comparison with experiments is reasonable. Besides the present thesis and Jacobsen and Fredsøe (2011), the work of Ontowirjo and Mano (2009) appear to be the only of the kind published to date.

2.5.3 Area Modelling

Numerical modelling of the development of coastal morphology, which is not limited by an assumption of longshore uniformity, is carried out using area models. These are either depth integrated shallow water equations or 3D-hydrostatic models. Both of these are coupled with a spectral wave model.

In the depth integrated version, the undertow is represented using a quasi-3D approximation, which is the approach used in the MIKE21 framework.

Another commonly used framework is Delft3D; a validation of the hydrodynamics and sediment transport modelling is found in Lesser *et al.* (2004). Reniers *et al.* (2004) used the depth integrated version of Delft3D for the morphological modelling of rip channel spacing.

The modelling of waves in both models is a spectral wave modelling approach of which a third generation approach is described in Booij *et al.* (1999). The numerical approach is implemented in the freely available software SWAN[§].

One of the more prominent differences between MIKE21 and Delft3D is the following: While MIKE21 relies on a localised approximation of the suspended sediment transport, an advection equation is solved in Delft3D. The advection equation includes a source term, which adapts the solution to a local equilibrium concentration. This difference will result in a different morphological response, when using either of the models in regions with large gradients in the bathymetry, e.g. when considering a current across a deep channel, the infilling will be faster when using MIKE21 due to the localisation of sediment transport computations.

2.5.4 This Thesis

In the present thesis, the solution to the combined continuity and momentum equations for free surface flows are used as a driver for sediment transport simulations. Based on the divergence in the sediment transport field, the morphological response feeds back to the hydrodynamics. The model is fully described in §3.

Such an approach has to the author's knowledge only (to some extent) been attempted once by Ontowirjo and Mano (2009) as already discussed in §2.5.2.

This thesis is considered by the author as an important step toward the capability of modelling nearshore morphodynamics with a significant reduction in assumptions compared to previous modelling frameworks. Furthermore, the model can be used to describe temporal and spatial lag effects in the nearshore region and especially in the region close to the breakpoint, which can be incorporated in less sophisticated deterministic models. These lag effects are hardly measured in neither laboratory nor field experiments.

[§]www.swan.tudelft.nl

Chapter 3

Model Description

This study is based on the numerical modelling of the physical processes taking place in the surf zone, where the key elements to capture are:

- An accurate modelling of the wave propagation, wave breaking, and the related processes such as wave setup, streaming and undertow.
- The dissipation of organised fluid motion into turbulent kinetic energy, k, and the dissipation of the latter into heat.
- The combination of organised motion and turbulence might result in both bed load sediment transport and sediment transport carried in suspension, hence these processes needs to be modelled as well.
- Finally the resulting sediment transport induces a bed level change, which needs to be modelled through the incorporation of a morphological module.

The basis of this model is the freely available open-source computational fluid dynamics toolbox OpenFoam®, which is distributed by OpenCFD®. Neither wave modelling, sediment transport nor the morphological updating of the bed level are included as a standard in the distribution. Therefore, a part of the present study has been to implement the necessary parts. A description of the methodology will be given in the following. In addition to the official release, the work has also gained significantly from the implementations made available through the OpenFoam-Extend community.* Version 1.5-dev is used throughout this thesis.

OpenFoam is discretised using a finite volume method on unstructured meshes, where the computational cell can have any arbitrary convex polyhedral shape, see Jasak (1996) for a thorough description of the finite volume

*See www.extend-project.de and http://sourceforge.net/projects/openfoam-extend

discretisation and time integration schemes. In the present study it is sufficient to note that an implicit Euler time integration scheme has been used (Ferziger and Peric, 2002) unless otherwise stated, and numerical schemes being second order in space are used.

3.1 Numerical Modelling of Two-Phase Flows

The approach for solving the fluid problem is to consider the two phases simultaneously using a tracking method for the interface. The flow field satisfies the incompressible continuity equation

$$\nabla \cdot \mathbf{u} = 0 \tag{3.1}$$

and the Reynolds averaged Navier-Stokes equations

$$\frac{\partial \rho \mathbf{u}}{\partial t} + \nabla \cdot \rho \mathbf{u}\mathbf{u}^T = -\nabla p + \rho \mathbf{g} + \nabla \cdot [\mu \nabla \mathbf{u} + \rho \boldsymbol{\tau}] + \sigma_T \kappa_\gamma \nabla \gamma \quad , \tag{3.2}$$

where $\mathbf{u} = (u,\ v,\ w)$ is the velocity field in Cartesian coordinates, ρ is the density, p the total pressure, $\mathbf{g}$ the acceleration due to gravity, μ is the dynamic molecular viscosity, and $\boldsymbol{\tau} = -\overline{\mathbf{u}'\mathbf{u}'^T}$ is the specific Reynolds stress tensor. Superscript T means transpose of a vector. The turbulence closure is discussed in §3.1.1. ∇ is the gradient operator given as

$$\nabla = \left(\frac{\partial}{\partial x}\ ,\ \frac{\partial}{\partial y}\ ,\ \frac{\partial}{\partial z} \right)^T \quad . \tag{3.3}$$

The last term on the right hand side in eq. (3.2) is the effect of surface tension, where κ_γ is the curvature of the interface, σ_T is the surface tension constant (0.074 kg/s^2 between air and water at 20°C), see e.g. Ubbink and Issa (1999) for a description of its handling.

The formulation in eq. (3.2) is given in terms of total pressure, thus the introduction of the excess pressure (see Rusche, 2002, chap 4 for details)

$$p^* = p - \rho \mathbf{g} \cdot \mathbf{x} \quad , \tag{3.4}$$

where $\mathbf{x} = (x,\ y,\ z)$ is the coordinate vector, eases the boundary condition formulation for the pressure. Inserting into eq. (3.2) yields

$$\frac{\partial \rho \mathbf{u}}{\partial t} + \nabla \cdot \rho \mathbf{u}\mathbf{u}^T = -\nabla p^* - \mathbf{g} \cdot \mathbf{x} \nabla \rho + \nabla \cdot [\mu \nabla \mathbf{u} + \rho \boldsymbol{\tau}] + \sigma_T \kappa_\gamma \nabla \gamma \tag{3.5}$$

The wave problem is inherently transient, so the PISO approach is adopted to solve the velocity-pressure coupling (Issa, 1986). The actual approach in OpenFoam is described in Jasak (1996).

The two phases of the flow are distinguished with a scalar quantity, γ, which represents water, when $\gamma = 1$, and air when $\gamma = 0$. This is the basis for the volume of fluid approach (VOF) first introduced by Hirt and Nichols (1981). Their approach considers the passive advection of γ under a velocity field $\mathbf{u}$

$$\frac{\partial \gamma}{\partial t} + \nabla \cdot \mathbf{u}\gamma = 0 \quad , \tag{3.6}$$

which is identified as a hyperbolic type equation. Considering the number of approaches for solving this differential equations, there are two fundamentally different approaches: (i) solving the partial differential equations in some form using ways to stabilise it and avoid diffusion of the interface or (ii) avoiding the differential equation and consider methods using geometrical approaches of various kinds.

Solving the equations in the differential forms offer some considerable advantages over the geometrical approach, as it can be solved "easily" on arbitrary mesh configurations. However, hyperbolic problems are notoriously hard to solve with issues such as boundedness of the solution and smearing of the interface over several cells adjacent to the "real" interface location. The former is typically handled using higher order bounded schemes, e.g. van Leer, Minmod or Superbee (see Leveque, 2007, p. 115). The latter is handled using several different kinds of interface compression such as those described by Ubbink and Issa (1999) with the use of compressive numerical schemes or the one by Rusche (2002), where eq. (3.6) is modified to

$$\frac{\partial \gamma}{\partial t} + \nabla \cdot \mathbf{u}\gamma + \nabla \cdot \mathbf{u}_{r,V}\gamma(1-\gamma) = 0 \quad . \tag{3.7}$$

Here $\mathbf{u}_{r,V}$ is a relative velocity and the additional source term yields low interface smearing. A similar method is used for the implementation in OpenFoam, which is adopted in the present study. The derivation of the used methodology is described in Berberović *et al.* (2009).

The methods using geometrical considerations for solving eq. (3.6) omit the partial differential equation. One of the methods applied is donating regions, where a region is defined, which is the source of fluid over a computational face. Different definitions exist, e.g. those in figure 3.1(a), where the gray area in all cases equals the face flux times Δt. The distribution of γ inside the cell can be constructed in several fashions, where the one depicted in figure 3.1(b) is based on the surface normal gradient, $\mathbf{n}_s = \nabla\gamma$. The vertically hatched area represents $\gamma = 1$ and the cross hatched area is the amount of γ, which is eventually advected over the right hand face. One drawback of many of these methods, however, is that they too can result in unbounded solutions, and the theoretical descriptions are mainly restricted to Cartesian orthogonal cells in two dimensions.

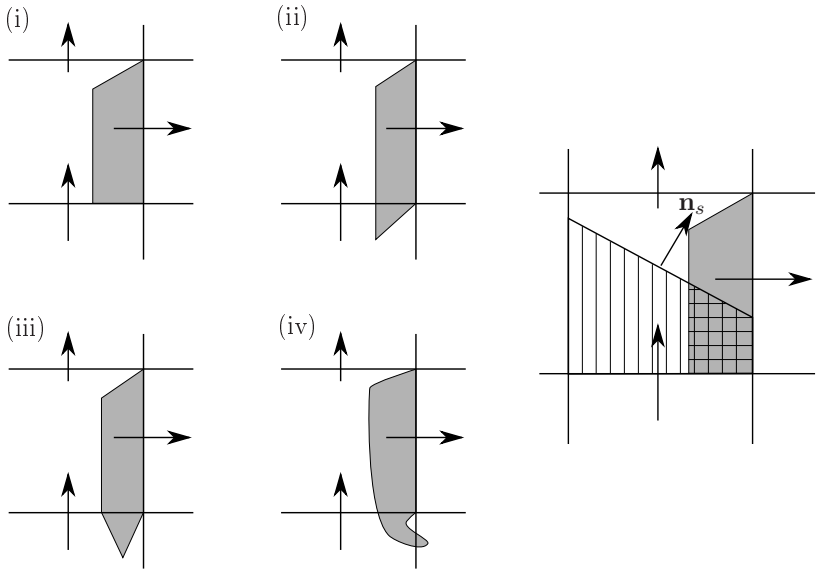

(a) Donating regions (b) Donating regions

Figure 3.1: *(a) Different lay-outs of the donating region as discussed in Harvie and Fletcher (2000) (After Harvie and Fletcher, 2000, their figure 17) (b) An example of the computation of the amount of γ advected over the right face. Based on the DDR-scheme by Harvie and Fletcher (2001).*

One method not having these limitations is the formulation by Zhang and Liu (2008). It takes arbitrary computational cell shapes, however, still only formulated for two dimensions. The method seems to have a large potential for accurate interface representation, and it is based on a backward translation in time of the computational cells in a Lagrangian manner followed by a forward translation in time of the matter in interest, i.e. $\gamma = 1$. This results in a net advection of γ. The method heavily depends on accurate interpolation schemes for the velocity field and methods for computing intersection between convex and concave polygons. Expanding this to 3-dimensions merely increase the level of complexity, and it has been found unsuitable for the present project.

Having obtained the distribution of γ, the fluid properties can be found as

$$\Phi = \gamma\Phi_1 + (1-\gamma)\Phi_0 \tag{3.8}$$

where Φ_0 and Φ_1 are quantities in the air and water respectively; these quantities can e.g. be ρ and ν.

3.1.1 Turbulence Closure

The process of wave breaking is also the transformation of organised motion into turbulence and subsequent heat. This means that the generation, advection and dissipation of turbulence must be modelled. Several turbulence closures has been applied in the case of wave breaking, namely $k-\epsilon$ models (Lemos, 1992; Lin and Liu, 1998; Bradford, 2000; Hieu *et al.*, 2004), a modified $k-\omega$ model (Mayer and Madsen, 2000), and large eddy simulations (LES) (Christensen and Deigaard, 2001; Christensen, 2006).

Firstly, LES was under consideration as the turbulence closure, because a considerable part of the mixing is resolved by the model. However, LES is strictly limited to 3-dimensional domains (Deardorff, 1970), and in the context of morphological development the flow problem must be solved over and over again even though convergence has been achieved in the flow problem. This would require as small as possible computational domains, thus 3-dimensions should be avoided. Furthermore, the stochastic nature of the flow, when using LES (see Sagaut, 2006, figure 1.1 and 1.3) reflects nonlinearly onto the sediment transport and results in large spatial gradients, hence the allowable morphological time step will be lowered considerably.

Therefore, the $k-\omega$ formulation has been chosen for this work, as it is known to handle adverse pressure gradients better compared to the $k-\epsilon$ turbulence closure (Wilcox, 2006, 2008). The $k-\omega$ formulation is easily adjusted to rough wall cases through the boundary condition for ω, and Patel and Yoon (1995) show that the prediction of wall shear stresses over rough boundaries is consistent with the Moody-diagram for a wider range of hydraulic roughnesses in the case of $k-\omega$ turbulence closure. Additionally, resolving the boundary layer through the viscous sublayer is inconsistent with the formulation for $k-\epsilon$ models, as the transport equation for ϵ becomes singular at the wall. The formulation of the $k-\omega$ model avoid this singularity, see Menter and Esch (2001).

The turbulence closure consists of two advection-diffusion equations with the relevant dissipation and production terms for the two variables k and ω. $k\left(=\frac{1}{2}\overline{(\mathbf{u}')^T\mathbf{u}'}\right)$ is the turbulent kinetic energy, where $\mathbf{u}'$ is the turbulent fluctuating velocity components. ω is interpreted in several ways, such as a characteristic frequency for the large scale turbulence (Menter and Esch, 2001), or simply the ratio between the turbulent kinetic energy, k, and the dissipation rate, ϵ (Speziale *et al.*, 1990).

The advection-diffusion equation for k[†] is given as

$$\frac{\partial \rho k}{\partial t} + \nabla \cdot \rho \mathbf{u} k = \mathcal{P}_k - \beta^* k\omega + \nabla \cdot \left[(\mu + \sigma^* \rho \nu_t)\nabla k\right] \tag{3.9}$$

and the one for ω takes the form

$$\begin{aligned}\frac{\partial \rho \omega}{\partial t} + \nabla \cdot \rho \mathbf{u} \omega =& \mathcal{P}_\omega - \beta \omega^2 \\ &+ \frac{\sigma_d}{\omega} \nabla k \cdot (\nabla \omega)^T + \nabla \cdot \left[\left(\mu + \sigma_\omega \frac{k}{\omega}\right) \nabla \omega\right]\end{aligned} \tag{3.10}$$

where the closure coefficients in the expressions take the following values $\alpha = 13/25$, $\beta = \beta_0 f_\beta$, $\beta^* = 9/100$, $\sigma_\omega = 1/2$, $\sigma^* = 3/5$, $\sigma_{do} = 1/8$ and

$$\sigma_d = \begin{cases} 0\ , & \nabla k \cdot (\nabla \omega)^T \leq 0 \\ \sigma_{do}\ , & \nabla k \cdot (\nabla \omega)^T > 0 \end{cases} \quad . \tag{3.11}$$

$\beta_0 = 0.0708$ and

$$f_\beta = \frac{1 + 85\chi_\omega}{1 + 100\chi_\omega} \quad , \tag{3.12}$$

where

$$\chi_\omega \equiv \left| \frac{\sum_n \left(\mathbf{e}_n^T \mathbf{\Omega}\right) \mathbf{\Omega} \left(\mathbf{S}\mathbf{e}_n\right)}{(\beta^* \omega)^3} \right| \quad \text{for} \quad n = x, y, z \quad . \tag{3.13}$$

Here, $\mathbf{e}_n$ is the unit vector along the axes in cartesian coordinates and the strain rate, $\mathbf{S}$, and rotation, $\mathbf{\Omega}$, tensors read

$$\mathbf{S} = \frac{1}{2}\left(\nabla \mathbf{u} + (\nabla \mathbf{u})^T\right) \quad , \quad \mathbf{\Omega} = \frac{1}{2}\left(\nabla \mathbf{u} - (\nabla \mathbf{u})^T\right) \quad . \tag{3.14}$$

The correction through f_β has an effect in the case of 3D flows, e.g. jets.

Following the isotropic assumption in the RANS formulation, it follows that

$$\boldsymbol{\tau} = 2\nu_t \mathbf{S} - \frac{2}{3} k \mathbf{I} \quad , \tag{3.15}$$

where $\mathbf{I}$ is the identity matrix and ν_t is the eddy viscosity, which in the $k-\omega$ framework is determined as

$$\nu_t = \frac{k}{\tilde{\omega}} \quad , \quad \tilde{\omega} = \max\left\{\omega, C_{lim}\sqrt{\frac{2\mathbf{S}:\mathbf{S}}{\beta^*}}\right\} \tag{3.16}$$

[†]N.B. The standard implementation in OpenFoam even for 2-phase (incompressible) flows is without ρ, which results in an excessive diffusion of turbulence over the interface and a resulting dampening of the wave, as $\nu_{t,0} \gg \nu_{t,1}$.

where **:** is the double inner product operator and C_{lim} takes the value 0.875.

The production term, $\mathcal{P}_k$, in eq. (3.9) is based on $\mathbf{S}$ in the standard formulation. It was shown by Mayer and Madsen (2000) using linear stability analysis that this formulation generates turbulent kinetic energy in a potential flow solution. This resulted in an increase in k, and hence ν_t, during the simulation, thus in the end the waves dissipated due to the presence of unphysical non-zero shear in the potential part of the water column outside the breakpoint. Mayer and Madsen (2000) suggested that the production based on curl of the velocity field could be modelled in the following way

$$\mathcal{P}_k = \rho\nu_t(\nabla \times \mathbf{u}) \cdot (\nabla \times \mathbf{u})^T \tag{3.17}$$

This eliminated the problem with spurious generation of turbulent kinetic energy. Similarly, $\mathcal{P}_\omega$ is given as

$$\mathcal{P}_\omega = \alpha\frac{\omega}{k}\mathcal{P}_k \quad . \tag{3.18}$$

Two kinds of turbulence closures have been considered in the present work. The first is a low Reynolds number version, which means that the boundary layer is that well resolved that the molecular viscosity has an effect (for smooth boundaries), and the other is a high Reynolds number version, i.e. the near wall behaviour is prescribed analytically.

Boundary Conditions for Low-Re Turbulence Closure

It was suggested by Roulund *et al.* (2005) that the boundary conditions for k near a rough boundary should not be set to 0 $\mathrm{m}^2/\mathrm{s}^2$, as experimental data contradicts this choice (e.g. Sumer *et al.*, 2003; Nezu and Nakagawa, 1993). Instead a zero flux boundary condition should be applied, i.e.

$$\mathbf{n}_s \cdot \nabla k = 0 \tag{3.19}$$

where $\mathbf{n}_s$ is the unit normal vector to the boundary. This boundary condition has been investigated in detail by Fuhrman *et al.* (2010), and it was found to yield good results and makes the near bed resolution dependent on the roughness height rather than the molecular viscosity. This is physically consistent, as the latter should not influence the near bed flow for large roughnesses due to Reynolds number independence.

The boundary condition for ω follows Wilcox (2006), however as he developed the rough boundary condition for $k = 0$, a re-calibration of the constants was performed by Fuhrman *et al.* (2010). Including their recommendations the boundary condition becomes

$$\omega = \frac{u_f^2 S_R}{\nu} \tag{3.20}$$

where

$$S_R = \begin{cases} \left(\frac{K_S}{k_N^+}\right)^2 & \text{for} \quad k_N^+ \leq 5 \\ \frac{K_R}{k_N^+} + \left[\left(\frac{K_S}{k_N^+}\right)^2 - \frac{K_R}{k_N^+}\right] e^{5.0-k_N^+} & \text{for} \quad k_N^+ > 5 \end{cases} \tag{3.21}$$

with $K_S = 200$ and $K_R = 180$ being calibration constants. The value of $K_R = 180$ differs from Wilcox (2006) due to the change in boundary condition for k. $k_N^+ = k_N u_f/\nu$ is the wall roughness in wall coordinates, where k_N is the Nikuradse' roughness height and u_f is the magnitude of the friction velocity vector.

Boundary Conditions for High-Re Turbulence Closure

Using a low Reynolds number turbulence closure in the case of surface water waves causes problems, because the cell dimension perpendicular to the boundary must obey $\Delta y \ll k_N$. As will be discussed in §3.3, the movement of the mesh is restricted to less than the cell discretisation for each time step, hence the limitation $\Delta y \ll k_N$ results in a huge number of mesh movements each wave period, each of which takes approximately the same time as a hydrodynamic time step. Therefore, a high Reynolds number turbulence closure is also tested.

The high Reynolds number implementation is inspired by the work of Nichols and Nelson (2004). In the present implementation, however, it has not been considered to derive a formulation that is transitional in terms of a generic low-to-high Reynolds number turbulence closure implementation. In this work $\Delta y/k_N = \mathcal{O}(1)$ has been used and the validity adjacent to this value is considered.

In the first cell next to the wall, ω is prescribed by (see e.g. Wilcox, 2006, p. 160)

$$\omega_{nw} = \frac{u_f}{\sqrt{\beta^*}\kappa\Delta y} \tag{3.22}$$

and similar

$$k_{nw} = \frac{u_f^2}{\sqrt{\beta^*}} \quad . \tag{3.23}$$

Using a large cell size has the drawback that the numerical evaluation of the velocity gradient is erroneous and the near wall momentum diffusion is wrong, if no measures are taken. The method is to fulfil

$$u_f^2 = (\nu + \nu_t)\frac{\delta\|\mathbf{u}_\tau\|_2}{\delta n} \tag{3.24}$$

by setting an artificially large eddy viscosity. Here δ indicates numerical differentiation and $\mathbf{u}_\tau$ is the velocity component tangential to the wall. The magnitude of the friction velocity, u_f, is found by

$$\frac{\|\mathbf{u}_\tau\|_2}{u_f} = \frac{1}{\kappa} \ln \frac{\frac{1}{2}\Delta y}{z_0} \tag{3.25}$$

where z_0 is the roughness being put to $k_N/30$ and κ the von Karman' constant set to 0.40.

It was considered to use the integrated momentum formulation in the boundary layer (see Fredsøe, 1984) to evaluate the bed shear stress. The near wall discretisation in the present project, however, is much smaller than the boundary layer thickness, so a momentum formulation would require "global" information, which does not conform with the localness in the remaining part of the model formulation.

Cox *et al.* (1996) found experimentally that a logarithmic layer is present over rough boundaries for almost the entire period both sea- and shoreward of the breakpoint. Their conclusions are based on one single set of wave parameters, roughness height, and bed slope.

Other Boundary Conditions

At the wave inlet and at the upper atmosphere boundary both k and ω are set to small constant values, however with values such that

$$\nu_t \simeq \frac{k}{\omega} \ll \nu \tag{3.26}$$

A Neumann condition is used at the outlet boundary.

3.1.2 Wave Generation and Absorption

Wave generation and absorption consist of two components, namely that at the boundary and that in the interior. These are described independently in the following.

Wave Boundary Conditions

Methods for wave generation are not distributed along with the standard distribution of OpenFoam, thus its implementation is part of the present study.

Several wave theories are applied in the present study, namely 1st and 2nd order Stokes theories (Dean and Dalrymple, 1991), 1st order cnoidal waves (Svendsen, 2006), and stream function theory (Rienecker and Fenton, 1981) for the case of monochromatic waves. The required information is

the potential flow solution of the chosen wave theory. The wave theory is enforced by specifying $\mathbf{u}_p$, η_p and $\partial p_p/\partial n$, where η_p is the surface elevation and the index 'p' refers to the potential flow solution.

Firstly, the boundary condition was implemented using the intuitive approach, where it was evaluated whether or not the boundary face was wet or dry based on the location of η_p relative to the centre of the boundary face, see figure 3.2 for an example of a boundary face. This gave rise to a binary behaviour in the value of γ on the boundary. Consequently, spurious oscillations were generated at the inlet, and these propagated into the domain and contaminated both the velocity and pressure distributions.

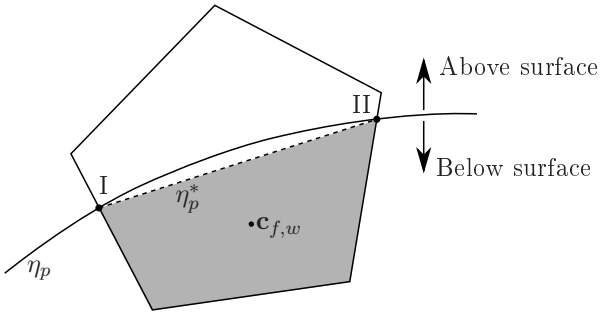

Figure 3.2: *Sketch of a boundary face intersected by the surface, η_p, giving rise to a subdivision into a wet and a dry part. The corresponding wet centre, $\mathbf{c}_{f,w}$, is of particular interest. Note that the boundary face can be an arbitrarily shaped convex polygon.*

It was needed to adopt a different approach. The chosen approach is sketched in figure 3.2. If the boundary face is intersected by η_p, there will be exactly two intersection points, as the length scale of the surface elevation is assumed much larger than the length scale of the boundary face. These two intersection points are computed, and a wet and a dry part of the boundary face is defined. Each of these has an area and a centre. At this intersected boundary face, $\mathbf{u}_p$ and $\partial p_p/\partial n$ are evaluated at the wet centre, $\mathbf{c}_{f,w}$ and assigned to the centre for the entire boundary face, $\mathbf{c}_f$. Furthermore, the boundary value for γ is the ratio between the wet area, $A_{f,w}$, and the total area, A_f, of the boundary face.

The introduction of this intersection technique resolved the problem with the spurious oscillations previously discussed.

Relaxation Zones

In Ohyama and Nadaoka (1991) the issue of outlet boundaries are considered for the modelling of water waves. Their approach relies on a boundary

element methods for surface water waves in terms of the velocity potential, ϕ. Firstly, they discuss the possibility of applying the Sommerfeldt boundary condition for the potential in the form

$$\frac{\partial \phi}{\partial t} \pm C \frac{\partial \phi}{\partial x} = 0 \tag{3.27}$$

where C is the long wave approximation to the wave celerity, $\sqrt{gh}$ with h being the water depth. This approach, however, is shown to give considerable reflection, when the assumption of long waves is not valid (Ohyama and Nadaoka, 1991). Therefore, they turn to the concept of sponge layers and apply a damping function in their formulation for ϕ. This yields reasonable results, however they show through mathematical analysis that the method has a complex behaviour based on the magnitude of the damping and the width of the sponge layer. This complex behaviour needs calibration for individual model setups.

Another method has been adopted in this work, namely the use of blending functions, which can modify an incoming wave field to any desired target function. This also extends the applicability of the sponge layer to inlet boundaries, as the target function could be that of the generated wave train. In the following the term sponge layers will be replaced by relaxation zones, as it is a more general term. The method is similar to the one used in Mayer *et al.* (1998) and the blending function is taken from Fuhrman *et al.* (2006).

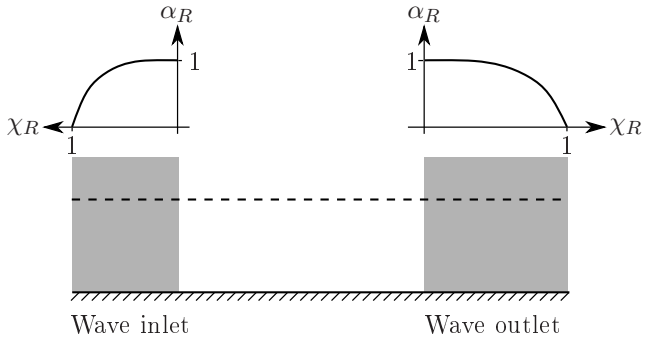

Figure 3.3: *A sketch of the variation of the blending function, α_R, in both inlet and outlet relaxation zones.*

The relaxation zone works as a blend between a target solution, e.g. $\mathbf{u}_p$, and the computed solution. The blend is applied explicitly each time step onto $\mathbf{u}$ and γ in the following way

$$\begin{aligned} \mathbf{u} &= (1 - \alpha_R)\mathbf{u}_{target} + \alpha_R \mathbf{u}_{model} \\ \gamma &= (1 - \alpha_R)\gamma_{target} + \alpha_R \gamma_{model} \end{aligned} \tag{3.28}$$

where the blending function, α_R is given as

$$\alpha_R = 1 - \frac{\exp(\chi_R^{3.5}) - 1}{\exp(1) - 1} \tag{3.29}$$

$\chi_R \in [0; 1]$ is a distance function defined linearly across the relaxation zone in such a way, that $\alpha_R = 0$ at the boundaries and hence yield an exact match between the boundary condition and the value in the relaxation zone, see figure 3.3.

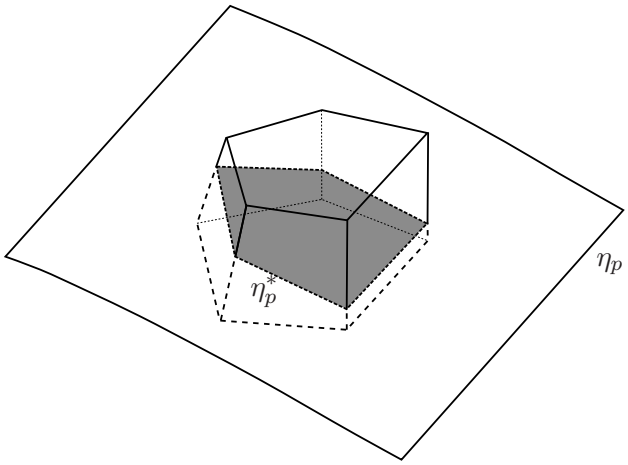

Figure 3.4: *A sketch of a computational cell intersected by a given surface (η_p). In the implementation the computational cell can have any convex polyhedral shape.*

Engsig-Karup (2006) discusses the functional form of the relaxation function, α_R. In the context of Discontinuous Galerkin methods it needs to fulfil the requirements $\alpha_R(0) = 1$ and $\alpha_R^{(n)}(0) = 0$ for $n = 1, \ldots$. This is in the present case fulfilled up to $\alpha_R^{(3)}(0)$ and it seems to be sufficient. The degree to which the requirement is fulfilled can be controlled by modifying the exponent in eq. (3.29).

The general idea is similar to the one applied for the wave boundary condition, see §3.1.2, where boundary faces intersected by the surface are cut into two. For the relaxation zone, the intersection plane through a computational cell is found, see figure 3.4. The corresponding wet centre, $\mathbf{c}_{V,w}$ is found together with the wet volume, V_w. From these it follows that $\mathbf{u}_{target} = \mathbf{u}_p(\mathbf{c}_{V,w}, t)$ and $\gamma_{target} = V_w/V$, where V is the volume of the entire computational volume.

The implementation into OpenFoam is made independent of the actual wave theory, let it be regular or irregular waves. This means that the func-

tionalities with respect to intersections between η_p and faces or computational volumes is made generic. Extensions to other wave theories is easily carried out, and it only requires knowledge of $\mathbf{u}_p$, η_p, and ∇p_p.

The description and validation of the boundary conditions and relaxation zone technique in addition to a general validation of the use of OpenFoam for wave simulation is also given in Jacobsen *et al.* (In print).

The boundary condition at the shoreline is a no-slip condition.

3.2 Sediment Transport Modelling

The sediment transport is handled in the standard way using a splitting into bed load and suspended sediment transport. The approach for the two types of sediment transport is detailed below. The sediment transport formulation is limited to uniform sand.

3.2.1 Bed Load Transport

Bed load transport is the part of the sediment transport taking place in conjunction with the bed, hence the computational mesh is the bottom boundary. A separate mesh for computing the bed load is constructed, see figure 3.5; a mesh that is also used as part of the morphological updating routine. This mesh is using the finite volume methodology implemented for general curved surfaces in 3-dimensional space. The method is called the finite area method (FAM). Besides the source code it is only documented in Tuković (2005), chap. 5[‡]. The FAM makes it possible to solve partial differential equations, which are only formulated on curve planes in the 3 dimensional space, which is the case for the Exner equation, see §3.3.

The chosen bed load formulation is the one detailed in Roulund *et al.* (2005), which is an extension of Engelund and Fredsøe (1976) to 3-dimensional space on arbitrary sloping beds, see figure 3.6[§]. The bed load is undertaken with a mean transport direction, $\mathbf{u}_b$ which differs in direction from the near wall tangential velocity, $\mathbf{u}_{nw,\tau}$, due to the action of gravity[¶]. $\mathbf{u}_{nw,\tau}$ may be taken as $a\mathbf{u}_f$ following Engelund and Fredsøe (1976), where a is a constant $\mathcal{O}(10)$ and

$$\mathbf{u}_f = u_f \frac{\mathbf{u}_{nw,\tau}}{\|\mathbf{u}_{nw,\tau}\|_2} \tag{3.30}$$

[‡]In Croatian.

[§]The formulation is kept in vectorial form, which bear resemblance to the formulation by Kovacs and Parker (1994), and as will be seen, this choice reduces the problem from 4 to 3 non-linear coupled algebraic equations.

[¶]Note that $\mathbf{u}_b \cdot \mathbf{N} = \mathbf{u}_\tau \cdot \mathbf{N} = 0$, where $\mathbf{N}$ is the bed normal vector, see e.g. figure 3.6

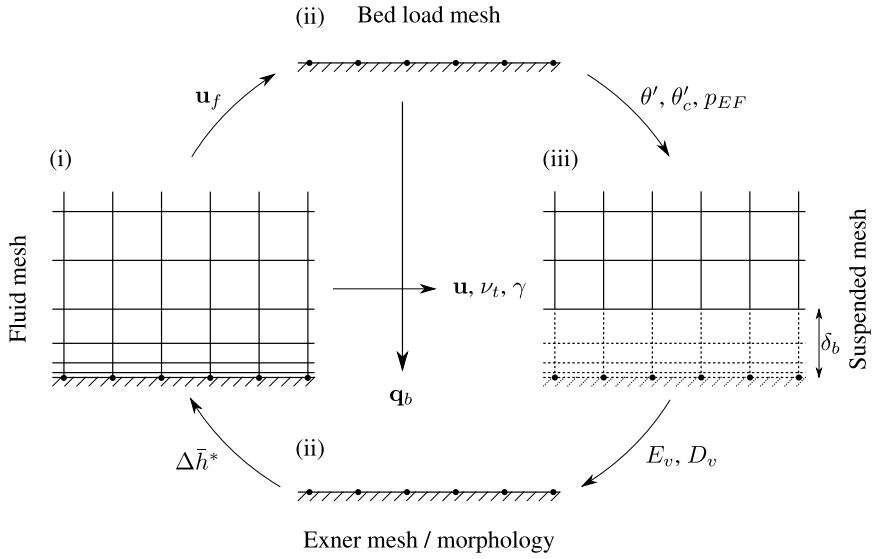

Figure 3.5: *A sketch of the coupling of the three meshes for the (i) Navier-Stokes equations, (ii) bed load and morphological computations and (iii) the suspended sediment transport. Variables defined throughout §§3.1-3.3*

is the friction velocity vector of magnitude u_f. $\mathbf{u}_{nw,\tau}$ is found as follows based on the near wall velocity, $\mathbf{u}_{nw}$, and the bed normal vector, $\mathbf{N}$,

$$\mathbf{u}_{nw,\tau} = \frac{1}{\|\mathbf{N}\|_2^2} \left[\mathbf{N} \times (\mathbf{u}_{nw} \times \mathbf{N})\right] \quad . \tag{3.31}$$

(The same method will be used throughout for the projection of some vector, $\boldsymbol{\phi}_{nw}$, onto the bed to yield $\boldsymbol{\phi}_{nw,\tau}$).

The rate of bed load is given as

$$\mathbf{q}_b = \frac{1}{6}\pi d \; p_{EF} \mathbf{u}_b \tag{3.32}$$

where p_{EF} is the probability of moving particles near the bed. This is given by

$$p_{EF} = \left[1 + \left(\frac{\frac{1}{6}\pi\mu_d}{\theta' - \theta'_c}\right)^4\right]^{-1/4} \quad . \tag{3.33}$$

d is the median grain diameter, θ' is the Shields parameter due to skin friction defined as

$$\theta' = \frac{u_f^2}{(s-1)gd} \tag{3.34}$$

where $g = \|\mathbf{g}\|_2$, s is the density of the sediment relative to the density of water, and θ'_c is the critical Shields parameter above which sediment is brought into motion. $\mu_d (= 0.60)$ is the dynamic friction coefficient. Following Roulund *et al.* (2005) θ'_c is computed as

$$\theta'_c = \theta'_{c0} \left(\cos\beta \sqrt{1 - \frac{\sin^2\alpha \tan^2\beta}{\mu_s^2}} - \frac{\cos\alpha \sin\beta}{\mu_s} \right) \quad , \tag{3.35}$$

and the expression includes includes the effect of the bed slope onto the magnitude of the bed load transport. The angles, α and β are defined in figure 3.6, $\theta'_{c0} = 0.05$, and μ_s is the static friction coefficient taken as 0.65, which equals an angle of repose of $\phi_r = 33°$.

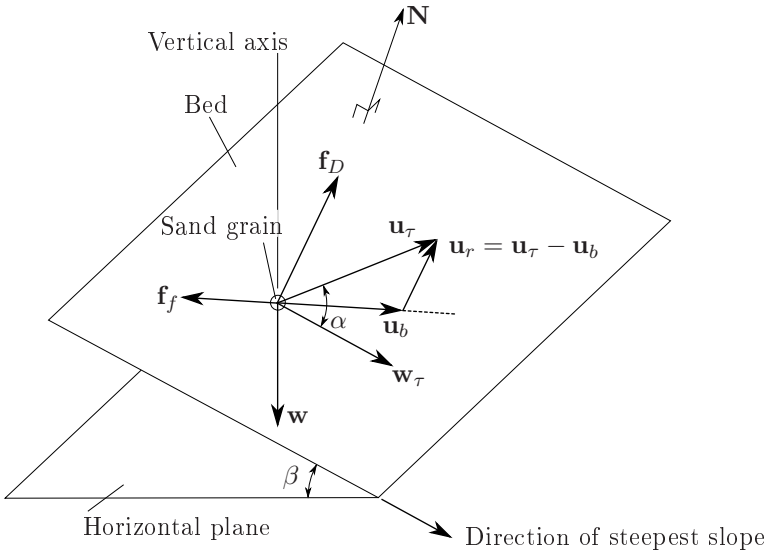

Figure 3.6: *Agitating and stabilising forces on a sand grain on a sloping bed. Only the gravity force on the sand grain,* $\mathbf{w}$*, is non-perpendicular to the bed normal,* $\mathbf{N}$*. (Modified from Roulund* et al.*, 2005)*

The gravity force, $\mathbf{w}$, acting on the sand grain is given as

$$\mathbf{w} = \frac{\pi}{6} \rho (s-1) d^3 \mathbf{g} \quad . \tag{3.36}$$

Due to the sloping bed, it is decomposed into a destabilising force in the direction of the steepest slope, namely

$$\mathbf{w}_\tau = \frac{1}{\|\mathbf{N}\|_2^2} \left[\mathbf{N} \times (\mathbf{w} \times \mathbf{N}) \right] \tag{3.37}$$

and a friction force, which is working in the opposite direction of sand grain motion

$$\mathbf{f}_f = -\frac{1}{\|\mathbf{N}\|_2}|\mathbf{w}\cdot\mathbf{N}|\mu_d\frac{\mathbf{u}_b}{\|\mathbf{u}_b\|_2} \quad . \tag{3.38}$$

The sand grain is further agitated by a combination of lift and drag due to its motion relative to the surrounding water. The force is given as

$$\mathbf{f}_D = \frac{1}{2}\rho c_s \frac{\pi}{4} d^2 \|\mathbf{u}_r\|_2 \mathbf{u}_r \tag{3.39}$$

where the relative velocity is given as

$$\mathbf{u}_r = \mathbf{u}_\tau - \mathbf{u}_b \quad . \tag{3.40}$$

Here c_s is a constant, which accounts for the drag and the reduction in the submerged weight due to lift on the particle. Following the experiments by Fernandez Luque (1974), c_s is written as

$$c_s = \frac{4\mu_d}{3a^2\frac{1}{2}\theta'_{c0}} \tag{3.41}$$

(Based on discussion in Engelund and Fredsøe, 1976, p. 298).

Assuming that the sand grain undertakes steady motion, the transport velocity, $\mathbf{u}_b$, can be found by solving

$$\mathbf{0} = \mathbf{f}_D + \mathbf{w}_\tau + \mathbf{f}_f \tag{3.42}$$

Substitution of eqs. (3.37), (3.38), (3.39) and (3.40) into (3.42) yields 3 non-linear equations, which can be solved for the three components in $\mathbf{u}_b$ and the bed load transport (eq. (3.32)) is readily evaluated. In the formulation by Roulund *et al.* (2005), 4 non-linear coupled equations needed to be solved in the general case.

Eq. (3.42) is solved in every computational cell in the FAM-mesh, hence the method takes the presence of ripples into account, if they are resolved in the model.

3.2.2 Suspended Sediment Transport

The conservation equation for suspended sediment is modelled using an advection-diffusion type equation

$$\frac{\partial c}{\partial t} + \nabla\cdot\left[(\gamma\mathbf{u} + \mathbf{w}_s(\mathbf{x}))c\right] = \nabla\cdot\left[\gamma(\nu + \tilde{\nu}_t)\nabla c\right] \tag{3.43}$$

where c is the volumetric suspended sediment concentration and $\mathbf{w}_s$ is the sediment fall velocity vector. The latter points toward the bed for $s > 1$.

$\tilde{\nu}_t$ is the sediment diffusivity coefficient given as ν_t/σ_c with σ_c being in the order of 1. In the rest of this work $\sigma_c = 1$. The modelling of the spatial variation in $\mathbf{w}_s$ is discussed below.

Please note that the rate of change and the term including $\mathbf{w}_s$ in eq. (3.43) are not multiplied by γ. This ensures that sediment, which accidentially is left in the air phase, drops out immediately after entering it.

Eq. (3.43) is solved fully implicit using the implicit Euler time integration. As the fall velocity significantly increases the vertical velocity field near the bed, the Courant number will exceed 1 if the time step from the solution to the Navier-Stokes equation is used. Instead of using smaller time steps throughout, eq. (3.43) is solved using a sub-time stepping method; e.g. eq. 3.43 adopts $\Delta t/10$ and it is solved ten times per global time step.

The bed boundary conditions for suspended sediment transport is specified at some distance from the bed, irrespectively of the approach, i.e. c_b-concepts as described by Engelund and Fredsøe (1976); Zyserman and Fredsøe (1994); van Rijn (1984) or entrainment/pickup function such as described by Nielsen (2009).

To handle this an additional mesh is introduced on which the suspended sediment transport is computed, see figure 3.5. This additional mesh is conformal to the mesh on which the Navier-Stokes equations are solved, however, the cells within a distance δ_b from the bottom are omitted. The necessary variables are mapped from the fluid mesh and the FAM mesh. The erosion and deposition due to suspended sediment transport are easily computed on this truncated mesh, as the bed boundary is well defined.

Spatial Variation of the Fall Velocity

Firstly it was considered to adopt the classical weighting in VOF-methods (eq. (3.8)) between the fall velocity in the air, $\mathbf{w}_{s,0}$, and that in the water, $\mathbf{w}_{s,1}$, to obtain the spatial variation, i.e.

$$\mathbf{w}_s = \gamma \mathbf{w}_{s,1} + (1-\gamma)\mathbf{w}_{s,0} \tag{3.44}$$

However, as can be seen in figure 3.7, this linear dependency causes large changes in $\mathbf{w}_s$ in the water even for small changes in γ, e.g. $\mathbf{w}_s = 2\mathbf{w}_{s,1}$ for $\gamma = 0.99$. Hence, instead it is decided to compute $\mathbf{w}_s$ as

$$\mathbf{w}_s(\mathbf{x}) = \mathbf{w}_s(\rho(\gamma(\mathbf{x})), \nu_1) \quad . \tag{3.45}$$

Note, that the kinematic molecular viscosity in water is used throughout, as the variation in $\nu(\mathbf{x})$ causes an unwanted spatial variation in $\mathbf{w}_s$ (Dashed line in figure 3.7). $\mathbf{w}_s$ is determined using a drag coefficient for natural sand, see Fredsøe and Deigaard (1992), pp. 198–199.

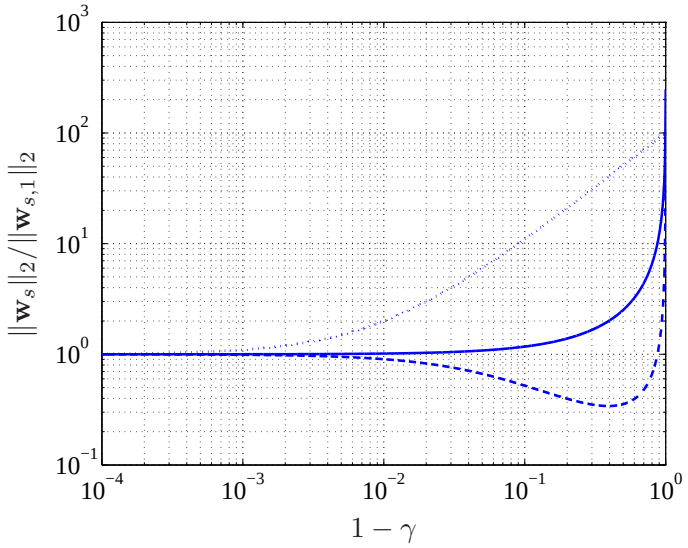

Figure 3.7: *The variation of* $\mathbf{w}_s$ *as a function of* γ *(*ρ*). Full: Eq.* (3.45)*. Dashed: Eq.* (3.45) *but with varying* ν *following eq.* (3.8)*. Dotted: Eq.* (3.44)*.*

Boundary Condition using c_b-Concept

Several formulations are given for the variation of c_b with the skin friction θ'. The formulations by Einstein (1950) and Engelund and Fredsøe (1976) are based on theoretical considerations, whereas the formulation by Zyserman and Fredsøe (1994) make a fit to experimental values of the suspended sediment transport thereby estimating $c_b(\theta')$. The formulation by Engelund and Fredsøe (1976) has been adopted in the present work.

It is given as

$$c_b = \frac{c_0}{(1+1/\lambda_b)^3} \tag{3.46}$$

where

$$\lambda_b^2 = \frac{\kappa^2\alpha_1^2}{0.013s\theta'}\left(\theta' - \theta_c - \frac{\pi}{6}\mu_d p_{EF}\right) \tag{3.47}$$

where λ_b is the so-called linear concentration and c_0 the maximum attainable volumetric concentration, see Fredsøe and Deigaard (1992). Further, p_{EF} is the propability given in eq. (3.33) and $\alpha_1(=2)$ is the multiple of d above the bed, where the velocity gradient in this deterministic approach is evaluated. For a full description, please refer to the original paper Engelund and Fredsøe (1976) or the summary given in Fredsøe and Deigaard (1992) pp 217–219.

This formulation, however, contains issues related to a sudden decrease in c_b. The extreme of this case is a settling tank, where the water is considered

still (neglecting the vertical flux of water due to the settling particles) with a non-zero concentration profile in the water column. As $\theta' = 0$, it follows that $c_b = 0$, and in the numerical model there will be a build-up of sediment in the lowermost computational cell. The solution to this problem is suggested by Justesen *et al.* (1986), where

$$c_b = \max\left[c_b(\theta'), c(\delta_b + w_s\Delta t, t - \Delta t)\right] \quad . \tag{3.48}$$

Hence, if the concentration close to the bed exceeds c_b, c_b takes the value of c in the water column. Due to a time step limited by a Courant number less than 1, the value is, in practice, taken from the cell adjacent to the boundary.

Boundary Condition at the Free Surface

For flows using a rigid lid approximation, the vertical balance between upward diffusion and downward settling must be enforced, which is formulated as

$$((\nu + \nu_t)\nabla c + \mathbf{w_s}c)\cdot \mathbf{n}_s = 0 \tag{3.49}$$

where $\mathbf{n}_s$ is the surface normal vector.

In the case of multiphase flows, however, this approach cannot be applied, as no well defined boundary exists at the surface. The condition is nearly satisfied through the large difference in $\mathbf{w}_s(\mathbf{x})$ over the interface. Suspended sediment are allowed to leave the computational domain through the atmospheric boundary, whereas "influx" of sediment occurs with $c = 0$.

3.2.3 Inclusion of Excess Turbulence in Sediment Transport Modelling

It has been considered whether or not it is feasible to include the effect of excess turbulence on the modelling of sediment transport. It was shown experimentally by Sumer *et al.* (2003) that the effect is considerable, however their experiments are limited to pure current and small θ'. The latter limitation requires excessive extrapolation to allow to incorporate the results in the present study, where θ' become as large as 3.0.

More knowledge is needed on the effect of excess turbulence, however, the current experimental evidence does not allow for an incorporation into this numerical model.

3.3 Morphological Updating Routine

Morphological changes to a given bathymetry occur, when there is an inequilibrium between deposited and eroded material in that region. If the amount

of deposited material exceeds the amount of eroded material, it leads to an increase in bed level and vice versa. This mechanism is described by the continuity equation for sediment (see e.g. Fredsøe and Deigaard, 1992, p. 265)

$$\frac{\partial h}{\partial t} = -\frac{1}{1-e_d}\left[\nabla\cdot \mathbf{q}_b + E + D\right] \tag{3.50}$$

The morphological change is split into contributions from the bed load transport ($\mathbf{q}_b$) and suspended sediment transport (E and D), where E and D are erosion and deposition respectively. Incorporating the porosity, e_d, in the contributing terms yield the Exners equation.

In eq. (3.50) E and D has been used to determine the net change due to suspended sediment transport. This is identical to the classical formulation (obtained by considering a control volume in 2D)

$$\nabla\cdot \int_{2d}^{h} \mathbf{q}_s\cdot \mathbf{e}_x \mathrm{d}y + \frac{\partial}{\partial t}\int_{2d}^{h} c\mathrm{d}y \tag{3.51}$$

where $\mathbf{q}_s(=c\mathbf{u})$ is the suspended sediment flux, y a vertical coordinate and x a horizontal one. The evaluation of eq. (3.51) is problematic on general unstructured meshes, hence the near bed treatment is preferable.

Eq. 3.50 is the instantaneous response to an instantaneous sediment transport rate. In the present work a time averaged bed level change, $\bar{h}$, is adopted instead, namely

$$\begin{aligned}\frac{1}{T_m}\int_t^{t+T_m}\frac{\partial h}{\partial t}\mathrm{d}t = \frac{\partial \bar{h}}{\partial t} &= -\frac{1}{1-e_d}\frac{1}{T_m}\int_t^{t+T_m}\left[\nabla\cdot \mathbf{q}_b + E + D\right]\mathrm{d}t \\ &= -\frac{1}{1-e_d}\left[\nabla\cdot \bar{\mathbf{q}}_b + \bar{E} + \bar{D}\right] \quad .\end{aligned} \tag{3.52}$$

Here

$$\{\bar{h}, \bar{\mathbf{q}}_b, \bar{E}, \bar{D}\} = \frac{1}{T_m}\int_t^{t+T_m}\{h, \mathbf{q}_b, E, D\}\mathrm{d}t \quad . \tag{3.53}$$

It is assumed that the interchange of the operators on the left hand side in eq. 3.52 is allowed. Here T_m is some characteristic morphological time scale, which for regular waves is naturally taken as the wave period, T.

3.3.1 Evaluation of Contributing Terms

The contributions from each of the terms in eq. (3.50) are described below.

Contribution Due to Bed Load

The bed load, $\mathbf{q}_b$, is computed in the centre of the computational face on the FAM-mesh. The evaluation of $\nabla\cdot\mathbf{q}_b$ is carried out through an adoption of the Gauss theorem, i.e interpolating $\mathbf{q}_b$ to the edges of the face and integrating along the boundary of the face, see also §3.3.3. The evaluation of this within the FAM framework yields a change in the normal direction to the face, however, the morphological updating is along the vertical axis, $\mathbf{e}_g$, hence a projection is needed.

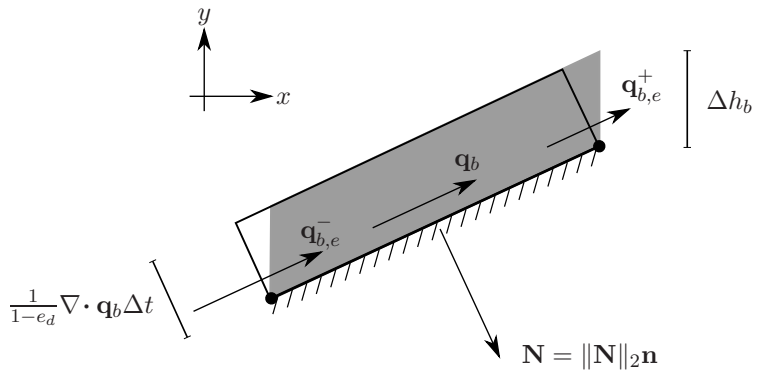

Figure 3.8: *Evaluation of the bed level change due to bed load transport. Subscript e is for edge interpolated transport rate.*

Considering figure 3.8, it is seen that the gray and empty trapezes have identical area but differs in orientation. From this, it is found that

$$\Delta h_b = -\frac{1}{1-e_d}\frac{\nabla\cdot\mathbf{q}_b}{|\mathbf{n}\cdot\mathbf{e}_g|}\Delta t \tag{3.54}$$

where $\mathbf{n}$ is the face unit normal. The area of the face is $\|\mathbf{N}\|_2$, where $\mathbf{n}\|\mathbf{N}$.

Erosion/Deposition using c_b-Concept

In figure 3.9(a) the balance between erosion and deposition over an arbitrarily oriented boundary face is sketched. The erosion, E_v, is given as[‖]

$$E_v = (\nu+\nu_t)\frac{\partial c}{\partial n}\|\mathbf{N}\|_2 = (\nu+\nu_t)\mathbf{N}\cdot\nabla c \quad \text{with} \quad \frac{\partial c}{\partial n} \le 0 \tag{3.55}$$

where n is a local coordinate normal to the boundary face. The contribution to the deposition, D_v, only comes from the projection of $\mathbf{w}_s+\mathbf{u}$ onto the face normal vector, i.e.

$$D_v = c_b|(\mathbf{w}_s+\mathbf{u})\cdot\mathbf{N}| \quad , \tag{3.56}$$

[‖]Note that $\partial c/\partial n$ cannot become positive due to eq. (3.48)

whereas the tangential projection, $w_{s,\tau}(= \|\mathbf{n} \times ((\mathbf{w}_s + \mathbf{u}) \times \mathbf{n})\|_2)$, does not contribute. Here E_v and D_v are the erosion and deposition rates in terms of m^3/s.

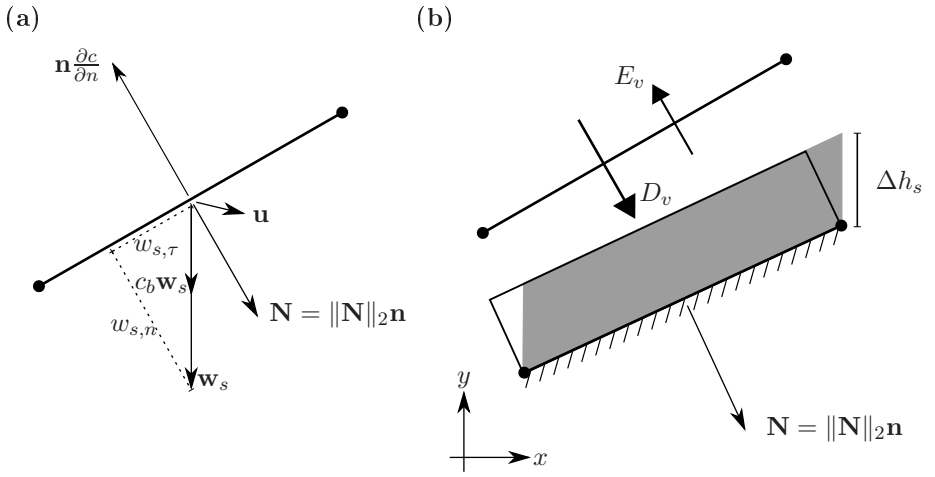

Figure 3.9: *(a) Direction of diffusion and settling of suspended sediment over a boundary face. (b) Resulting bed level change, Δh_s, due to combined erosion/deposition. $\|\mathbf{N}\|_2$ equals the area of the boundary face.*

The velocity over the boundary must be taken into consideration, as the computational mesh for suspended sediment transport does not coincide with the boundary for the computational mesh, which is used for solving the Navier-Stokes equations (see figure 3.5).

Bed Level Change Due to Erosion/Deposition

The bed level change due to erosion and deposition, Δh_s, is sketched in figure 3.9(b). The volume of the empty rectangle equals the net deposition, i.e.

$$V_{\text{empty}} = \frac{1}{1 - e_d}(D_v - E_v)\Delta t = |\mathbf{e}_g \cdot \mathbf{N}|\Delta h_s \tag{3.57}$$

where the last equality is the volume of the gray trapeze in the same figure. From this, the bed level change is easily evaluated.

Sand Slide Mechanism

It has been found necessary to include a sand slide mechanism to limit the bed slope to below the angle of repose, see an example in §C.2. The method described in Niemann *et al.* (2011) (a method similar to that of Marieu *et al.*

(2008)) is used in this work. It should be noted that another method was derived, which has better numerical performance in terms of computational time, however, the implementation was not entirely robust, thus the robustness of the method by Niemann *et al.* (2011) was preferred. The derived method is described in §C.1. Neither approach is easily applicable to 3 dimensions.

3.3.2 Numerical Approach

Time Integration

The new bed level, $\bar{h}^{i+1}$, as such is not of interest, but rather the change, $\Delta\bar{h}^{i+1}$. This is computed using the third order Adam-Bashforth explicit time integration scheme (see Ferziger and Peric, 2002, p. 139), which reads

$$\frac{\Delta\bar{h}^{i+1}}{\Delta T_m} = \frac{1}{12}\left[23\bar{F}^{i} - 16\bar{F}^{i-1} + 5\bar{F}^{i-2}\right] \tag{3.58}$$

where

$$\bar{F} = -\frac{1}{1-e_d}\left[\nabla\cdot\bar{\mathbf{q}}_b + \bar{E} + \bar{D}\right] = \frac{\Delta\bar{h}_b + \Delta\bar{h}_s}{\Delta T_m} \quad . \tag{3.59}$$

and i is the index of the present discrete time step.

This time integration scheme has been chosen based on its successful adoption in the simulation of river dunes in Niemann *et al.* (2011). An explicit time integration scheme is needed, as no way of solving eq. (3.50) implicitly over T_m is computational feasible, if at all possible.

Stability of the Exner Equation

The evaluation of eq. (3.50) has the same properties of a hyperbolic equation, as the bed level change due to suspension is evaluated independently of the bed load, i.e. firstly

$$\frac{\partial h}{\partial t} = -\frac{1}{1-e_d}\frac{\nabla\cdot\mathbf{q}_b(\mathbf{x},h,t)}{|\mathbf{n}\cdot\mathbf{e}_g|} \tag{3.60}$$

is computed. The stability of this type of partial differential equations has attracted significant attention, and specifically in the framework of the Exner equation, it has been discussed by e.g. Johnson and Zyserman (2002); Callaghan *et al.* (2006); Long *et al.* (2008).

Two different approaches illustrate the stability issues, namely by considering non-linear sediment transport as a function of h (Johnson and Zyserman, 2002) and by considering the truncated version of eq. (3.60) to numerical accuracy (Callaghan *et al.*, 2006). Both approaches prove that

measures need to be taken to avoid numerical instabilities, however, in the latter case only for divergence schemes of order higher than 1. The measures considered can be put into two categories:

- Numerical filtering as a post-processing step
- Adoption of numerical schemes, which suppress spurious oscillations

These two approaches will be discussed separately.

Numerically filtering has been widely used to ensure stability in works such as Jensen *et al.* (1999); Niemann *et al.* (2011) where the filter is applied onto h or in Andersen and Fredsøe (1999), where the sediment transport is filtered. Both of these approaches are used in Roelvink and Brøker (1993). The filter must be chosen carefully, as it might either filter a too large wave length or not be efficient enough. The predictor-corrector filter proposed by Jensen *et al.* (1999) is an example of a filter, which can be tuned to filter shorter and shorter wave lengths based on the number of corrections. An analysis of the filter performance is given by Johnson and Zyserman (2002).

Methods to avoid the numerical filter have also been considered on the grounds that the effect of the numerical filter might not be easy to control. This has lead to the adoption of modified numerical scheme, which should avoid the introduction of spurious oscillations. One such scheme is WENO (Weighted Essentially Non-Oscillatory, originally suggested by Liu *et al.*, 1994), which in the work by Long *et al.* (2008) is seen to have good shock capturing properties in test cases for non-linear advection equations using explicit Euler time integration. They apply the method for phase-resolved morphological development, and the method is seen to be stable. The method needs large stencils, which is inappropriate for unstructured computational meshes. The method, however, is not applied successfully for all types of morphology, as Marieu (2007) experienced stability problems near the crest of wave generated ripples in a simulation of phase-resolved morphological development.

Another method, which is considered by both Callaghan *et al.* (2006) and Marieu *et al.* (2008) in various forms, is the NOCS (Non-Oscillatory Centred Scheme). These methods use flux limiters to prevent over-shooting. Callaghan *et al.* (2006) uses the version by Jiang *et al.* (1998), where the morphological change is solved on a staggered grid arrangement and subsequently mapped back onto the original grid. The method is somewhat more diffusive than on a true staggered grid version, however, it avoids the use of a characteristic velocity in the evaluation, which is problematic as discussed below. The method by Marieu *et al.* (2008) on the other hand uses the

characteristic velocity of the bed form locally estimated as

$$\frac{\partial q_b}{\partial h} \tag{3.61}$$

in one dimension. This is notoriously hard to evaluate robustly around minima, maxima or horizontal stretches of the bathymetry. At these locations Marieu *et al.* (2008) used a polynomial fit based on neighbouring values, which are easily evaluated. In the present work with long stretches of flat bed this method will not be robust, and further Marieu (2009) comment that for small sediment flux gradients, the numerical diffusion is so large that morphologically unstable perturbations are diminished in size after a morphological time step.

Until now, only the inclusion of the bed load transport has been considered. Adding the source terms E and D changes the situation somewhat as $E + D$ contains oscillations with wave lengths of 2 computational cells (i.e. the Nyquist frequency), thus in the present work the filtering approach has been chosen for both bed load and suspended load under one. The approach by Jensen *et al.* (1999) is adopted.

The filter consists of a predictor step yielding $\bar{h}^{*,i+1}$. It is obtained by an interpolation of $\bar{h}^{i+1}$ to the edges of the computational faces and an additional interpolation back to the face centres. For equidistant meshes this reads for the j'th face

$$\bar{h}_j^{*,i+1} = 0.25\left(\bar{h}_{j-1}^{i+1} + \bar{h}_{j+1}^{i+1}\right) + 0.5\bar{h}_j^{i+1} \tag{3.62}$$

The corrector steps are applied onto $\delta\bar{h}^{i+1} = \bar{h}^{*,i+1} - \bar{h}^{i+1}$ with the same double interpolation routine yielding $\delta\bar{h}^{*,i+1}$. The corrected bed level change then reads

$$\bar{h}^{**,i+1} = \bar{h}^{*,i+1} + \delta\bar{h}^{*,i+1} \tag{3.63}$$

The predictor step is performed N_{outer} times and per each outer loop, the corrector step is performed N_{inner} times. As N_{inner} increases, the filtering effect approaches zero, see the analysis by Johnson and Zyserman (2002). The filter is found to be mass conserving.

Soforth ripples are present in the model, but only resolved by 5–10 computational cells, the outlined smoothing algorithm will affect the ripple formation.

Morphological Time Step

The morphological time step needs to be chosen as a constant in this model formulation. This is a consequence of the period averaging of the resulting

bed level change. Hence, choosing a varying time step results in a non-conservative formulation. This can e.g. be realized by considering a case with bichromatic waves. The smaller waves in the wave group breaks close to the shoreline and leads to rapid erosion (and suspension) and afterwards the suspended sediment settles more slowly (while the large wave break farther offshore). If the time step had been based on a Courant criterion, where the characteristic velocity is either the erosion- or deposition rates, then this example would result in a net deposition.

The morphological time step is multiplied by a factor, f_m, to speed up the morphological development. The acceleration factor leads to an apparent lack of sediment conservation, as net-erosion from the bed is not balanced by an equal increase in suspended sediment.

Coupling Between Hydrodynamic and Morphological Modules

The transient nature of the wave breaking requires a complete coupling between the hydrodynamics and the morphological response. This is achieved by both updating the morphology and computing the hydrodynamics each and every time step. The computational mesh for the fluid part (see figure 3.5) is moved according to

$$\nabla \cdot [\gamma_m \nabla \mathbf{u}_m] = \mathbf{0} \quad , \tag{3.64}$$

where $\mathbf{u}_m$ is the velocity of the mesh vertices and γ_m is a mesh diffusion parameter. γ_m can be interpreted as a local stiffness of the computational mesh. At the bed, where the height of the cell is small, a large stiffness is needed to maintain the boundary layer resolution and avoid poor mesh quality, whereas the larger cells away from the bed can be allowed to move more freely. In the present case

$$\gamma_m \propto \frac{1}{\lambda_m^2} \tag{3.65}$$

with λ_m being the shortest distance from the bottom boundary to the computational cell. The method adopted here is described in Jasak and Tuković (2006).

The inter-coupling means that an additional stability criterion must be introduced, namely that the spatial movement of the mesh should locally be less than the dimensions of the computational cell. As the bed level change each wave period exceeds the near bed resolution, the bed response is applied over several time steps for a period not exceeding $\Delta T_{up} < T_m$.**

**If the morphological updating requires smaller time steps than that based on the velocity field, the former is chosen, and the morphological change takes ΔT_{up}. On the other hand, if the velocity field dominates the Courant criterion, the morphological change can be completed over a time interval smaller than ΔT_{up}.

The boundary condition for $\mathbf{u}_m$ is a slip condition on the vertical walls and the atmosphere is kept fixed, i.e. $\mathbf{u}_m = \mathbf{0}$. At the bottom, the boundary condition is given as

$$\mathbf{u}_m = \frac{\varpi \Delta \bar{h}^{**,i+1}}{\Delta t} \mathbf{e}_g \tag{3.66}$$

where ϖ is chosen such that the mesh Courant number is less than 1 and such that the accumulated movement equals $\Delta \bar{h}^{**,i+1}$.

The movement of the mesh vertices is mapped to the other computational meshes, see figure 3.5, thus conformity is ensured at each time step. Further the additional flux due to the mesh movement is computed as in Jasak and Tuković (2006).

3.3.3 Limitations of the Morphological Module

A number of limitations are present in the implementation of the morphological module. These will be discussed here. Furthermore, the list of limitation can also be considered as a suggestion to future improvements on the morphological module.

Curvature Effects

The FAM performs all of the computations on a curved grid, hence some issues related to the curvature effects are addressed in the following. In figure 3.10 a couple of faces on the finite area mesh are depicted. The linear interpolation of the bed load vector onto the edge, e, is given as

$$\mathbf{q}_{b,e} = \frac{1}{\Delta N + \Delta P} \left(\mathbf{q}_{b,N} \Delta P + \mathbf{q}_{b,P} \Delta N \right) \tag{3.67}$$

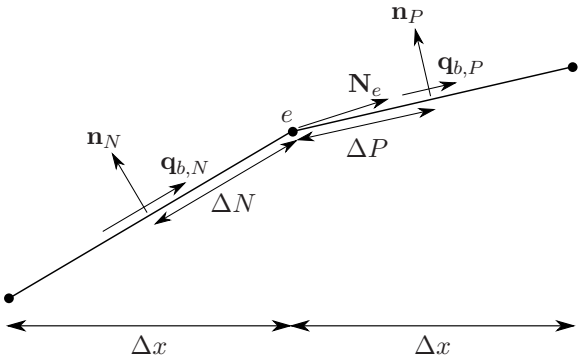

Figure 3.10: *Sketch of the FAM mesh and the bed load and normal vectors.*

Furthermore, the evaluation of the divergence $\nabla\cdot\mathbf{q}_b$ is given as

$$\nabla\cdot\mathbf{q}_b \simeq \sum_e \mathbf{q}_{b,e}\cdot\mathbf{N}_e \quad , \tag{3.68}$$

where $\mathbf{N}_e$ is the normal vector to the edge, tangential to the bed, and having a magnitude equal to the length of the edge.

As $\mathbf{q}_{b,e}$ and $\mathbf{N}_e$ are not necessarily parallel, an error is committed due to the curvature effects.

A simple estimate is carried out in 2D (which allows the use of the $\hat{\square}$ operator). It is assumed that $\mathbf{q}_{b,P} = \mathbf{0}$ and

$$\mathbf{N}_e = -\frac{1}{2}\left(\hat{\mathbf{n}}_N + \hat{\mathbf{n}}_P\right) \tag{3.69}$$

Since $\mathbf{q}_{b,P} = \mathbf{0}$, $\mathbf{q}_{b,e} \propto -\hat{\mathbf{n}}_N$. So without any curvature effect, the flux over the edge should be proportional to $\|\mathbf{N}_e\|_2 = 1$. However, the true flux is

$$\mathbf{N}_e\cdot\mathbf{q}_{b,e} \propto \frac{1}{2}\left(\hat{\mathbf{n}}_N + \hat{\mathbf{n}}_P\right)\cdot\hat{\mathbf{n}}_N = \frac{1}{2}\left(1 + \hat{\mathbf{n}}_N\cdot\hat{\mathbf{n}}_P\right) \tag{3.70}$$

and the resulting error is thus

$$\epsilon_C = \frac{1}{2} - \frac{1}{2}\hat{\mathbf{n}}_N\cdot\hat{\mathbf{n}}_P \tag{3.71}$$

From this, it is seen that the error due to curvature effects is only implicitly controlled by the spatial discretisation. The implicit control comes as finer discretisation typically yields smoother beds and more parallel normal vectors. However, for two faces both at the angle of repose, but with opposite slope, the normal vectors are

$$\begin{aligned} \hat{\mathbf{n}}_N &= \frac{1}{\sqrt{1+\tan^2\phi_r}}\begin{pmatrix} 1 \\ \tan\phi_r \end{pmatrix} \\ \hat{\mathbf{n}}_P &= \frac{1}{\sqrt{1+\tan^2\phi_r}}\begin{pmatrix} 1 \\ -\tan\phi_r \end{pmatrix} \end{aligned} \tag{3.72}$$

and the error is large ($\epsilon_C = 0.265$), thus under these assumptions there is an error of 26.5% of the bed load transport over the edge. Note that the curvature effect is only present in the bed load formulation. Thus locally, the error can be large but under the assumption of $\mathbf{q}_{b,P} = \mathbf{0}$ it is only of the same order of magnitude as the reduction due to the interpolation scheme.

Match between Morphological Module and Wave Relaxation

The combination of wave generation in relaxation zones, sediment transport and morphological change needs special handling. The relaxation zone requires that the bed is kept plane, otherwise the generated waves are not

strictly valid, and the velocity field imposed below bed level, in case of erosion, cause pressure fluctuations in the solution. Thus, no morphological change is allowed for in the relaxation zone, however, large gradients are present as there is a significant spatial variation in the bed shear stress in the relaxation zone. This spatial variation is present as the boundary layer at the inlet is of zero thickness, and it become increasingly thicker through the relaxation zone. This results in a decrease in the bed shear stress through the relaxation zone away from the inlet.

The way to handle this is to apply a weight of 0 to the morphological change in the relaxation zone and let it increase smoothly to 1 outside the computational domain. The transition function is given as a sine.

This brute force method can be improved upon, if a starving bed mechanism is implemented, as it will avoid the below-bed-level issue and reduced or remove the gradients in the sediment transport.

Parallelisation of the Morphological Module

Due to a bug in the mesh motion routine in OpenFoam-1.5-dev, it is not possible to run the morphological updating routine in parallel. As a consequence, the morphological calculations will be limited in size compared to computations of sediment transport over fixed beds, i.e. static meshes.

This can be solved by a migration of the computational framework to OpenFoam 1.6-ext.

Chapter 4

Model Validation

In the present chapter a validation of the model described in §3 will be undertaken. The applicability of OpenFoam in modelling non-breaking waves is considered in §4.1. In this section the implemented method for wave generation and relaxation is also addressed. The validation of the applied turbulence models for wave boundary layers in single phase flows are addressed in §4.2. The ability of modelling breaking waves is described in §4.3. The chapter is completed by validating the modelling of suspended sediment transport in both closed channels and below breaking and broken waves.

The numerical parameters for the discretisation in both space and time can be found in table 4.1.

4.1 Validation of Non-Breaking Wave Modelling

The present section considers 5 different test cases with non-breaking wave in both 2 and 3 dimensions. All test cases have laminar wave boundary layers, as the Reynolds number is less than 10^5 (Jensen *et al.*, 1989). Furthermore, due to the fact that the computational domains are short relative to the wave length, the energy dissipation is assumed negligible and a slip condition is applied at the bed (see Fredsøe and Deigaard, 1992, pp. 50–51 for a discussion).

The test cases cover the physical processes of fully reflecting walls, wave shoaling, triad wave-wave interaction, release of higher bound harmonics and diffraction around a surface piercing obstacle.

4.1.1 Determination of the Location of the Surface

The location of the interface has to be determined in a consistent manner. The interface is between two points, if $\gamma = 1$ and $\gamma = 0$ in these two points respectively. The obvious choice is to define the interface at $\gamma = 0.5$, however,

Table 4.1: *Numerical discretisation parameters for free surface validation cases.*

Case	**Section**	Δx / Δz [m]	Δy at $y = 0$ [m]	**Co. No.** [-]	AR [-]	**No. of cells** $\cdot 10^3$
Reflection coefficient	4.1.3	0.030	0.0033	0.25	9.0	126-168
Triad interaction	4.1.4	0.030	0.0033	0.25	9.0	117
Standing wave	4.1.5	0.0092	0.0001	0.25	92.0	132
Shoaling over bar	4.1.6	0.01	0.0027	0.20	3.8	221
Linear diffraction	4.1.7	0.015	0.00047	0.20	32.0	2290
Wave breaking	4.3	Varying		0.25	1.0 / 2.0	107.2 / 53.6

the interface in the VOF-method can become smeared leading to several neighbouring cells having $\gamma \in]0, 1[$. It is chosen to define the location of the surface, η, such that

$$\eta = \int_{y_{\gamma=1}}^{y_{\gamma=0}} \gamma \mathrm{d}y - y_{\gamma=1} \tag{4.1}$$

Here, the integration limits are vertical coordinates being above and below the interface. This approach yields a consistent value of the location of the interface, given as the height of the water column above the level $y_{\gamma=1}$.

4.1.2 Harmonic Analysis

In the validation cases, the amplitude of the higher harmonics is used for comparison. One approach is to evaluate the amplitude based on a power spectrum computed using a Fourier Transform. This approach is inappropriate for monochromatic waves, as the energy is limited to discrete frequencies, however computing the Fourier Transform will yield a broadening of the spectrum.

For a monochromatic input, the frequencies in the domain can only be an integer times the first order frequency, σ, hence the expression

$$\eta_i \simeq a_0 + \sum_{j=1}^{N} a_j \cos(j\sigma t_i) + b_j \sin(j\sigma t_i) \tag{4.2}$$

for

$$t_i = t_0, t_0 + \Delta t, \ldots, t_0 + (M-1)\Delta t \tag{4.3}$$

describes the surface elevation in a given location based on a set of coefficients a_j and b_j up to a given order N. While $2N + 1 < M$, the system is over-determined and the system of equation is solved in a least-square sense, where $\sum_i (\eta_i - \tilde{\eta}_i)^2$ is minimised. Here $\tilde{\eta}_i$ is the computed surface elevation based on the truncated series in eq. (4.2) and η_i is the modelled surface elevation. Note that the choice of N is limited by

$$2 \leq \frac{2\pi}{\sigma \Delta t} \frac{1}{2N} \tag{4.4}$$

stating that the highest frequency must be resolved with at least 2 points to avoid aliasing.

This approach is suitable for monochromatic, unidirectional propagating waves, however evaluating the frequencies in e.g. standing wave patterns does not yield the correct amplitude. Therefore, an extension of (4.2) is needed. The present extension is limited to bound harmonics of non-linear

reflected waves, where $k_j = jk$ with k being the wave number for the first order harmonic wave. Under these assumptions (4.2) is extended to

$$\begin{aligned}\eta_{i,1} &= a_0 + \sum_{j=1}^{N} a_j^I \cos(j\theta_1^-) + b_j^I \sin(j\theta_1^-) + a_j^R \cos(j\theta_1^+) + b_j^R \sin(j\theta_1^+) \\ \eta_{i,2} &= a_0 + \sum_{j=1}^{N} a_j^I \cos(j\theta_2^-) + b_j^I \sin(j\theta_2^-) + a_j^R \cos(j\theta_2^+) + b_j^R \sin(j\theta_2^+)\end{aligned} \tag{4.5}$$

for (4.3), where $\theta_l^{\pm} = \sigma t_i \pm k x_l$. Furthermore, the distance $|x_2 - x_1|$ is so small that it is assumed that the amplitudes are not affected by energy exchange between the harmonics, see §4.1.4 for a discussion. In this manner, the direction of wave energy propagation can be quantified. The method in eq. (4.5) bears resemblance to that described by Liu and Yue (1998). The main difference is that they filter the surface elevation signal to leading order before computing the leading order harmonic coefficients, whereas the present method fits the coefficient to the unfiltered signal.

4.1.3 Reflection from an Outlet Relaxation Zone

In the present work, the relaxation zone is an important feature, hence the efficiency of the relaxation zone to absorb wave energy is analysed in this section. The setup is sketched in figure 4.1. The waves are allowed to propagate over a distance of 21 m followed by a relaxation zone of varying width, λ. It is analysed how the magnitude of the reflection coefficient

$$R = \left\| \left(a_1^R;\, b_1^R\right) \right\|_2 / \left\| \left(a_1^I;\, b_1^I\right) \right\|_2 \tag{4.6}$$

varies with λ. The coefficients in eq. (4.6) are found using eq. (4.5) with $x_1 = 20.0$ m and $x_2 = 20.1$ m.

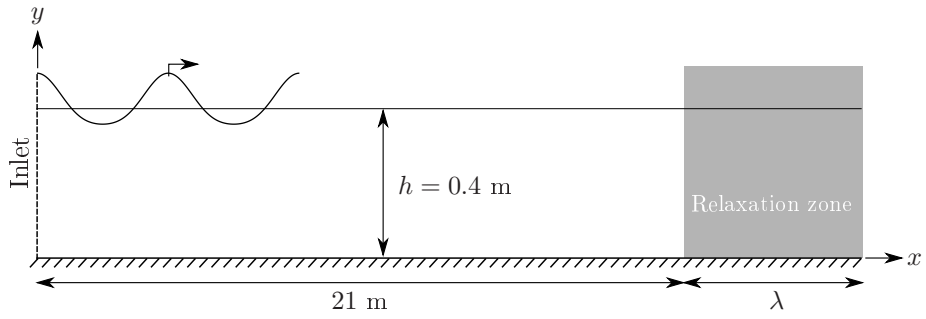

Figure 4.1: *Sketch of the setup of the numerical system for testing numerical reflection from outlet relaxation zone.*

The tests are carried out for 6 different widths of the relaxation zone, namely $k\lambda/(2\pi) = 0.50, 0.75, 1.00, 1.25, 1.50, 2.00$, where $T = 3.5$ s. In addition to this, a set of height-to-depth ratios has been considered. The waves are generated based on stream function theory of order 32, which will avoid the generation of spurious waves (see §4.1.4). The wave numbers for the harmonics are given as $k_j = jk$ assuming that no bound waves are released due to reflection.

R is depicted in figure 4.2 both as a function of λ/L (L is the wave length ($= 2\pi/k$)) and $\lambda h/(LH)$. The latter approach is found to combine the curves onto one common trend with decreasing R for increasing length of the relaxation zone. As a rule of thumb $\mathcal{O}(R) < 1\%$ is achieved for $\lambda/L > 1$.

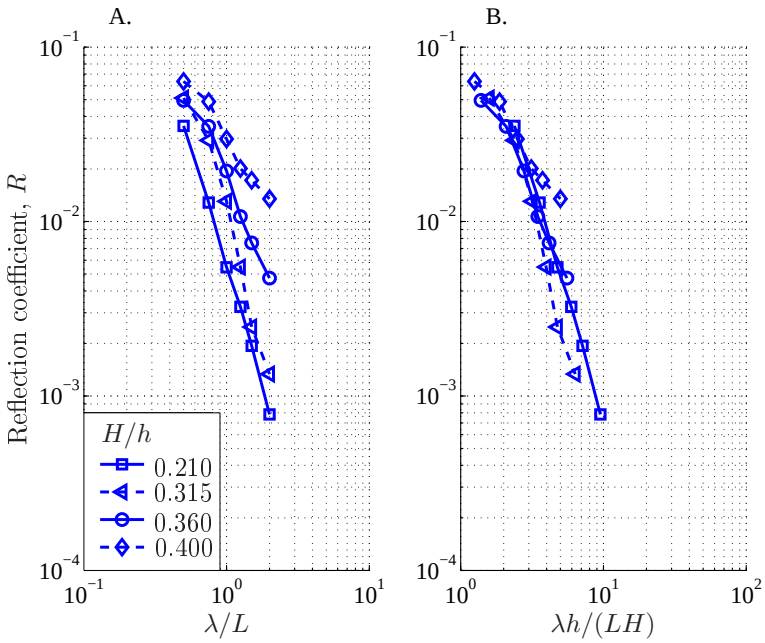

Figure 4.2: *The reflection coefficient as a function of the length of the outlet relaxation zone for $T = 3.5$ s and 4 different values of H/h.*

Simulations without relaxation on γ has been carried out, however, this leads to significant reflection and must be avoided. The reason is that the momentum is relaxed, but the elevation is kept unchanged and only modified due to the missing momentum, thus a pressure gradient is present, which re-accelerates the water and a significant amount of momentum is reflected back to the computational domain.

From the present test, it is expected that the adopted relaxation tech-

nique is applicable in or near the shallow water limit. Experiments similar to those by Clément (1996) for a wide range of frequencies from deep to shallow water would be useful to uncover the full range of applicability.

4.1.4 Triad Wave-Wave Interactions on a Flat Bed

In the previous section the waves were generated using stream function theory yielding a wave propagation with constant form. In this section the experimental study by Chapalain *et al.* (1992) is used to validate the ability of the numerical model to predict triad wave-wave interactions. When forcing any given boundary with linear wave theory, wave-wave interaction will result in the generation of a bound second order harmonic at the boundary. This is directly realised by taking the linear signal and evaluating the response from the convective terms in the Navier-Stokes equations, i.e. $\cos\sigma t \rightarrow 1/2(\cos 2\sigma t + 1)$.

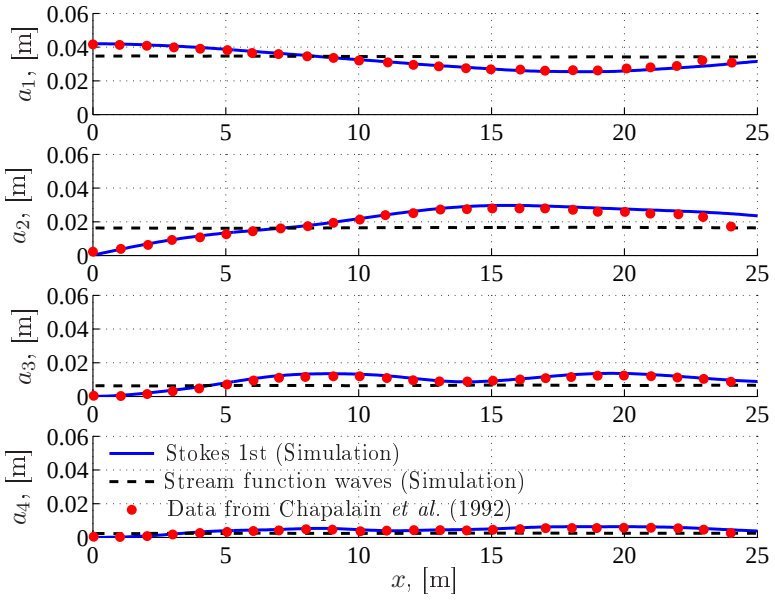

Figure 4.3: *Comparison between the experimental results from Chapalain* et al. *(1992) and the corresponding results obtained with the present numerical model. Results using stream function theory are included.*

At the boundary, however, the boundary condition still needs to be fulfilled, hence a free wave with a second order frequency is created with the same amplitude as the bound harmonic but with opposite phase. Since it is a free wave it has its own wave number $k_{\text{free}} \neq k_{\text{bound}}$. Non-linear interactions between these modes create an energy transfer between the different

harmonics. This interaction can be identified as beat lengths in the harmonic amplitudes, see e.g. Madsen and Sørensen (1993).

In the experiment by Chapalain *et al.* (1992), the water depth is 0.4 m, the wave period is 3.5 s and the wave height is 0.084 m. The numerical flume is identical to the one used for the reflection analysis in the previous section, see figure 4.1, with the only difference that the relaxation zone is placed 26 m from the inlet. In figure 4.3 a comparison between the experimentally obtained spatial variation of the amplitude of the harmonics is compared to those obtained numerically. It is seen that the comparison is close to perfect.

Further the numerical results obtained using stream function waves are shown in figure 4.3. It is seen that the first four harmonics are constant in space, hence the model correctly captures the propagation with constant form (over $\mathcal{O}(4)$ wave lengths).

4.1.5 Standing Waves in Front of a Fully Reflecting Sea-Wall

In §4.1.3 the relaxation zone technique was shown to be useful for absorbing waves at the outlet. In the numerical simulations of breaking waves, see among others §§4.3, 5, and 6, reflection occur from the beach and the presence of an undertow will interact with the inlet boundary, as discussed by Bradford (2000). This will pollute the final results, thus the applicability of the relaxation zone to remove reflected waves in front of the inlet is tested through the ability to model standing waves. Without a relaxation zone at the inlet boundary, the standing wave pattern will extend to the inlet boundary and a discontinuity will develop in γ, which eventually leads to a break-down of the numerical model.

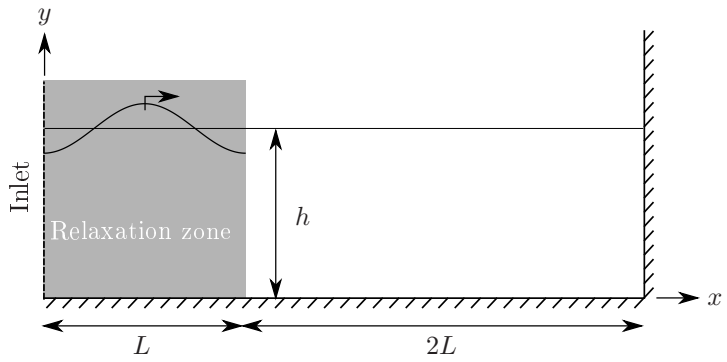

Figure 4.4: *Sketch of the setup of the numerical system for testing numerical reflection from the inlet relaxation zone.*

The standing wave is modelled as sketched in figure 4.4. A linear wave ($H = 0.001$ m, $T = 2$ s, $h = 0.4$ m) is generated at the inlet and in the relax-

ation zone. A fully reflecting wall is modelled at the right hand side of the computational domain using a slip condition. The reflected wave is weighted in the relaxation zone and in this fashion removed at the inlet boundary. In figure 4.5 a comparison is shown between the analytical standing wave (e.g. see Dean and Dalrymple, 1991, p. 57) and the corresponding numerical simulation. From the comparison it is found that the relaxation zone is able to absorb most of the energy and simulate a standing wave pattern in the non-relaxed part of the computational domain. The amplitude of the standing wave is slightly larger in the computational domain relative to the analytical expression. This is attributed to the fact that the relaxation zone is slightly reflective (see §4.1.3). Further the transition from a propagating to a standing wave is easily identified.

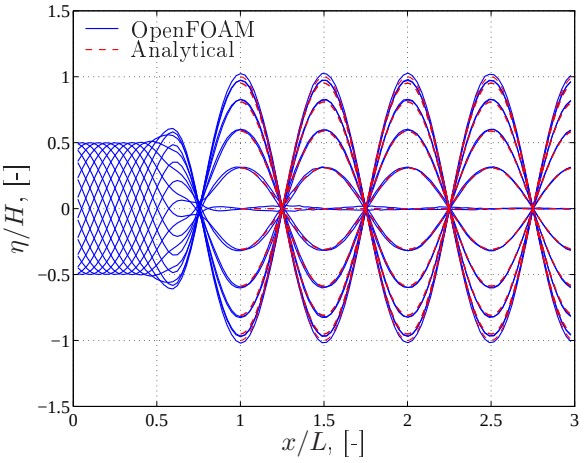

Figure 4.5: *Comparison between the modelled and analytical solution to the standing wave problem. The relaxation zone is also shown. Both solutions are plotted at intervals of* $T/20$.

4.1.6 Wave Transformation over a Submerged Bar

The experimental study by Luth *et al.* (1994) has become a standard benchmark test for surface wave problems. It is used to validate Boussinesq models (e.g. Engsig-Karup *et al.*, 2006) and VOF-solvers (e.g. Morgan *et al.*, 2010). The test case consists of 2nd order Stokes waves generated at the inlet, see figure 4.6. The wave field propagates along a channel with a submerged bar 6 m from the inlet. The wave period is 2.02 s, the wave height is 0.02 m, and the water depth at the inlet is 0.4 m.

As the waves reach the bar they begin to shoal, a process which increases the non-linearity of the waves, i.e. all the harmonics constituting the waves

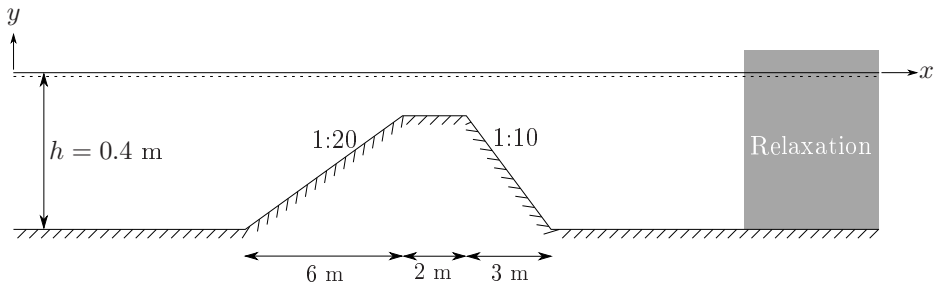

Figure 4.6: *Sketch of the experimental setup for wave transformation over a submerged bar.*

increase in amplitude. On the far side of the submerged bar, the water depth increases and the amplitude of the higher harmonics is too large to remain bound to the first order harmonics, thus free higher order harmonic waves are released. The bound and free waves are then allowed to interact on the far side of the bar and an exchange of energy takes place, similar to the process described in §4.1.4.

In figure 4.7, the time variation in the surface elevation is depicted at 4 different locations along the wave flume. It can be seen that the surface elevation is well described from the inlet up to the top of the bar, however as the water depth increases and the free harmonics are released, the predictions of the model become less accurate. Based on an amplitude analysis (figure 4.8) it is found that the Crank-Nicholson scheme is the most accurate of the two. This is especially found as the energy increase of the second order harmonic is considerably better captured.

The discrepancies on the back of the bar can be explained by a combination of numerical errors arising from time discretisation, and the fact that the spatial scheme is of second order. As discussed by Engsig-Karup *et al.* (2009) the propagation speed is much better predicted using higher order spatial schemes. The exchange of energy is a function of the propagation speed (Madsen and Sørensen, 1993), hence if it is not modelled with sufficient accuracy, the energy exchange will differ. Nevertheless, the results are satisfactory, and comparable in accuracy to the results by Morgan *et al.* (2010), who also use a VOF method.

A similar release of higher order harmonics is seen in the experimental study by McNair Jr. and Sorensen (1970) where the reforming of broken waves onshore of the longshore bar is considered. In their experiments, waves with double the frequency attained slightly larger spectral densities than the corresponding at the generated frequency. This release of higher harmonics is a dissipative version of the one considered in the present section.

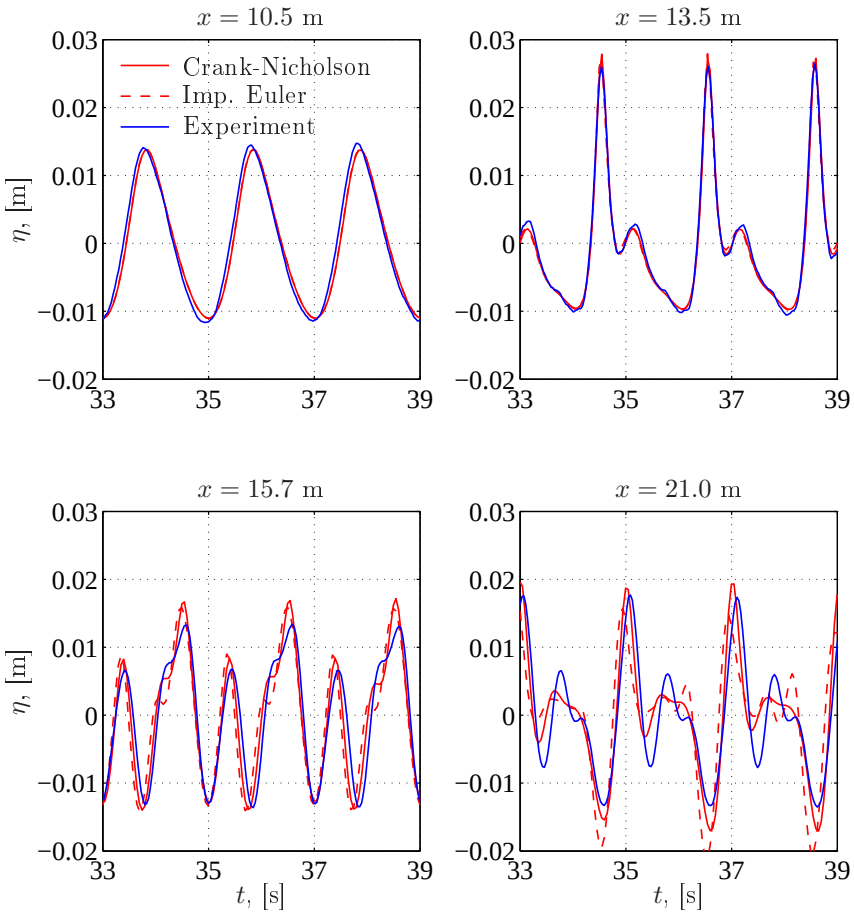

Figure 4.7: *Comparison between the experimental results and numerical simulation using either implicit Euler or Crank-Nicholson for time integration of the momentum equation.*

4.1.7 Wave Diffraction Through a Breakwater Gap

The theoretical linear solution to the diffraction problem through a gap of finite width in an otherwise infinite breakwater is presented by Penney and Price (1952) for constant water depth and normal incident waves. The numerical setup for validation is shown by the plan view layout as seen in figure 4.9. The water depth is 0.125 m. The waves are generated using 1st order Stokes theory with a wave height of 0.005 and a wave period of 0.67 s; 25 wave periods have been simulated. The symmetry around the mid point of the gap has been utilised and a symmetry boundary condition has been applied along the axis of wave propagation through this point. Relaxation zones have been used for the inlet and outlet boundaries.

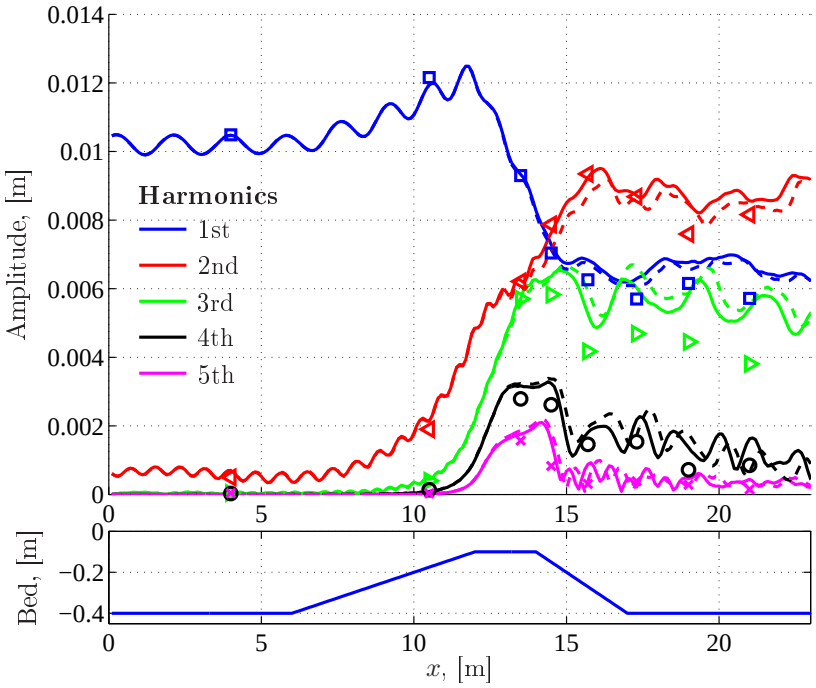

Figure 4.8: *Variation in the harmonic components. Full line: Crank-Nicholson time integration. Dashed line: Implicit Euler time integration.*

The width of the inlet is $2L$, as it was pointed out by Pos and Kilner (1987) that even though the theory by Penney and Price (1952) is valid for widths larger than or equal to L, a larger width is needed to achieve sufficient accuracy.

The comparison between the analytical and numerical results are shown in figure 4.10, and they are generally seen to be favourable. Along the line $z/L = x/L$ the wave height is diminished faster than along either $x = \text{const}$ or $z = \text{const}$. This is probably due to the fact that the computational domain is laid out in a Cartesian grid, hence the resolution of the wave length is worse along the diagonal.

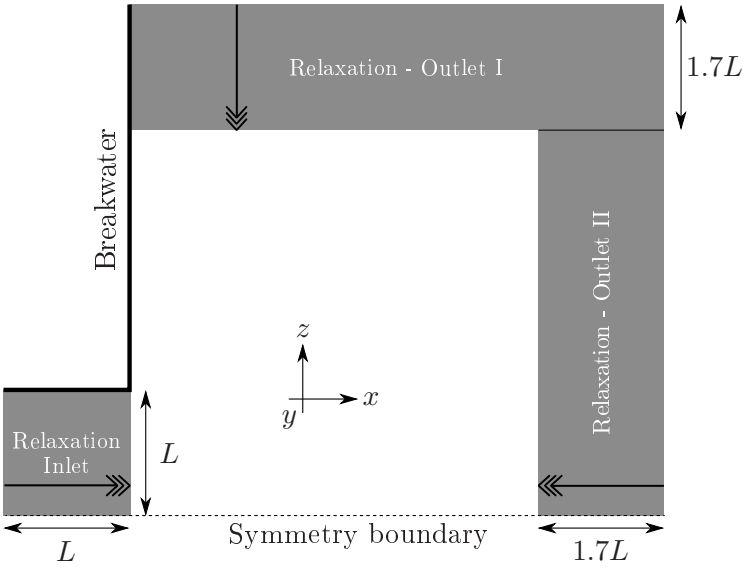

Figure 4.9: *The plan view of the computational domain used for diffraction computations. The arrows (⋙) points towards full weighting of the computed solution.*

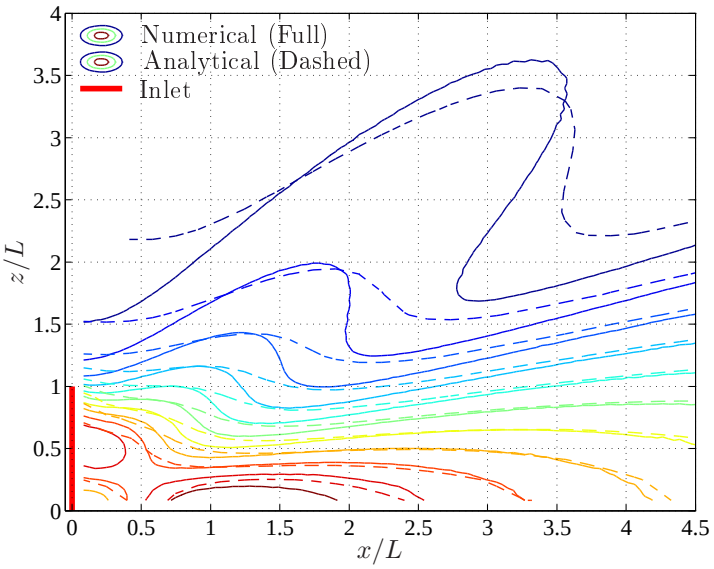

Figure 4.10: *Comparison between analytical and modelled results for linear diffraction.*

4.2 Validation of the Turbulence Models

The computation of wave boundary layers is part of the validation of the turbulence model. A comparison with test 13 by Jensen *et al.* (1989) is depicted in figure 4.11, where results using low Reynolds number closures are included. It is seen that the turbulence closure captures the magnitude and the phaselag of the variation in the friction velocity, u_f. For a more thorough discussion see §A.

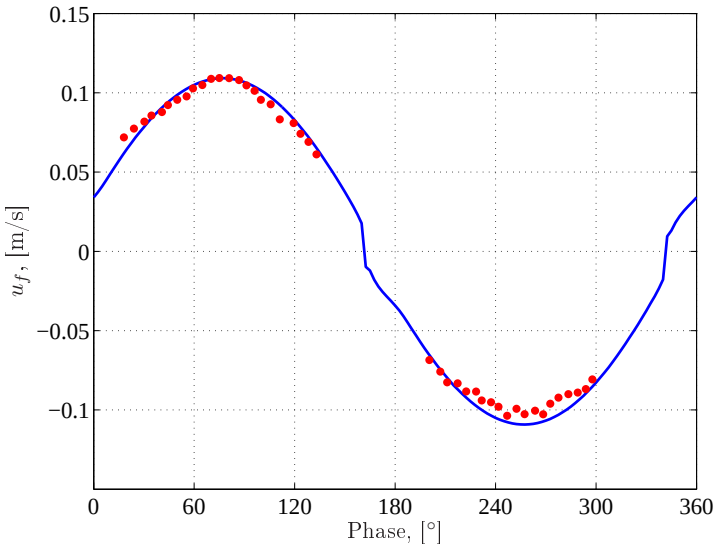

Figure 4.11: *Comparison of the friction velocity in a rough turbulent oscillatory boundary layer. (Dots) Experimental data from Jensen* et al. *(1989), test 13 (Full line) Simulation using the low Reynolds number turbulence model.*

4.3 Validation of the Modelling of Breaking Waves

The applicability of OpenFoam for simulating wave breaking has been tested against the laboratory experiment by Ting and Kirby (1994) in the case of spilling breakers. Waves are generated on a horizontal bed, where the still water depth is 0.4 m, see figure 4.12. The waves are 0.125 m high and have a period of 2 s; stream function waves have been used. At the inlet a relaxation zone 4 m in length is used to allow for long simulation time (Bradford, 2000). As seen in figure 4.12 a cut-off is applied, where the swash zone was supposed to be. This is necessary, as the coupling between the VOF-method and the momentum equation is not robust at the surface/wall intersection, when the

computational cells have a large aspect ratio. This is needed at the wall boundary in order to resolve the boundary layer. $h' = 0.01$ m.

It is found that the turbulence closure coefficient α (see eq. (3.18)) should take the value 0.4. The deviation from standard turbulence closure is due to the change in production term.

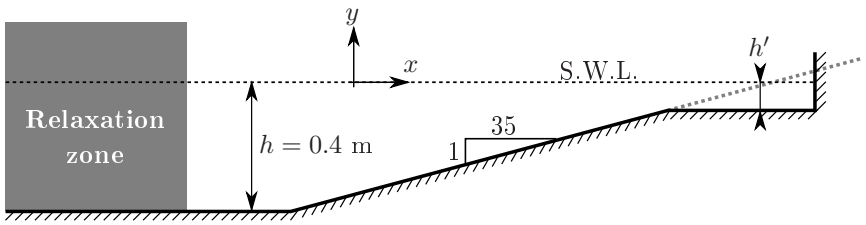

Figure 4.12: *Layout of the computational domain for computing spilling breaking waves. The dashed gray line is the layout of the original physical experiment. The horizontal distance from origo to the toe is 0.7 m.*

This test case has been considered by several other authors such as (Lin and Liu, 1998; Bradford, 2000; Mayer and Madsen, 2000; Hieu *et al.*, 2004; Christensen, 2006) to name a few with varying success. The results by Hieu *et al.* (2004) are generally highly encouraging, however, their simulation time is limited to 25 s warm-up (i.e. $t/T = 12.5$) and the subsequent averaging was limited to 5 wave periods. This limited simulation time is common for the cited papers and the reported results are at best quasi-steady. Contrary to the other cited papers, Hieu *et al.* (2004) applies the Defined Donating Region method (DDR by Harvie and Fletcher (2001)) for the interface tracking, which is thought to have some interesting properties with respect to the breaking description. It must be noted, however, that they perform a mesh sensitivity analysis (see Hieu *et al.*, 2004, figure 16), and despite considerable changes with increasing resolution, no better resolved simulation are presented than that, which matches the experimental data nicely.

The roughness is not explicitly stated in Ting and Kirby (1994), however it is assumed smooth and $k_N = 0.1$ mm is used together with the high Reynolds number turbulence closure. The computational cells outside the boundary layer do all have the same aspect ratio and aspect ratios (AR) of 1 and 2 are considered. The averaging of the hydrodynamic properties is performed over 50 wave periods from $t/T = 80$ to $t/T = 130$. This choice is based on figure 4.13, which depicts the volume of water in the computational domain ($V_\gamma = \sum_{domain} V\gamma$) as a function of time. V_γ exhibits a transient behaviour which indirectly describes the build up of the set-up. The results are at least affected by this transient behaviour up to $t/T = 40$. A problem

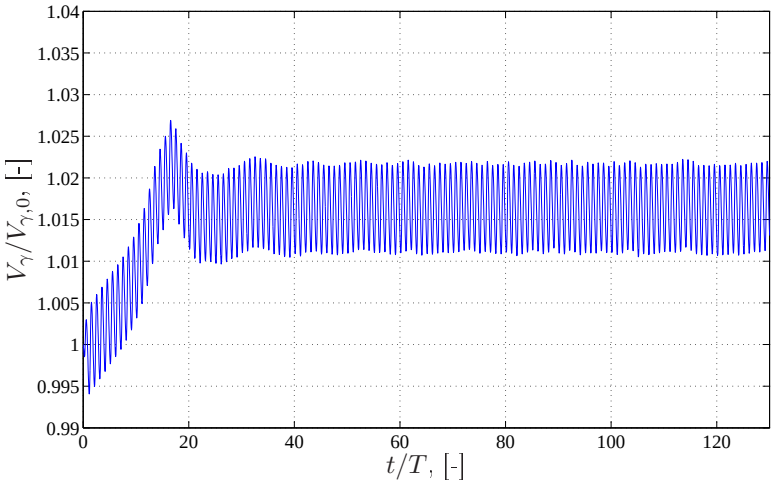

Figure 4.13: *Relative variation in the total amount of water (V_γ) in the computational domain.*

in extracting data too early is the lack of mass conservation, which was noted by Christensen *et al.* (2002) in the simulation by Lin and Liu (1998).

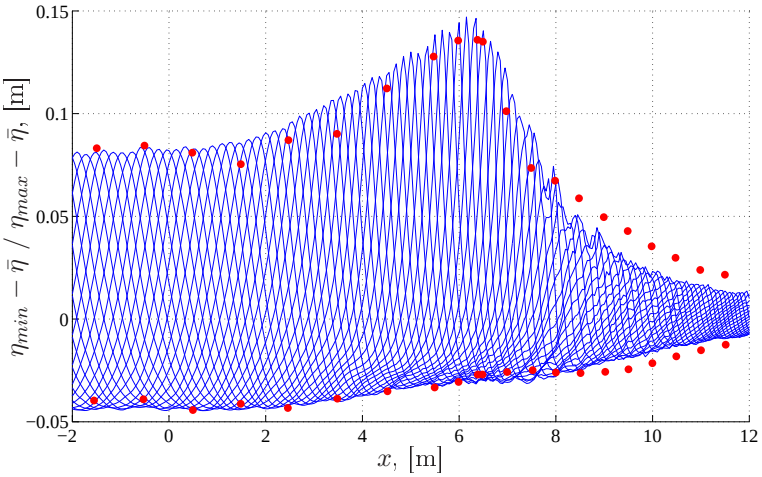

Figure 4.14: *Measured (Dots: Ting and Kirby, 1994) and simulated surface elevation in the surf zone in the case of spilling breakers. $AR = 1$.*

The surface elevation through the surf zone can be seen in figures 4.14 ($AR = 1$) and 4.15 ($AR = 2$). There is a noticeable difference between the two simulations, as the breaking occurs much earlier compared to the measurements for $AR = 2$, whereas the comparison is good for $AR = 1$.

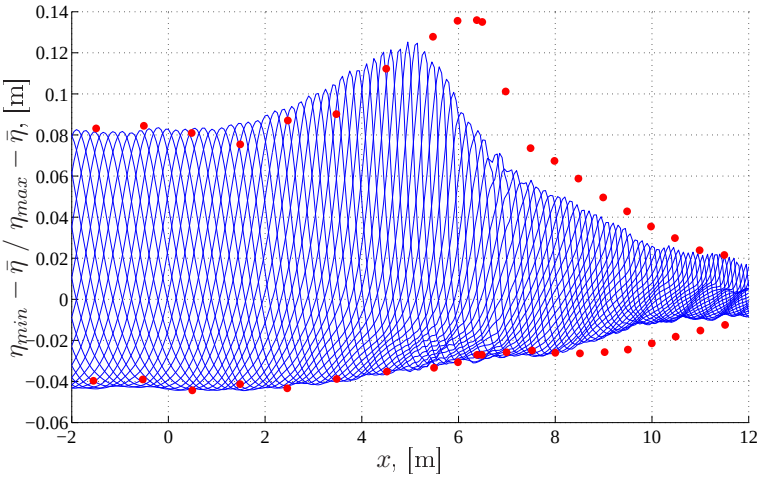

Figure 4.15: *Measured (Dots: Ting and Kirby, 1994) and simulated surface elevation in the surf zone in the case of spilling breakers. $AR = 2$.*

This premature breaking is thought to be explained by the nature of the VOF-method. If the γ-content is larger than 0, there will be a flux of γ over the cell faces irrespectively of the actual location of the water. Consider a computational cell with large (> 1) aspect ratio, then as soon as water enters from the left there will be a flux of γ across the right face. This will lead to a premature steepening of the surface elevation and hence lead to premature wave breaking. This should not happen in the DDR method, as it considers a reconstruction of the γ-distribution.

The resulting undertow profile is depicted in figure 4.16 and the comparison is generally favourable for $AR = 1$. The considerable discrepancy for the measuring positions F, G and H is explained by the too rapid surface elevation decay in the inner surf zone, which causes a steeper wave setup. In the case of $AR = 2$, it is seen that the undertow profiles differ from those with $AR = 1$ and the signature of the undertow with large flow velocities at the bed is found farther offshore. This is a direct consequence of the premature wave breaking. The two solutions are nevertheless still comparable.

Ting and Kirby (1994) also measured the turbulence in the surf zone. In figure 4.17 a comparison with the modelled results in shown. Two quantities are shown, namely $\bar{k}_k$, which is the average value of the turbulence based solely on k computed from eq. 3.9 and $\bar{k}_k + \bar{k}_{\mathbf{u}}$ (see below). As considerable stochastic motion is identified in the surf zone, the terms $\widetilde{u'^2}$ and $\widetilde{v'^2}$ are evaluated. These terms are the period average of the ensemble averaged turbulent quantities relative to the combine wave orbital and mean flow. The contribution to the turbulence is defined similarly to Ting and Kirby

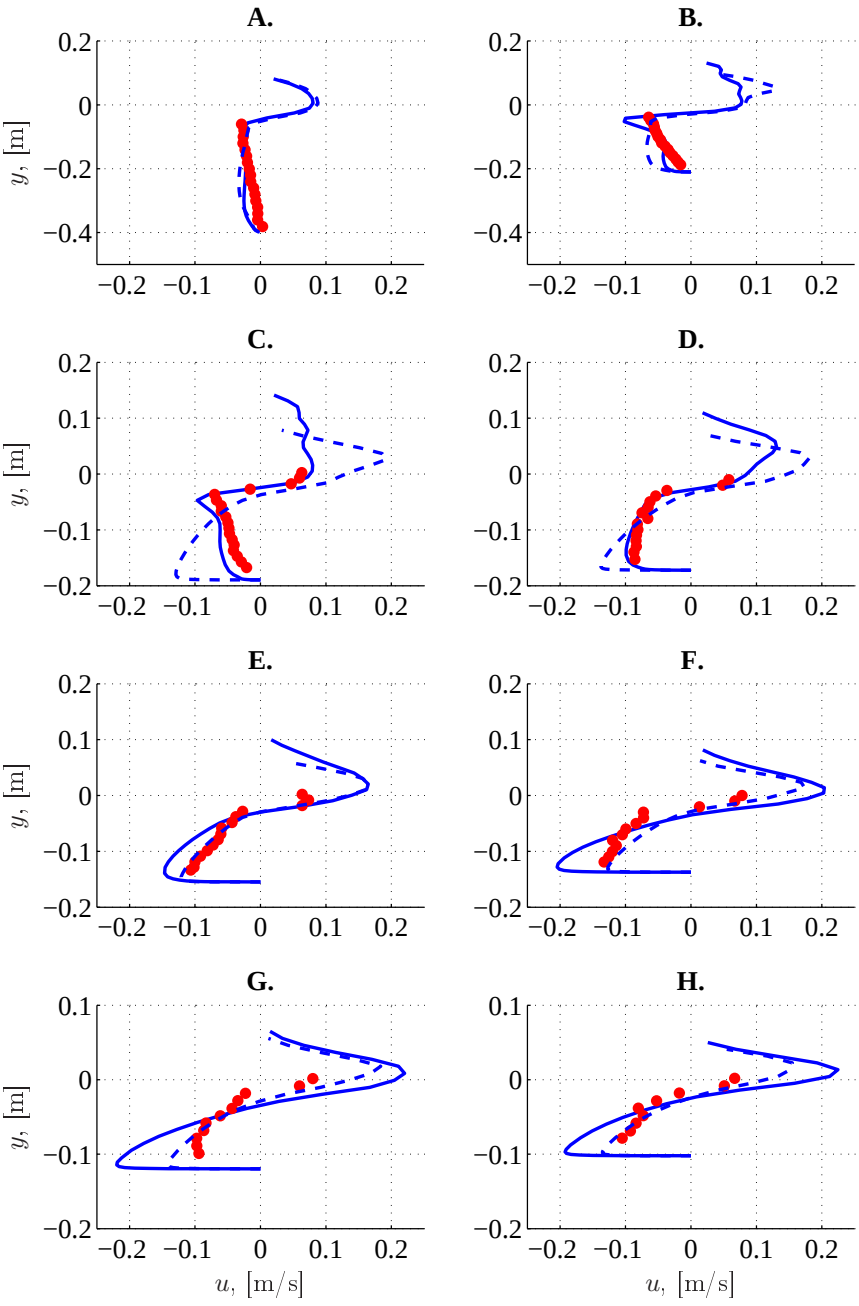

Figure 4.16: *Measured (Dots: Ting and Kirby, 1994) and simulated undertow profile at A) $x = -1.265$ m, B) $x = 5.945$ m, C) $x = 6.665$ m, D) $x = 7.275$ m, E) $x = 7.885$ m, F) $x = 8.495$ m, G) $x = 9.110$ m, H) $x = 9.725$ m. (•) Experiment. (−) AR = 1. (−−) AR = 2.*

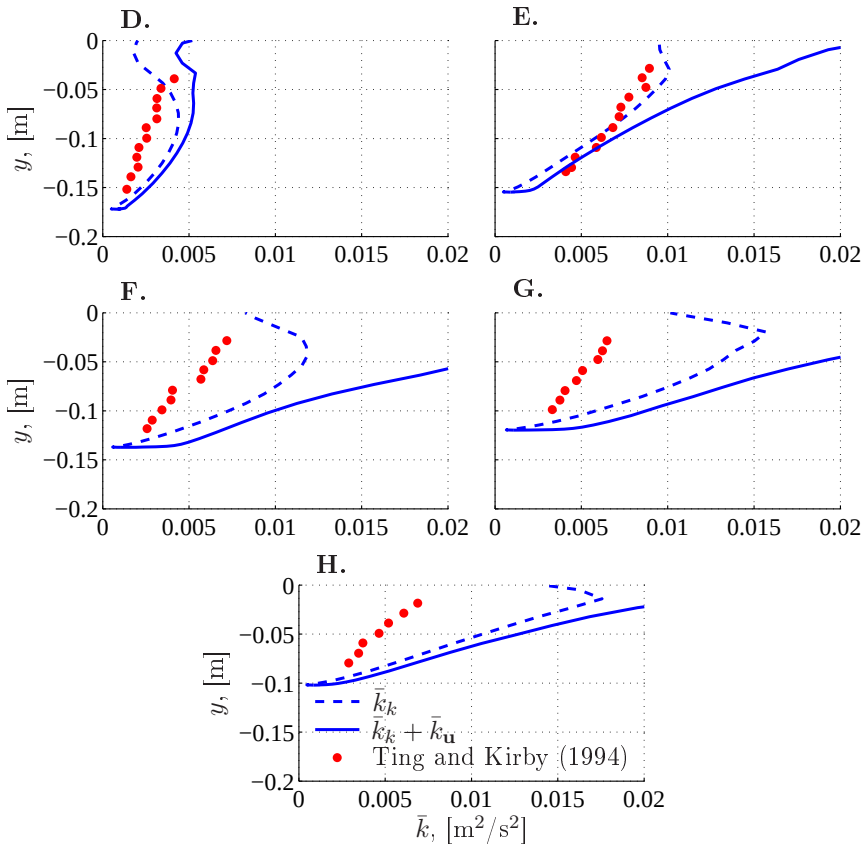

Figure 4.17: *Measured (Dots: Ting and Kirby, 1994) and simulated turbulence for* $AR = 1$. *Positions are the same as in figure 4.16*

(1994) with

$$\bar{k}_\mathbf{u} = \frac{1.33}{2.0}\left(\widetilde{u'^2} + \widetilde{v'^2}\right) \quad . \tag{4.7}$$

This formulation is used, because the transverse velocity component is not modelled.

The comparison shows that similar to other authors (Bradford, 2000; Christensen, 2006), the turbulence is overestimated within the inner part of the surf zone, hence more research in adequate turbulence models for this kind of flows is needed.

The modelling of breaking waves has been conducted on finer meshes, on which the same dependency of AR is also found. Furthermore, it has been evaluated with cnoidal wave theory, but no considerable difference is found between this and stream function waves.

4.4 Validation of Suspended Sediment Transport Model

4.4.1 Equilibrium Concentration Profile

The classical equilibrium solution to the suspended sediment concentration profile in a pure current is called the Vanoni distribution (see Fredsøe and Deigaard, 1992, pp. 227–229), and it is given as

$$c = c_b \left(\frac{D-y}{y} \frac{\delta_b}{D-\delta_b} \right)^{\frac{w_s}{\kappa u_f}} \quad , \tag{4.8}$$

where δ_b is the distance from the bed to the bed level at which the reference concentration, c_b, is valid (see figure 3.5); D is the water depth. The parameter $w_s/(\kappa u_f)$ is called the Rouse parameter, in short Z. The concentration profile in eq. (4.8) is based on the assumption that the eddy viscosity follows the parabolic distribution

$$\nu_t = \kappa u_f y \left(1 - y/D\right) \quad . \tag{4.9}$$

Eq. 4.9, however, is not descriptive for the true distribution, as ν_t remain finite at $y = D$. van Rijn (1984) suggests an alternative distribution for ν_t given as

$$\nu_t = \begin{cases} \kappa u_f y \left(1 - y/D\right) & \text{for} \quad y \leq \frac{D}{2} \\ \frac{1}{4} \kappa u_f D^2 & \text{for} \quad y > \frac{D}{2} \end{cases} \quad . \tag{4.10}$$

This correction leads to a distribution of the suspended sediment, which for the lower half equals that of the Vanoni distribution, which also provides the boundary condition at $y = D/2$ for the upper distribution. The corrected distribution is

$$c = \begin{cases} c_b \left(\frac{D-y}{y} \frac{\delta_b}{D-\delta_b} \right)^{\frac{w_s}{\kappa u_f}} & \text{for} \quad y \leq \frac{D}{2} \\ c_b \left(\frac{\delta_b}{D-\delta_b} \right)^{\frac{w_s}{\kappa u_f}} \exp\left[\frac{-4}{D^2} \frac{w_s}{\kappa u_f} \left(y - \frac{D}{2} \right) \right] & \text{for} \quad y > \frac{D}{2} \end{cases} \quad . \tag{4.11}$$

This distribution differs from that in van Rijn (1984), as the latter includes the effect of hindered settling and suppression of turbulence due to the suspension of sediment. Both of these effects are disregarded in the Vanoni distribution (eq. 4.8) and in the current numerical model.

The comparison between the two theoretical distributions and a simulated one is depicted in figure 4.18 for $Z = 0.25$ and $Z = 2.0$. It is seen that the simulated results fit well with both theoretical distributions. The results also support the conclusion by van Rijn (1984), namely that the corrected distribution is important for the net sediment transport for small values of Z, as the constant value of ν_t for $y > D/2$ can sustain considerably larger volume concentrations.

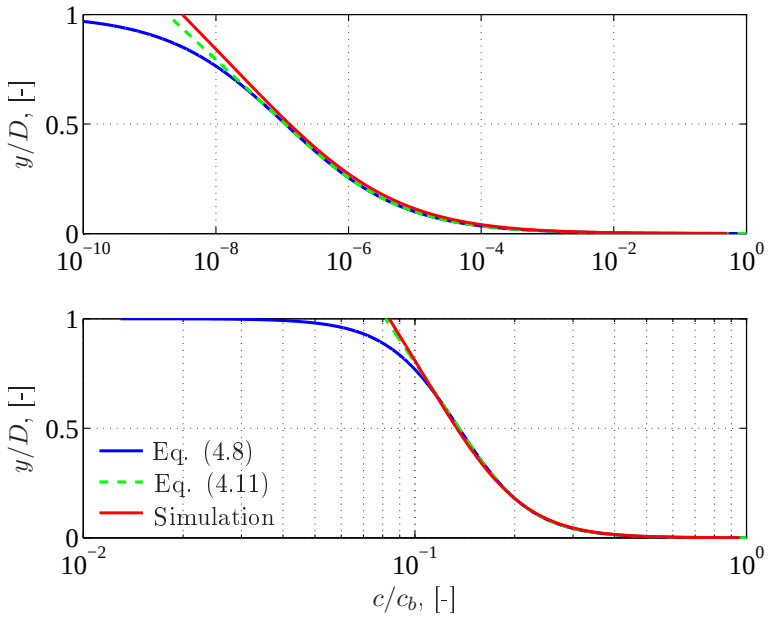

Figure 4.18: *Comparison between the two theoretical distributions of suspended sediment (eqs.* (4.8) *and* (4.11)*) and the results obtained by simulation. (top)* $Z = 2.0$. *(bottom)* $Z = 0.25$.

4.4.2 Spatial Development of Concentration Profile

The alongstream development of the suspended sediment concentration has been considered theoretically by Hjelmfelt and Lenau (1970), where clear water enters over a loose sediment bed. The effect of scour at the inlet is initially disregarded in their analysis. Hjelmfelt and Lenau (1970) also assume a parabolic eddy viscosity distribution. For a value of $Z = 0.5$ their analytical expressions takes a simple form.

As discussed in §4.4.1, the distribution of $c(\mathbf{x})$ differs between the solutions for a parabolic distribution of ν_t and the numerical solution to the same quantity. This is especially true for small values of Z, where non-negligible volume concentrations must be anticipated above $y = D/2$. Therefore, the present section will consider the predictive ability of the numerical scheme rather than discussing the outcome of different distributions of ν_t.

The solution of the spatial distribution of c is simulated using eq. (4.9) and a uniform velocity profile. For $u_f = 0.055$ m/s, $\|\mathbf{w}_s\|_2 = 0.011$ m/s and a water depth of $D = 1$ m, the numerical and analytical solutions are plotted in figure 4.19(a) using upwind scheme and in figure 4.19(b) using central difference. Not surprisingly, the predicted distribution is best for a linear scheme, however, the numerical solution is reasonable for the upwind

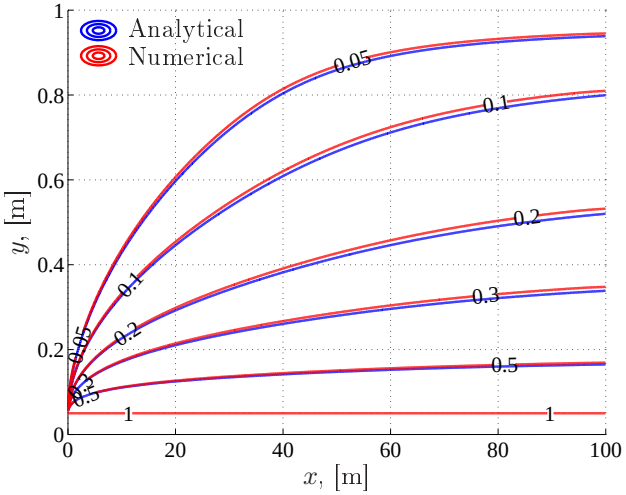

(a) Upwind scheme

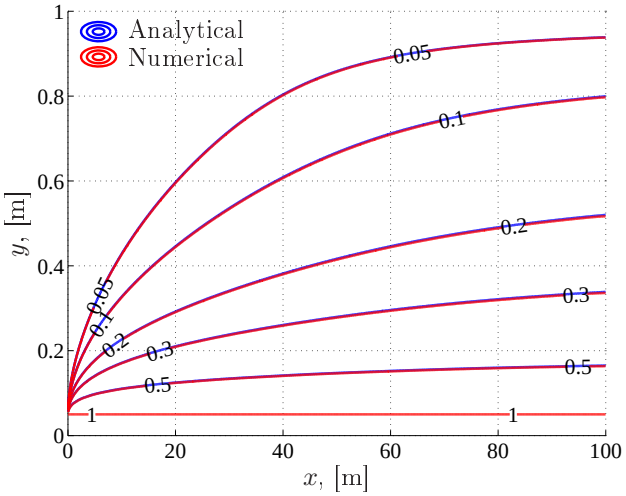

(b) Central difference scheme

Figure 4.19: *Analytical (Hjelmfelt and Lenau, 1970) and numerical solution to the spatial distribution of relative suspended sediment concentration (c/c_b) for clear water entering over loose bed.*

scheme as well.

The small deviation between the linear and upwind schemes support that upwind can be used throughout. This is also needed in the context of

resolved wave boundary layers, since the eddy viscosity is so small during part of the wave period that the local Péclet number becomes larger than 2 at the boundary, which, combined with large gradients in c, results in numerical instabilities (e.g. Ferziger and Peric, 2002).

4.4.3 Suspension of Sediment under Breaking Waves

Suspended sediment concentrations have been measured under breaking regular waves in the CRIEPI wave flume, Japan (Shimizu and Ikeno, 1996). The measurements are conducted over a loose sediment bed after 8 hours of wave exposure by waves of $T = 5$ s and $H = 1$ m (test L1). The initial bed profile is a plane slope of 1:20. The developed beach profile is plotted in figure 4.20 together with the profile used in the numerical simulation, which has a cut-off above $y = -0.10$ m. The bed consists of sand with a median grain diameter of 1.0 mm and a grain size distribution ranging from 0.2 mm to 1.3 mm ($d_{16} = 0.4$ mm, $d_{84} = 1.2$ mm, and $\sigma_g = \sqrt{d_{84}/d_{16}} = 1.73$, where the latter is the geometric standard deviation). The median value is used initially.

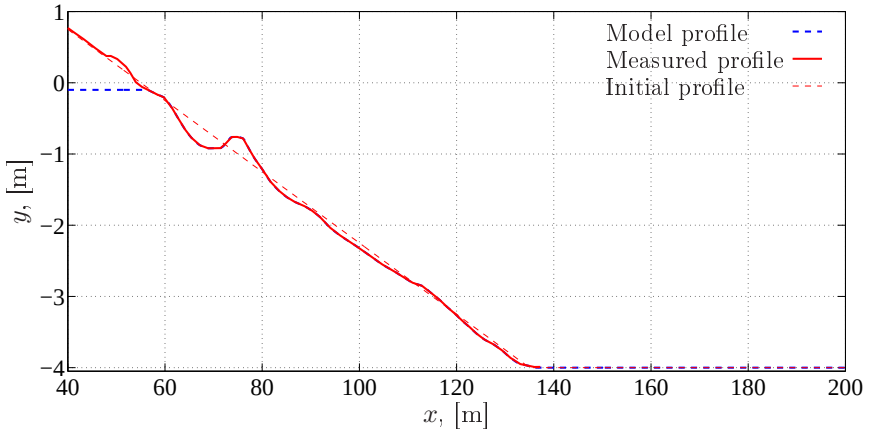

Figure 4.20: *Initial and final profile (after 8 hours) under regular wave forcing (Shimizu and Ikeno, 1996) test L1. The profile used in the numerical simulation is also included.*

The measured undertow profile is compared with the computed one in figure 4.21 and the comparison is good. Especially considering the temporal evolution of the free surface inside the surf zone, see figure 4.22. From this figure it is quite clear that the numerical model has a problem with dissipating the wave energy, as the instantaneous surface is in some sense boiling. Such a behaviour has not been seen in the case of spilling breakers. The breaking is clearly plunging (figure 4.22(c)). The behaviour is explained

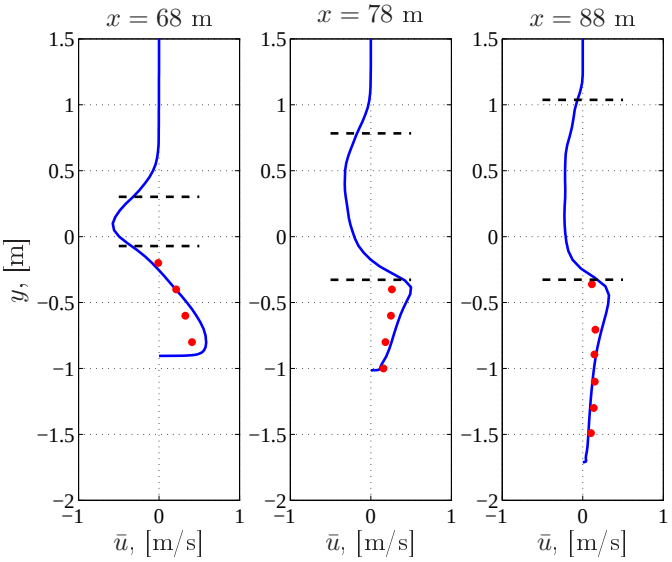

Figure 4.21: *A comparison between the computed and measured undertow profile, $\bar{u}$, from test L1 in the CRIEPI experiment (Shimizu and Ikeno, 1996). Dashed lines are the ensemble averaged maximum and minimum surface elevation in the numerical model.*

by the generation of large scale vortical motion in the initial breaking process, which, due to the two dimensionality of the simulation, cannot properly decay into scales, where the turbulence model can dissipate the remaining energy. The presence of this organised and violent motion will considerably effect the eddy viscosity and hence all diffusion processes.

A comparison between measured and modelled suspended sediment concentrations are shown in figure 4.23. Using the median diameter, the comparison is quite poor at the three measuring locations. One explanation is the behaviour of the water motion in the surf zone, which definitely can cause too large suspended sediment concentrations, i.e. for $x = 68$ m and $x = 78$ m. Outside the surf zone ($x = 88$ m) the predicted concentrations are orders of magnitude smaller than the measured, however, no information on the grain distribution at the specific levels are given in Shimizu and Ikeno (1996). Therefore, the sediment grains in suspension might be considerably smaller than the median diameter. As seen in §4.4.1 a small change in Z cause an order of magnitude change in c. Such a change in Z is not unrealistic because of the wide range of sediment diameters.

The measurements are conducted after 8 hours of wave forcing, thus a certain degree of cross shore sorting of the sediment must be anticipated, however, this is not addressed by Shimizu and Ikeno (1996). This sorting

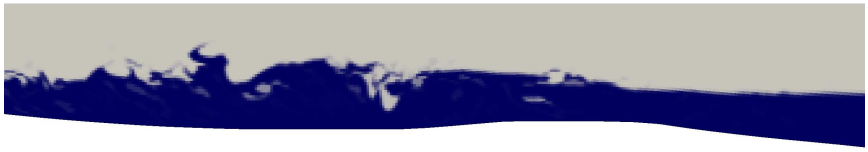

(a) $t/T = 0.00$

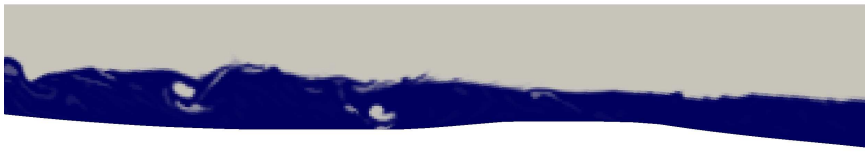

(b) $t/T = 0.24$

(c) $t/T = 0.48$

(d) $t/T = 0.72$

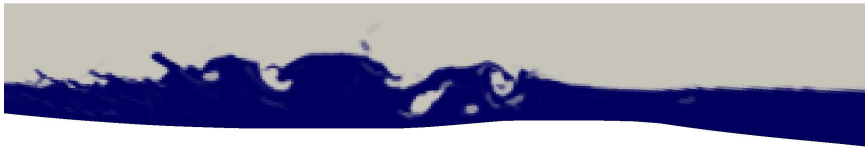

(e) $t/T = 1.00$

Figure 4.22: *Five snapshots of the surface tracking during breaking. Dark is water and light is air.*

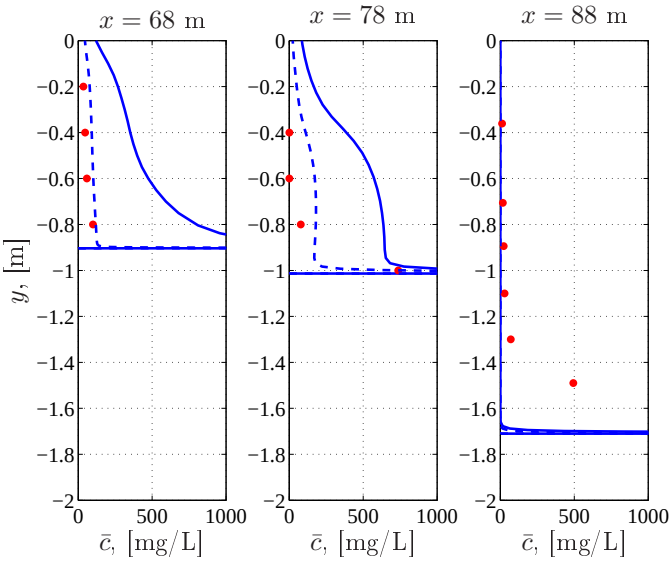

Figure 4.23: *A comparison between the computed and measured (dots) average concentration profiles, $\bar{c}$, from test L1 in the CRIEPI experiment (Shimizu and Ikeno, 1996). (Full): $d = 1.0$ mm. (Dashed): $d = 1.3$ mm. The measured data is also reported on a linear scale.*

would lead to a coarsening in the surf zone and a fining outside the surf zone due to the longer settling time of the finer sediment grain and the net undertow/return flow. Such a sorting in the field is reported by e.g. Greenwood and Davidson-Arnott (1975) and Komar (1998), figure 3.8. The sorting has been incorporated by setting the grain diameter in the numerical model to $d = 1.3$ mm. The result is plotted in figure 4.23 and they compare well with the measured concentrations. Actual simulations with graded sediment is currently not possible with this numerical model.

The larger sediment diameter does improve on the predictions, however, a comparison with an experimental study, where the waves are spilling and the sediment is nearly uniform would be important for the further validation of the model. The former requirement is to avoid the behaviour as seen in figure 4.22, and the latter to have fewer uncertainties with respect to the degree of sorting and the effect of a gradation of the sediment over the vertical. The results presented in this section, however, are encouraging with respect to the validity of the suspended sediment transport model under breaking waves.

Chapter 5

Bed of Constant Slope

The hydrodynamics and sediment transport patterns over a bed of constant slope are considered in this chapter. In all, 9 test cases are simulated, where two planar bed slopes of 1:50 and 1:35 are used. The 9 test cases vary in the Irribaren number, ζ_0, from spilling to plunging breakers. The test case parameters are summarised in table 5.1. There is an overlap of two Irribaren number between the two slopes in order to quantify the significance of the latter.

Table 5.1: *Wave parameters for simulations on a constant sloping bed. Naming: (A): Slope (=* $\tan\beta$*) is 1:50. (B): Slope is 1:35. (S) is spilling and (P) is plunging breakers based on table 2.1.* H_0 *is based on linear shoaling (Dean and Dalrymple, 1991).* $\zeta_0 = \tan\beta\sqrt{H_0/L_0}$*, see §2.3.2,* $\Omega = H_B/(w_s T)$*, see §2.2, and* $\Omega_{HK} = H_0/(w_s T)\tan\beta$*, see §5.2*

Test	$\tan\beta$ [-]	H_h [m]	H_0 [m]	T [s]	h [m]	ζ_0 [-]	Ω [-]	Ω_{HK} [-]	Type
FA1	1:50	3.000	3.234	6.0	6.0	0.083	27.7	0.52	(S)
FA2	1:50	2.000	2.156	6.0	6.0	0.102	19.7	0.35	(S)
FA3	1:50	1.500	1.482	8.5	6.0	0.174	13.0	0.17	(S)
FA4	1:50	0.800	0.682	12.5	6.0	0.378	6.9	0.05	(S)
FB1	1:35	1.000	1.074	5.0	4.0	0.172	12.6	0.30	(S)
FB2	1:35	1.000	0.860	10.0	4.0	0.385	8.4	0.12	(S)
FB3	1:35	1.000	0.718	15.0	4.0	0.632	5.9	0.07	(P)
FB4	1:35	0.750	0.501	17.5	4.0	0.882	3.8	0.04	(P)
FB5	1:35	0.650	0.408	20.0	4.0	1.118	3.1	0.03	(P)

The grain diameter is kept constant at $d = 0.2$ mm, which corresponds to a bed roughness of $k_N = 0.5$ mm. The computational mesh has an aspect

ratio of 1 in the upper part of the computational domain. The lowermost cell has a height of d, and a vertical stretching is applied to match the outer vertical mesh discretisation, see the description in §B. An example of the computational mesh is shown in figure 5.1. Similarly to the argumentation in §4.3, a cut-off at $y = -0.1$ m is applied, where the swash zone should have been.

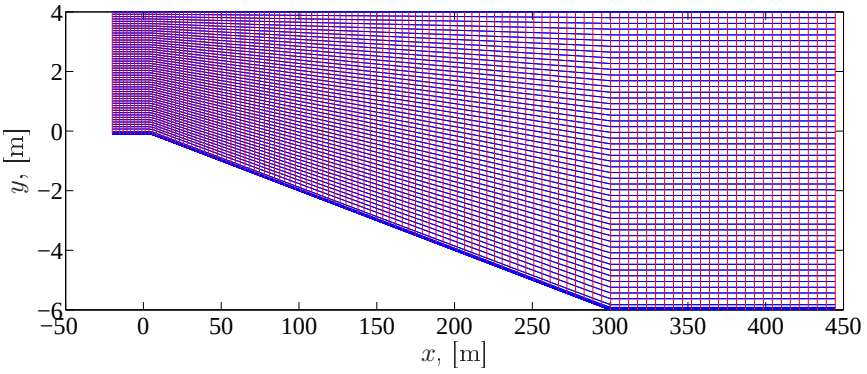

Figure 5.1: *Example of the computational mesh for the simulations with a bed of constant slope. Note that only every 30th vertical mesh line are preserved in the plot.*

The results presented in the following are discussed using different statistical quantities. The quantities are the period averaged value defined as

$$\bar{\phi} = \frac{1}{mT} \int_{t_0}^{t_0+mT} \phi(t') \mathrm{d}t' \quad , \tag{5.1}$$

the ensemble averaged value defined as

$$\tilde{\phi}\left(\frac{t-t_0}{T}\right) = \frac{1}{m} \sum_{i=1}^{m} \phi(t+iT) \quad , \quad t \in [t_0,\ t_0+T[\quad , \tag{5.2}$$

and the r.m.s. values defined as

$$\phi_{\mathrm{rms}} = \sqrt{\frac{1}{mT} \int_{t_0}^{t_0+mT} \left(\phi(t') - \bar{\phi}\right)^2 \mathrm{d}t'} \quad . \tag{5.3}$$

Here t_0 is some offset ensuring steady state conditions, m is an integer, and ϕ any quantity. Furthermore, the cross shore integrated suspended sediment flux is considered, which reads

$$\bar{Q}_s = \int_0^{h \tan\beta} \bar{q}_s(x) \mathrm{d}x \tag{5.4}$$

where

$$q_s = \int_{-h}^{\eta} \text{sign}(\mathbf{n}_s \cdot \mathbf{e}_x)\mathbf{n}_s \cdot [(\mathbf{u} + \mathbf{w}_s)c - (\nu + \nu_t)\nabla c]\, \mathrm{d}y \quad . \tag{5.5}$$

q_s is the flux of suspended sediment transport over vertical mesh lines, where the flux is due to both advection and diffusion processes. The term "sign($\mathbf{n}_s \cdot \mathbf{e}_x$)" is included to account for changing directions of $\mathbf{n}_s$. q_s is positive in the offshore direction. In the following $q_b \equiv \mathbf{q}_b \cdot \mathbf{e}_x$.

5.1 Instantaneous Velocity Field

The velocity field induced by the breaking process is depicted as a series of snap shots in the figures 5.2–5.3 for test case FB5. This test case is clearly breaking as a plunging breaker. Each frame is separated by 0.2 s ($0.01T$), and it is seen that in the beginning of the breaking process, the overturning part of the breaker initially bounces off the water surface and create a set of successive vortical structures. These vortical structures are not propagating, but are being advected by the velocity field, e.g. consider the structure generated for $t/T = 49.84$ at $x = 35.5$ m. It moves shoreward much slower than the propagation speed of the broken wave. The third tongue of water penetrates through the water surface and creates a large vortical structure, which reaches the bottom ($t/T = 49.89 - 49.93$). As in §4.4.3, however, important 3-dimensional effects might have been omitted in the flow description, as it is likely that this vortical structure and the water/air interaction would disperse differently in 3D. It should, however, be mentioned that bottom penetrating plunging breakers are found in experiments (e.g. see photographs in Peregrine, 1983).

The interaction between vortical structures and the bed is reflected in the bed shear stress distribution also depicted in the figures*. The bed shear stress is clearly due to that of the propagating wave in the beginning. The final vortical structure (see figure 5.3, $t/T = 49.90$), on the other hand, influences the bed to such an extent that the bed shear stress becomes directed in the seaward direction. This flow picture resembles that reported by Miller (1976), on which he suggests his bar forming hypothesis, see §2.4.2.

In §D similar snapshots are depicted for the two test cases FA1 and FB2. FB2 also exhibits some plunging breaking type properties, thus the above description also apply to FB2. FA1 on the other hand is more a spilling breaker type and the interaction between the top and bottom of the water column is much less pronounced.

*Recall that a negative bed shear stress is directed onshore.

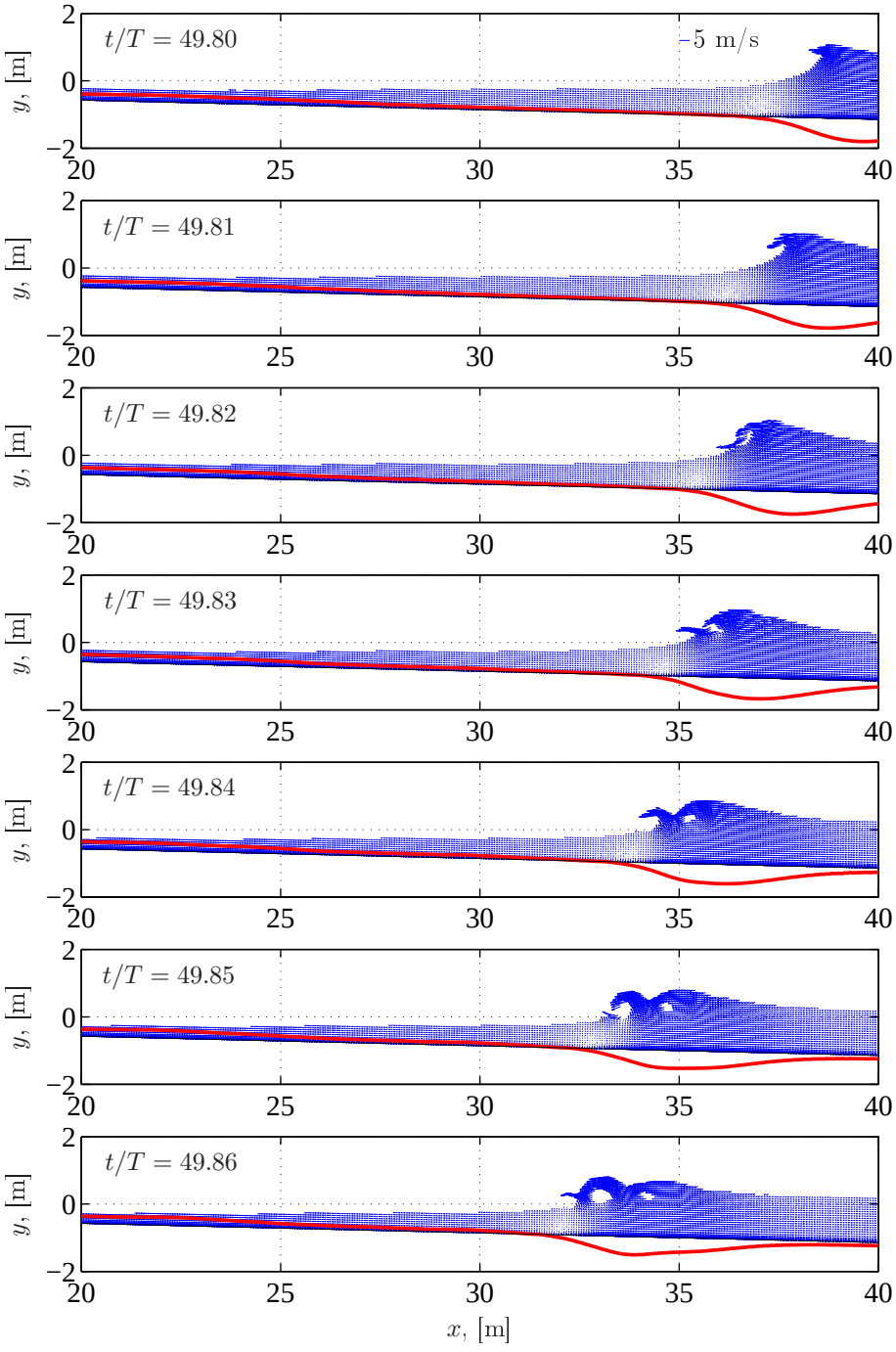

Figure 5.2: *Snapshots of velocity field from FB5 ($\zeta_0 = 1.118$, $T = 20$ s). Full line is $50u_f|u_f|$ depicted relative to the bed. Vectors plotted for $\gamma > 0.9$. $u_f|u_f| > 0.0$ when directed offshore.*

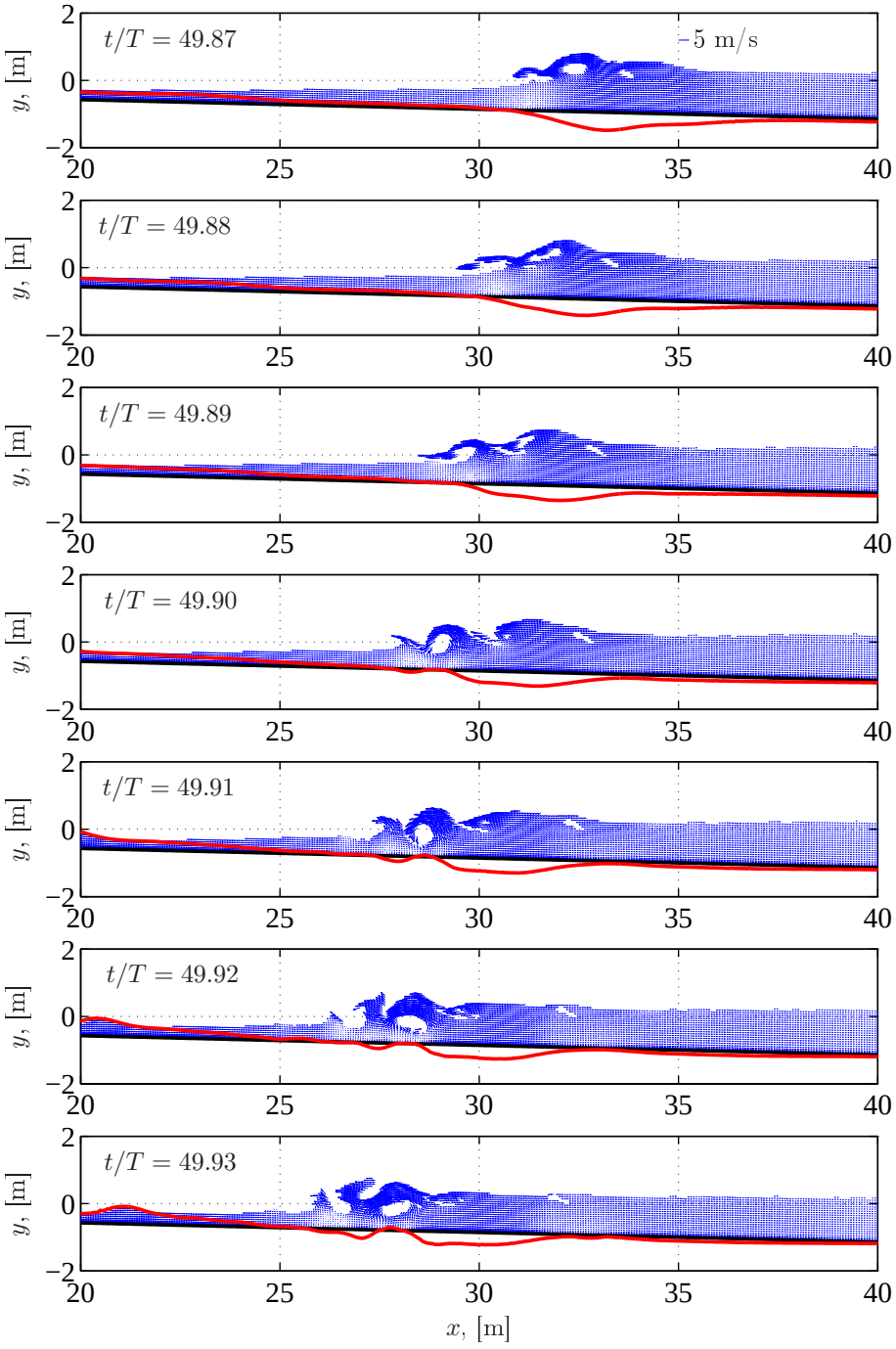

Figure 5.3: *As in figure 5.2*

5.2 Period Averaged Results

Wave Height, Breaking, and Setup

The simulated distribution of the wave height across the surf zone is depicted in figure 5.4 for the FA runs. It is seen that the break point moves shoreward with an increase in ζ_0. This is governed by the necessary decrease in H_h with increasing ζ_0[†]. The variation is similar in the FB runs. The setup, $\bar{\eta}$, is also depicted in figure 5.4, and it is clearly seen that there exists a spatial lag between the maximum wave height and the onset of setup. This mechanism is already discussed in §2.3.4, and it is due to a rotational momentum flux, which cannot be estimated based on potential theory.

The ratio of wave height to water depth at breaking, $(H/h)_B$, varies for the results depicted in figure 5.4. $(H/h)_B$ deviates from the typically saturation values for random wave of 0.6–0.8 as reported by Battjes and Stive (1985) or as low as 0.3 (Aagaard and Masselink, 1999, p. 77). As a validation, the numerical results are compared with those from the laboratory studies for regular waves on slopes of 1:50 (Iversen, 1952) and 1:35 (Svendsen and Hansen, 1976). The comparison is shown in figure 5.5, where the wave length at breaking is estimated using Stokes theory. The comparison is good and the large values for $(H/h)_B$ in the case of plunging type breakers are well captured.

Sediment Transport

$\bar{q}_s$ and $\bar{q}_b$ are plotted across the surf zone for 4 different values of ζ_0 in figure 5.6. First of all, it is seen that the suspended sediment transport load is dominating in this case. Furthermore, it is seen that the maximum transport fluxes decrease with a decrease in the breaker height, $\bar{H}_B$. Again, the same pattern is found for the FB series, however, with less drastic changes, which merely reflect the smaller interval of H_h in the latter test series. The dominance of suspended sediment transport load over bed load is clearly a consequence of the choice of $d = 0.2$ mm. The variation in the dominating transport type with the grain diameter under constant environmental forcing has not been considered over beds of constant slope. The effect of grain diameter is considered in terms of the morphological response, see §6, and it is seen that the importance of bed load relative to that of suspended sediment load increases, when the grain diameter become larger.

The location of the maximum wave height is indicated in figure 5.6. It is seen that

[†]The decrease in H_h is needed, as the range in ζ_0 would otherwise be more narrow for reasonable value of T. Reasonable values are needed to allow for feasible simulation times.

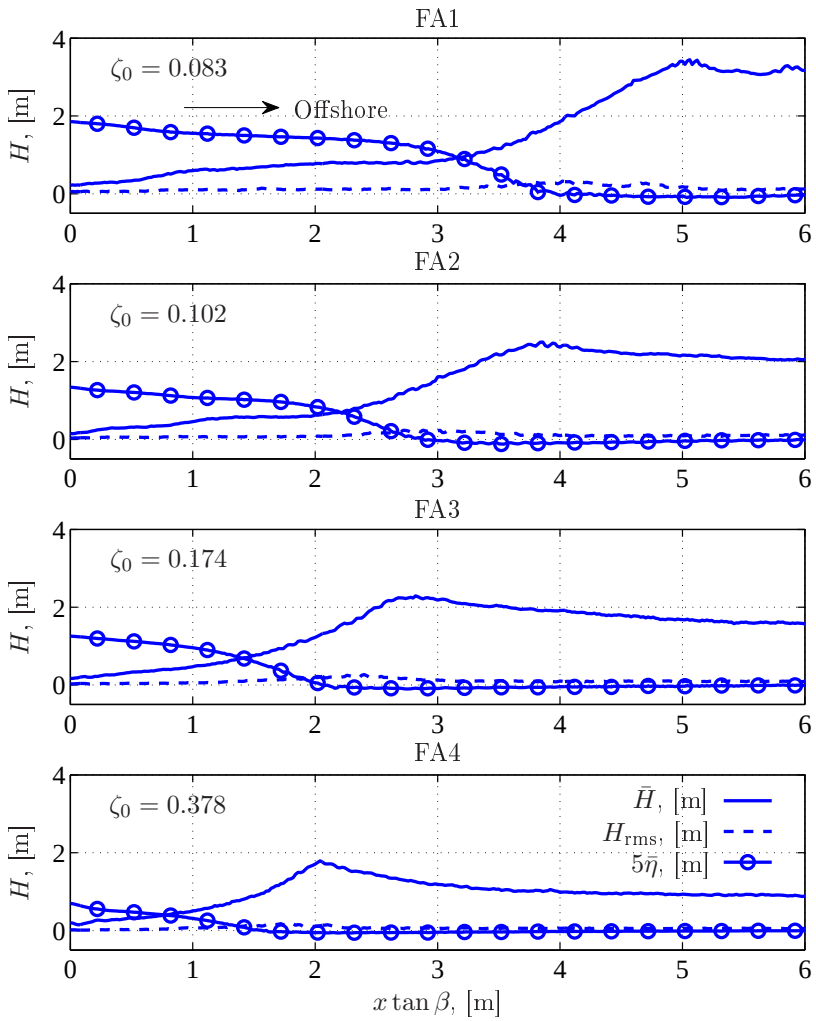

Figure 5.4: *The wave height distribution in the surf zone as a function of* ζ_0. $\tan\beta = 1:50$.

- the maximum sediment fluxes are found shoreward of this point as expected due to excess turbulence and the effect of the undertow, which depends on gradients in $\bar{\eta}$,
- the shape of the sediment transport flux resembles those from laboratory measurements (e.g. Baldock *et al.*, 2010),
- there is a considerable spatial lag between the maximum flux and the point of maximum $\bar{H}$,
- and the transport fluxes are shoreward offshore of the breakpoint (even

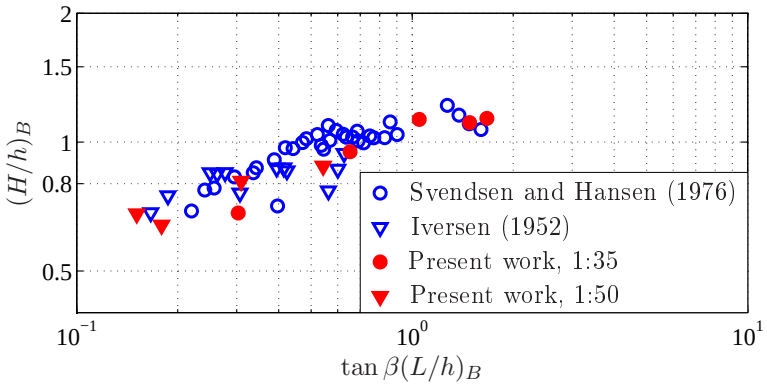

Figure 5.5: *Comparison between laboratory data for wave height at breaking and simulated results in a prototype scale numerical model. Iversen (1952):* $\tan\beta = 1:50$. *Svendsen and Hansen (1976):* $\tan\beta = 1:35$.

though it cannot be seen from the figure, as the quantities are quite small).

The spatial lag will be discussed in more detail below. The crest of the breaker bar in an initial state of development would be shoreward of the breakpoint, as also seen in laboratory experiments (e.g. Nadaoka and Kondoh, 1982; Dally, 1987; Baldock *et al.*, 2010).

Integrated Cross Shore Sediment Flux

The integrated cross shore flux of suspended sediment, $\bar{Q}_s$, is depicted in figure 5.7A as a function of ζ_0 for both test series. For comparison, $\bar{Q}_s$ has been non-dimensionalised by $\bar{H}_B^2\sqrt{gh_B}$, a choice following from the similar dependency for the longshore sediment flux in the CERC formulae. It is seen that $\bar{Q}_s$ consistently decreases with increasing ζ_0, however, with no "universal" curve for the two data sets. The decrease in $\bar{Q}_s$ is consistent with the notion of storm and mild weather conditions, where the beach profile is accretive in the latter case. There seems to be a better overlay for the two bed slopes, when $\bar{Q}_s$ is plotted against Dean's parameter, Ω, as in figure 5.7B.

Hattori and Kawamata (1980) suggested another scaling parameter, namely $\Omega_{HK} = H_0/(w_s T)\tan\beta$, i.e. taking the width of the surf zone into consideration. They suggested a limit for Ω_{HK} of $C/(2\pi)$ below which, the sediment transport is shoreward. Based on combined laboratory and field experiments they gave $C = 0.5 \pm 0.2$. The integrated cross shore sediment flux is plotted against this parameter in figure 5.7C, and it is seen to give a a better cluttering of the simulated results around $\bar{Q}_s = 0.0$. Furthermore,

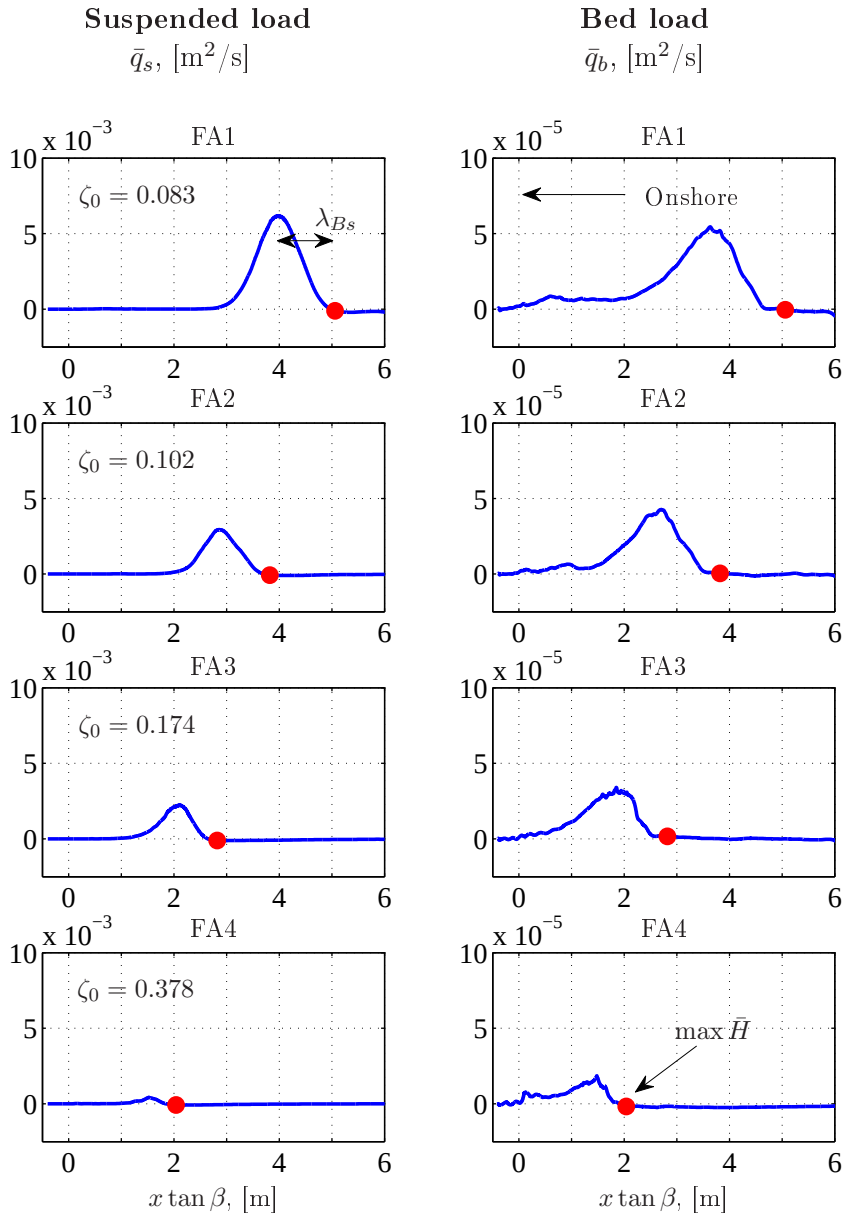

Figure 5.6: *The period averaged sediment transport fluxes as a function of space and* ζ_0. *(Left):* $\bar{q}_s$. *(Right):* $\bar{q}_b$. $\tan\beta = 1/50$. *The dot indicate the location of* $\max \bar{H}$. *Note the scale for the two transport mechanisms.*

the zero crossing is found for $\Omega_{HK} \simeq 0.05$, i.e. $C \simeq 0.31$, which is the lower limit specified by Hattori and Kawamata (1980). This can be explained by the use of regular waves in the numerical model.

As only one grain diameter is used, it could be interesting to make sim-

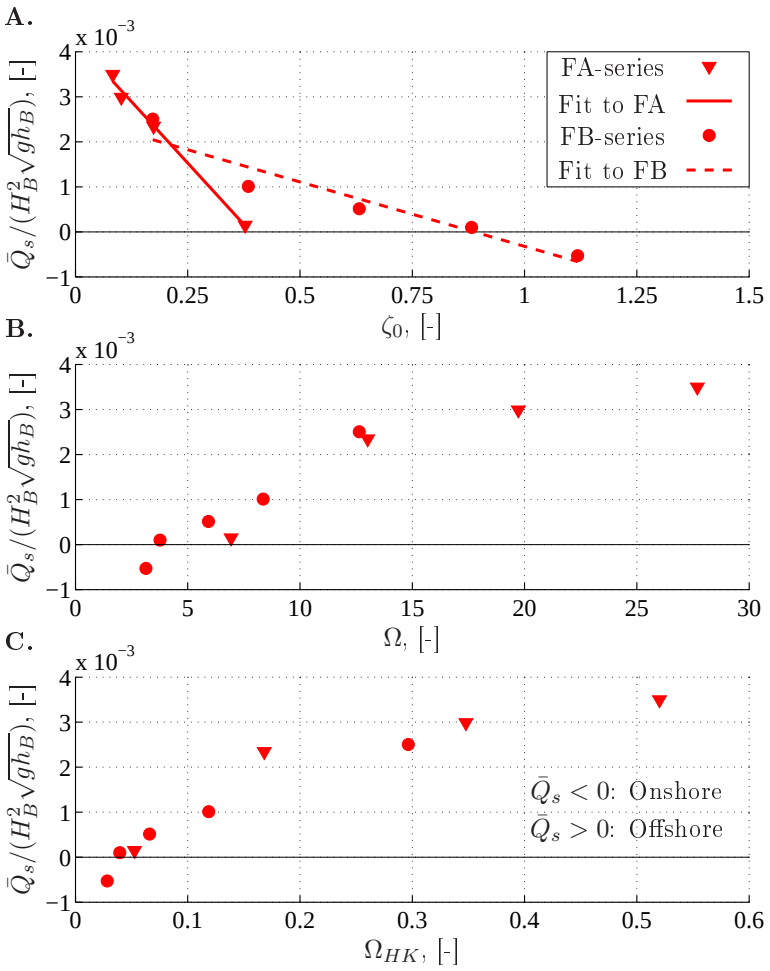

Figure 5.7: *The non-dimensionalised cross shore flux of suspended sediment, $\bar{Q}_s$. A: A function of ζ_0. B: A function of Ω. C: A function of Ω_{HK}.*

ulations with varying values d and furthermore include experimental results in the comparison. Based on the present comparison, it seems that the use of Ω_{HK} yield the means of distinguishing between erosive and accretive conditions.

Spatial Lag Effects

The spatial lag between the location of $\max \bar{H}$ and $\max \bar{q}_s$ is called λ_{Bs}, see definition in figure 5.6. Its variation for the two test series as a function of ζ_0 is depicted in figure 5.8A, and as a function of Ω in figure 5.8B. λ_{Bs} is made non-dimensional with an estimate of the wave length at break-

ing, i.e. $T\sqrt{gh_B}$. The data coincide on a common line and show that the non-dimensional spatial lag generally decreases with increasing ζ_0 and decreasing Ω. Thus, the more the plunging breaking type the smaller the non-dimensional distance between the breakpoint and the corresponding maximum offshore sediment transport flux. For the simulated range in ζ_0, it seems that the spatial lag levels off around 0.25 for large ζ_0. For large Ω, $\lambda_{Bs}/(T\sqrt{gh_B})$ levels off around 1.25, thus [0.25, 1.25] is a good estimate of the range for regular waves. It has been investigated, whether sensible results are found by making λ_{Bs} non-dimensional with h_B or H_B, however, it only produced scattered results. No visual improvement is found by replacing Ω with Ω_{HK}.

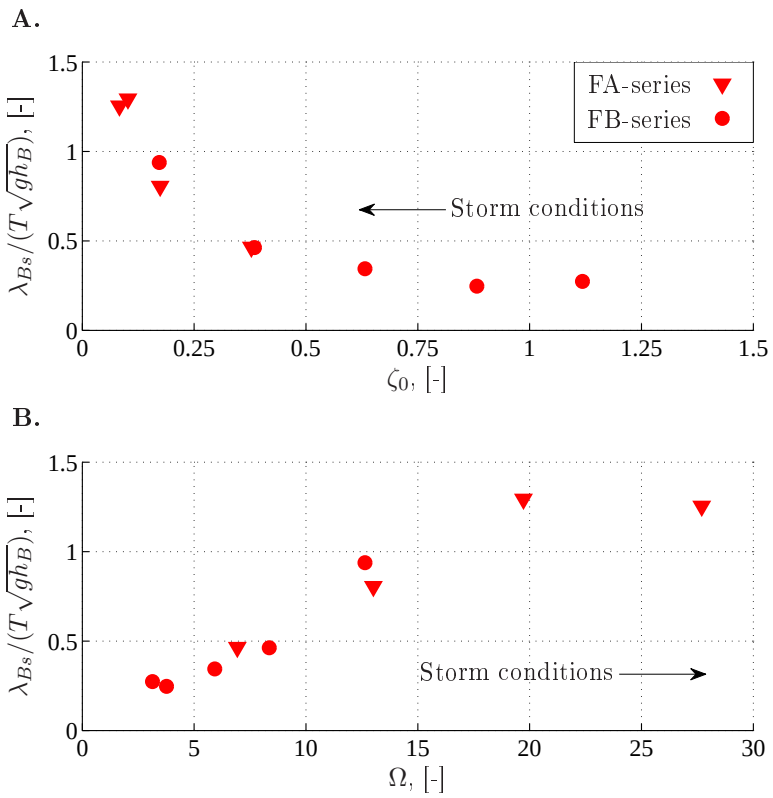

Figure 5.8: *The spatial lag, λ_{Bs}, between the location of* $\max \bar{H}$ *and* $\max \bar{q}_s$ *as a function of ζ_0 (A) and Ω (B). λ_{Bs} is made non-dimensional with an estimate of the wave length at breaking, $T\sqrt{gh_B}$.*

The spatial lag is of course related to both the magnitude of the bed shear stress and the strength of the undertow, all of which are discussed in §§5.3 and 5.4. Another feature in causing this phase lag could be found in the detailed description of the advection and diffusion of k. As described

in Lin and Liu (1998) for spilling breakers, the downward diffusion of k is to some extend counteracted by the vertical upward advection of the same quantity. This upward flow is a combination of the wave orbital motion and that of the period averaged circulation in the surf zone, see figure 2.7. In plunging breakers on the other hand, the vertical downward advection is pronounced just after the point of breaking as seen from the velocity fields depicted in figure 5.2–5.3. Thus the spreading of turbulence and the ability to sustain large amounts of sediment in suspension is more rapid relative to the location of the breakpoint.

Comparison with Experimental Results

Based on the analysis in figure 5.7 it is suggested that either Ω or Ω_{HK} are the best scaling parameter for the integrated cross shore flux. In the experiment by Baldock *et al.* (2010), the cross shore sediment transport can be computed for a case with regular waves, where $\Omega = 6.5$ and $\Omega_{HK} = 0.70$. In the former, test case FB3 have a similar value for Ω and in the latter, the largest value present in these simulations is found in FA1, namely $\Omega_{HK} = 0.52$.

The breaker height is not reported by Baldock *et al.* (2010), but using figure 5.5, it is estimated to be $(H/h)_B = 0.9$, where $h_B = 0.18$ m. This yields $\bar{Q}_s/(H_B^2\sqrt{gh_B}) = 3.0 \cdot 10^{-4}$. A comparison with figure 5.7B,C shows that the corresponding value based on Ω is $5.0 \cdot 10^{-4}$, whereas it is an order of magnitude larger, when estimated based on Ω_{HK}.

5.3 Bed Shear Stresses under Breaking Waves

The period averaged bed shear stress, $\overline{u_f|u_f|}$, and the skewness of the friction velocity, $\overline{u_f^3}$, is plotted in figure 5.9. It is seen that $\overline{u_f|u_f|}$ is directed shoreward outside the surf zone and seaward inside. The shoreward directed bed shear stress suggests that the streaming component is resolved. On the same figure the corresponding value of $\overline{\theta'}$ is indicated and values larger than 1 are found in the interior of the surf zone. $d = 0.2$ mm in the computation of θ'. The quantity $\overline{u_f^3}$ is a proxy for the bed load transport, e.g. similar to an energetics approach for bed load sediment transport. It can be noted that the zero-crossing of $\overline{u_f^3}$ coincide with a change in direction of $\bar{q}_b$. The temporal variation of $\tilde{u}_f$ is considered in space-time plots in §5.5, and values as large as $\theta' = 3.0$ are found in these simulations.

Phase Lead in Bed Shear Stresses over Surface Elevation

In figure 5.10, the phase lead of the maximum shoreward friction velocity over the wave crest, ϕ_{crest}, and that of the maximum seaward friction veloc-

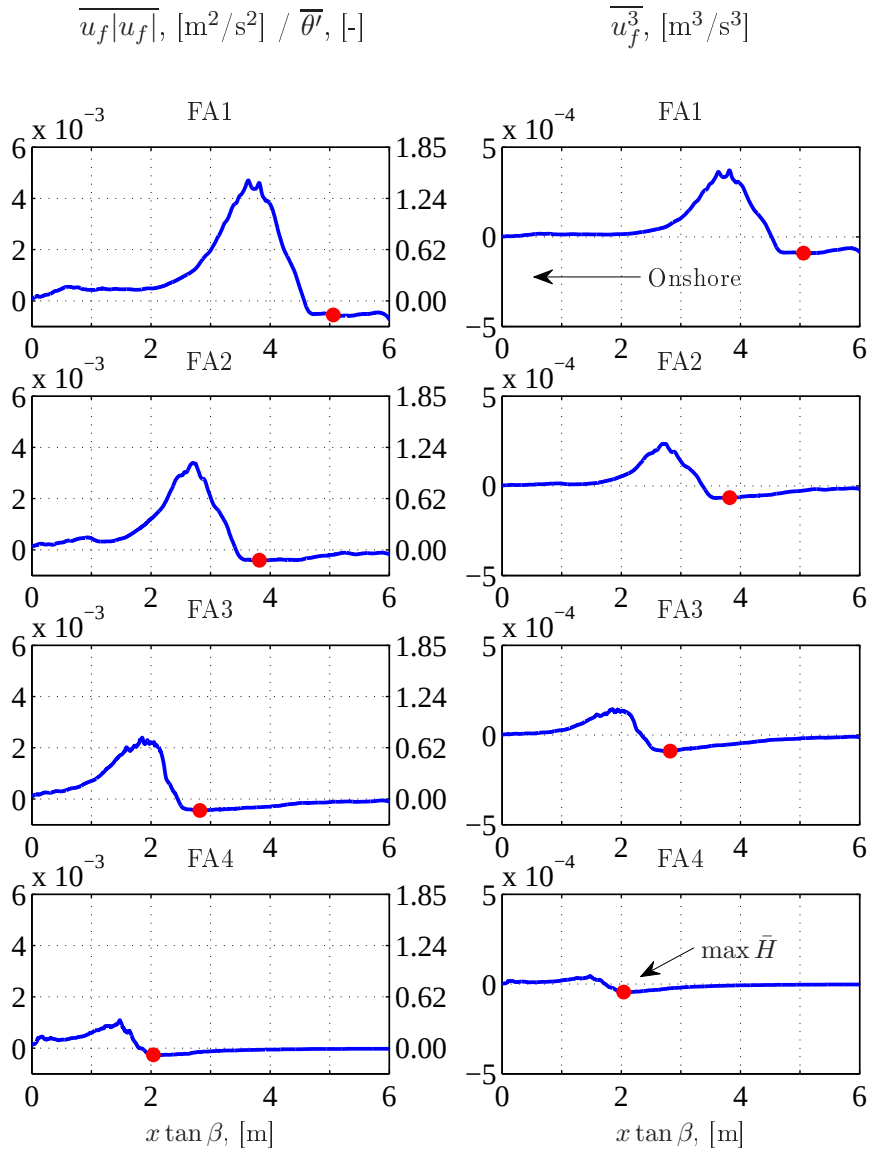

Figure 5.9: *The variation of the friction velocity across the surf zone for the FA-series. (Left): $\overline{u_f|u_f|}$ on the left axis and $\overline{\theta'}$ on the right axis. $d = 0.2$ mm in the computation of θ'. (Right): $\overline{u_f^3}$.*

ity over the wave trough, ϕ_{trough} is depicted. Outside the surf zone, ϕ_{crest} is approximately 10°, which correspond to the value for a fully turbulent boundary layer as given by Fredsøe (1984). In the outer part of the surf zone, the phase lead is noisy, however, it does become negative and in the inner surf zone, the phase lead levels out around 5°. The latter value is also

reported in Fredsøe *et al.* (2003), where the effect of external turbulence on an oscillatory boundary layers is considered experimentally. The decrease in phase lead is due to an increased vertical momentum exchange. In sinusoidal waves, $\phi_{\text{crest}} = \phi_{\text{trough}}$, which is not seen in these simulations, where $\phi_{\text{crest}} < \phi_{\text{trough}}$. Throughout the computational domain, ϕ_{trough} varies between $15° - 50°$, and such values are also found in simulations of oscillatory flows with a velocity skewness (see Fuhrman *et al.*, 2009, their figure 7).

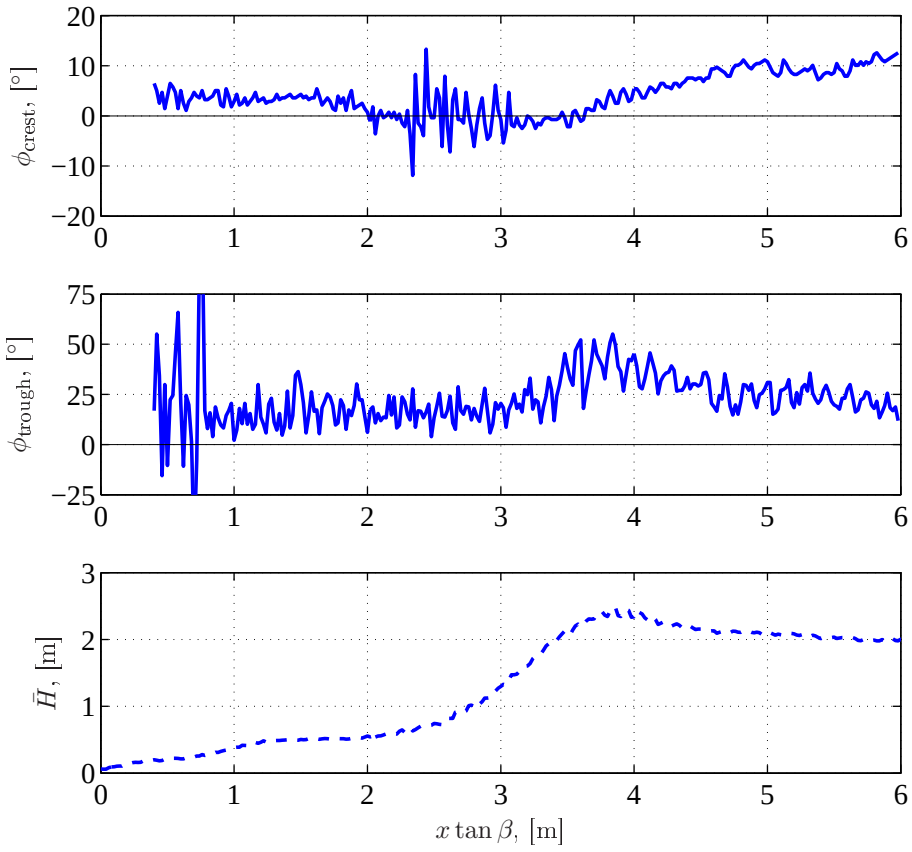

Figure 5.10: *The variation in phase leads in- and outside of the surf zone for test case FA2. (Top): ϕ_{crest}. (Middle): ϕ_{trough}. (Bottom): $\bar{H}$.*

Cox (1995) measured the surface elevation and velocity profiles over a rough boundary in a small scale laboratory wave flume. The bed had a constant slope of 1:35. Using his figures 4.4, 4.5, 4.7, and 4.9, ϕ_{crest} at breaking is estimated to 6° and approximately one wave length shoreward in the range $[-3°, 4°]$. The latter value is given as a range, as both the near bed velocity and the surface elevation are flat around the maximum value. The near bed velocities are measured 0.2 cm above the bed, thus proportionality

between this quantity and the friction velocity can be assumed. ϕ_{trough} has been estimated to 20.5° in the surf zone and to 26° ± 7° at the point of breaking. The values correspond to those from the present numerical model.

Similar results are obtained by Hansen (2009), who studied laboratory scale plunging breakers over a smooth PVC bed installed with a slope of 1:14 (his figure 4.80). Outside the breakpoint the phase lead of the measured bed shear stress over the maximum free stream velocity is 17°, and it drops to 0° followed by an increase to 20° in the shoreward direction. His higher values are probably due to the smoothness of the bed in combination with laboratory scale waves, thus the boundary layer is not fully turbulent.

5.4 Undertow and Return Flow

The undertow and return flow have, as already seen in §4.3, two different velocity distributions. The undertow is strongest near the bed, while the return flow is strongest at a larger distance from the bed. In the following, two related quantities are considered based on period averaged velocity profiles. The first quantity is the average undertow/return flow velocity, which is given as

$$\bar{u}_r(x) = \frac{1}{\Delta h_u(x)} \int_{\Delta h_u} \bar{u}(x) \mathrm{d}y \tag{5.6}$$

integrated over the offshore directed flow velocities. Here the height of the undertow is defined as Δh_u being the difference between the maximum and minimum vertical elevation of the undertow profile. The second quantity is the relative centroid position of the undertow profile, which is defined as

$$y_u(x) = \frac{1}{\Delta h_u(x)} \frac{\int_{\Delta h_u} \bar{u}(x)(y(x) - y_{bed}(x)) \mathrm{d}y}{\int_{\Delta h_u} \bar{u}(x) \mathrm{d}y} \tag{5.7}$$

again integrated over the undertow profile, where y_{bed} is the local bed level.

These quantities are plotted in figure 5.11, where it is seen that the undertow is strongest inside the surf zone, and it has a fast decay toward the breakpoint after which the remaining part, namely the return flow, decreases slowly. Furthermore, it can be seen that y_u is almost constantly found at $y_u = 0.37$ in the surf zone. This ratio increases to 0.6 just shoreward of the point of breaking. This maximum in the undertow shoreward of the breakpoint has also been identified in the field (Masselink and Black, 1995).

The separation of the undertow is explained in the following manner. The setup ends shoreward of the breakpoint, and it turns into a small setdown, i.e. a weak adverse pressure gradient. In combination with the diverging geometry, the undertow cannot stay attached to the wall and it separates.

The variation in 5.11 fits with the variation in $\bar{q}_s$ and $\overline{u_f|u_f|}$ in figures 5.6 and 5.9.

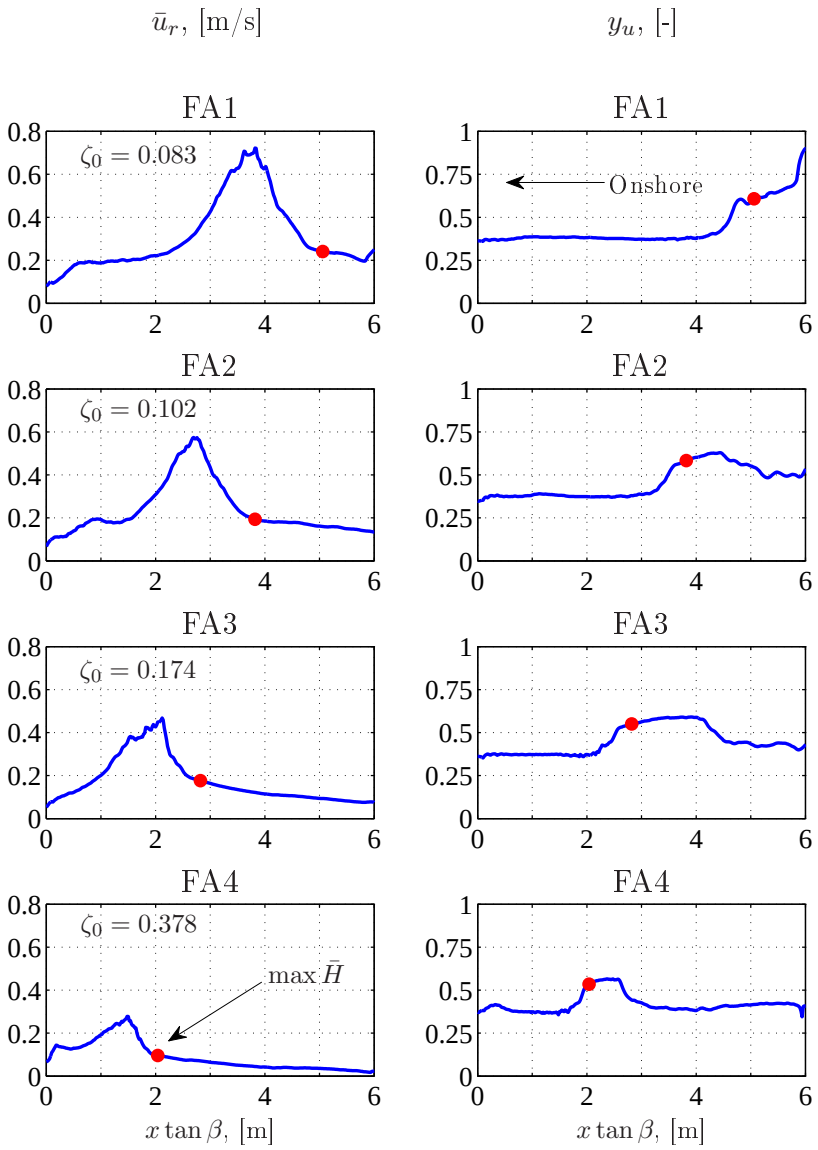

Figure 5.11: *(Left): Variation in average undertow and return flow velocity, $\bar{u}_r$. (Right): Position of the centroid relative to the undertow height, y_u.*

The steep gradients in $\bar{u}_r$ also reflect the circulation in the surf zone (see figure 2.7), where there is a vertical upward flux around the breakpoint and a corresponding downward flux in the interior of the surf zone. The height of the undertow increases in the seaward direction, however, with a smaller rate

than the decrease in $\bar{u}_r$. From $x \tan\beta = 3.84$ to 4.78 in case FA1 it results in a decrease in the offshore directed flux of water of 0.72 m^2/s. The range in $x \tan\beta$ corresponds to 47 m. The decrease in horizontal flux results in an averaged vertical velocity of 0.015 m/s at the top of the undertow profile. This order of magnitude difference between the undertow strength and the vertical velocities in the cross shore circulation cells is measured by Nadaoka and Kondoh (1982) in a small scale laboratory experiment.

5.5 Temporal Sediment Transport Patterns under Breaking Waves

Contour plots of $\tilde{\eta}$, $\tilde{u}_f$ and $\tilde{q}_s$ for the test cases FA1, FB2 and FB5 are shown in the figures 5.12–5.14. These figures reveal the complex spatial and temporal variations in the hydrodynamics and sediment transport patterns found in the surf zone. The spatial and temporal lags discussed in §§5.2 and 5.3 are readily identified.

Besides the easy identification of lag effects, the following can also be seen from the figures:

- The more the plunging type breaking, (increasing ζ_0) the shorter the distance between the maximum (offshore) and minimum (onshore) values of $\tilde{u}_f$. The onshore value is found around the breakpoint and the offshore value inside the surf zone occurring due to the combination of orbital wave motion in the trough and the undertow.

- For increasing values of ζ_0, there is a decrease in the spatial extend, where the offshore suspended sediment flux is considerable. This spatial extend is considered relative to the wave length.

  For small ζ_0 this spatial extend is in the order of 2 wave lengths, and it decreases to less than half a wave length for the largest value of ζ_0.

- A comparison between 5.6 and 5.12 clearly shows the order of magnitude difference between the instantaneous suspended sediment fluxes and the residual effect. The morphological response depends on the latter, and underline the difficulties in modelling cross shore sediment transport and cross shore breaker bar migration.

The effect of a reflected wave can be identified in figure 5.14 both in $\tilde{u}_f$ and $\tilde{q}_s$. The interaction between a breaking wave and this reflected wave at $\{x \tan\beta,\ t/T\} = \{0.6,\ 0.5\}$ yields a peak in the offshore directed sediment transport. $\tilde{u}_f$ exhibits a clear convexity of the trajectory of the reflected wave relative to x, which reflects the spatial variation in propagation speed.

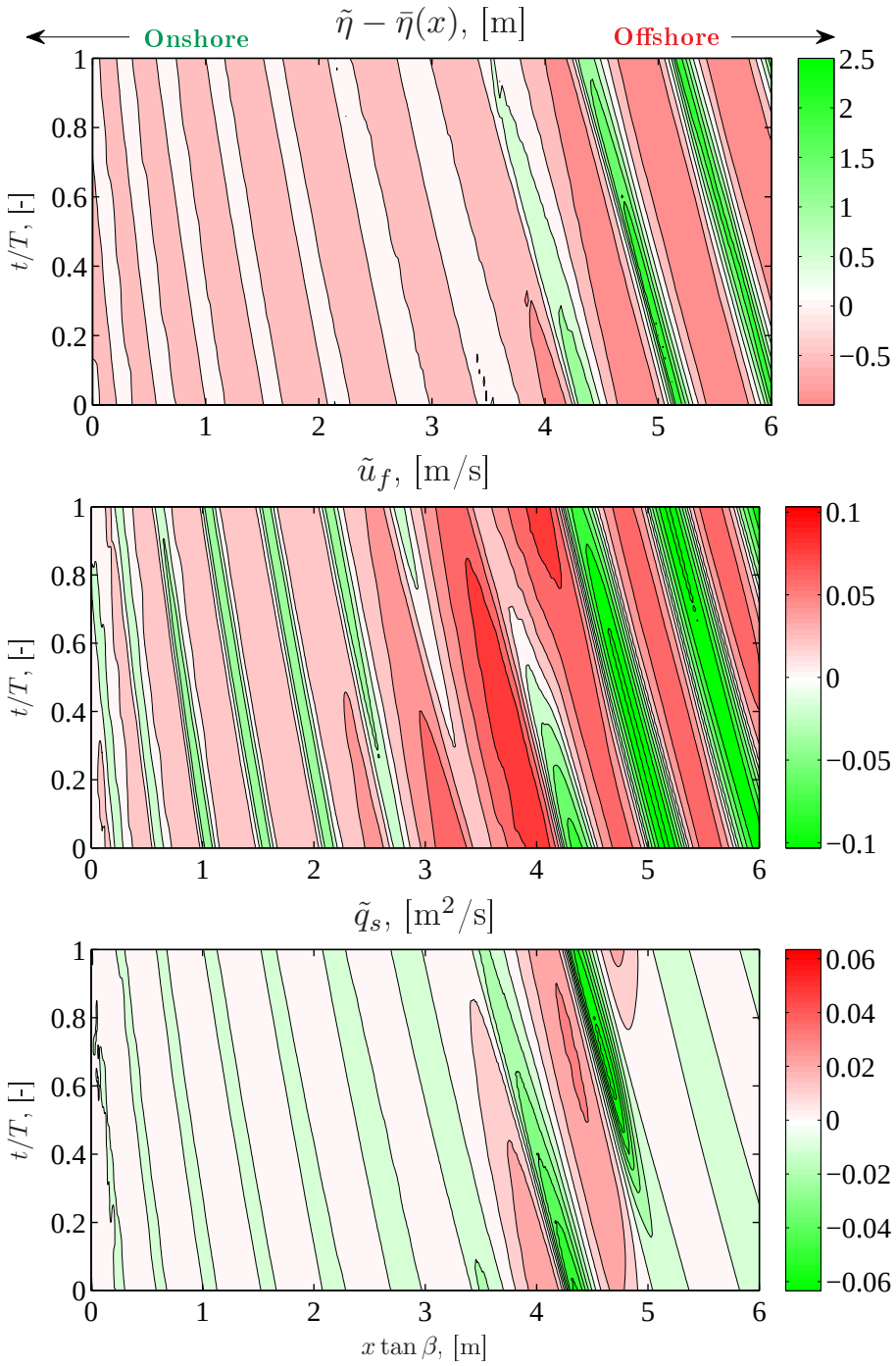

Figure 5.12: *Ensemble averaged quantities for test case FA1* ($\zeta_0 = 0.083$ *and* $\tan\beta = 1:50$). *(Top): Surface elevation,* $\tilde{\eta}$. *(Middle): Friction velocity,* $\tilde{u}_f$. *(Bottom): Suspended sediment transport flux,* $\tilde{q}_s$. $\tilde{u}_f = 0.1$ *m/s corresponds to* $\tilde{\theta}' = 3.1$ *for* $d = 0.2$ *mm.*

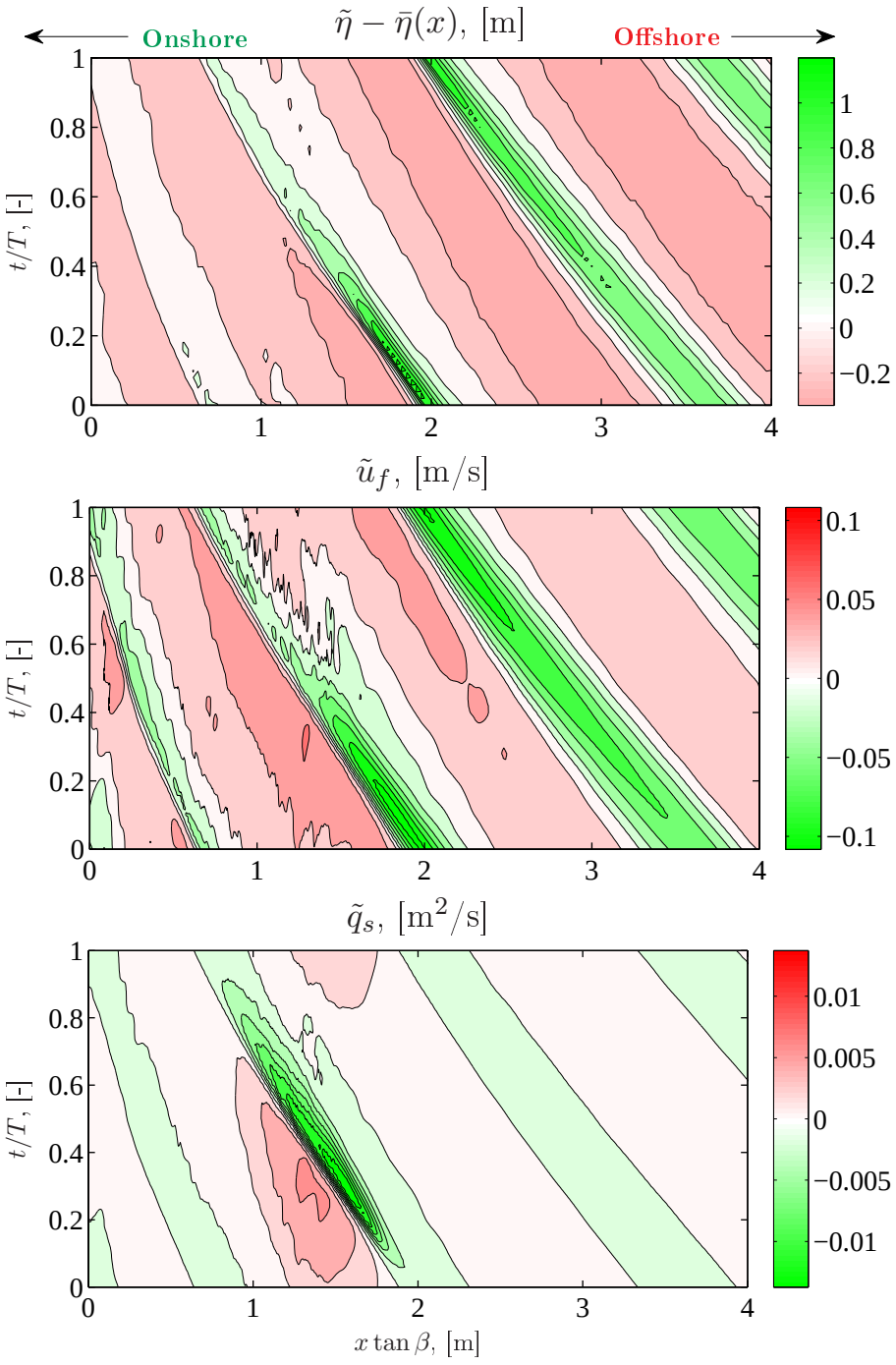

Figure 5.13: *Ensemble averaged quantities for test case FB2 ($\zeta_0 = 0.385$ and $\tan\beta = 1 : 35$). (Top): Surface elevation, $\tilde{\eta}$. (Middle): Friction velocity, $\tilde{u}_f$. (Bottom): Suspended sediment transport flux, $\tilde{q}_s$. $\tilde{u}_f = 0.1$ m/s corresponds to $\tilde{\theta}' = 3.1$ for $d = 0.2$ mm.*

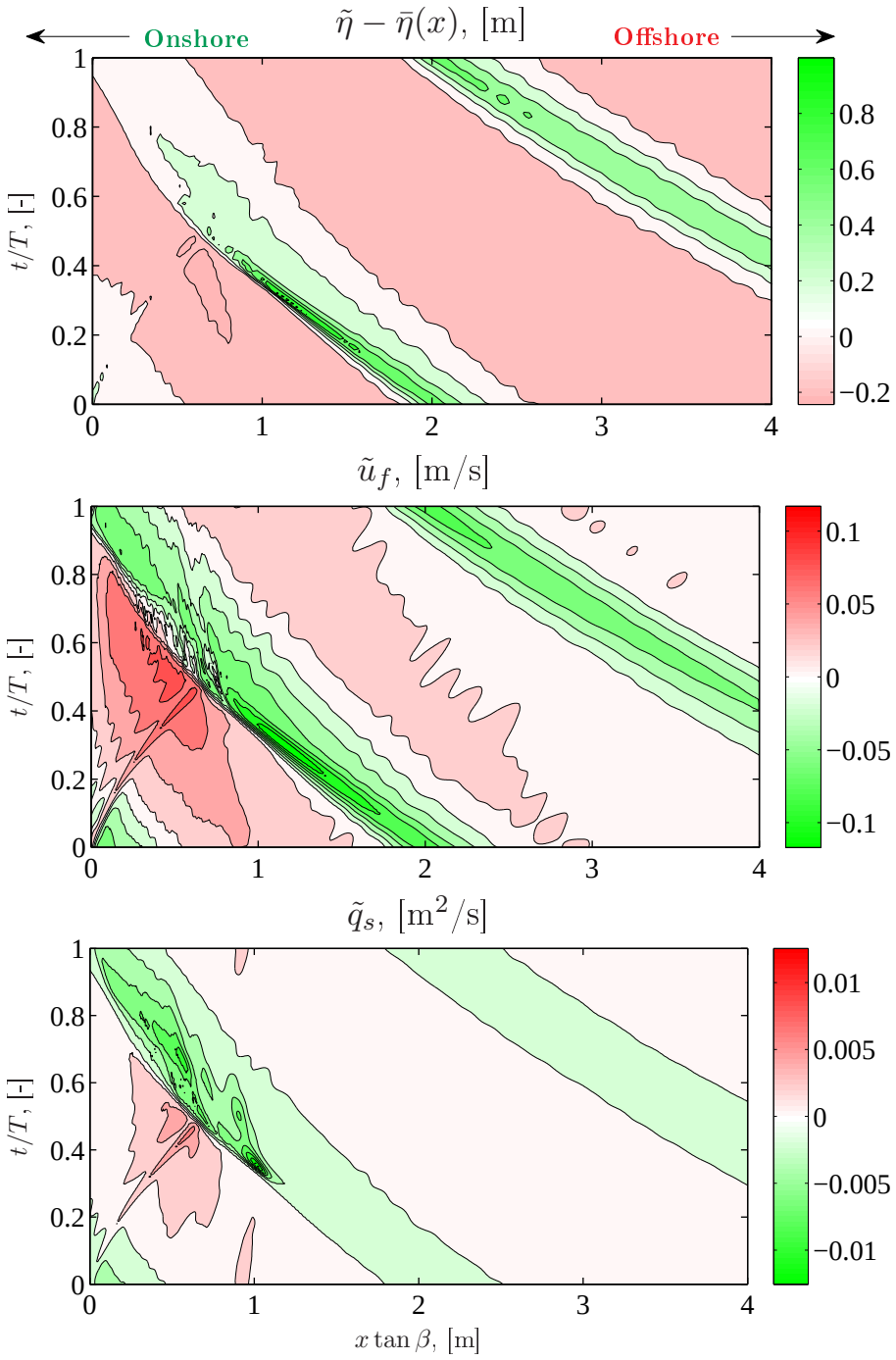

Figure 5.14: *Ensemble averaged quantities for test case FB5* ($\zeta_0 = 1.118$ *and* $\tan\beta = 1 : 35$). *(Top): Surface elevation,* $\tilde{\eta}$. *(Middle): Friction velocity,* $\tilde{u}_f$. *(Bottom): Suspended sediment transport flux,* $\tilde{q}_s$. $\tilde{u}_f = 0.1$ *m/s corresponds to* $\tilde{\theta}' = 3.1$ *for* $d = 0.2$ *mm.*

Chapter 6

Morphodynamic Description

The morphological development of breakers bars will be considered in the present chapter. The development is considered for both laboratory scale waves (§6.1) and for prototype waves (§6.2). Preliminary results of the former simulations are also presented in Jacobsen and Fredsøe (2011).

A cut-off is applied around the swash zone to avoid numerical problems in both the laboratory and prototype scale simulations, see §4.3. The morphological development with or without such a cut-off is considered experimentally by Barnet and Wang (1988), where a sea wall is installed at the shoreline. They found no considerable morphological difference, hence the approach is reasonable in these numerical simulations.

The cell aspect ratio is kept larger than 1.0, as the computational time would otherwise be so large as to make the proposed simulations infeasible. The effect of this choice is a discrepancy between the modelled and actual location of the breakpoint, i.e. a horizontal displacement. The physical processes are also subject to a corresponding horizontal displacement due to an increase in the surf zone width. Nevertheless, these processes are captured correctly in their new location, which is seen in §4.3.

An additional time scale is introduced in the following, namely $t_m = f_m t$. This is the morphological time, which is used to distinguish between hydrodynamic and morphodynamic times. f_m is the morphological acceleration factor also discussed in §3.3.2.

6.1 Laboratory Scale

The laboratory scale layout is based on that shown in figure 4.12, and the bed is made of loose sediment with $d = 0.1$ mm, which corresponds to a roughness height of $k_N = 0.25$ mm. Two sets of environmental forcing are used, namely regular waves with $H = 0.125$ m and $T = 2.0$ s and a bichromatic wave having $H_{\text{rms}} = 0.125$ and $T = 1.67,\ 2.00$ s. These two periods yield a

repeat period of 10 s. The morphological development for the two beach profiles is depicted in figure 6.1 at $t_m = 2864$ s. From this comparison it can be noted that the outer bar is farther offshore for the bichromatic case. This occurs, as the superimposed wave height in the bichromatic case is larger than for regular waves, hence it breaks farther offshore. This is also seen in the laboratory experiment by Baldock *et al.* (2011). The profile between the outermost trough and the shoreline has a smaller response under bichromatic forcing than for regular waves, in which two breaker bars have developed. The swash area exhibits large morphological changes in the case of bichromatic waves, which are not seen in the case of regular waves. The swash erosion is caused by the smaller waves in the wave group, which can pass unhindered over the outer bar and subsequently break at the shoreline.

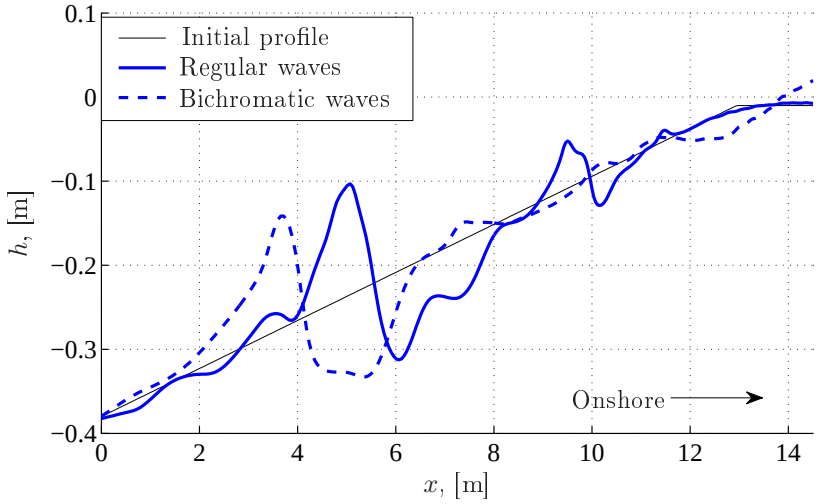

Figure 6.1: *Comparison of the morphological development under regular waves ($f_m = 4.0$) and bichromatic waves ($f_m = 2.5$). Comparison is made at $t_m = 2864$ s.*

Temporal Development

The temporal development of the cross shore profile under the two different forcings is depicted in figure 6.2. It is seen that the regular wave forcing produces a much faster growth of the breaker bar, and it reaches its maximum crest level, while it is migrating seaward. The simulation has not reached an equilibrium crest elevation in the case of bichromatic waves, however, it is seen to migrate offshore as well.

An inner bar is developed under regular wave forcing at $x = 9$ m. This bar appears late in the morphological development, and it is found to coincide

with the cessation of wave breaking in the trough. The waves recover to a state of non-breaking waves in the trough, merely to break farther shoreward and initiate the development of the inner bar. The migration of the outer breaker bar in figure 6.2A slows down with time. This is considered in more detail below.

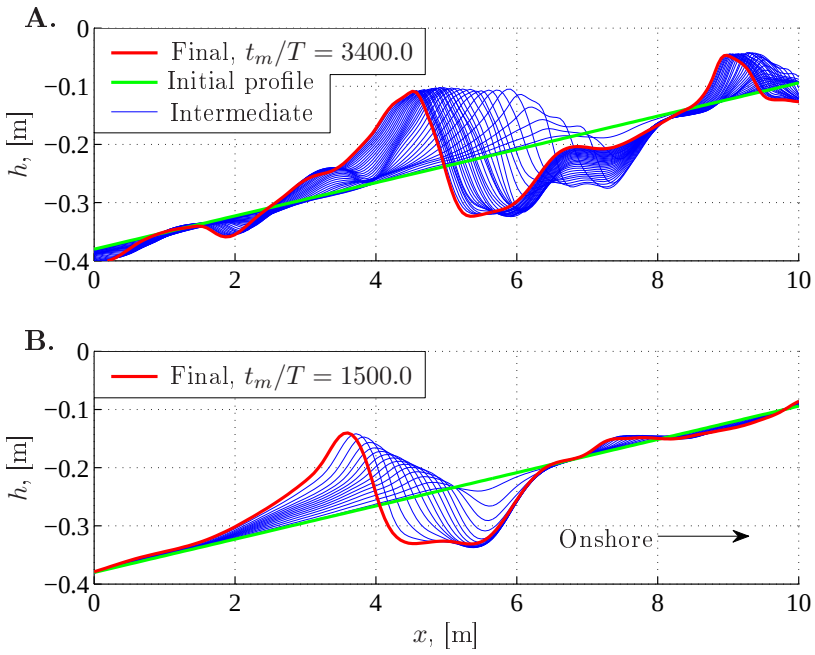

Figure 6.2: *The temporal morphological development of the laboratory scale test cases. There are* $\Delta t_m = 100T$ *between each line, where* $T = 2$ *s is used in the bichromatic case. A: Regular waves,* $f_m = 4.0$*. B: Bichromatic waves,* $f_m = 2.5$*.*

A detailed analysis of the temporal variation of the x and y locations of the crest of the outer bars shows that while the regular wave development changes without any periodicity in the signal, a similar analysis shows a period of 10 s for bichromatic waves. This suggests a coupling between this period and the repeat period of the bichromatic waves. The crest decreases in height under the small waves in the wave group, and it increases in height under the larger waves. In the case of bichromatic waves it is also realised that the growth in the crest level is preceded by an erosion of the trough. As a consequence of the period averaging over 2 s, it is not possible to state anything about the magnitude of the phase-lag.

Bed Shear Stress on the Crest of the Breaker Bar

The temporal variation of the bed shear stress ($\tilde{\tau}_b/\rho_1 = \widetilde{u_f|u_f|}$) and the Shields parameter (θ') on the bar crest is depicted in figure 6.3. The crest is defined as the location, where $\partial h/\partial x = 0$. It is seen that for both regular and bichromatic waves, the bed shear stress is initially directed offshore most of the time. As the bar increases in height, the onshore directed component becomes increasingly larger, however, still smaller than the offshore component. This increase in the bed shear stress is expected due to the decrease in the water depth. As the bar crest reaches the steady level, the envelope of the bed shear stress levels off at an approximately constant value. This levelling off is not seen for bichromatic waves in figure 6.3B, because the bar has not reached a steady level.

Note that for the final shape of the profiles, it is reasonable to assume that no ripples can exist on the crest, because $\theta' > 1.0$ for a part of the wave period (Nielsen, 2009).

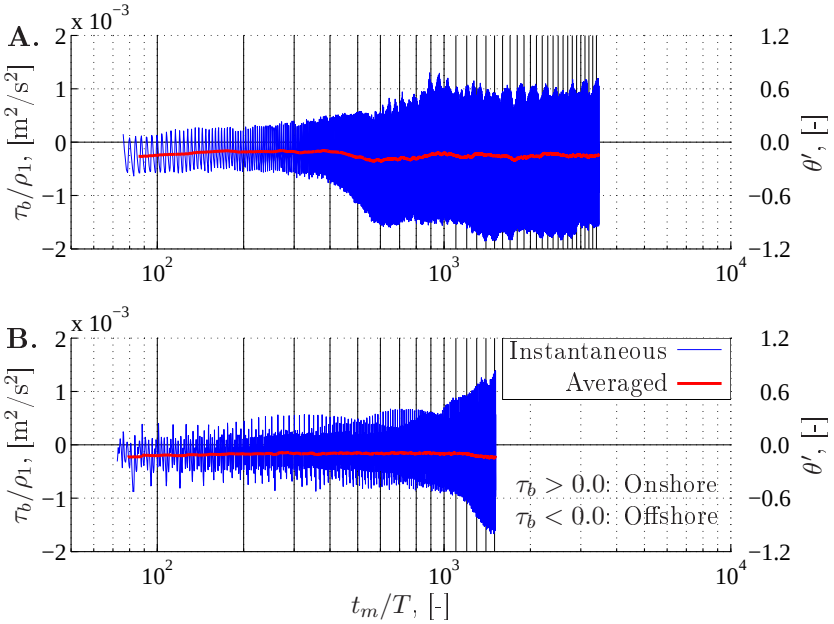

Figure 6.3: *The bed shear stress and the corresponding Shields parameter on the outer bar as a function of time. Both given as instantaneous and period averaged over $t = 10$ s. Vertical lines represent the instances in figure 6.2. A: Regular waves ($f_m = 4.0$). B: Bichromatic waves ($f_m = 2.5$).*

Migration Speed of the Breaker Bar

The migration speed for the three bars in figure 6.2A,B is depicted in figure 6.4. It is computed as a running average over $\Delta t_m = 60T$. It shows that the migration speed is a decreasing function with time, however, the migration speed is more constant for the bichromatic wave, probably because it has not reach a steady crest level yet. The decrease in migration speed is explained by

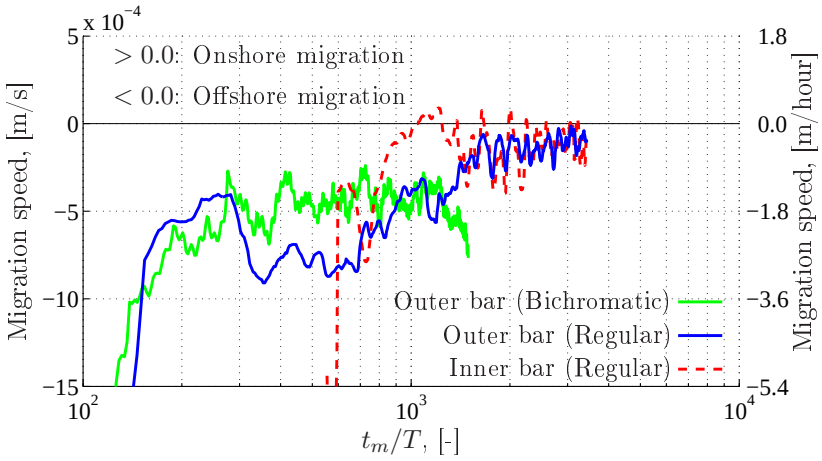

Figure 6.4: *The migration speeds of the inner and outer bars for the regular waves ($f_m = 4.0$) and for the (outer) bar for bichromatic waves ($f_m = 2.5$). The migration speed is given in both m/s and m/hour.*

– The higher the breaker bar, the more sediment is required to move the breaker bar one unit length. This explanation is, however, too simplistic, as it is just seen that the bed shear stress increases in magnitude with an increase in breaker bar height. Therefore, the decrease in migration speed is, as an isolated phenomenon, a balance between the requirement of moving more sediment and an increasing exciting force on the sediment grains.

– It is especially clear from figure 6.2A that the trough only erodes to a given level. Furthermore, the inner part of the trough is slowly being filled, meaning that the migration of the bar is self-sustaining. By this, it is meant that once the trough reaches a mature state, the shoreward side of the bar is merely subject to a pure translation, and it seems that the sediment transport delivery across the trough in the seaward direction is small.

From the laboratory experiments by Dally (1987) and Baldock *et al.* (2010) the migration speed of a breaker bar has been estimated to $\mathcal{O}(5 \cdot 10^{-5})$ m/s, which is only 2–3 times smaller than the migration speed of the mature outer bar for the regular waves, i.e. figure 6.4 for $t_m/T > 2000$.

6.2 Prototype Scale

The morphological development of breaker bars under prototype scale waves is considered in this section. The investigated combinations of grain diameters and environmental forcing are listed in table 6.1. All of the simulations are carried out using regular waves described by stream function theory. Some simulations are carried out with bed load as the only transport mechanism and others with a combination of bed load and suspended load. In addition to these runs, a series of runs is considered, where the outer breaker bar is subject to a net shoreward current. This shoreward current mimics the presence of a rip circulation system, see figure 2.2.

Table 6.1: *The parameters used in the simulations of breaker bar development. $u_{c,h}$ is the current strength at the inlet, where the water depth is 7.0 m. (*) Initial profile is taken from A02SB at $t = 609.6$ s ($t_m/T = 769$). The profile is partly frozen for these computations.*

Test Name	d [mm]	H_h [m]	T [s]	Transport mechanism	$u_{c,h}$ [m/s]	f_m [-]
Bed Load Transport						
A02B	0.2	1.3	4.8	B	–	12.5
A05B	0.5	1.3	4.8	B	–	20.0
Combined Sediment Transport						
S02SB	0.2	3.0	6.0	S+B	–	8.0
S05SB	0.5	3.0	6.0	S+B	–	15.0
A02SB	0.2	1.3	4.8	S+B	–	6.25
A05SB	0.5	1.3	4.8	S+B	–	15.0
Combined Sediment Transport - Net Shoreward Current						
A02SBC0 *	0.2	1.3	4.8	S+B	0.000	6.25
A02SBC1 *	0.2	1.3	4.8	S+B	0.018	6.25
A02SBC2 *	0.2	1.3	4.8	S+B	0.054	6.25
A02SBC3 *	0.2	1.3	4.8	S+B	0.090	6.25

The initial profile is that of Dean (e.g. Cowell *et al.*, 1999, p. 59), namely

$$h = Ax^{2/3} \quad , \tag{6.1}$$

where the parameter $A = 0.067(100w_s)^{0.44}$ depends on the grain diameter. Two values of d is used, thus the average value of the two is applied for the determination of $A(= 0.1304)$ $\mathrm{m}^{1/3}$. The profile has an upper cut-off at 0.10 m and become horizontal at 7.0 m. The roughness height, k_N, is set to $2.5d$.

The two applied environmental forcings are a storm situation on the Danish West Coast and an average event. Offshore measurements of wave height and period are obtained from the Danish Coastal Authorities (DCA), see figure 6.5.

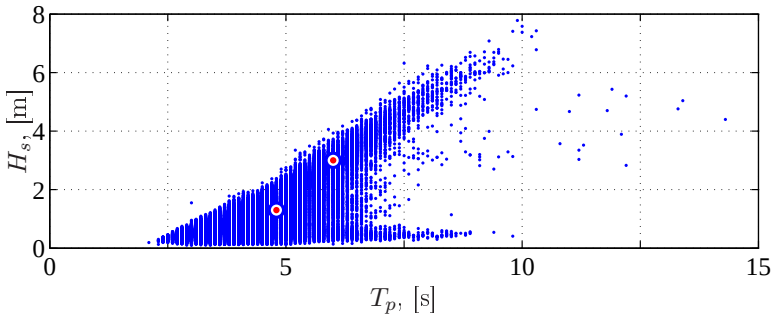

Figure 6.5: *Wave climate off the Danish North Sea Coast in measuring point 2041. Data from DCA. Red dots are the chosen wave events.*

6.2.1 Breaker Bar Development with only Bed Load

The morphological development with and without suspended sediment transport is compared in this section. The morphological development with only bed load for the chosen parameters is rather weak and will hence not be considered directly.

The accumulated bed level change for either bed load (Δh_b) or combined transports ($\Delta h_s + \Delta h_b$) is depicted in figure 6.6A for a comparison between A02B and A02SB ($d = 0.2$ mm) and in figure 6.6B for a comparison between A05B and A05SB ($d = 0.5$ mm). For $d = 0.2$ mm it is seen that the effect of bed load is approximately two orders of magnitude less important than suspended sediment transport. In the case of $d = 0.5$ mm, this ratio is decreased to approximately one order of magnitude.

Since the bed load transport is computed based on a localised formulation, and because Δh_b is small, Δh_b does also, to a certain degree, reflect the initial response of the cross shore profile to the wave forcing. This reveals that while both the inner ($x = 35$ m) and outer ($x = 90$ m) bar in figure 6.6A are migrating, it is only the case for the inner bar ($x = 25$ m) in 6.6B. This can also be verified by considering the temporal development in figure 6.7A,B.

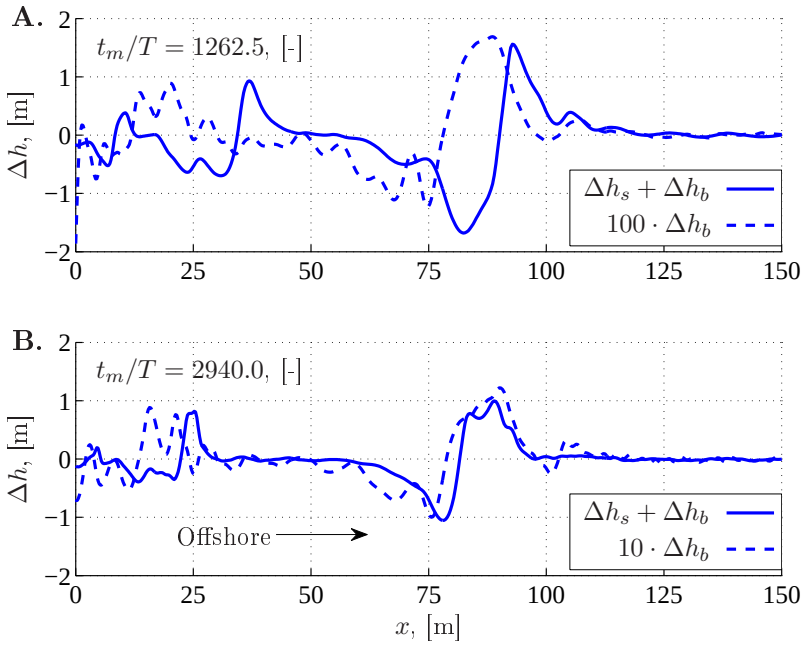

Figure 6.6: *Intercomparison between the morphological development with only bed load (Δh_b) and combined bed load and suspended sediment transport ($\Delta h_s + \Delta h_b$). $T = 4.8$ s and $H_h = 1.3$ m. A: $d = 0.2$ mm. B: $d = 0.5$ mm.*

6.2.2 Breaker Bar Development with Combined Transport

The morphological development for simulated breaker bars under combined sediment transport processes are depicted in figure 6.7. The test cases are A02SB, A05SB, S02SB and S05SB. The details are given in table 6.1. Several features can be identified from this temporal representation:

- The morphological development for $d = 0.2$ mm is faster than for $d = 0.5$ mm. This holds for both the yearly average and the storm event.

- The outermost breaker bar has larger dimensions for the storm conditions relative to the yearly average, and the breaker bar is found farther seaward.

- In figure 6.7A,B the crest level of the bars located around $x = 25 - 35$ m is larger in the case of $d = 0.5$ mm than for $d = 0.2$ mm. The breaker bar attains a constant level in both cases. This suggests that the sediment grain mobility is of importance for the steady crest level.

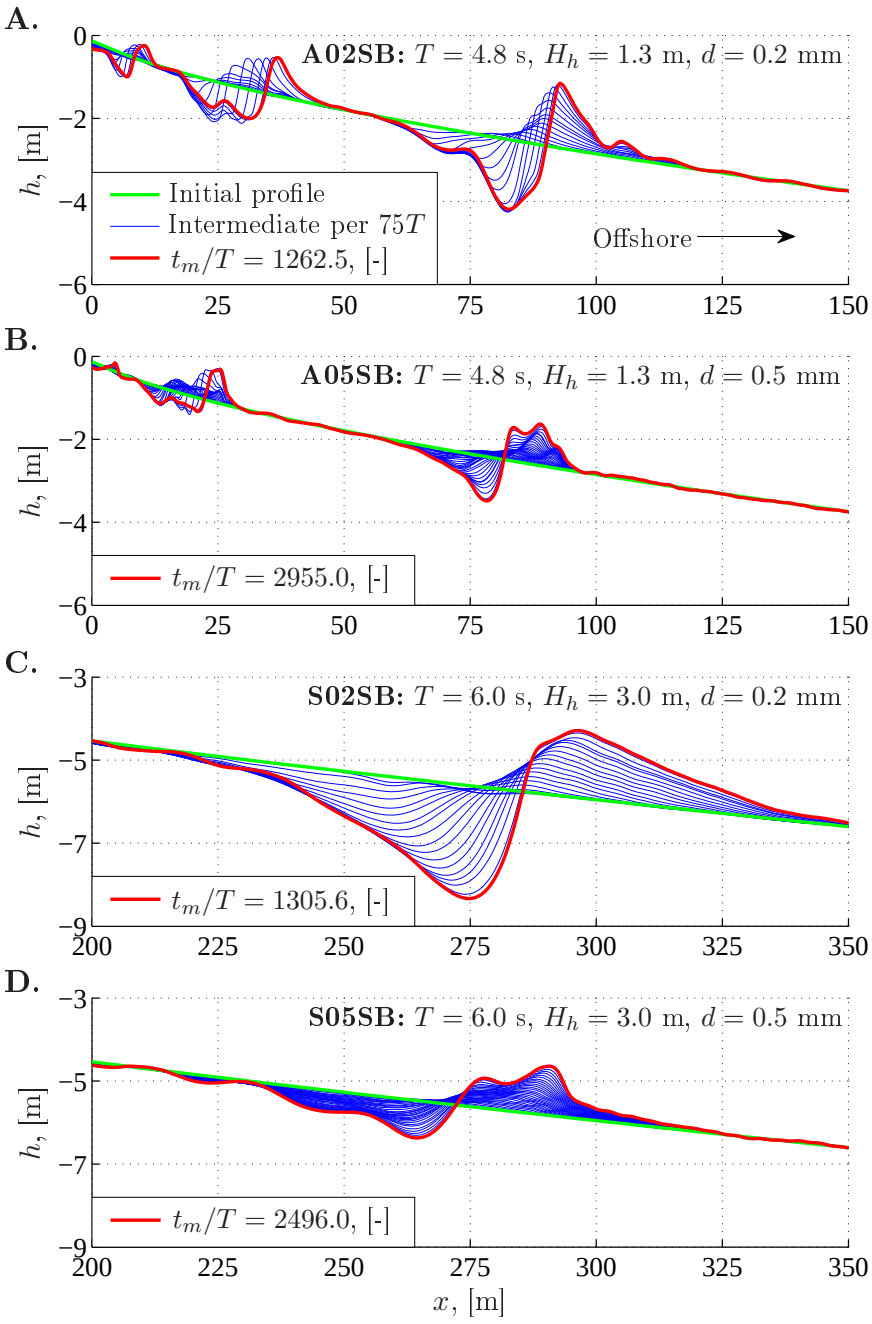

Figure 6.7: *The temporal development in the morphology for the four test cases for combined transport without a net current. The intermediate lines are given for every $\Delta t_m = 75T$. Note that the spatial scale is identical in all plots. For S02SB and S05SB the plot is truncated to only contain the outermost breaker bar.*

- The bars are steeper on the shoreward side than on the seaward side, which is in accordance with experimental evidence.

- The inner bars begin to form once the outermost trough becomes sufficiently deep to allow for the waves to recover in the trough. This allows for the propagating of non-breaking waves, which can successively break farther shoreward.

- Consider the breaker bar positions in figure 6.7A and assume that the final state is measured e.g. in the field. This profile clearly has three breaker bars, where the distance between them increases with the distance to the shore. This is in line with the infragravity hypothesis, however, as the offshore waves are regular, it does not make sense to consider infragravity waves. Therefore, the increase in breaker bar spacing is also achieved in systems, which have a zero infragravity wave energy.*

Bed Shear Stress on the Crest of the Breaker Bar

The bed shear stress at the outer bar crest is depicted in figure 6.8. It is seen that the bed shear stress qualitatively follow the same pattern as is found for laboratory waves (§6.1), however, with considerably larger corresponding Shields parameters. None of the plots shows a tendency to a levelling off in the envelope of the bed shear stress. This is explained with the fact that none of the simulations has reached a steady crest level, see §6.1.

Migration Speed of the Breaker Bar

The migration speed for A02SB and S02SB is depicted in figure 6.9. The migration speed is considerably larger than those measured in the field, see e.g. §2.4.3. This discrepancy will partly be due to (i) the fact that they have not reached a stable height, and thus migrates faster as also seen in figure 6.2 and (ii) the effect of irregular waves will smooth the sediment transport fluxes in the cross shore direction and directly affect the migration speed. The effect of irregular waves is discussed in §2.4.1, and the decrease in migration speed is due to a spreading of the sediment transport processes across the surf zone, and therefore a corresponding decrease in the spatial gradients in the transport field.

*It was tested, which infragravity frequencies could have generated the "measured" pattern. One distinct period, T_{IG}, was found per breaker bar. The range in T_{IG} is 11.0 s–17.0 s. These estimates are based on the expressions given in Dally (1987).

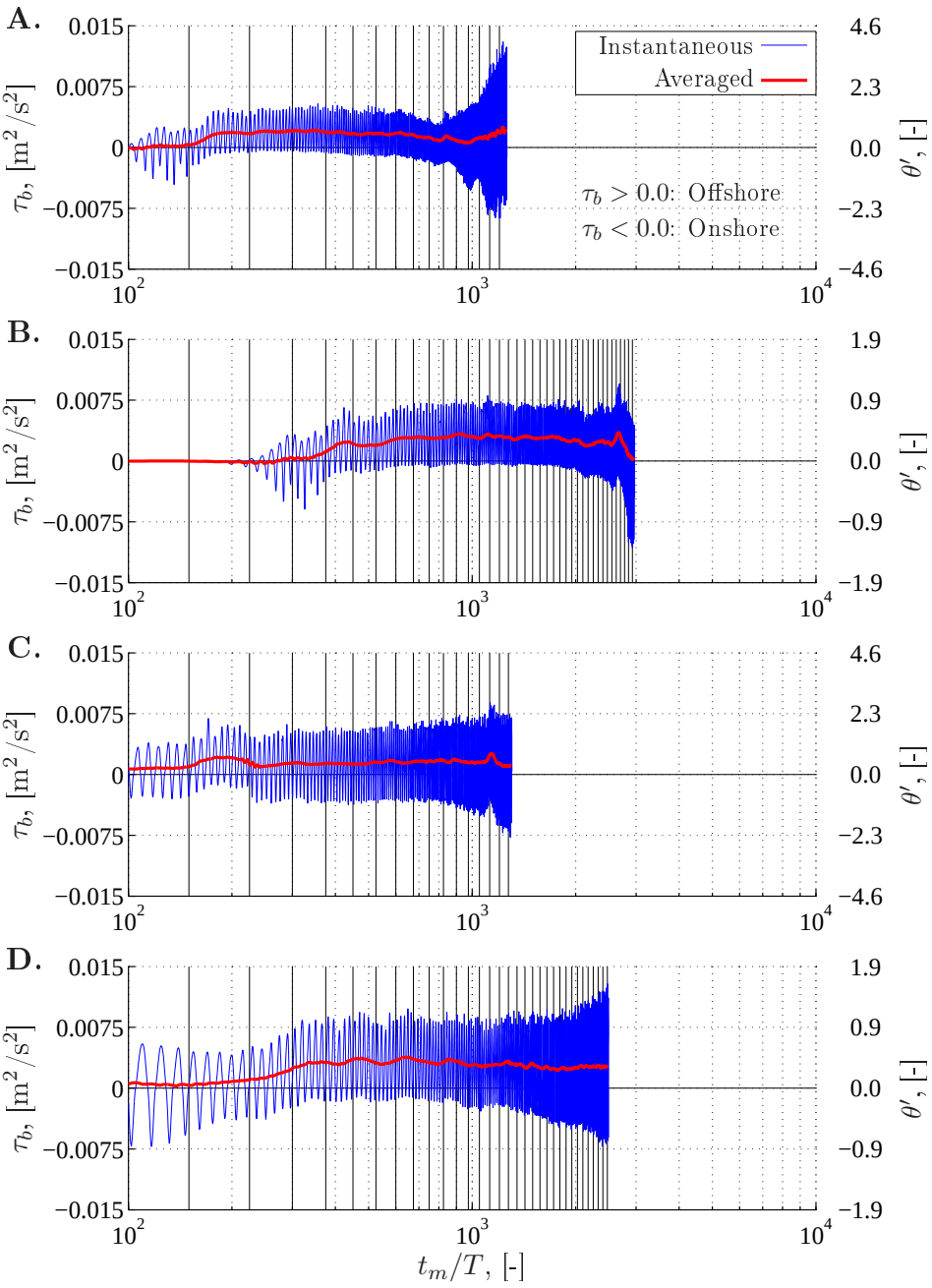

Figure 6.8: *The instantaneous and period averaged bed shear stresses on the outer bar crest as a function of time. Same conditions as in figure 6.7. Vertical lines correspond to the lines in figure 6.7. The corresponding value of the Shields parameter is depicted along the right axis.*

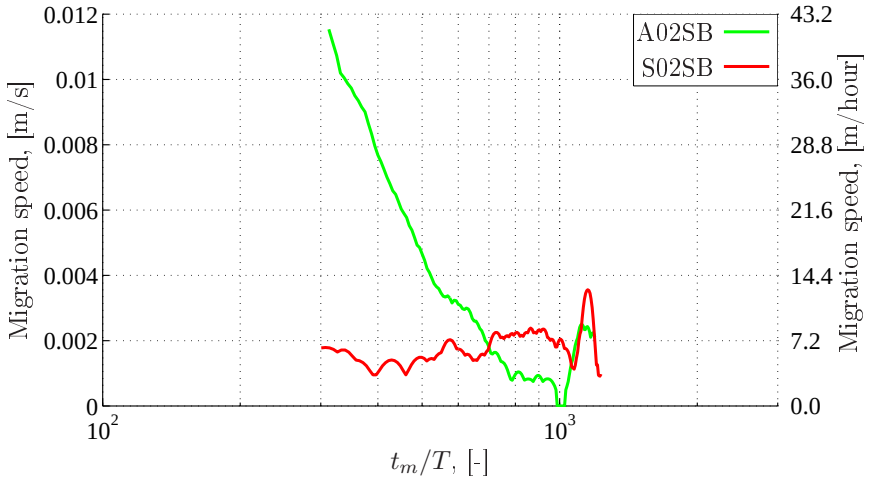

Figure 6.9: *The magnitude of the offshore migration speed for the outer bars in test case A02SB and S02SB.*

6.2.3 Morphological Development with a Net Current

Some of the beach states discussed in §2.2 feedback to the hydrodynamics in such a way that circulation cells in the horizontal plane are created. In these circulation cells, there is a net shoreward current over the breaker bar and a net seaward current in the rip channels. The present section considers the part of the profile, which is subject to a net onshore current. All the simulations are initiated on a partly developed profile based on A02SB extracted at $t_m/T = 769$. At this time in the morphological development, the outer bar is still building up to reach its maximum crest height. The profile is plotted in figure 6.12A.

The net cross shore current at the inlet, $u_{c,h}$, corresponds to an average net current over the initial crest level of 0.06, 0.19 and 0.32 m/s. These velocities are considerable compared to the magnitude of the undertow of 0.6 m/s, see figure 6.11, but not unrealistic. Garnier *et al.* (2010) found current speeds over a crescentic bar of approximately 0.2 m/s for incident waves of $H = 1$ m and $T = 6$ s in a numerical model. As they used a depth integrated model, the undertow strength is not resolved in their model.

The magnitude of the shoreward velocity has been tried verified using field data, however, the strength of the seaward current in the rip channel is reported rather than the shoreward velocity over the bars. Values of 0.5–1.0 m/s are commonly experienced (e.g. Aagaard and Masselink, 1999, p. 92), and extreme values as large as 2 m/s are reported (MacMahan *et al.*, 2004). Those values can be used to give an order of magnitude approximation for

the current speed over the breaker bars. Based on the dimensions of the rip channel and breaker bar systems in Holman *et al.* (2006), it is reasonable to assume that the length of the breaker bar is 5 times the width of the rip channel, and that the rip channel is deeper than the depth over the bar, say with a factor of two. This yields a net current over the bars in the range of 0.2–0.8 m/s for the above reported current speeds in the rip channels.

Numerical Handling of Net Current

The current is included into the numerical model by simulating a drain in the surf zone. Firstly, it was tested to have the drain just shoreward of the outer bar for $x \in [55,\ 65]$ m. This did prove to cause unphysical feedback onto the morphology in terms of a local scouring. This scouring has a much shorter time scale than the time scale of the breaker bar development and migration, why the results became contaminated by the scouring. Therefore, the drain is placed shoreward of the inner bar for $x \in [19,\ 24.5]$ with the top of the drain at $y = -1.0$ m, i.e. below the trough level of the wave. The bathymetry for the morphological simulations is kept rigid for $x \in [-10, 35]$ m. This means that these simulations only reflect the morphological response of the outer bar.

Hydrodynamics with a Frozen Bed

As an intermediate step toward the fully coupled hydro- and morphodynamic development of the breaker bar as a function of $u_{c,h}$, the hydrodynamics over a frozen bed is considered. The frozen bed is described by the initial barred profile. The results are summarised into the two figures 6.10 and 6.11, where the former considers the temporal variation in $\tilde{\tau}_b/\rho_1$ in the trough and on the crest. The latter figure depicts the period averaged velocity field in the bar-trough region together with the undertow profiles in the trough and over the crest. All of these are depicted for the four values of $u_{c,h}(= \{0.000,\ 0.018,\ 0.054,\ 0.090\}$ m/s).

Firstly, the bed shear stress in the trough is considered (figure 6.10A), and it is realised that $\tilde{\tau}_b$ become more offshore directed with an increasing onshore current. For $u_{c,h} = 0.0$ m/s, $\tilde{\tau}_b$ is zero over part of a wave period, however, the bed shear stress become exclusive offshore directed for increasing values of $u_{c,h}$. This can be explained by the velocity field in the trough, which is discussed below.

The bed shear stress over the crest on the other hand becomes more and more onshore directed with an increase in $u_{c,h}$, i.e. opposite to the variation in the trough. For $u_{c,h} = 0.0$ m/s the largest absolute $\tilde{\tau}_b$ occur in the offshore direction, and this is changed to occur in the onshore direction for $u_{c,h} = 0.09$

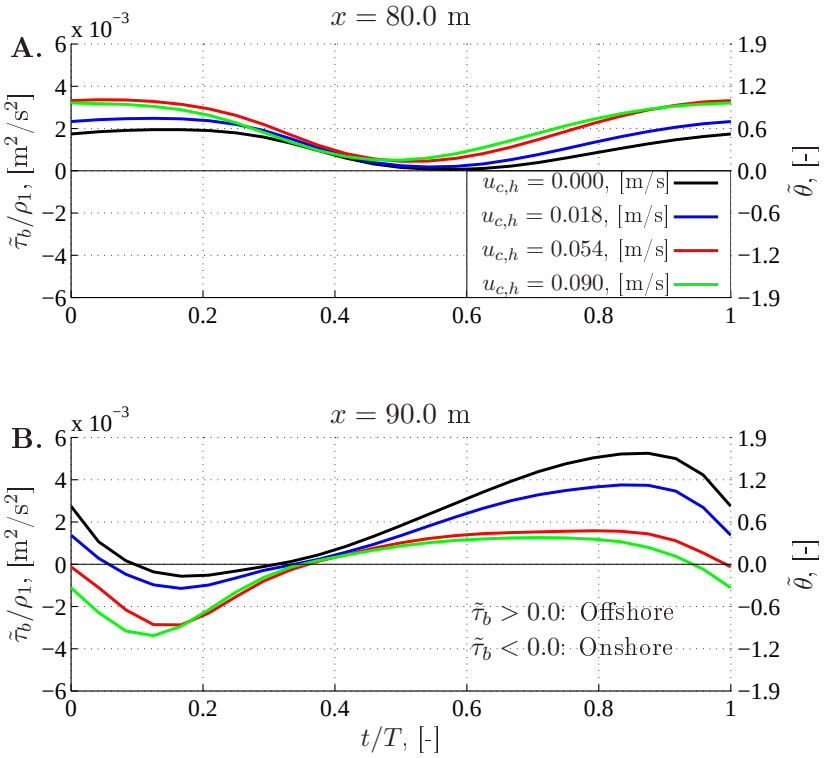

Figure 6.10: *The temporal variation of the ensemble average of the bed shear stress, $\tilde{\tau}_b/\rho_1 = \widetilde{u_f|u_f|}$, for the four different current magnitudes. Ensemble average taken over 30 periods. A: The bed shear stress in the trough at $x = 80.0$ m. B: The bed shear stress at the crest at $x = 90.0$ m.*

m/s. In the process $\max|\tilde{\tau}_b|$ is lowered form 0.0053 to 0.0034, i.e. nearly a 40% reduction. This change from offshore to onshore directed bed shear stresses is due to the decrease in the offshore directed near bed velocity. As the near bed velocity become less offshore directed, the offset in τ_b/ρ_1 from zero, which equals $\bar{\tau}_b/\rho_1$, is equally lowered.

The velocity field and undertow profiles are depicted in figure 6.11. The undertow profile over the crest (figure 6.11F) reveals that with increasing $u_{c,h}$, the net offshore flux near the bed is suppressed and replaced by a shoreward current over the entire vertical profile (outside the figure a shore-

Figure 6.11 *(facing page): A-D: The period averaged velocity field over the outer bar as a function of net shoreward current. The contour shows sign$(\bar{u})\|\bar{\mathbf{u}}\|$, where a positive value is in the offshore direction. E: Period averaged flow over y at $x = 80$ m. F: Period averaged flow over y at $x = 90$ m.*

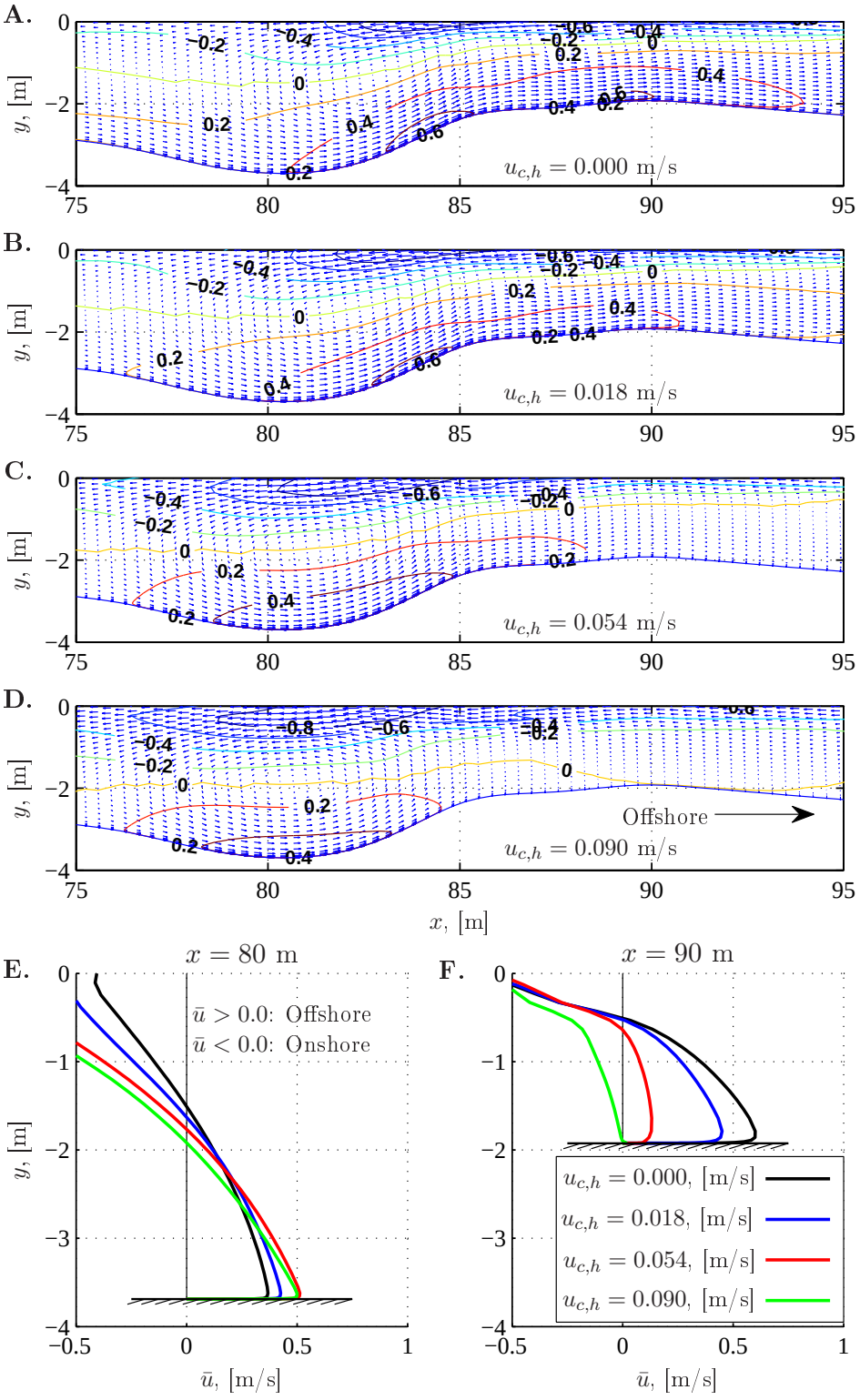
A.
B.
C.
D.
E.
F.
$u_{c,h} = 0.000$ m/s
$u_{c,h} = 0.018$ m/s
$u_{c,h} = 0.054$ m/s
$u_{c,h} = 0.090$ m/s
Offshore
y, [m]
x, [m]
$x = 80$ m
$x = 90$ m
$\bar{u} > 0.0$: Offshore
$\bar{u} < 0.0$: Onshore
$\bar{u}$, [m/s]
$u_{c,h} = 0.000$, [m/s]
$u_{c,h} = 0.018$, [m/s]
$u_{c,h} = 0.054$, [m/s]
$u_{c,h} = 0.090$, [m/s]

ward flux between the wave trough and the wave crest is dominating for all $u_{c,h}$). The transition in profile shape from $u_{c,h} = 0.00$ m/s to $u_{c,h} = 0.09$ m/s suggests that the net shoreward current is almost uniformly distributed over the depth, e.g. a logarithmic velocity profile.

The undertow in the trough given in figure 6.11E increases in magnitude with increasing $u_{c,h}$, but the offshore component occurs over a smaller vertical distance. Simultaneously, the undertow over the crest decreases and eventually vanishes, which reveals that there must be a pronounced circulation in the trough region and pronounced vertical accelerations on the shoreward side of the bar crest. This can be identified in the figures 6.11A-D. This in combination explains the increase of $\tilde{\tau}_b$ in the trough with increasing values of $u_{c,h}$.

The combination of undertow profiles, temporal variation in the bed shear stress and the period averaged velocity field suggests that the local offshore directed sediment transport over the crest will be smaller for increasing $u_{c,h}$, whereas the opposite will happen in the trough. This will result in smaller spatial gradients in the sediment transport and thus smaller bed level changes with increasing $u_{c,h}$.

Morphodynamic Development with a Live Bed

The bed is now allowed to develop around the outer bar. The result is depicted in figure 6.12. It is seen that the morphological development for a finite value of $u_{c,h}$ causes a slower migration speed relative to the one in the reference simulation ($u_{c,h} = 0.0$ m/s). In the reference solution, the bed is also frozen for $x \leq 35$ m. The migration speed is seen to decrease with an increase in $u_{c,h}$, which is expected from the analysis on a frozen bed.

The bar development under the strongest current actually shows a tendency to have an almost stationary crest location throughout the simulation, and the shoreward side of the bar merely steepens. It attains the angle of repose over a large portion of the shoreward side of the breaker bar.

The simulated average cross shore sediment transport has been estimated through a convolution of the Exner equation. This takes the form

$$q_t(x, t_0, t_m) = -(1 - e_d) \int_{x_0}^{x} \frac{h\,(t_m, x') - h\,(t_0, x')}{t_m - t_0} \mathrm{d}x' \quad , \tag{6.2}$$

where x_0 is an offshore limit, t_0 is the time for the initial profile, and t_m is the current morphological time step. It is assumed that $q_t = 0$ is zero at this offshore boundary. q_t attains a finite value at this offshore limit, however, it is several orders of magnitude smaller than that in the surf zone and therefore omitted.

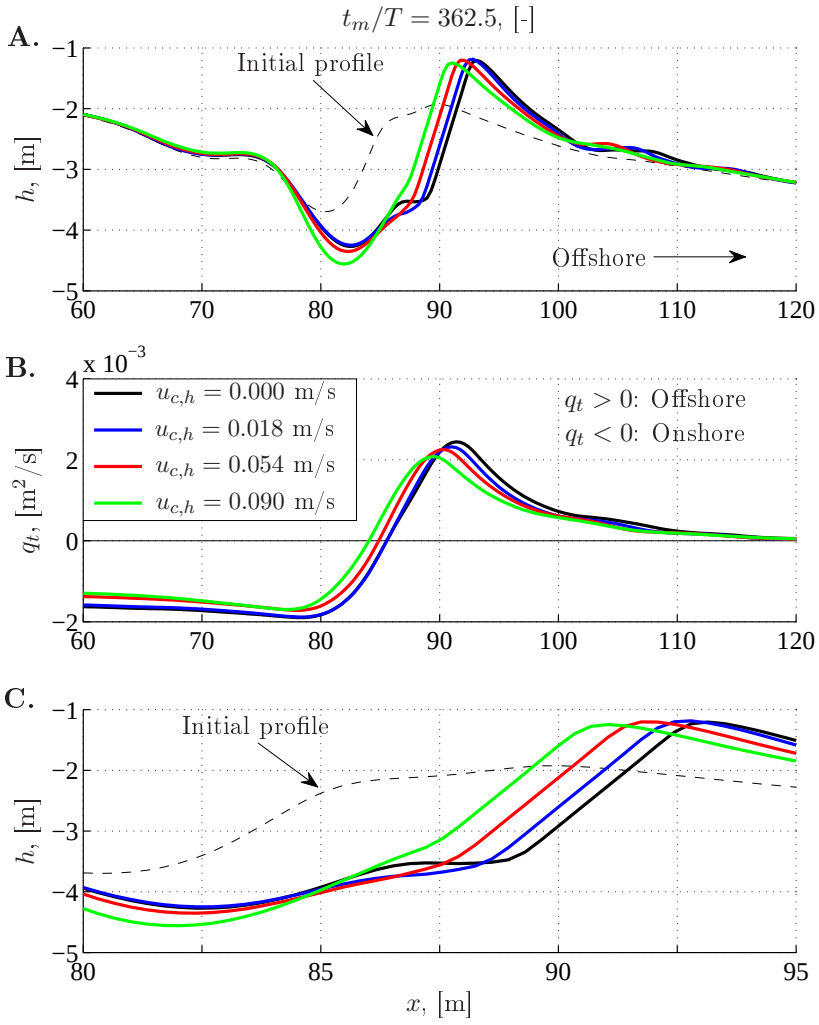

Figure 6.12: *Simulations of the morphological development as a function of the strength of the net current. A: The development of the breaker bar at* $t_m/T = 362.5$. *B: The corresponding sediment transport flux,* q_t, *computed from eq. 6.2. C: A detailed view on A.*

The cross shore variation in q_t is depicted in figure 6.12B, and it is seen that the maximum and minimum sediment fluxes decrease in their absolute value, i.e. yielding smaller spatial transport gradients with an increase in $u_{c,h}$. The shape of the transport fluxes are qualitatively similar. Note that the coincidence of $\max q_t$ and the intersection between $h(t_0)$ and $h(t_m)$ is a property of eq. 6.2.

Consider the morphological development in figure 6.12C. The profile lines exhibit a property, which can also be found in e.g. figure 6.7A. At some point

the shoreward side of the breaker bar is divided into two parts migrating with different speeds, thus the lower part flattens, whereas the upper part continue to migrate seaward persistently with a slope around the angle of repose. This is thought to be a part of the cessation of trough erosion, which is discussed previously in §6.1.

Unfortunately, none of the simulations with a net shoreward current has attained a steady crest level. Furthermore, even A02SBC3 ($u_{c,h} = 0.09$ m/s) has a slight offshore migration of the crest of the breaker bar. The combination of these two results poses some questions:

- What happens when the breaker bar attains a steady crest level? This is an interesting question, as it will result in an increased current speed over the crest, but will it be large enough to result in an onshore breaker bar migration or a stationary crest?

- The magnitude of the currents are reasonable compared to those reported from field measurement, see above. Therefore, which magnitude of the current speed is needed to cause an onshore migration under regular wave forcing?

- The use of irregular waves would cause an increase in the importance of the cross shore current, when compared to the corresponding regular wave case. At what magnitude of the current speed would a shoreward migration be identified under irregular waves?

These questions will be left unanswered here, however, the answers are important for the estimation of the longterm cross shore exchange of sediment and hence the overall erosion/accretion patterns of the complete nearshore area.

Chapter 7

Discussion

The following discussion will be divided into three parts. The first part will place the present work into a broader perspective, the second is devoted to a discussion of numerical topics, and in the third part topics of physical origin are discussed. The two last parts also contain elements regarding suggestions to future work.

7.1 Advances Relative to Previous Works

In this work, a new approach to the modelling of the complex hydro- and morphodynamic system in the surf zone is presented; an approach which can help researchers to gain more insight into the processes responsible for the cross shore sediment exchange and the resulting morphological features. The model builds on a complete intercoupling of the processes, where the near field of the breakpoint is modelled with only few prescribed assumption. This approach has not to date been described, implemented, and utilised as comprehensively as done in this work. The advances of this model approach over previous approaches are discussed below.

Expanding to Three Dimensions

In this work the model has only been applied in two dimensions, however, due to the way the model is formulated, there are only a few additional steps toward a full three dimensional model of the surf zone processes and the corresponding morphodynamic feedback. The modelling functionalities, which are not derived for three dimensions, are the sand slide routine (§3.3.1) and the morphological filtering routine (§3.3.2). The other modelling functionalities with respect to hydrodynamics, sediment transport and bed level change are given without constraints on neither the number of spatial dimensions nor the actual geometry under consideration, e.g. the model could potentially

also be used for coasts with longshore non-uniformity, scour computations, or river morphology.

The previous work, which is closest to the above proposed three dimensional modelling, is the work by Christensen (2006), however, he only considered the hydrodynamics under breaking waves in three dimensions.

Approaches Taken on the Modelling of Wave Breaking

The small step lacking toward a general three dimensional model for the description of the surf zone processes is in stark contrast to the generally applied methodology up to present. Firstly, the wave breaking was initially described through an energy conservation approach (§2.5.2). However, since the work of Rakha *et al.* (1997), the use of a Boussinesq wave formulation with an additional momentum term has been state of the art, when simulating combined hydro- and morphodynamics. This approach has essentially been left unchanged since then. More advanced models have, nevertheless, been used for the hydrodynamic description and sediment transport simulations (Lin and Liu, 1998; Bradford, 2000; Christensen, 2006; Ontowirjo and Mano, 2008).

The approach, which relies on Boussinesq waves, has the limitation that the effect of wave breaking on the hydrodynamics, in terms of the spatial distribution and temporal behaviour of the additional momentum term, is prescribed in the model (see §2.5.2). The present model, on the other hand, adapts the wave breaking, so it responds to the incident waves and the shape of the cross shore profile in an implicit manner.

The Modelling of the Mean Flow

The mean flow in the surf zone is of critical importance for the magnitude and direction of the sediment transport, which is seen in §5.2. It was also found that the undertow, and its subsequent separation, follows a characteristic pattern (§5.4). This, with the exception of Wenneker *et al.* (2011), is not included in previous models, where the undertow is instead described using a local fulfilment of a prescribed variation in the vertical shear stress distribution as a function of local wave parameters (Rakha *et al.*, 1997) or using explicit expressions (Karambas and Koutitas, 2002). These approaches omit the inertia of the undertow, whereby introducing the need of a smoothing of the sediment transport field, see e.g. the models by Dally and Dean (1984); Drønen and Deigaard (2007). This requirement for smoothing is found to be circumvented (§5) through the inclusion of the more accurate physical description in the present model, which does not rely on prescribed behavioural patterns.

The model by Wenneker *et al.* (2011) does solve the flow field in a non-local approach, however, the flow model (Delft3D) is based on a hydrostatic assumption. This assumption can hardly be expected to resolve the period averaged circulation cell, which is discussed in §§2.3.4 and 5.4. It is even less likely that the model will be able to predict the flow field described in 6.2.3, where considerable vertical accelerations are encountered.

The Modelling of Turbulent Properties

An important property for the modelling of suspended sediment transport is the magnitude and distribution of the eddy viscosity. As with the other hydrodynamic properties, the modelling of the turbulence, and thus also the eddy viscosity, relies explicitly on an empirical formulation of the production of turbulence, however, also implicitly on the prescribed wave decay, because the production of turbulence is related to the dissipation of wave energy (Rakha *et al.*, 1997). Other models simply omit the dependency of the eddy viscosity on the suspended sediment transport, and the latter is described by empirical formulae (Wenneker *et al.*, 2011).

The production, advection and dissipation of turbulent kinetic energy is an inherent part of the present model description and rely to a lesser extend on behavioural assumptions. The main assumption in this work is that the turbulence is isotropic. This is known from experiments (Nadaoka *et al.*, 1989; Scott *et al.*, 2005) not to be the case, however, numerical model tests with anisotropic turbulence models (Lin and Liu, 1998) does not show advantages over isotropic models (Bradford, 2000).

Implications on Sediment Transport

The individual components in the nearshore flow all have an effect on the sediment transport patterns in the surf zone. The modelling of the wave decay has a direct influence on the near bed (freestream) velocity, which controls the boundary layer development (Fredsøe, 1984). The effect of the eddy viscosity is easily comprehended by considering §3.2.2.

Another impact originates from the circulation cell in the cross shore direction. The vertical velocities predicted in §§5.4 and 6.2.3 are a large fraction of the sediment fall velocity, and thereby they have a direct influence on the vertical distribution of suspended sediment and the sediment transport fluxes. The vertical velocities are computed in Wenneker *et al.* (2011), but they can only be artificial, because of the hydrostatic assumption. They, however, does not solve the conservation equation for suspended sediment, but rely on empirical formulae for the suspended sediment transport flux.

As seen in the description of bed load (§3.2.1) and suspended sediment

transport (§3.2.2) both depends non-linearly on the hydrodynamic forcing, thus small errors in the hydrodynamics are enhanced when computing the sediment transport, which finally affect the morphological response. The use of the present model limits the number of assumptions in the hydrodynamic behaviour, which thereby produces a more realistic and smoother result for the sediment transport and resulting morphology.

7.2 Discussion of Topics of Numerical Nature

The Inclusion of Air in the Hydrodynamic Modelling

The simulations presented in this thesis are based on a two-phase solver, where the interplay between water and air is modelled. It was suggested by Christensen (2006) that the presence of air in the simulations would improve on the prediction of the distribution of turbulent kinetic energy. This is, however, not observed (§4.3); at least not to the adopted level of resolution in the present work, where individual bubbles are not resolved.

On the other hand, the presence of the air causes large velocities, as the wave is essentially experienced as a fast moving wall by the air, whereby inducing large velocities. These large velocities limits the time step due to the Courant criterion, and they make the computations less feasible. It was suggested by Liu and Garcia (2008) to set $\mathbf{u} = \mathbf{0}$ m/s in the air phase each time step, however, this results in a dissipation of 35% of the wave energy over a distance of merely 3 wave lengths*. The approach by Liu and Garcia (2008) was tested using the computational settings in §4.1.4. An improvement to the present model would be the development of a surface tracking method, where the air phase is removed as in Nielsen (2003). This would furthermore ease the application of boundary conditions for k, ω and c on the water surface.

The Aspect Ratio Limitations in the VOF-Implementation

The limitations in the VOF method with respect to the cell aspect ratio (§4.3) are problematic, because it makes longterm simulations infeasible. Simply discretising the computational domain with $AR = 1$ for the morphological simulations would be so computationally time consuming that the results in §6 could not have been achieved within a reasonable time. The present results are completed in computational times counted in months, where $AR = 3$ is used. Adopting $AR = 1$ would increase the simulation time by at least a

*This dissipation takes place because of the introduction of a shear force along the surface of the water due to the bounding of the velocities in the air to $\mathbf{0}$ m/s.

factor of 9[†]. This calls for other methods for solving the surface tracking as discussed in §§3.1 and 4.3.

In practical terms, the simulations in §6.2 are carried out with $AR = 3$, and this choice has caused an increase of the surf zone width of 25%.

Additionally, a practical consideration is that it could prove difficult to preserve an aspect ratio of 1.0, simply because the mesh is deforming due to the morphological response.

The Velocity Field Induced by the Mesh Movement

The tight coupling between the hydro- and morphodynamics induces a velocity field due to the movement of the bed. The magnitude of this movement comes from a period averaged evaluation of the Exner equation. The maximum velocity perpendicular to the bed is approximately 0.25 cm/s for the simulations in §6.2. From the results of the instantaneous sediment fluxes presented in §5.5, the instantaneous rate of bed level change is estimated using

$$\frac{\partial h}{\partial t} \simeq -\frac{1}{1-e_d}\frac{\partial \tilde{q}_s}{\partial x} \tag{7.1}$$

of which the maximum absolute value is 1.0–2.0 cm/s ($f_m = 1.0$). The storage term and contribution from the bed load transport is omitted for simplicity in eq. (7.1). The instantaneous rate of bed level change is thus found to be substantially larger than the period average rate of change, and it can be concluded that the induced velocities from the bed movement do not attain unphysicly large values.

7.3 Discussion of Topics of Physical Nature

The Effect of a Third Dimension

The simulations of the hydro- and morphodynamics under breaking waves are restricted to two dimensions in the present thesis. As discussed in §§4.4.3 and 5.1, the behaviour of the surface in the case of plunging breaking, and to a smaller extend for spilling breakers (§D), could be due to the lack of a third dimensions, in which the vortical structures are allowed to be stretched. The discussion is left inconclusive in this thesis, however, the validity of the assumption of two-dimensionality ought to be tested in future works.

[†]Three times the number of computational cells and a resulting necessary decrease in f_m is seen to be a factor of 9. On top of this, a small decrease in the time step will be experienced. The time step will not decrease by a factor of 3.0, as it is mostly controlled by the vertical discretisation. The use of parallel computations would affect these considerations (§3.3.3)

Another mechanism, which is omitted by assuming 2-dimensionality, is the obliquely descending eddies as already discussed in §2.3.2. Nadaoka *et al.* (1988b) find that the obliquely descending eddies can bring large amounts of sediment in suspension. In terms of nearshore sediment transport, this could (i) change the phase lags already identified in the model and (ii) change the magnitude of the suspended sediment fluxes. The obliquely descending eddies are local features, which are not affecting the entire bed each wave period, e.g. Nadaoka *et al.* (1988b) only identified the hydrodynamic fingerprint on a fixed location in 1/10 of the measured wave periods. Therefore, to attribute an equivalent amount to the sediment transport as e.g. undertow combined with excess turbulence due to wave breaking, the importance of the obliquely descending eddies should be an order of magnitude larger than the more permanent processes.

This order of magnitude increase in volumetric concentrations are not supported by the measurements by Nadaoka *et al.* (1988b), and it is therefore reasonable to exclude this effect in the present study.

The Scaling of the Cross Shore Processes

The discussion of the scaling of the integrated cross shore sediment flux, $\bar{Q}_s$, in §5.2, and the attempt of comparing between laboratory scale experiments and prototype scale simulations are left inconclusive. The numerical model is nevertheless a powerful tool in further pursuing some definite answers.

First, the model needs to be further tested against experimental results, which is not part of the present work simply due to time constraints. Having validated the numerical approach, it is suggested that a more comprehensive parametric study than that in §5 is undertaken, which as a minimum investigate the parameters H_B, T, $\tan\beta$, w_s, and the shape of the cross shore profile. This would yield a set of integrated cross shore sediment fluxes, which can be analysed as a function of ζ_0, Ω and Ω_{HK}. The values for these parameters should be chosen intelligently, such that 2–3 of the combinations yield the same value of the dependent variable. If $\bar{Q}_s$, in non-dimensional form, then takes the same value, it would strengthen the conclusion on the appropriate form of the dependent variable.

The focus in §5 was on the dependency of ζ_0, however, in hindsight it is less likely that this is the appropriate scaling parameter for $\bar{Q}_s$, because it does not take the sediment properties into consideration. ζ_0 could nevertheless be important for the hydrodynamic response, which only to a small extend depends on the grain diameter through the value of the roughness height (assuming flat bed). The dependency between ζ_0 and λ_{Bs} in figure 5.8, where the latter is related to sediment transport, is explained by the fact that the peak in $\bar{q}_s$ is coinciding with the peak in the undertow velocity, $\bar{u}_r$,

which is a purely hydrodynamic property. This is identified by comparing the figures 5.6 and 5.11. This means that figure 5.8 also describe the spatial lag between wave breaking and the maximum in the depth integrated undertow velocity.

The Effect of Irregular Waves

This thesis has focused mostly on regular wave forcing, because previous modelling attempts, where such wave forcing is used, have shown that smoothing is needed in the rate of bed level change (§2.5.2). It was already noted by Roelvink and Brøker (1993) that using irregular waves would "remove" this problem because of the cross shore smearing of the surf zone processes. This approach, however, is merely a resort to circumvent a known problem.

It is proved in this work that the high level of complexity in the present model removes the requirement of smoothing of the cross shore sediment distribution, before it is used for morphological updating. This means that the issue must originate from an incomplete model formulation of the hydrodynamics, which is already discussed in §7.1.

The sediment transport pattern under irregular waves are of considerable importance for engineering purposes. Some of the unanswered questions are:

- The scaling analysis proposed above should initially concentrate on regular waves, however, irregular waves would cause a change in the cross shore sediment flux. It is hypothesised that for large Ω, e.g. larger than 10.0, the effect of irregular waves would result in a decrease of the offshore directed cross shore flux (Rakha *et al.*, 1997). On the other hand, the experiments by Baldock *et al.* (2011) show that for Ω in the intermediate range ($\Omega \simeq 1.0 - 6.0$), the opposite behaviour is seen, namely increasing sediment fluxes with the introduction of irregular waves. Therefore, what is the effect of irregular waves on the integrated cross shore sediment flux? How does this behaviour relate to the behaviour under regular wave forcing?

- Is it possible to find a consistent regularisation of the irregular waves based on statistical properties of the wave spectrum? For instance similar to that done for the suspended sediment transport flux in combined wave-current boundary layers (Zyserman and Fredsøe, 1988)?

- Is there a difference in the steady level of the breaker bar crest due to irregular waves, when it is compared to a regular wave reference case? Or is the time scale in the development merely different? (Assuming that it is known, how the corresponding reference solution under regular wave forcing is to be defined).

- What is the effect of the irregular waves on the migration speed? This is partly answered in §6.1, though not for a breaker bar, which has attained a steady crest level.
- Of the many unanswered questions with respect to a net shoreward current (§6.2.3), the knowledge of which current speed causes a change in direction of the bar migration is of practical importance, because this would aid in the evaluation of longterm beach response and in the description of the fate of nourished sand on or close to breaker bars.

Chapter 8

Conclusion

A complex model used to study the hydro- and morphodynamics in the surf zone is presented in this thesis. It is shown that it is possible to apply OpenFoam as a tool for the modelling of wave breaking under some constraints on the cell aspect ratio (§4.3).

The emphasis in this thesis has been on the surf zone processes, and it is shown that the increased complexity in the model formulation allows for the simulation of a smooth distribution of the sediment transport fluxes across the breakpoint (§5.2). This has not been achieved in the previous model approaches using regular waves (§7.1).

The simulations, where the morphological response is turned off, reveal several spatial and temporal lag-effects in the surf zone. A valuable result is the variation in the non-dimensional spatial lag between the breakpoint and the maximum undertow strength with the surf similarity parameter. A range for the former quantity of $[0.25,\ 1.25]$ is suggested (§5.2), and it can be used as input in less sophisticated modelling tools, which rely on empirical relations.

In the simulations with a full coupling (§6), it is seen that by using a modelling framework with this level of complexity, it is possible:

- To model the morphological development of breaker bars due to the breaking of regular waves without any smoothing of the processes (except on the level of Nyquist frequencies due to a numerical instability of the Exner equation, §3.3.2).

- It has been shown that the development of a breaker bar is due to an erosional process in the trough. The development in the breaker bar slows down as the erosion in the trough ceases, which happens, when the trough becomes too wide and too deep to allow for any further erosion.

- To predict a steady crest of level of the breaker bar both for the inner and the outer ones (§§6.1 and 6.2).
- To model a quasi-steady solution to the breaker bar, which is found in §6.1, where the migration speed of the outer bar becomes small.

Furthermore, it is described how an onshore directed current, which mimics the presence of a horizontal circulation system, affect the hydro- and morphodynamics of a breaker bar. A pronounced circulation is found in the trough, because the period averaged flow over crest becomes shoreward directed, which inhibits the offshore directed flow in the trough to escape seaward. It is found that the offshore migration speed decreases with increasing current strength of the breaker bar. This result can also be derived qualitatively from the presented analysis of the hydrodynamics over a frozen and barred cross shore profile.

These accomplishments are attributed to the fact that the near field description of the hydrodynamics in the surf zone includes a high level of complexity. Especially around the breakpoint, which is the natural transition point for two different prevailing transport mechanisms and their corresponding transport directions.

Bibliography

Aagaard, T. and Masselink, G. (1999). *The Surf Zone*, chapter 4, 72–118. Wiley, 1st edition. From *Handbook of Beach and Shoreface Morphodynamics*. Editor: A.D. Short.

Aagaard, T., Davidson-Arnott, R., Greenwood, B., and Nielsen, J. (2004). Sediment supply from shoreface to dunes: linking sediment transport measurements and long-term morphological evolution. *Geomorphology*, **60**(1-2), 205–224.

Andersen, K. H. and Fredsøe, J. (1999). How to Calculate the Geometry of Vortex Ripples. *Proceeding to Coastal Sediments*, **I**, 78–93.

Bailard, J. A. (1981). An Energetics Total Load Sediment Transport Model for a Plane Sloping Beach. *Journal of Geophysical Research - Oceans and Atmospheres*, **86**(NC11), 938–954.

Baldock, T., Alsina, J., Caceres, I., Vicinanza, D., Contestabile, P., Power, H., and Sanchez-Arcilla, A. (2011). Large-scale experiments on beach profile evolution and surf and swash zone sediment transport induced by long waves, wave groups and random waves. *Coastal Engineering*, **58**(2), 214–227.

Baldock, T. E., Manoonvoravong, P., and Pham, K. S. (2010). Sediment transport and beach morphodynamics induced by free long waves, bound long waves and wave groups. *Coastal Engineering*, **57**(10), 898–916.

Barnet, M. R. and Wang, H. (1988). Effects of a Vertical Seawall on Profile Response. *Proceeding to Coastal Engineering Conference*, **II**, 1493–1507.

Battjes, J. A. (1988). Surf-Zone Dynamics. *Annual Review of Fluid Mechanics*, **20**, 257–293.

Battjes, J. A. and Stive, M. J. F. (1985). Calibration and Verification of a Dissipation Model for Random Breaking Waves. *Journal of Geophysical Research - Oceans*, **90**(NC5), 9159–9167.

BBC (2009). South pacific. DVD Movie. Episode: Ocean of Islands.

Berberović, E., Van Hinsberg, N. P., Jakirlić, S., Roisman, I. V., and Tropea, C. (2009). Drop impact onto a liquid layer of finite thickness: Dynamics of the cavity evolution. *Physical Review E - Statistical, Nonlinear, and Soft Matter Physics*, **79**(3), Art.no: 036306.

Birkemeier, W. A. (1984). Time Scales of Nearshore Profile Changes. *Proceeding to Coastal Engineering Conference*, **II**, 1507–1521.

Booij, N., Ris, R. C., and Holthuijsen, L. H. (1999). A third-generation wave model for coastal regions - 1. Model description and validation. *Journal of Geophysical Research-Oceans*, **104**(C4), 7649–7666.

Bowen, A. J. (1969). Generation of Longshore Currents on a Plane Beach. *Journal of Marine Research*, **27**(2), 206–215.

Bowen, A. J. (1997). Patterns in the water: Patterns in the sand? *Coastal Dynamics - Proceedings of the International Conference*, **I**, 1–10.

Bradford, S. F. (2000). Numerical simulation of surf zone dynamics. *Journal of Waterway, Port, Coastal, and Ocean Engineering – ASCE*, **126**(1), 1–13.

Bruun, P. (1962). Sea-level rise as cause of shore erosion. *ASCE – Proceedings – Journal of the Waterways and Harbors Division*, **88**, 117–130.

Callaghan, D. P., Saint-Cast, F., Nielsen, P., and Baldock, T. E. (2006). Numerical solutions of the sediment conservation law; a review and improved formulation for coastal morphological modelling. *Coastal Engineering*, **53**(7), 557–571.

Chapalain, G., Cointe, R., and Temperville, A. (1992). Observed and Modeled Resonantly Interacting Progressive Water-Waves. *Coastal Engineering*, **16**(3), 267–300.

Christensen, E. D. (2006). Large eddy simulation of spilling and plunging breakers. *Coastal Engineering*, **53**(5-6), 463–485.

Christensen, E. D. and Deigaard, R. (2001). Large Eddy Simulation of Breaking Waves. *Coastal Engineering*, **42**(1), 53–86.

Christensen, E. D., Jensen, J. H., and Mayer, S. (2000). Sediment Transport under Breaking Waves. *Proceeding to Coastal Engineering Conference*, **III**, 2467–2480.

Christensen, E. D., Walstra, D. J., and Emerat, N. (2002). Vertical variation of the flow across the surf zone. *Coastal Engineering*, **45**(3-4), 169–198.

Clarke, D. J. and Eliot, I. G. (1988). Low-frequency changes of sediment volume on the beachface at Warilla Beach, New South Wales, 1975-1985. *Marine Geology*, **79**(3-4), 189–211.

Clément, A. (1996). Coupling of two absorbing boundary conditions for 2D time-domain simulations of free surface gravity waves. *Journal of Computational Physics*, **126**(1), 139–151.

Coco, G. and Murray, A. B. (2007). Patterns in the sand: From forcing templates to self-organization. *Geomorphology*, **91**(3-4, Sp. Iss. SI), 271–290.

Cowell, P. J., Hanslow, D. J., and Meleo, J. F. (1999). *The Shoreface*, chapter 3, 39–71. Wiley, 1st edition. From *Handbook of Beach and Shoreface Morphodynamics*. Editor: A.D. Short.

Cox, D. T. (1995). *Experimental and Numerical Modeling of Surf Zone Hydrodynamics*. Ph.D. thesis, University of Delaware.

Cox, D. T., Kobayashi, N., and Okayasu, A. (1996). Bottom shear stress in the surf zone. *Journal of Geophysical Research - Oceans*, **101**(C6), 14337–14348.

Dally, W. R. (1987). Longshore bar formation - surf beat or undertow? *Coastal Sediments '87, Proceedings of a Specialty Conference on Advances in Understanding of Coastal Sediment Processes.*, **1**, 71–86.

Dally, W. R. and Dean, R. G. (1984). Suspended Sediment Transport and Beach Profile Evolution. *Journal of Waterway, Port, Coastal, and Ocean Engineering – ASCE*, **110**(1), 15–33.

Dalrymple, R. A., MacMahan, J. H., Reniers, A. J. H. M., and Nelko, V. (2011). Rip currents. *Annual Review of Fluid Mechanics*, **43**, 551–581.

de Vriend, H. J., Capobianco, M., Chesher, T., de Swart, H. E., Latteux, B., and Stive, M. J. F. (1993). Approaches to Long-Term Modeling of Coastal Morphology - A Review. *Coastal Engineering*, **21**(1-3), 225–269.

Dean, R. G. (1973). Heuristic Models of Sand Transport in the Surf Zone. *Proceeding of the First Australian Coastal Engineering Conference*, 208–214.

Dean, R. G. and Dalrymple, R. A. (1991). *Water Wave Mechanics for Engineers and Scientists*, volume 2 of *Advanced Series on Ocean Engineering*. World Scientific, 1st edition.

Deardorff, J. W. (1970). A numerical study of three-dimensional turbulent channel flow at large reynolds numbers. *Journal of Fluid Mechanics*, **41**, 453–480.

Deigaard, R. (1989). Mathematical Modelling of Waves in the Surf Zone. *Prog. Rep.*, **69**, 47–60. ISVA, Tech. Uni. of Denmark.

Deigaard, R. (1993). A Note on the 3-Dimensional Shear-Stress Distribution in a Surf Zone. *Coastal Engineering*, **20**(1-2), 157–171.

Deigaard, R. and Fredsøe, J. (1989). Shear-Stress Distribution in Dissipative Water-Waves. *Coastal Engineering*, **13**(4), 357–378.

Deigaard, R., Fredsøe, J., and Hedegaard, I. B. (1986). Suspended Sediment in the Surf Zone. *Journal of Waterway, Port, Coastal, and Ocean Engineering – ASCE*, **112**(1), 115–128.

Deigaard, R., Mikkelsen, M. B., and Fredsøe, J. (1991a). Measurements of the bed shear stress in a surf zone. *Prog. Rep.*, **73**, 21–30. ISVA, Tech. Uni. of Denmark.

Deigaard, R., Justesen, P., and Fredsøe, J. (1991b). Modeling of Undertow by a One-Equation Turbulence Model. *Coastal Engineering*, **15**(5-6), 431–458.

Deigaard, R., Drønen, N., Fredsøe, J., Jensen, J. H., and Jørgensen, M. P. (1999a). A morphological stability analysis for a long straight barred coast. *Coastal Engineering*, **36**(3), 171–195.

Deigaard, R., Jakobsen, J., and Fredsoe, J. (1999b). Net sediment transport under wave groups and bound long waves. *Journal of Geophysical Research - Oceans*, **104**(C6), 13559–13575.

Dingemans, M. W., Radder, A. C., and de Vriend, H. J. (1987). Computation of the Driving Forces of Wave-Induced Currents. *Coastal Engineering*, **11**(5-6), 539–563.

Drønen, N. and Deigaard, R. (2007). Quasi-three-dimensional modelling of the morphology of longshore bars. *Coastal Engineering*, **54**(3), 197–215.

Dyhr-Nielsen, M. and Sørensen, T. (1970). Some Sand Transport Phenomena on Coeasts with Bars. *Proceeding to Coastal Engineering Conference*, **II**, 855–865.

Eagleson, P. S., Glenne, B., and Dracup, J. A. (1963). Equilibrium Characteristics of Sand Beaches. *Journal of the Hydraulics Division – ASCE*, **89**, 35–55.

Einstein, H. A. (1950). Bed-load function for sediment transportation in open channel flows. *United States Department of Agriculture – Technical Bulletin*, (Bul 1027).

Elgar, S., Herbers, T. H. C., and Guza, R. T. (1994). Reflection of Ocean Surface Gravity-Waves from a Natural Beach. *Journal of Physical Oceanography*, **24**(7), 1503–1511.

Engelund, F. and Fredsøe, J. (1976). Sediment Transport Model for Straight Alluvial Channels. *Nordic Hydrology*, **7**(5), 293–306.

Engsig-Karup, A. (2006). *Unstructured Nodal DG-FEM Solution of High-Order Boussinesq-Type Equations*. Ph.D. thesis, Technical University of Denmark.

Engsig-Karup, A. P., Hesthaven, J. S., Bingham, H. B., and Madsen, P. A. (2006). Nodal DG-FEM solution of high-order Boussinesq-type equations. *Journal of Engineering Mathematics*, **56**(3), 351–370.

Engsig-Karup, A. P., Bingham, H. B., and Lindberg, O. (2009). An efficient flexible-order model for 3D nonlinear water waves. *Journal of Computational Physics*, **228**(6), 2100–2118.

Fenton, J. D. (1990). *Nonlinear Wave Theories*, chapter 1, 3–25. Wiley. From *The Sea. Ideas and Observations on Progress in the Study of the Seas. Part A*. Editors: B. Le Méhauté and D. M. Hanes.

Fernandez Luque, R. (1974). *Erosion and Transport of Bed Sediment*. Ph.D. thesis, Krips Repro B.V. - Meppel, The Nederlands.

Ferziger, J. H. and Peric, M. (2002). *Computational Methods for Fluid Dynamics*. Springer, 3rd edition.

Fredsøe, J. (1984). Turbulent Boundary-Layer in Wave-Current Motion. *Journal of Hydraulic Engineering – ASCE*, **110**(8), 1103–1120.

Fredsøe, J. and Deigaard, R. (1992). *Mechanics of Coastal Sediment Transport*, volume 3 of *Advanced Series on Ocean Engineering*. World Scientific, 1st edition.

Fredsøe, J. and Justesen, P. (1986). Turbulent Separation around Cylinders in Waves. *Journal of Waterway, Port, Coastal, and Ocean Engineering – ASCE*, **112**(2), 217–233.

Fredsøe, J., Sumer, B. M., Kozakiewicz, A., Chua, L. H. C., and Deigaard, R. (2003). Effect of externally generated turbulence on wave boundary layer. *Coastal Engineering*, **49**(3), 155–183.

Fuhrman, D. R., Madsen, P. A., and Bingham, H. B. (2006). Numerical simulation of lowest-order short-crested wave instabilities. *Journal of Fluid Mechanics*, **563**, 415–441.

Fuhrman, D. R., Fredsøe, J., and Sumer, B. M. (2009). Bed slope effects on turbulent wave boundary layers: 2. Comparison with skewness, asymmetry, and other effects. *Journal of Geophysical Research - Oceans*, **114**, Art.no. C03025.

Fuhrman, D. R., Dixen, M., and Jacobsen, N. G. (2010). Physically-consistent wall boundary conditions for the $k-\omega$ turbulence model. *Journal of Hydraulic Research*, **48**(6), 793–800.

Garnier, R., Dodd, N., Falqués, A., and Calvete, D. (2010). Mechanisms controlling crescentic bar amplitude. *Journal of Geophysical Research - Earth Surface*, **115**, Art.no. F02007.

Gislason, K., Fredsøe, J., Deigaard, R., and Sumer, B. M. (2009). Flow under standing waves Part 1. Shear stress distribution, energy flux and steady streaming. *Coastal Engineering*, **56**(3), 341–362.

Gourlay, M. R. (1968). Beach and dune erosion tests. Technical Report No. M935/M936, Delft Hydraulics Laboratory.

Greenwood, B. and Davidson-Arnott, R. G. D. (1975). *Marine Bars and Nearshore Sedimentary Processes, Kouchibouguac Bay, New Brunswick*, chapter 6, 123–150. Wiley, 1st edition. From *Nearshore Sediment Dynamics and Sedimentation - An Interdisciplinary Review*. Editors: Hails, J. and Carr, A.

Hansen, H. F., Deigaard, R., and Drønen, N. (2004). A Numerical Hybrid Model for the Morphology of a Barred Coast with a River Mouth. *Proceeding to Coastal Engineering Conference*, **III**, 2607–2619.

Hansen, N. M. (2009). *Experimental Investigation of Bed Shear Stress on a Sloping Bed under Waves*. Master's thesis, Technical University of Denmark, Department of Mechanical Engineering.

Harvie, D. J. E. and Fletcher, D. F. (2000). A new volume of fluid advection algorithm: The Stream scheme. *Journal of Computational Physics*, **162**(1), 1–32.

Harvie, D. J. E. and Fletcher, D. F. (2001). A new volume of fluid advection algorithm: the defined donating region scheme. *International Journal for Numerical Methods in Fluids*, **35**(2), 151–172.

Hattori, M. and Kawamata, R. (1980). Onshore-Offshore Transport and Beach Profile Change. *Proceeding to Coastal Engineering Conference*, **II**, 1175–1193.

Hieu, P. D., Katsutoshi, T., and Ca, V. T. (2004). Numerical simulation of breaking waves using a two-phase flow model. *Applied Mathematical Modelling*, **28**(11), 983–1005.

Hirt, C. W. and Nichols, B. D. (1981). Volume of Fluid (VOF) Method for the Dynamics of Free Boundaries. *Journal of Computational Physics*, **39**(1), 201–225.

Hjelmfelt, A. T. and Lenau, C. W. (1970). Nonequilibrium Transport of Suspended Sediment. *Journal of the Hydraulics Division – ASCE*, **96**, 1567–1586.

Holman, R. A., Symonds, G., Thornton, E. B., and Ranasinghe, R. (2006). Rip spacing and persistence on an embayed beach. *Journal of Geophysical Research - Oceans*, **111**(C1), Art.no. C01006.

Huang, Z.-C., Hwung, H.-H., Hsiao, S.-C., and Chang, K.-A. (2010). Laboratory observation of boundary layer flow under spilling breakers in surf zone using particle image velocimetry. *Coastal Engineering*, **57**(3), 343–357.

Hughes, M. and Turner, I. (1999). *The Beachface*, chapter 5, 119–144. Wiley, 1st edition. From *Handbook of Beach and Shoreface Morphodynamics*. Editor: A.D. Short.

Issa, R. I. (1986). Solution of the Implicitly Discretized Fluid-Flow Equations by Operator-Splitting. *Journal of Computational Physics*, **62**(1), 40–65.

Iversen, H. W. (1952). *Laboratory Study of Breakers. Gravity Waves*, 9–32. U.S. Gov. Printing Off., Wash., D.C. Nat. Bur. Standards, Circ. 521.

Jacobsen, N. G. and Fredsøe, J. (2011). A Full Hydrodynamic Modelling of 2D Breaker Bar Development. *Proceeding to Coastal Sediments*.

Jacobsen, N. G., Fuhrman, D. R., and Fredsøe, J. (In print). A Wave Generation Toolbox for the Open-Source CFD Library: OpenFoam®. *International Journal for Numerical Methods in Fluids*.

Jasak, H. (1996). *Error Analysis and Estimation for the Finite Volume Method with Applications to Fluid Flows*. Ph.D. thesis, Imperical College of Science, Technology and Medicine.

Jasak, H. and Tuković, Ž. (2006). Automatic Mesh Motion for the Unstructured Finite Volume Method. *Transactions of FAMENA*, **30**(2), 1–20.

Jensen, B. L., Sumer, B. M., and Fredsøe, J. (1989). Turbulent Oscillatory Boundary-Layers at High Reynolds-Numbers. *Journal of Fluid Mechanics*, **206**, 265–297.

Jensen, J. H., Madsen, E. O., and Fredsøe, J. (1999). Oblique flow over dredged channels. II: Sediment transport and morphology. *Journal of Hydraulic Engineering – ASCE*, **125**(11), 1190–1198.

Jiang, G. S., Levy, D., Lin, C. T., Osher, S., and Tadmor, E. (1998). High-resolution nonoscillatory central schemes with nonstaggered grids for hyperbolic conservation laws. *SIAM Journal on Numerical Analysis*, **35**(6), 2147–2168.

Johnson, H. K. and Zyserman, J. A. (2002). Controlling spatial oscillations in bed level update schemes. *Coastal Engineering*, **46**(2), 109–126.

Justesen, P., Fredsøe, J., and Deigaard, R. (1986). The Bottleneck Problem for Turbulence in Relation to Suspended Sediment in the Surf Zone. *Proceeding to Coastal Engineering Conference*, **II**, 1225–1239.

Karambas, T. V. and Koutitas, C. (2002). Surf and swash zone morphology evolution induced by nonlinear waves. *Journal of Waterway, Port, Coastal, and Ocean Engineering – ASCE*, **128**(3), 102–113.

Kimmoun, O. and Branger, H. (2007). A particle image velocimetry investigation on laboratory surf-zone breaking waves over a sloping beach. *Journal of Fluid Mechanics*, **588**, 353–397.

Komar, P. D. (1998). *Beach Processes and Sedimentation*. Prentice Hall, 2nd edition.

Kovacs, A. and Parker, G. (1994). A New Vectorial Bedload Formulation and Its Application to the Time Evolution of Straight River Channels. *Journal of Fluid Mechanics*, **267**, 153–183.

Lamb, H. (1945). *Hydrodynamics*. Dover Publications, 6th edition.

Lemos, C. M. (1992). *Wave Breaking - A Numerical Study*. Springer-Verlag, 1st edition.

Lesser, G. R., Roelvink, J. A., van Kester, J. A. T. M., and Stelling, G. S. (2004). Development and validation of a three-dimensional morphological model. *Coastal Engineering*, **51**(8-9), 883–915.

Leveque, R. J. (2007). *Finite Volume Methods for Hyperbolic Problems*. Cambridge Texts in Applied Mathematics, 1st edition. 5th reprint.

Lin, P. Z. and Liu, P. L. F. (1998). A numerical study of breaking waves in the surf zone. *Journal of Fluid Mechanics*, **359**, 239–264.

Lippmann, T. C. and Holman, R. A. (1990). The spatial and temporal variability of sand bar morphology. *Journal of Geophysical Research*, **95**(C7), 11575–11590.

Liu, X. and Garcia, M. H. (2008). Three-dimensional numerical model with free water surface and mesh deformation for local sediment scour. *Journal of Waterway, Port, Coastal, and Ocean Engineering – ASCE*, **134**(4), 203–217.

Liu, X. D., Osher, S., and Chan, T. (1994). Weighted Essentially Nonoscillatory Schemes. *Journal of Computational Physics*, **115**(1), 200–212.

Liu, Y. M. and Yue, D. K. P. (1998). On generalized Bragg scattering of surface waves by bottom ripples. *Journal of Fluid Mechanics*, **356**, 297–326.

Long, W., Kirby, J. T., and Shao, Z. (2008). A numerical scheme for morphological bed level calculations. *Coastal Engineering*, **55**(2), 167–180.

Longuet-Higgins, M. S. (1953). Mass Transport in Water Waves. *Philosophical Transactions of the Royal Society of London Series A-Mathematical and Physical Sciences*, **245**(903), 535–581.

Longuet-Higgins, M. S. (1970a). Longshore currents generated by obliquely incident sea waves I. *Journal of Geophysical Research*, **75**(33), 6778–6789.

Longuet-Higgins, M. S. (1970b). Longshore currents generated by obliquely incident sea waves II. *Journal of Geophysical Research*, **75**(33), 6790–6801.

Longuet-Higgins, M. S. and Stewart, R. W. (1964). Radiation Stresses in Water Waves - A Physical Discussion, with Applications. *Deep-Sea Research*, **11**(4), 529–562.

Luth, H. R., Klopman, B., and Kitou, N. (1994). Project 13G: Kinematics of Waves Breaking Partially on an Offshore Bar: LDV Measurements for Waves with and without a net Onshore Current. Technical Report H1573, Delft Hydraulics.

MacMahan, J. H., Reniers, A. J. H. M., Thornton, E. B., and Stanton, T. P. (2004). Infragravity rip current pulsations. *Journal of Geophysical Research - Oceans*, **109**(C1), Art. no. C01033.

Madsen, P. A. and Schäffer, H. A. (1998). Higher-order Boussinesq-type equations for surface gravity waves: derivation and analysis. *Philosophical Transactions of the Royal Society of London Series A-Mathematical, Physical and Engineering Sciences*, **356**(1749), 3123–3184.

Madsen, P. A. and Sørensen, O. R. (1993). Bound waves and triad interactions in shallow water. *Ocean Engineering*, **20**(4), 359–388.

Marieu, V. (2007). *Modélisation de la dynamique des rides sédimentaires générées par les vagues*. Ph.D. thesis, EPOC, Bordeaux 1 University, Talence, France.

Marieu, V. (2009). Personal correspondance.

Marieu, V., Bonneton, P., Foster, D. L., and Ardhuin, F. (2008). Modeling of vortex ripple morphodynamics. *Journal of Geophysical Research - Oceans*, **113**(C9), Art.no. C09007.

Mason, C., Sallenger, A. H., Holman, R. A., and Birkemeier, W. A. (1984). DUCK82 - A Coastal Storm Processes Experiment. *Proceeding to Coastal Engineering Conference*, **II**, 1913–1928.

Masselink, G. and Black, K. P. (1995). Magnitude and Cross-Shore Distribution of Bed Return-Flow Measured on Natural Beaches. *Coastal Engineering*, **25**(3-4), 165–190.

Masselink, G. and Turner, I. (1999). *The Effect of Tides on Beach Morphodynamics*, chapter 8, 204–229. Wiley, 1st edition. From *Handbook of Beach and Shoreface Morphodynamics*. Editor: A.D. Short.

Masselink, G., Russell, P., Coco, G., and Huntley, D. (2004). Test of edge wave forcing during formation of rhythmic beach morphology. *Journal of Geophysical Research - Oceans*, **109**(C6), Art.no. C06003.

Mayer, S. and Madsen, P. A. (2000). Simulation of Breaking Waves in the Surf Zone using a Navier-Stokes Solver. *Proceeding to Coastal Engineering Conference*, **I**, 928–941.

Mayer, S., Garapon, A., and Sørensen, L. S. (1998). A fractional step method for unsteady free-surface flow with applications to non-linear wave dynamics. *International Journal for Numerical Methods in Fluids*, **28**(2), 293–315.

McNair Jr., E. C. and Sorensen, R. M. (1970). Characteristics of Waves Broken by a Longshore Bar. *Proceeding to Coastal Engineering Conference*, **I**, 415–434.

Mei, C. C. (1999). *The Applied Dynamics of Ocean Surface Waves*, volume 1 of *Advanced Series on Ocean Engineering*. World Scientific, 1st, 3rd reprint edition.

Menter, F. and Esch, T. (2001). Elements of industrial heat transfer predictions. In *16th Brazilian Congress of Mechanical Engineering*.

Miller, R. L. (1976). *Role of Vortices in Surf Zone Prediction: Sedimentation and Wave Forces*, 92–114. Soc. of Economic Paleontologists and Mineralogists, Spec. Publ. No. 24, 1st edition. In: R.A. Davis and R.L. Ethington (Editors), Beach and Nearshore Sedimentation.

Morgan, G. C. J., Zang, J., Greaves, D., Heath, A., Whtilow, C. D., and Young, J. R. (2010). Using the rasInterFoam CFD Model for Wave Transformation and Coastal Modeling. *Proceeding to Coastal Engineering Conference*, page . https://journals.tdl.org/ICCE/.

Nadaoka, K. and Kondoh, T. (1982). Laboratory measurements of velocity field structure in the surf zone by ldv. *Coastal Engineering in Japan*, **25**, 125–145.

Nadaoka, K., Ueno, S., and Igarashi, T. (1988a). Field observation of three-dimensional large-scale eddies and sediment suspension in the surf-zone. *Coastal Engineering in Japan*, **31**(2), 277–287.

Nadaoka, K., Ueno, S., and Igarashi, T. (1988b). Sediment Suspension due to Large Scale Eddies in the Surf Zone. *Proceeding to Coastal Engineering Conference*, **II**, 1646–1660.

Nadaoka, K., Hino, M., and Koyano, Y. (1989). Structure of the turbulent flow field under breaking waves in the surf zone. *Journal of Fluid Mechanics*, **204**, 359–387.

Nezu, I. and Nakagawa, H. (1993). *Turbulence in Open-Channel Flows*. A. A. Balkema, 1st edition.

Nichols, R. H. and Nelson, C. C. (2004). Wall function boundary conditions including heat transfer and compressibility. *AIAA Journal*, **42**(6), 1107–1114.

Nielsen, K. B. (2003). *Numerical Prediction of Green Water Loads on Ships*. Ph.D. thesis, Technical University of Denmark, Dep. of Mechanical Engineering. (www.skk.mek.dtu.dk/Publikationer/PHD-rapporter.aspx).

Nielsen, P. (2009). *Coastal and Estuarine Processes*, volume 29 of *Advanced Series on Ocean Engineering*. World Scientific, 1st edition.

Niemann, S. L., Fredsøe, J., and Jacobsen, N. G. (2011). Sand Dunes in Steady Flow at Low Froude Numbers: Dune Height Evolution and Flow Resistance. *Journal of Hydraulic Engineering – ASCE*, **137**(1), 5–14.

Ohyama, T. and Nadaoka, K. (1991). Development of a Numerical Wave Tank for Analysis of Nonlinear and Irregular Wave Field. *Fluid Dynamics Research*, **8**(5-6), 231–251.

Ontowirjo, B. and Mano, A. (2008). A Turbulent and Suspended Sediment Transport Model for Plunging Breakers. *Coastal Engineering Journal*, **50**(3), 349–367.

Ontowirjo, B. and Mano, A. (2009). Examination of Unified Sediment Transport and Cross Shore Morphology Model. In Zhang, C.K. and Tang, H.W., editor, *Advances in Water Resources and Hydraulic Engineering, Vols 1-6*, 1272–1276. Int. Association of Hydraulic Engineering & Research, Tsinghua University Press.

Patel, V. C. and Yoon, J. Y. (1995). Application of Turbulence Models to Separated Flow over Rough Surfaces. *Journal of Fluids Engineering - Transactions of the ASME*, **117**(2), 234–241.

Pedersen, C., Deigaard, R., Fredsøe, J., and Hansen, E. A. (1995). Simulation of Sand in Plunging Breakers. *Journal of Waterway, Port, Coastal, and Ocean Engineering – ASCE*, **121**(2), 77–87.

Penney, W. G. and Price, A. T. (1952). Part I. The Diffraction Theory of Sea Waves and the Shelter Afforded by Breakwaters. *Philosophical Transactions of the Royal Society of London. Series A, Mathematical and Physical Sciences*, **244**(882), 236–253.

Peregrine, D. H. (1983). Breaking Waves on Beaches. *Annual Review of Fluid Mechanics*, **15**, 149–178.

Plant, N. G., Holman, R. A., Freilich, M. H., and Birkemeier, W. A. (1999). A simple model for interannual sandbar behavior. *Journal of Geophysical Research - Oceans*, **104**(C7), 15755–15776.

Plant, N. G., Freilich, M. H., and Holman, R. A. (2001). Role of morphologic feedback in surf zone sandbar response. *Journal of Geophysical Research - Oceans*, **106**(C1), 973–989.

Pos, J. D. and Kilner, F. A. (1987). Breakwater Gap Wave Diffraction - An Experimental and Numerical Study. *Journal of Waterway, Port, Coastal, and Ocean Engineering – ASCE*, **113**(1), 1–21.

Rakha, K. A., Deigaard, R., and Brøker, I. (1997). A phase-resolving cross shore sediment transport model for beach profile evolution. *Coastal Engineering*, **31**(1-4), 231–261.

Reniers, A. J. H. M., Roelvink, J. A., and Thornton, E. B. (2004). Morphodynamic modeling of an embayed beach under wave group forcing. *Journal of Geophysical Research - Oceans*, **109**(C1), Art.no. C01030.

Rienecker, M. M. and Fenton, J. D. (1981). A Fourier Approximation Method for Steady Water-Waves. *Journal of Fluid Mechanics*, **104**, 119–137.

Roelvink, J. A. and Brøker, I. (1993). Cross-Shore Profile Models. *Coastal Engineering*, **21**(1-3), 163–191.

Roelvink, J. A. and Stive, M. J. F. (1989). Bar-Generating Cross-Shore Flow Mechanisms on a Beach. *Journal of Geophysical Research - Oceans*, **94**(C4), 4785–4800.

Roulund, A., Sumer, B. M., Fredsøe, J., and Michelsen, J. (2005). Numerical and experimental investigation of flow and scour around a circular pile. *Journal of Fluid Mechanics*, **534**, 351–401.

Ruessink, B. G., van Enckevort, I. M. J., Kingston, K. S., and Davidson, M. A. (2000). Analysis of observed two- and three-dimensional nearshore bar behaviour. *Marine Geology*, **169**(1-2), 161–183.

Rusche, H. (2002). *Computational Fluid Dynamics of Dispersed Two-Phase Flows at High Phase Fractions*. Ph.D. thesis, Imperical College of Science, Technology and Medicine. Available at: http://powerlab.fsb.hr/ped/kturbo/OpenFOAM/docs/HenrikRuschePhD2002.pdf.

Sagaut, P. (2006). *Large Eddy Simulation for Incompressible Flows - An Introduction*. Springer, 3rd edition.

Sallenger, A. H., Holman, R. A., and Birkemeier, W. A. (1985). Storm-Induced Response of a Nearshore-Bar System. *Marine Geology*, **64**(3-4), 237–257.

Schäffer, H. A., Madsen, P. A., and Deigaard, R. (1993). A Boussinesq Model for Waves Breaking in Shallow-Water. *Coastal Engineering*, **20**(3-4), 185–202.

Scott, C. P., Cox, D. T., Maddux, T. B., and Long, J. W. (2005). Large-scale laboratory observations of turbulence on a fixed barred beach. *Measurement, Science & Technology*, **16**(10), 1903–1912.

Shimizu, T. and Ikeno, M. (1996). Experimental Study on Sediment Transport in Surf and Swash Zones Using Large Wave Flume. *Proceeding to Coastal Engineering Conference*, **III**, 3076–3089.

Short, A. D. (1999). *Wave-Dominated Beaches*, chapter 7, 173–203. Wiley, 1st edition. From *Handbook of Beach and Shoreface Morphodynamics*. Editor: A.D. Short.

Short, A. D. and Aagaard, T. (1993). Single and multi-bar beach change models. *Journal of Coastal Research*, **15**(Special Issue), 141–157.

Short, A. D. and Masselink, G. (1999). *Embayed and Structurally Controlled Beaches*, chapter 9, 230–250. Wiley, 1st edition. From *Handbook of Beach and Shoreface Morphodynamics*. Editor: A.D. Short.

Speziale, C. G., Abid, R., and Anderson, E. C. (1990). A critical evaluation of two-equation models for near wall turbulence. *AIAA Paper 90-1481*.

Sumer, B. M. and Fredsøe, J. (2001). Wave scour around a large vertical circular cylinder. *Journal of Waterway, Port, Coastal, and Ocean Engineering – ASCE*, **127**(3), 125–134.

Sumer, B. M., Chua, L. H. C., Cheng, N. S., and Fredsøe, J. (2003). Influence of turbulence on bed load sediment transport. *Journal of Hydraulic Engineering – ASCE*, **129**(8), 585–596.

Sunamura, T. and Irie, I. (1988). *Nearshore Dynamics and Coastal Processes - Theory, Measurements and Predictive Models*, 136–166. University of Tokyo Press, 1st edition. Editor: Horikawa, K.

Svendsen, I. A. (1984). Mass Flux and Undertow in a Surf Zone. *Coastal Engineering*, **8**(4), 347–365.

Svendsen, I. A. (2006). *Introduction to Nearshore Hydrodynamics*, volume 24 of *Advanced Series on Ocean Engineering*. World Scientific, 1st edition.

Svendsen, I. A. and Hansen, J. B. (1976). Deformation up to Breaking of Periodic Waves on a Beach. *Proceeding to Coastal Engineering Conference*, **I**, 477–496.

Symonds, G., Huntley, D. A., and Bowen, A. J. (1982). Two-Dimensional Surf Beat - Long-Wave Generation by a Time-Varying Breakpoint. *Journal of Geophysical Research - Oceans and Atmospheres*, **87**(NC1), 492–498.

Thornton, E. B. (1970). Variation of Longshore Current Across the Surf Zone. *Proceeding to Coastal Engineering Conference*, **I**, 291–308.

Ting, F. C. K. and Kirby, J. T. (1994). Observation of Undertow and Turbulence in a Laboratory Surf Zone. *Coastal Engineering*, **24**(1-2), 51–80.

Torres-Freyermuth, A., Losada, I. J., and Lara, J. L. (2007). Modeling of surf zone processes on a natural beach using Reynolds-Averaged Navier-Stokes equations. *Journal of Geophysical Research - Oceans*, **112**(C9), Art.no. C09014.

Tuković, Ž. (2005). *Metoda Kontrolnih Volumena Na Domenama Promjenjivog Oblika (Finite Volume Method on Domains of Variable Shape)*. Ph.D. thesis, University of Zagreb. (In Croatian).

Ubbink, O. and Issa, R. I. (1999). A method for capturing sharp fluid interfaces on arbitrary meshes. *Journal of Computational Physics*, **153**(1), 26–50.

van Enckevort, I. M. J., Ruessink, B. G., Coco, G., Suzuki, K., Turner, I. L., Plant, N. G., and Holman, R. A. (2004). Observations of nearshore crescentic sandbars. *Journal of Geophysical Research - Oceans*, **109**(C6), Art.no. C06028.

van Rijn, L. C. (1984). Sediment transport, part II: Suspended load transport. *Journal of Hydraulic Engineering*, **110**(11), 1613–1641.

Wenneker, I., van Dongeren, A., Lescinski, J., Roelvink, D., and Borsboom, M. (2011). A Boussinesq-type wave driver for a morphodynamical model to predict short-term morphology. *Coastal Engineering*, **58**(1), 66–84.

Wilcox, D. C. (2006). *Turbulence Modeling for CFD*. DCW Industries, 3rd edition.

Wilcox, D. C. (2008). Formulation of the $k-\omega$ Turbulence Model Revisited. *AIAA Journal*, **46**(11), 2823–2838. AIAA 45th Aerospace Sciences Meeting and Exhibit, Reno, NV, 2007.

Wright, L. D. and Short, A. D. (1984). Morphodynamic Variability of Surf Zones and Beaches - A Synthesis. *Marine Geology*, **56**(1-4), 93–118.

Zhang, Q. and Liu, P. L. F. (2008). A new interface tracking method: The polygonal area mapping method. *Journal of Computational Physics*, **227**(8), 4063–4088.

Zyserman, J. A. and Fredsøe, J. (1988). Numerical Simulation of Concentration Profiles of Suspended Sediment under Irregular Waves. *Prog. Rep.*, **68**, 15–26. ISVA, Tech. Uni. of Denmark.

Zyserman, J. A. and Fredsøe, J. (1994). Data-Analysis of Bed Concentration of Suspended Sediment. *Journal of Hydraulic Engineering – ASCE*, **120**(9), 1021–1042.

Appendix A

Modelling of Wave Boundary Layers

A.1 Low Reynolds Number Closure

The simulation of turbulent wave boundary layers has been verified against the experimental data of Jensen *et al.* (1989), where the friction velocity, $u_f = \|\mathbf{u}_f\|_2$, is determined over a rough boundary using a log-fit method. The experiments are conducted in an oscillatory tunnel with a height of 0.28 m. The period is $T = 9.72$ s, the maximum nearbed orbital velocity is $u_m = 2.0$ m/s, and the bed is made rough by glueing sand paper with a roughness height of 0.85 mm onto the bed.

In figure A.1 the experimental data is compared with the simulated friction velocity using the low Reynolds number closure. It is seen that the magnitude and temporal variation of the bed shear stress is well predicted.

The near bed boundary condition for k at rough boundaries was suggested (Roulund *et al.*, 2005) to be set to $\mathbf{n}_s \nabla k = 0$, where $\mathbf{n}_s$ is the unit normal vector to the boundary. This is based on physical considerations and measurements of the distribution of the turbulent kinetic energy close to rough boundaries, where the turbulence does not go to zero, but rather approach a finite value, see e.g. the experimental data reported by Nezu and Nakagawa (1993); Sumer *et al.* (2003). These arguments were considered in detail by Fuhrman *et al.* (2010) for the convergence properties as a function of near bed resolution for a current. Preliminary estimates suggest that a reasonable accuracy can be achieved for a near bed resolution of $\Delta y / k_N < 0.01$, where Δy is the near bed resolution.

The same approach is used in unsteady motion, where the rate of convergence in the maximum friction velocity, $u_{f,m}$, as a function of Δy and $k^+_{N,m} = k_N u_{f,m} / \nu$ is considered. This is depicted in figure A.2. The results

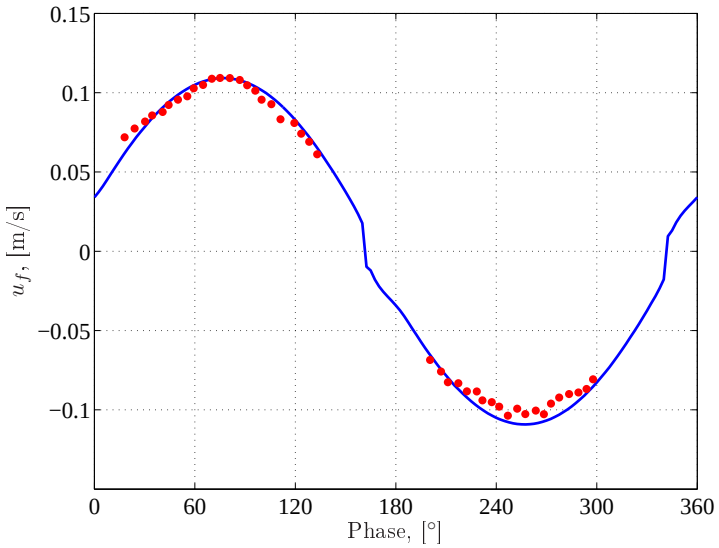

Figure A.1: *Comparison of the friction velocity in a rough turbulent oscillatory boundary layer. (Dots): Experimental data from Jensen* et al. *(1989), test 13 (Full line): Simulation using the low Reynolds number closure model.*

clearly show that the method reported by Fuhrman *et al.* (2010) is also applicable to unsteady flows and confirm the rule of thumb of $k_N/\Delta y = \mathcal{O}(100)$ for a near wall discretisation.

A similar comparison is depicted for k_{nw} in figure A.3, and the same conclusions can be drawn on the existence of a unique convergence curve for a large range of roughness heights.

A.2 High Reynolds Number Closure

The high Reynolds number closure has been tested against the low Reynolds number closure model, see §A.1. Three wave boundary layers are considered, all of which are turbulent (Jensen *et al.*, 1989, figure 8). The period and free stream velocity amplitude are (i) $T = 9.72$ s and $u_m = 2$ m/s, (ii) $T = 1.0$ s and $u_m = 2$ m/s, and (iii) $T = 0.1$ s and $u_m = 20$ m/s. The high Reynolds number closure is solved for different near wall discretisation, namely $\Delta y/k_N = \{0.5,\ 1.0,\ 1.5,\ 2.5,\ 3.0\}$. The results from this analysis is depicted in figure A.4.

It is seen that both the amplitude and the phase-lag is well captured by the high Reynolds number model. For decreasing wave period, however, larger and larger discrepancies are found between the high and low closure

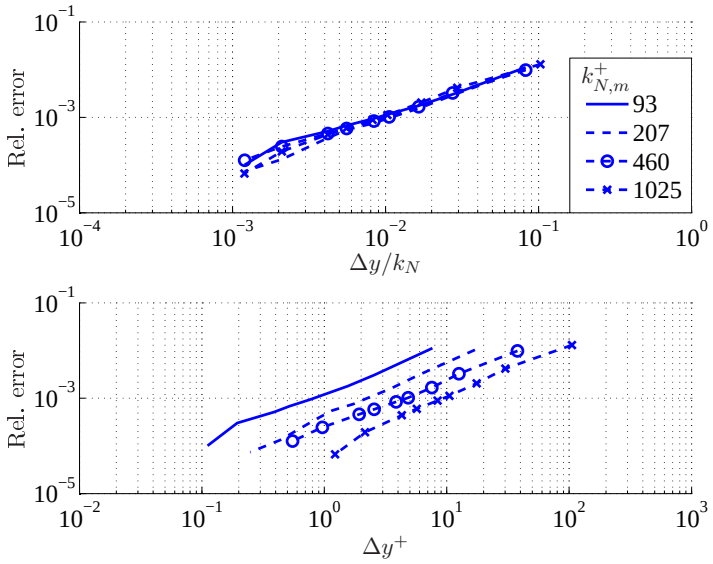

Figure A.2: *Convergence of $u_{f,m}$ as a function of (a) $\Delta y/k_N$ and (b) $\Delta y^+ = u_{f,m}\Delta y/\nu$ for 4 values of $k^+_{N,m}$.*

models around zero-crossing. This discrepancy is almost non-existing for $T = 9.72$ s, whereas it is pronounced for $T = 0.1$ s. In order to maintain the fully turbulent assumption, the simulations needed to be run with unrealistically large values of u_m, hence around zero-crossing the acceleration becomes more and more important relative to the magnitude of $\mathbf{u}$ in the determination of the friction velocity. The importance of the acceleration term suggests that an improvement of the method could be obtained by using a log-linear profile (e.g. Fredsøe and Justesen, 1986) instead of the logarithmic profile assumption. Nevertheless, such large acceleration seem unrealistic in the present study near the boundary. The maximum acceleration for $T = 1$ s is approximately $1.3\|\mathbf{g}\|_2$. Such accelerations are experienced in the surf zone, however, they are found at the crest of the wave in the initial part of the wave breaking process (Peregrine, 1983).

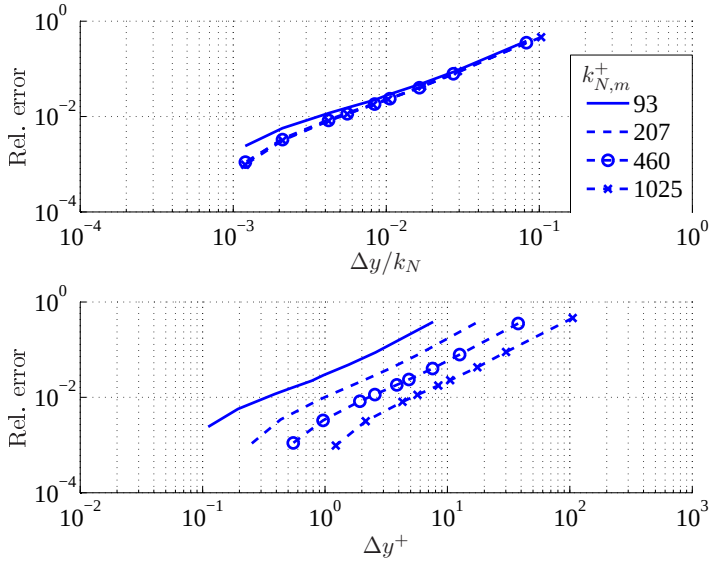

Figure A.3: *Convergence of k_{nw} as a function of (a) $\Delta y/k_N$ and (b) $\Delta y^+ = u_{f,m}\Delta y/\nu$ for 4 values of $k^+_{N,m}$.*

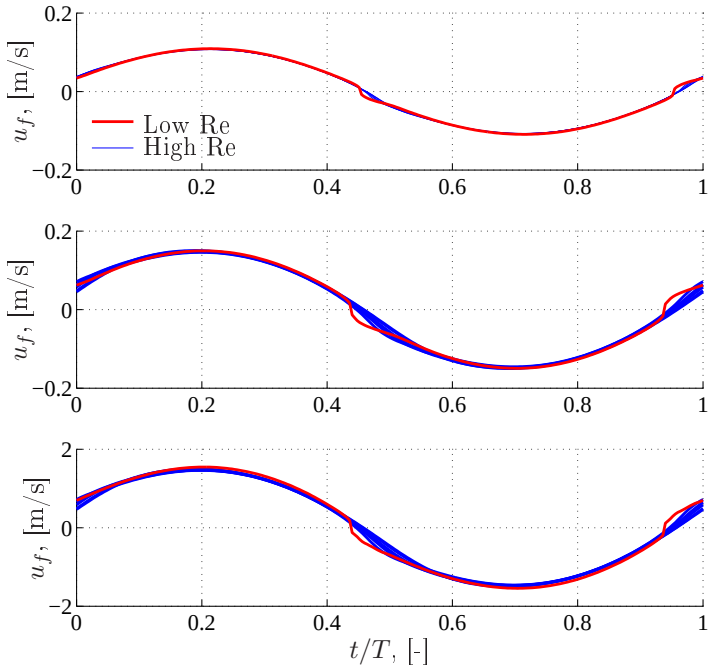

Figure A.4: *The friction velocity for $\Delta y/k_N = \{0.5,\ 1.0,\ 1.5,\ 2.5,\ 3.0\}$. (top): $T = 9.72\ s$ and $u_m = 2\ m/s$ (middle): $T = 1.0\ s$ and $u_m = 2\ m/s$ (bottom): $T = 0.1\ s$ and $u_m = 20\ m/s$*

Appendix B

Mesh Generation

The mesh generation for the wave breaking simulations follows the same basic procedure. The mesh consists of three horizontal layers, see figure B.1, denoted I, II and III. Additionally the lower, y_L, and upper bounds, y_U, need to be defined.

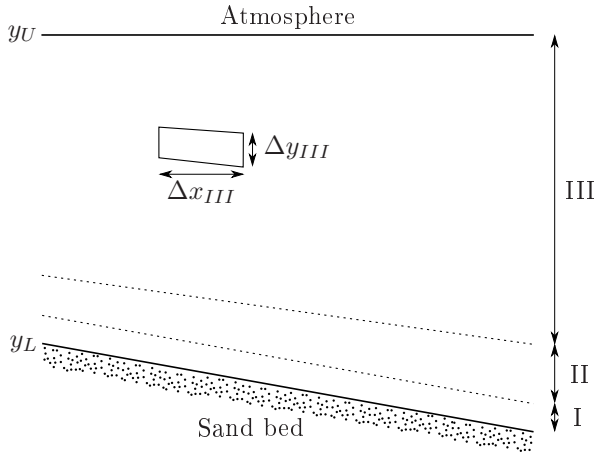

Figure B.1: *Sketch of the 3 horizontal layers used in the mesh generation.*

Layer I is equidistantly discretised and it consists of cells being order d in height. This layer is introduced to be able to control the near bed mesh, so a mesh line is placed exactly δ_b from the bed as discussed in §3.2. In the outer layer, III, the mesh is also equidistantly discretised over the vertical, however, $\Delta y_I \ll \Delta y_{III}$. To connect these two layers, layer II is non-uniformly discretised with a vertical stretching. Each layer consists of a

number of predefined cells, N_I, N_{II}, and N_{III}. The discretisation must fulfil

$$y_U - y_L = \Delta y_I N_I + \sum_{i}^{N_{II}} G^{(i-1)} \Delta y_I + N_{III} \Delta y_{III} \tag{B.1}$$

in addition to

$$G^{N_{II}-1} \Delta y_I = \Delta y_{III} \quad . \tag{B.2}$$

The latter produces a smooth transition over the vertical between layer II and III. In the horizontal direction, the spacing between the vertical mesh lines is controlled by keeping the aspect ratio, $AR = \Delta x_{III}/\Delta y_{III}$, constant.

Appendix C

The Sand Slide Mechanism

C.1 Sand Slide Routine

The sand slide routine in Niemann *et al.* (2011) considers each face of the computational boundary individually and fulfil the sand slide criterion on these faces locally by adjusting the vertical coordinate of the nodes (a similar method is used by Marieu *et al.* (2008)). This localised approach might lead to an exceedance of the angle of repose on the faces to either side of the current face. The correction of their slope, however, might result in an exceedance of the angle of repose of the original face. This recursive sliding approach results in an $\mathcal{O}(M^3)$ numerical "efficiency". Fortunately, M is typically small, say $\mathcal{O}(10)$, so the computational burden is generally small compared to e.g. the solution to the pressure equation.

The method described below was tested and it is found to scale as $\mathcal{O}(M)$. The practical part of the implementation, however, turned out to be unstable, thus the present work is based on the method by Niemann *et al.* (2011) as time was too limited to investigate the source of this instability, hence the more robust and slower algorithm was preferred*. Nevertheless, the method is outlined below.

Similarly to the method of Niemann *et al.* (2011), the proposed method considers a geometrical redistribution of the sediment. First, consider the point B in figure C.1. The face to its left will be subject to a slide failure, hence a lowering of point B. This could successively lead to sliding to the right of B. The two points A and B holds between them a connected set of faces, which exceeds the angle of repose, thus after the sliding mechanism is completed, they should all have a slope of $\tan\beta_{stable}$.

The lines, ℓ_{A} and ℓ_{B}, are the bounds of extreme limits to the stable slope, neither of which are the actual stable solution due to the requirement

*The stated numerical efficiencies are derived based on practical experience.

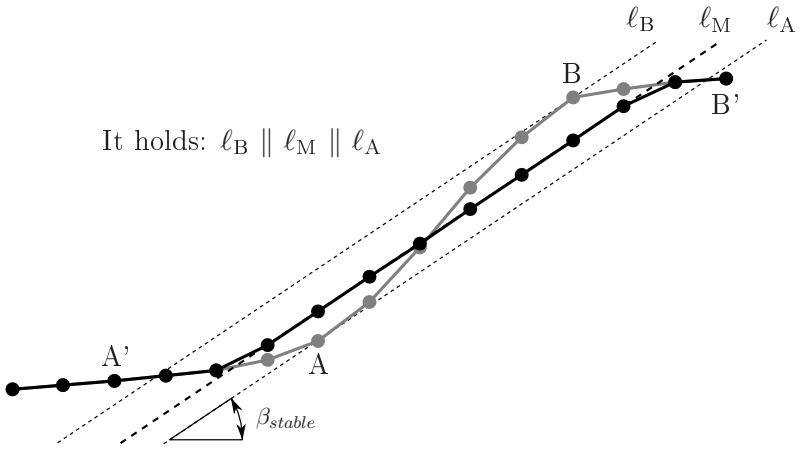

Figure C.1: *Sketch of the sand slide mechanism. The grey line is the original bed and the black line adjust to the constraints given by the line ℓ_M*

of sediment mass conservation. They are merely lower and upper bounds, respectively. The points A' and B' are the points just outside these bounds, hence unchanged during and after the sliding.

Any line, ℓ_M, between the two bounds describes a possible stable solution. ℓ_M adjusts the profile such that all points between A and B (these included) are moved vertically to lie on ℓ_M. The points between A' and A and B and B' are either moved to ℓ_M or maintain their original position depending on their position relative to the line, see figure C.1. The line, which yields the final stable solution, is the one, which result in mass conservation. The solution is in practical terms found using a bisection routine.

C.2 Example of the Exceedance of Angle of Repose

The sliding mechanism has been turned on in §6. This is needed, as the breaking of regular waves result in a constant forcing in the same place, which can maintain a unidirectional flow (see figure C.3) over a complete wave period. This unidirectional flow can sustain extremely large bed slopes in the order of $\mathcal{O}(40°\text{-}50°)$, see figure C.2(a). The mechanism in the model responsible for these large slopes and the mechanisms, which are responsible for the subsequent break-down of the model, are discussed here, exemplified by test run A02SB without sand slide; see table 6.1 for the environmental parameters. The analysis will be restricted to two dimensions, where $\alpha = 0°$ for down-slope flow and $\alpha = 180°$ for up-slope flow.

Eq. (3.35) for the critical Shields parameter reads

$$\theta_c' = \theta_{c0}' \left(\cos\beta \sqrt{1 - \frac{\sin^2\alpha \tan^2\beta}{\mu_s^2}} - \frac{\cos\alpha \sin\beta}{\mu_s} \right) \quad .$$

For $\alpha = 180°$, θ_c' is strictly positive for all values of $\beta \in [0,\ 90°]$, thus effectively increasing the critical Shields parameter relative to that on a flat bed. Suppose that β become larger than the angle of repose and the flow direction changes ($\alpha = 0°$), then it is easily identified that θ_c' become negative, which physically does not make sense and is not handled by the current implementation (numerical break-down).

This happens in test case A02SB. The bed level evolution is depicted in figure C.2(a), and it is evident that the bed slope by far exceed the angle of repose on the shoreward side on the inner breaker bar ($x = 25$ m). Furthermore, it can be seen that the increase in slope occur rapidly, which is due to the generation of a vortex on the shoreward side of the bar. The bed shear stress below this vortex is constant in the offshore direction during this period. The rapid increase in the shoreward slope is explicitly depicted in figure C.2(b), where the maximum and minimum slopes along the entire profile are shown.

The flow field on the shoreward side of the inner breaker bar is depicted in figure C.3 for 5 snapshots over one wave period. In the top panel a breaking wave rush over the bar crest, but due to the steepness of the shoreward side of the bar, the flow separates. The resulting offshore directed nearbed velocities are maintained over an entire wave period. The direction is firstly maintained because of flow separation while the surface roller passes the shoreward slope, and afterwards it is the combination of undertow and offshore directed orbital motion in the trough.

Figure C.3 also depicts the intrawave description of the bed level change. It is seen that the shoreward side of the bar is more or less rotated around the bar crest leading to a steepening of the crest profile. The offshore movement of the shoreward side is consistent with the local hydrodynamic forcing.

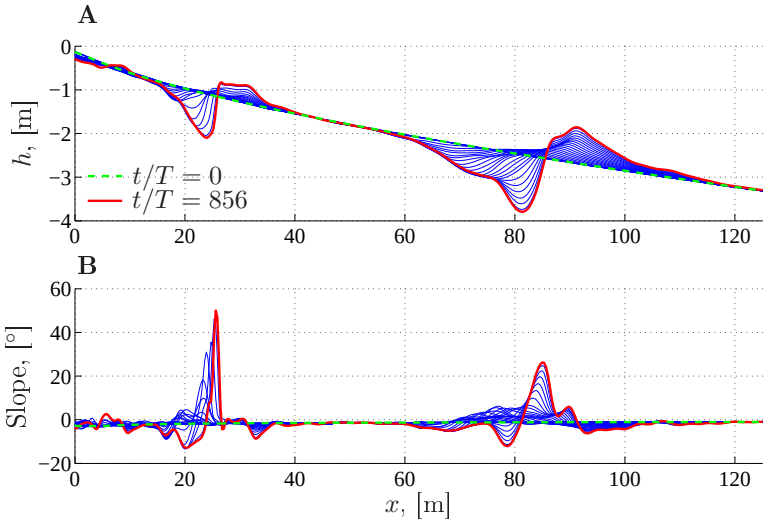

(a) Profile evolution

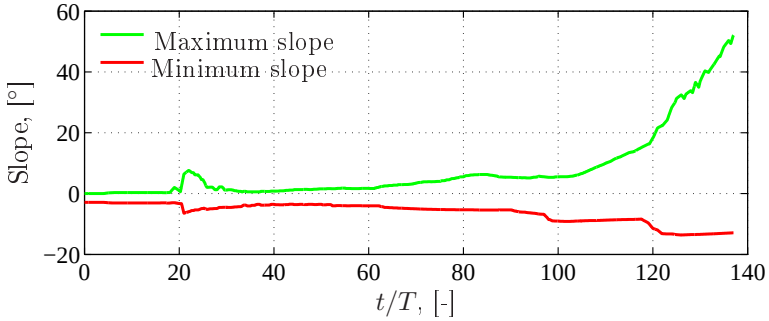

(b) Minimum and maximum slope

Figure C.2: *(a): The temporal development of the breaker bars for A02SB in the case of no sand slide mechanism.* $f_m = 6.25$. *(b): Minimum and maximum profile slope as a function of time.*

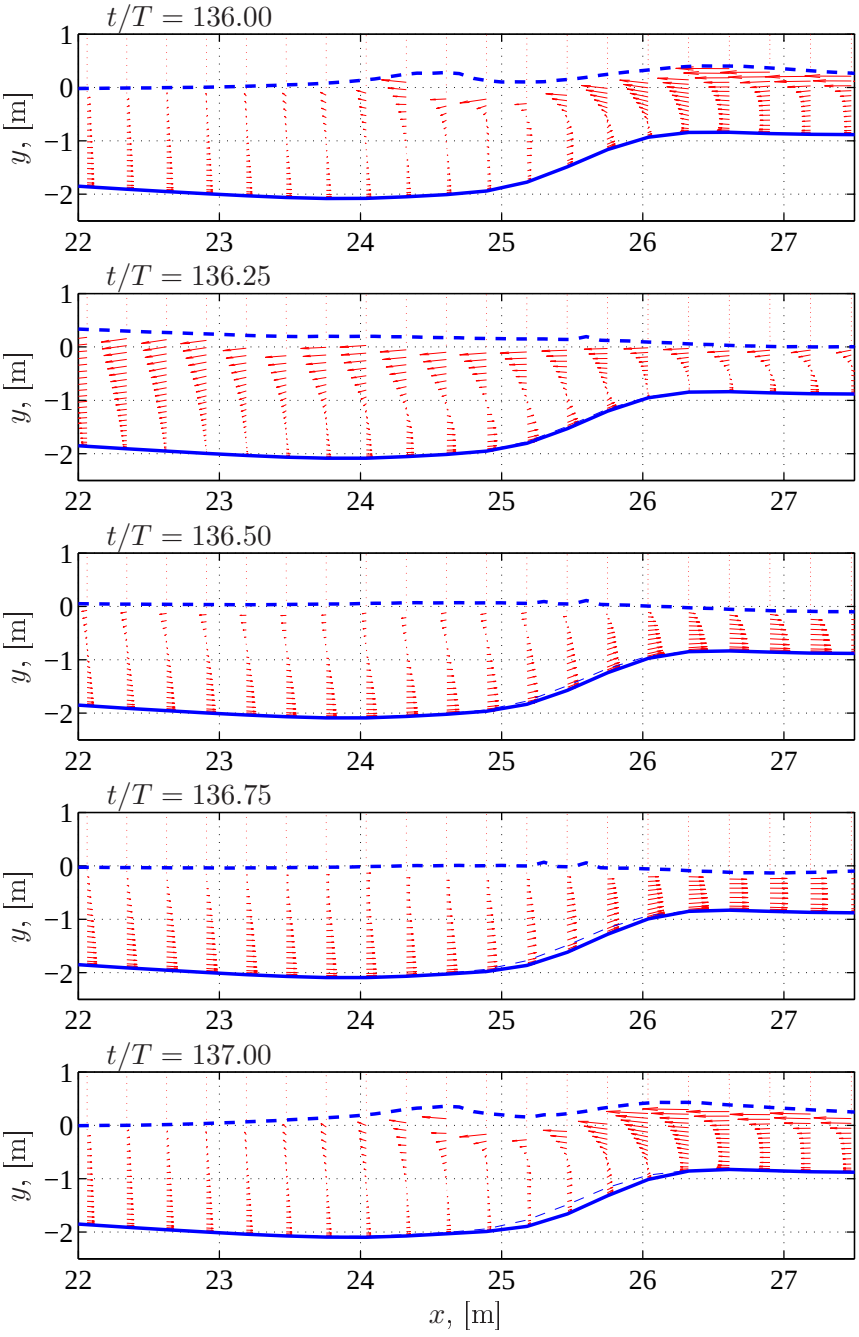

Figure C.3: *The velocity field on the shoreward side of the inner bar taken at 5 hydrodynamic time instances. The lowermost panel correspond to morphological time* $t_m/T = 856$ *where* $f_m = 6.25$. *(Full, thick): Current bed level. (Dashed, thin): Bed level at* $t/T = 136$. *(Dashed, thick): Instantaneous surface elevation. Note that axes are not to scale.*

Appendix D

Velocity Field in Breaking Waves

The velocity field is depicted for test cases FA1 and FB2 around the breaking point in the figures D.1–D.4. See §5.1 for a discussion of the results.

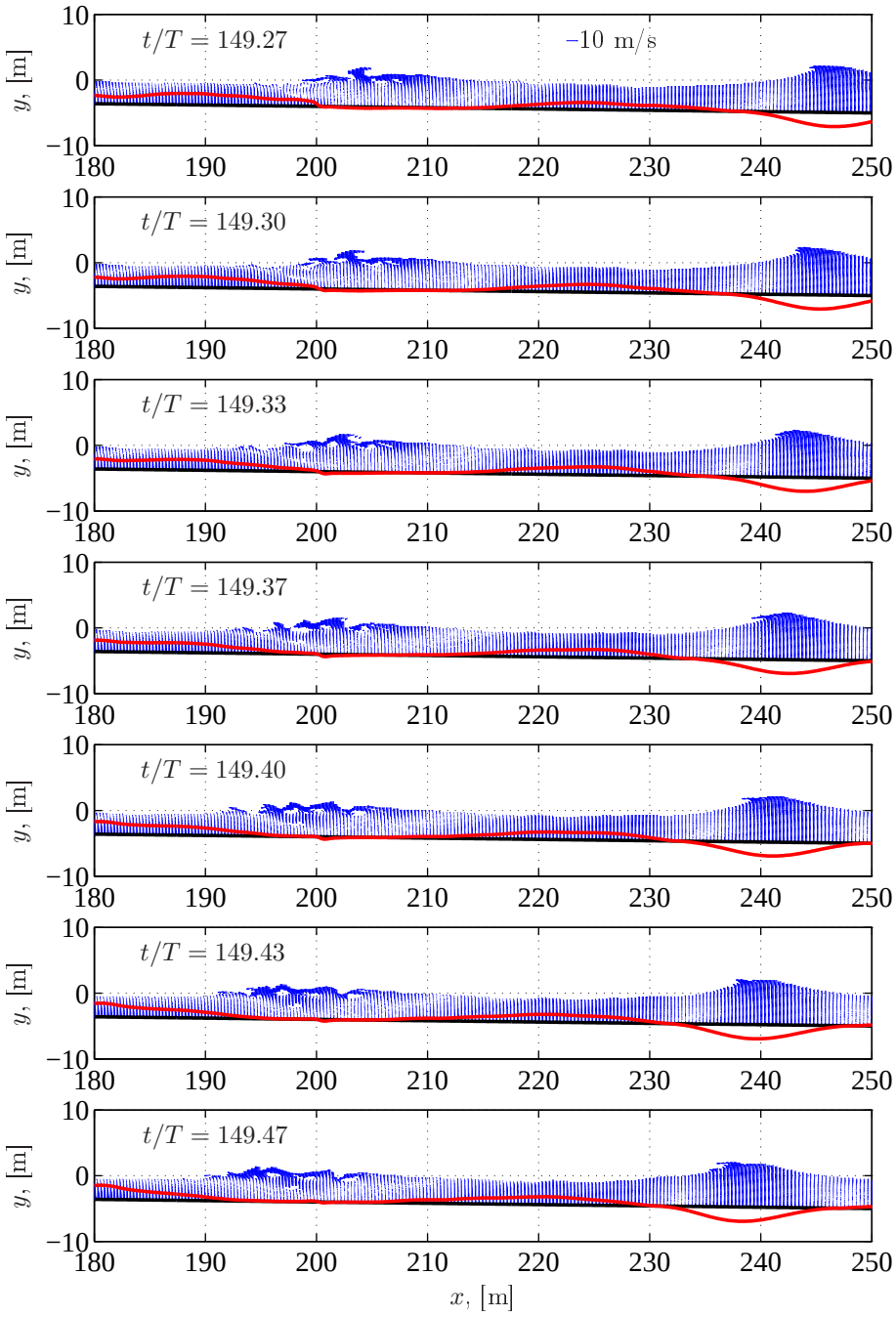

Figure D.1: *Snapshots of velocity field from FA1 ($\zeta_0 = 0.083$, $T = 6$ s). Full line is $200u_f|u_f|$ depicted relative to the bed. Every second vertical line of data is omitted for clarity. Vectors plotted for $\gamma > 0.9$. $u_f|u_f| > 0.0$ when directed offshore.*

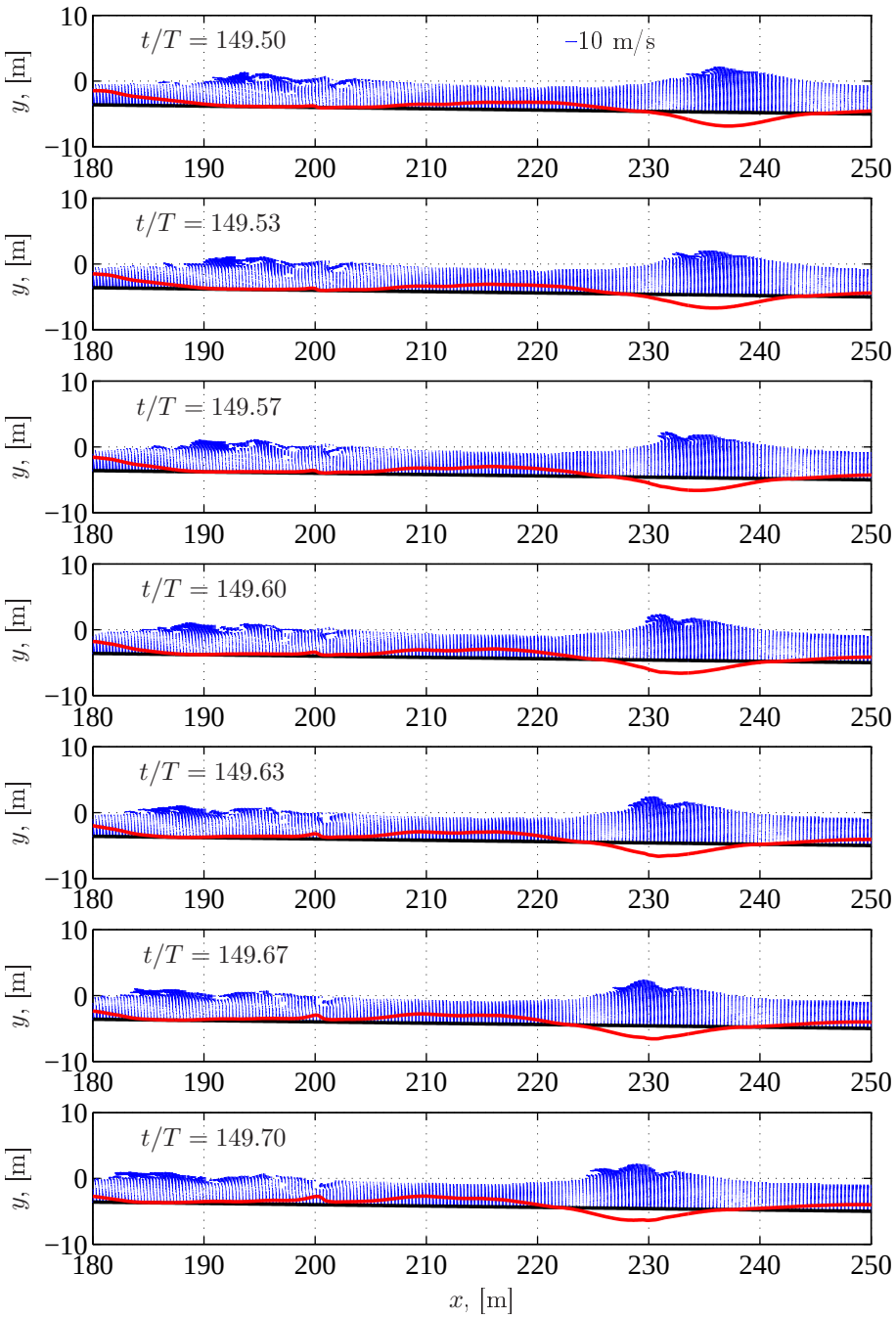

Figure D.2: *As in figure D.1*

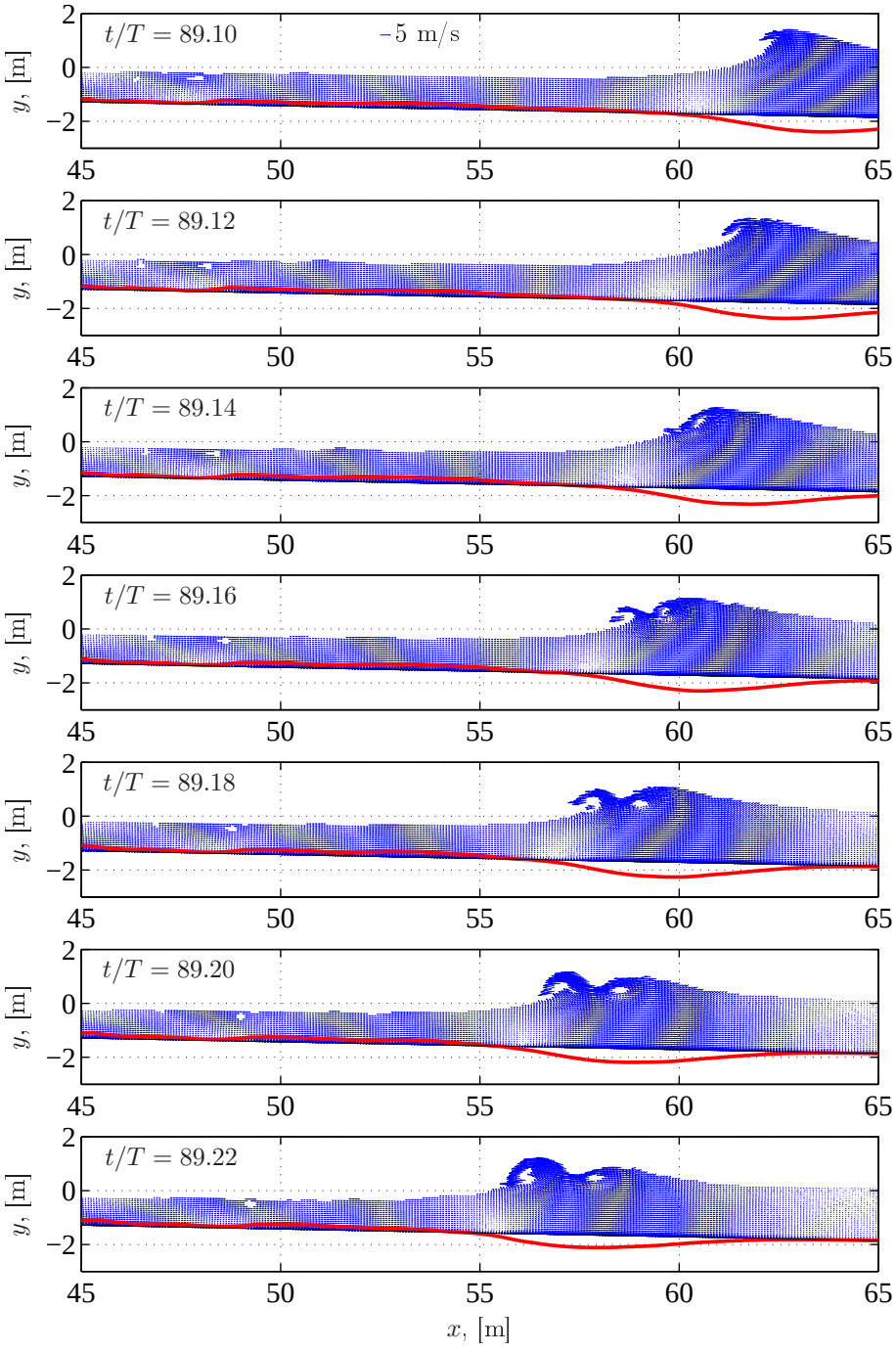

Figure D.3: *Snapshots of velocity field from FB2 ($\zeta_0 = 0.385$, $T = 10$ s). Full line is $50u_f|u_f|$ depicted relative to the bed. Vectors plotted for $\gamma > 0.9$. $u_f|u_f| > 0.0$ when directed offshore.*

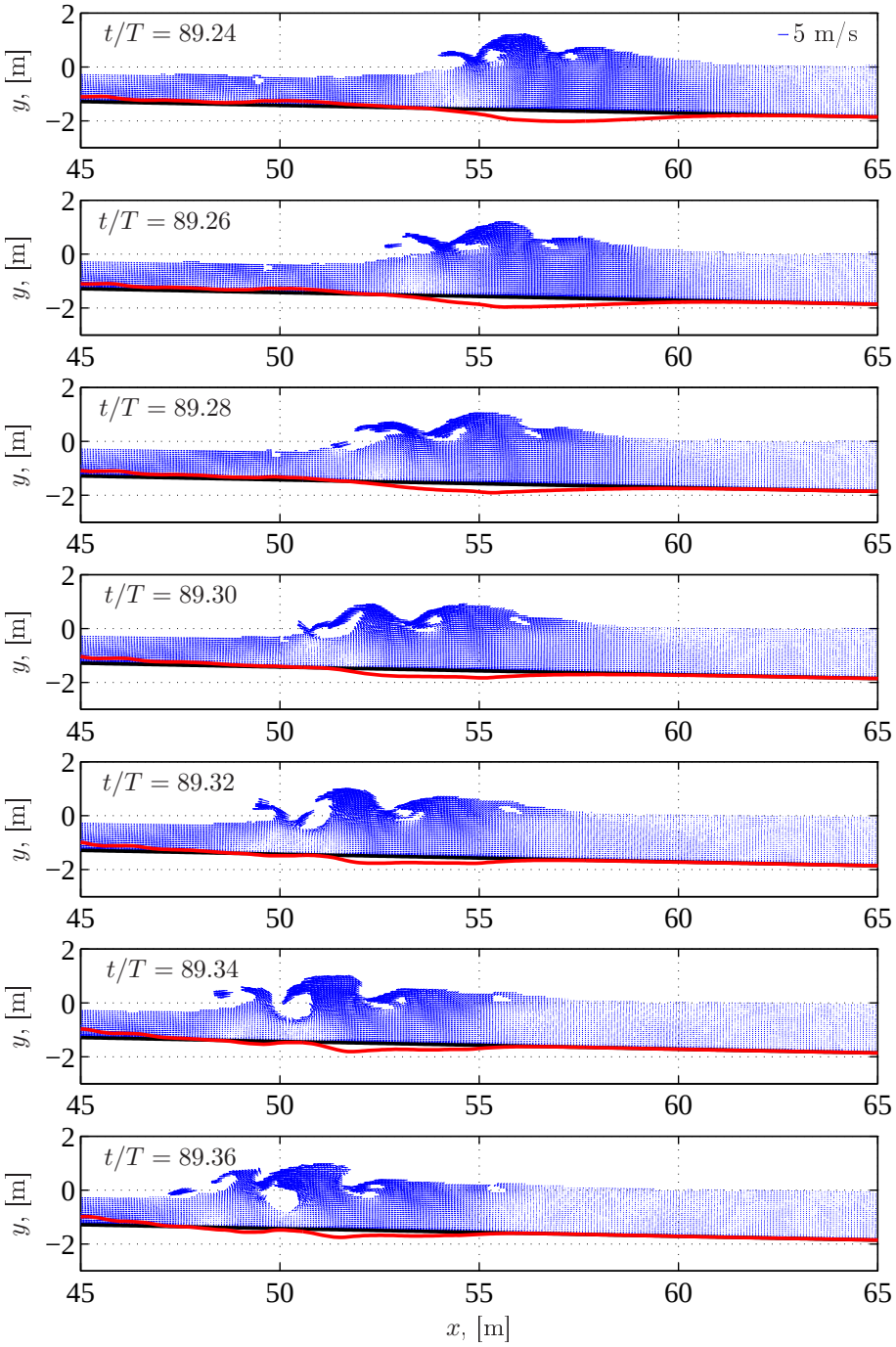

Figure D.4: *As in figure D.3*

DTU Mechanical Engineering
Section of Coastal, Maritime and Structural Engineering
Technical University of Denmark

Nils Koppels Allé, Bld. 403
DK- 2800 Kgs. Lyngby
Denmark
Phone (+45) 45 25 13 60
Fax (+45) 45 88 43 25
www.mek.dtu.dk
ISBN: 978-87-90416-64-5

DCAMM
Danish Center for Applied Mathematics and Mechanics

Nils Koppels Allé, Bld. 404
DK-2800 Kgs. Lyngby
Denmark
Phone (+45) 4525 4250
Fax (+45) 4593 1475
www.dcamm.dk
ISSN: 0903-1685